Hierarchical structure and diagenesis of Sauropod long bones using advanced characterization techniques

Dissertation
zur
Erlangung des Doktorgrades (Dr. rer. nat.)
der
Mathematisch-Naturwissenschaftlichen Fakultät
der
Rheinischen Friedrich-Wilhelms-Universität Bonn

vorgelegt von
Maïtena Dumont
aus
Clermont-Ferrand, Frankreich

Bonn, 2012

Angefertigt mit Genehmigung der Mathematisch-Naturwissenschaftlichen Fakultät der Rheinischen Friedrich-Wilhelms-Universität Bonn

Angefertigt mit Genehmigung der Mathematisch-Naturwissenschaftlichen Fakultät der Rheinischen Friedrich-Wilhelms-Universität Bonn

1. Gutachter: Prof. Dr. P. Martin Sander
2. Gutachter: Prof. Dr. Anke Kaysser-Pyzalla
Tag der Promotion: 17.04.2012
Erscheinungsjahr: 2013

To my father

Acknowledgements

First of all I would like to express my sincere gratitude to my supervisors, Prof.Dr.-Ing Anke Rita Kaysser-Pyzalla and Prof. Martin Sander for encouraging way to guide me to an understanding in my work and their invaluable comments, help, discussions and patience during my research.

Furthermore, I would like to acknowledge the financial supports of the project the DFG as well as Helmholtz Zentrum of Berlin.

I would also like to express my special thanks to Prof. Andras Borbely and Dr. Aleksander Kostka, who’s precious advises, help in the techniques, shared of their knowledge accompanied me constantly in my work.

I would like also to thank Benjamin Breitbach for his help for performing X-Ray diffraction measurement, and Monika Nellesen for her help in TEM sections preparation.

I would also like to thank all the people from administration of different institute for their patience and their help for all the administrative paper: Frau Adrian (Max Planck Institut), Frau Heitplatz (University of Bonn), Frau Gruber and Frau Ulrich (Helmholtz Zentrum Berlin)

My sincere thanks go to many friends and colleagues from MPIE: Pedro Brito, Hauke, Rodrigo, Federico, Maria, Marcin, Rosario, Pedro Silva, Lais, Leonardo, Clara, David, Augusta, Haroldo, Lucas, Nahid, Anahita, Nimah… for their joy, their help and their good laugh in the office. A big thank to my flatmate Alessandro.

I would also thank some the DFG member research of sauropod biology for their scientific discussions.

I would like as well to say a big thanks to the French paleontology crew (for their support, the good time share with them in excavation/in conference): Alida, Anne-Claire, Sophie, Alexandra, Lionel, Cyril, Vincent, Sandrine, Damien, Petit Seb, Nathalie, Nicolai, Pong. I would like to thank as well the two people who always support during all my studies Jean Le Loeuff et Christel Souillat (merci pour tous ses bons moments sur les fouilles d’Esperaza).

I would also thank my best friends: Marjorie, Marvin, Nath and Sandrine.

My last but not least thanks go to my family, specially my mother and my brother Axel for their steady encouragement over all these years. I would like to dedicate this work to them and to my father, who passes on his passion for geology, minerals and fossils in general and who always believed in my work.

Table of contents

Published as Dumont, M., Zoeger, N., Streli, C., Wobrauschek, P., Falkenberg, G., Pyzalla, A.R. 2009. Synchrotron XRF analyses of element distribution in fossilized sauropod dinosaur bones. Powder diffraction 24(2):190-194

Acronyms

Symbols

α	rotation angle (in normal direction)
β	rotation angle (in longitudinal direction)
d	interplanar distance
eV	electronVolts
ε	apparent crystallite size (scherrer equation)
K	Shape factor
λ	wavelength
mm	millimeter
µm	micrometer
nm	nanometer
sin	sinus of angle
T	time
t	true crystallite size
θ	diffraction angle
φ	azimuthal angle

Abbreviations

BF	Bright field
BSE	Backscattered electrons
DF	Dark field
EDX	Energy dispersive X-Rays
FWHM	Full Width Half Maximum
FBL	FibroLamellar Bone
FIB	Focused ion beam
HA	Hydroxyapatite
HOS	Histological ontogenetic stage
HRTEM	High resolution TEM
LAGs	Lines of arrested growth
LD	Longitudinal direction
µ-XRF	micro- X-Ray Fluorescence
mrd	multiple random distribution
ND	Normal direction
ODF	Orientation distribution function
PIXE	Proton induced X-Ray emission
PL	Polarized light
SAD	Selected area diffraction
sp.	species
SR-µ-XRF	Synchrotron micro X-Ray Fluorescence
SEM	Scanning electron microscopy
STEM	Scanning TEM
TD	Transverse direction
TEM	Transmission electron microscopy
XRD	X-Ray diffraction
wt.%	weight percent

Abstract

Sauropod dinosaurs are one of the most fascinating animals, mainly because of the extreme size that they could reach. This gigantism led to the hypothesis that sauropod long bones adopted an optimized hierarchical structure to resist the high loads caused by their heavy weight in excess of 100 tons. The present work aims at evaluating this hypothesis with the following objectives: (1) Investigate modifications linked to diagenesis at different hierarchical levels of the sauropod fossil using new techniques and methods. (2) Analyze the structure of bone samples in terms of crystallographic orientation, crystal size as well as the general arrangement of fibrolamellar (FBL) and secondary bone observed in sauropod cortical bone.

In the first part, diagenetic effects appearing during fossilization process were studied with different techniques. Synchrotron-X-Ray fluorescence was used for the first time on fossil material, allowing investigations of considerably higher resolution compared to conventional techniques. Furthermore, a combination of X-Ray diffraction and energy dispersive X-Ray analysis during scanning electron microscopy (SEM-EDX) as well as transmission electron microscopy (TEM-EDX) was used to evaluate diagenetic changes at different hierarchical levels of fossil bones. Infillings of secondary minerals were mostly detected in natural pores of bones (vascular canals and osteocyte lacunae). The combination of the different analysis techniques applied in this study revealed that although seemingly unaffected at the histological level, the sauropod fossils endured strong diagenetic changes. Additionally, pronounced differences concerning the diagenesis and secondary mineral infillings between bone samples of a same postmortem burial environment could be observed.

In the second part, crystallographic investigations were carried out in an ontogeny series of *Apatosaurus sp.*. The basic crystallographic orientation of sauropod bones as measured by X-Ray diffraction is shown to be a <001> texture, where the *c*-axes of the crystals are aligned parallel to the longitudinal axis of the bone. This texture, which was also accounted for in bones of recent animals, indicated that these long bones are mainly loaded in compression. The remodeling and consecutive lamellar bone reconstruction does not seem to be affected by the general crystallographic orientation. A pronounced texture found in sauropod and elephant bone seems to be linked to the comparatively large weight of these animals. Crystal size in long bones of *Apatosaurus sp.* was additionally investigated, but the observations are made difficult by postmortem alterations that these bones are submitted to, as crystal size generally increases in fossil bones. The results obtained in this study failed to show an increase of the crystal size and aspect ratio along with the growth of the sauropod. Based on these findings, the nanostructure of FBL bone and secondary lamellar bone were further analyzed using TEM methods. The observed crystallographic organization is different between the two bone tissues: Even if the crystals of primary bone seem to be randomly oriented the <001> texture is present in the first stage of development along the sauropod cortical bone, as shown with diffraction experiments. The secondary lamellar bone observed in the sauropod bone, on the other hand, display different crystallographic orientations in a rotate plywood model, similar to observations of recent bones.

The results obtained in the present study do not confirm the initial hypothesis that sauropod bone exhibits a superior high-strength structure compared to bones of recent large mammals.

Chapter 1 Introduction

1 Motivation

Sauropod dinosaurs due to their gigantism have been among the most interesting terrestrial animals; they were one magnitude larger than any other land animal, living or extinct. The sauropods' size estimated to reach over 100 tons (Alexander 1989, Gunga et al. 2008, Seebacher 2001), had effects on their biology, physiology and ecology which have been subject of different studies (Sander et al. 2011a). One of the scientific questions is which mechanical consequences their gigantism had.

The structure developed by sauropod dinosaurs in the process of functional adaptation is thus, hypothesized to have special features that suited it to particularly heavy load conditions. Therefore, the major aim of this present work is to investigate sauropod bone structure and properties that enabled them to carry such a high weight. This should be achieved by an exploration of the hierarchical structure in relation to these mechanical constraints. The only remains from sauropod dinosaurs are mineralized elements (bones and teeth) which were buried during millions years. Even though many histological details have been conserved in dinosaur bones, changes from original apatite bone are still under study and should be considered carefully.

2 Bone: a composite hierarchical material

2.1 Levels of the bone

Bone is hard and has a stress-strain relationship (stress being the force per area and strain the deformation of the bone due to stress) similar to many engineering materials. However, it is generally difficult to predict the mechanical behavior of bone and understand its formation because the bone material itself has a complex hierarchical structure (see Weiner and Traub 1992, Rho et al. 1998; Weiner & Wagner 1998; Currey 2002, Fratzl and Weinkamer 2007) (Figure 1.1)

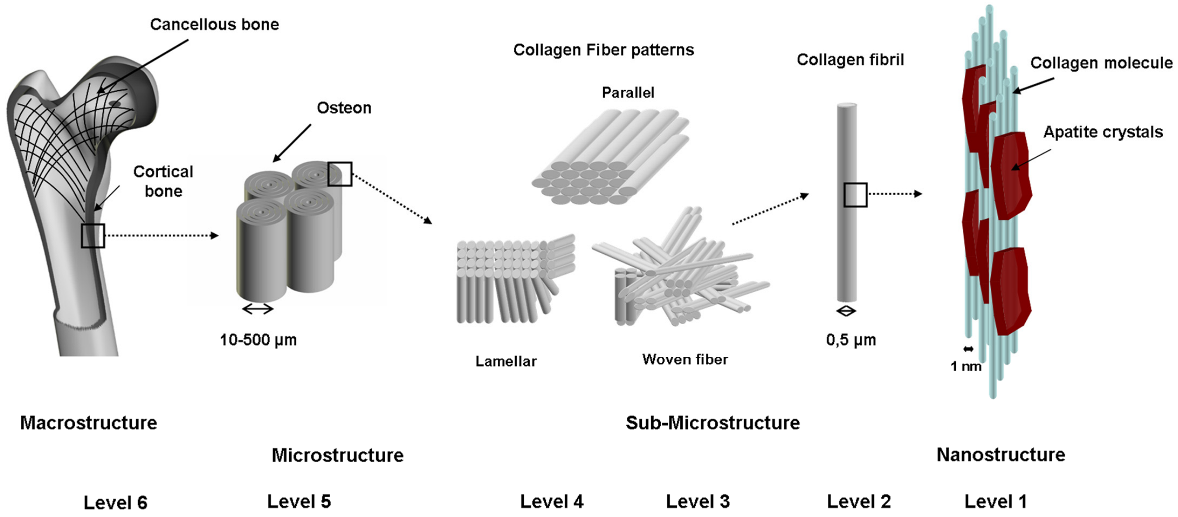

Figure 1.1: The 6 different hierarchical levels in the bone (modified by Rho et al. 1998). They represent the bone structure from the macrostructure (macroscopic level) to the nanostructure (molecular level)

Figure 1.1 shows an arrangement of bone structures (of mammal bone) at many different hierarchical levels. The basic constituents of bone (level 1) are mainly organic collagen and small mineral particles (crystals of carbonated hydroxyapatite $Ca_3(PO_4)_2$ $CaOH_2$). The crystal size varies from 20 to 37 nm length (from chicken to herring bone respectively (Kim et al. 1995) and breadth between 12.2 to 15.4 nm. These hydroxyapatite crystals are arranged along the length of the collagen fibrils (Weiner and Traub 1986, Traub et al. 1989, Weiner et al. 1991, Landis et al. 1993, 1996, Cui et al. 2007). The mineralized collagen fibrils (level 2), running parallel to each other, are assembled into fibers (level 3). The fibers arrays can also be arranged in different patterns of organization (level 4): parallel, woven (packed fibrils without any preferred spatial arrangement), and lamellar (sets of parallel fibers forming layers, each layer having a different orientation of fibers) (for more details, see Francillon-Vieillot et al. 1990; Pritchard 1956; Weiner et al. 1997). At the next hierarchical level, lamellae can be in some cases (i.e., mammalian and sauropod bone) arranged in concentric layers around a central canal to form a primary or secondary osteon (level 5). The osteon resembles a cylinder, in the case of secondary osteons often running parallel to the long axis of the cortical bone. At this level the distinction between primary and secondary bone is identifiable. The macroscopic level considers the bone as a whole entity, distinguishing only between typically solid cortical bone and cancellous bone (level 6), which are composed of the same histological elements but are organized differently. The cortical bone is relatively dense, while cancellous bone has a spongy structure composed of a network of bone trabeculae.

2.2. Mechanical properties of the cortical bone

Bone strength is determined from both its material and its structural properties. This hierarchically organized structure of bone displays a specific arrangement, with the orientation of the components making it a heterogeneous and anisotropic material. This means that the mechanical properties of bone, such as strength (property of being strong), toughness (ability to resist shock loading and crack propagation), and stiffness (resistance to deformation), depend on the relative position of the applied force with regard to the direction of the bone axis (Rho et al. 1998). In this work, the bone structure was focused on the cortical bone mechanical adaptation. General assumption of bone mechanic is summed up above (for more details see Currey 2002, Cowin 2002).

Macroscopic level

At the macroscopical level, diameter and thickness of cortical bone have a dramatic impact on the biomechanics of the bone (Meulen et al. 2001, Turner 2002). In long bones, the strength is increased with bone growth, when the cortex is moved away from the neutral axis: the bending strength of the bone is proportional to its distance from the neutral axis (Currey 2002). In the case of sauropod bone, an increase in the diameter of cortex with increase of cortical thickness is visible (Sander and Tückmantel 2003). This diameter increase (with ontogenetical age of animal) will increase the general bone strength (Beck et al. 2001); a large bone diameter with thick cortices is ideal for strength and fracture prevention.

The cortical porosity is also another factor leading to mechanical consequences. It is known that an increase in porosity will lead to a loss in strength (Turner 2002). Size and expansion porosity through the cortical wall section will have different cost (Currey 1988, Sevostianov and Kachanov 2000, Shawn-Davison et al. 2006); the ideal strength model is a bone presenting the minimal porosity.

Microscopic and sub-microscopic level

Bone mechanical properties at this level mainly refer to the collagen fibrils organization patterns observed in the bone. Mineralized fibrils arrays are anisotropic (i.e. the properties of these arrays are different in different directions). In compression, the highest modulus (or resistance) values will be indeed manifest in a direction parallel to the fibril long axes.

Differences will be seen at the next level of organization, which is more diversified in its structure (Level 3-4 in Figure 1.1). As sauropod bones is mainly composed of woven and parallel arrays in its early growth stage, and further by plywood lamellar bone (see section 1.3). These three different fiber patterns will be described:

The woven bone, a quite common skeleton tissue appears in the first stages of bone formation (e.g. in mammalian embryo (Pritchard 1956). As suggested by Weiner and Wagner (1998), woven bone develops rapidly and is considered an embryonic tissue; it is suggested to not be weight-bearing bone. It is also the bone type tissue which is formed just after fracture or other pathologic conditions probably because it is formed rapidly (Amprino 1947). Even if its tissue seems to be disorganized, it was shown that this disorder reflects a clear anisotropy (Su et al. 2003) in its mechanical properties when measuring microhardness and elastic modulus of cross and longitudinal sections of the bone.

The second fiber patterns observed in sauropod bones are organized in parallel arrays, making up the lamellar bone of osteons. This pattern presents a structure with a more pronounced anisotropy compare of to the woven bone: fibril arrays will be packed parallel and aligned in a specific direction which will be the principal stress direction, direction where the bone exhibits greatest strength. Actually measurements show that parallel fibered bone has much higher modulus value in direction parallel to the bone axis compare to the orthogonal direction (Reilly and Burstein 1974, 1975, Ziv et al. 1996).

The third fiber pattern type is the lamellar or plywood pattern observed in secondary osteon (or haversian tissue, forming with remodeling of the bone). This pattern is described by fibers arrays which rotated progressively (for more details see Weiner et al. 1997). Ziv et al. (1996) have demonstrated that this pattern is highly anisotropic with higher mechanical properties in the plane perpendicular to the bone axis. They also conclude that the rotation present in the plywood structure could imply more isotropic properties, to resist in many directions to compressive bone forces. But studies on this fiber pattern are still needed to understand this particular structure, quite common in the nature.

Nanoscopic level

In fossil bones, the mechanical properties at this level will majorly concern the crystals as collagen is rarely preserved after diagenesis (see section 1.4). In recent living animal, bone is a composite. Apatite crystals are stiff and strong (young´smodulus along the axis is about 165 GPa, that is comparable with steel´s one of 200GPa). The collagen in the other hand does not obey Hooke´s law but its tangent modulus is about 1.24 GPa. The young modulus of the bone will show an intermediate value (e.g 18 GPa for human femur in tension, 26 GPa for bovine femur, 24.5 GPa for horse femur (Reilly and Burstein 1975, Currey 2002)). But as a good composite material it is higher than either apatite or collagen because the softer components prevent the brittleness of the crystals, while the stiff component prevents the soft from yielding.

Crystal size and shape are playing a major role in mechanical properties of the bone. Higher degrees of crystallinity are indeed linked to bone brittleness. It was noticed that crystal size increase with the growth and general age increase in recent animal (Handshin and Stern 1995, Eppell et al. 2001, Tong et al. 2003). This increase will then result in an increase of brittleness. During remodeling and secondary mineralization, this trend is even more pronounced with an increase in number of crystals but also in size. The optimal bone strength will be reflected in wide distribution of crystal size (Shawn-Davison et al. 2006).

The process of remodeling (see section 1.3.2) will have an impact on the bone architecture. For example a high turnover will have consequences on cortical porosity and result in a loss of bone mass. The resorption spaces created will also be likely linked to areas with higher stress risers. Remodeling activity has a direct impact on almost all of the components of bone strength and requires therefore further investigations as to its impact on bone properties.

3 Sauropod bone growth and fibrolamellar bone

3.1 Fibrolamellar bone

The bone microstructure of birds, large herbivorous mammals (e.g. horses, elephants) and sauropods consits of fibrolamellar bone tissue (also called plexiform), see Figure 1.2b. This type of bone consists of alternating layers of woven bone and parallel or lamellar bone. Figure 1.2.a (Currey 2002) shows a sketch of the formation of this complex tissue. An initial layer of woven bone is laid quickly around blood vessels on the bone surface by specialized cells called osteoblasts. These blood vessels then become incorporated into the framework of woven bone. Progressively, the resulting vascular canals are filled centripetally by lamellar bone, forming primary osteon (Currey 1960).

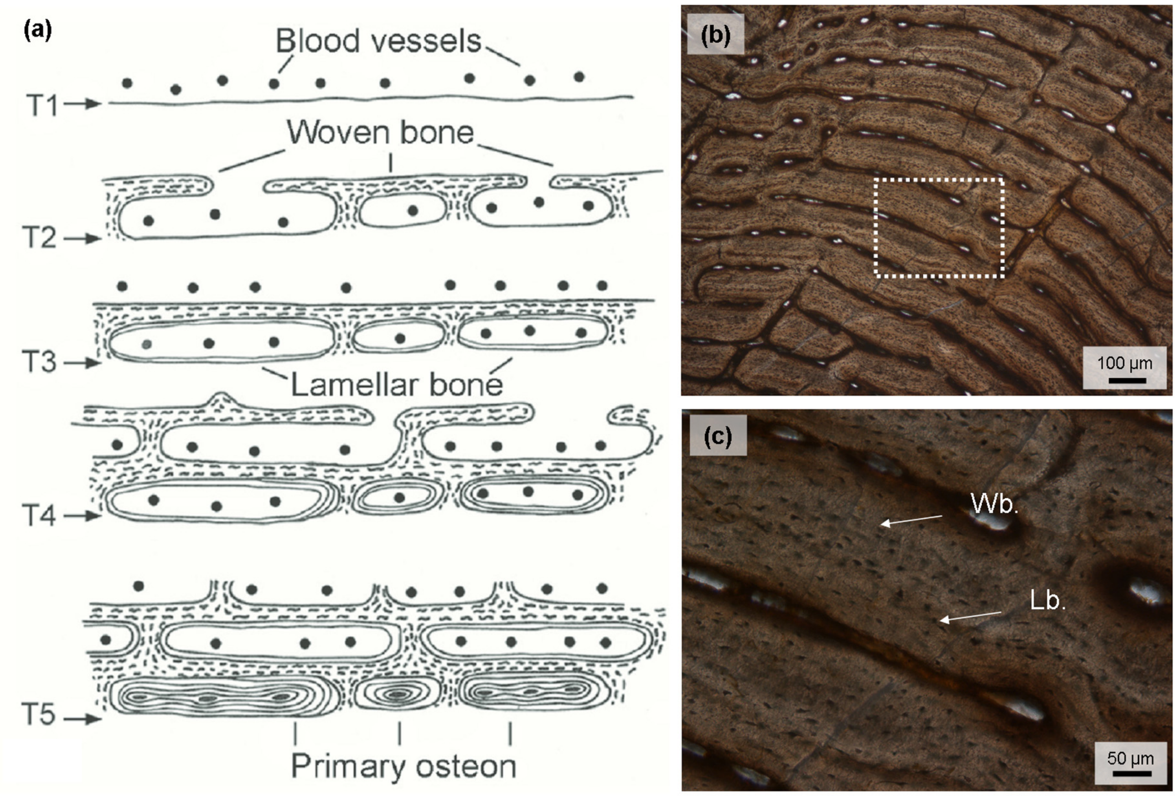

Figure 1.2: (a) Laminar fibrolamellar bone tissue: formation of bone tissue traced over time T. The succession of alternating woven bone matrix (also called lamina) and the successive infilling of vascular canal (becoming primary osteon) (for more details see Currey 2002, Sander et al. 2011b). Optical micrographs of fibrolamellar bone of an *Apatosaurus sp.* (BYU 725-17014) (b) (c). In (b) it can be noticed that the bone microstructure is formed with lumina which starts to be filled by lamellar bone. The zoom in (c) displays the two bones type woven bone (Wb.) with larger osteocyte lacunae and lamellar bone (Lb.) with more flattened osteocytes. In polarized light their disctintion is easily recognized

Fibrolamellar bone (FBL) tissue in general is densely vascularized with various arrangements of vascular canals (Francillon-Vieillot et al. 1990, Curry Rogers and Erickson 2005). Both the sauropod bone and the cow bone in Figure 1.3 are dominated by circumferential vascular canals, resulting in a laminar appearance of the bone tissue. However, in the cow bone (Figure 1.3b), these circumferential canals are additionally connected by radial canals, forming a vascularization pattern called plexiform (see Francillon-Vieillot et al. 1990 for more details). This microstructure has already been noted in other large herbivorous mammals (e.g., Sander and Andrassy 2006) and was previously mentioned by Enlow and Brown (1956, 1958) and Currey (1960, 1962). FBL bone tissue is interpreted as resulting from the rapid but normal deposition of new compact bone (Amprino 1947). Indeed, as a result of the high mass of large mammals and sauropods, their bones must increase in circumference quickly.

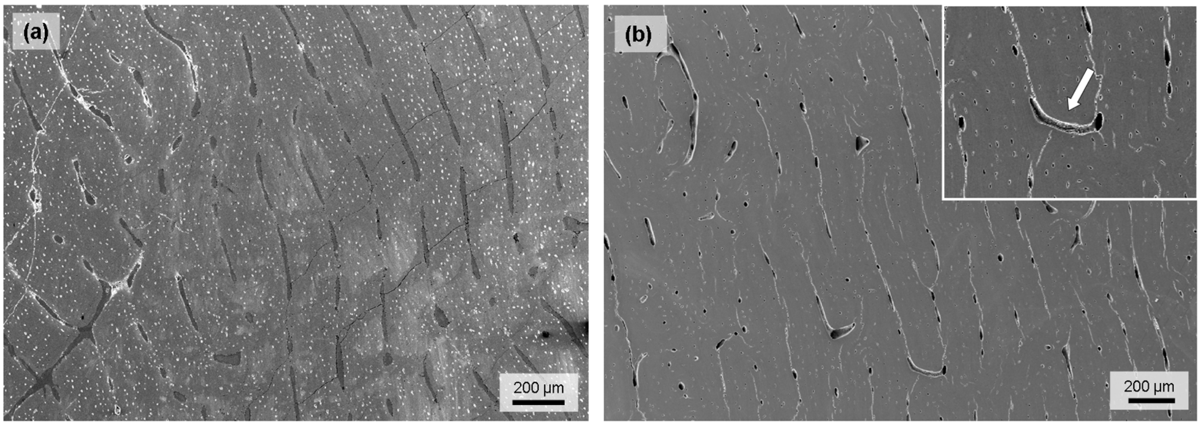

Figure 1.3: SEM micrographs of laminar FBL bone tissue in cross section of an Apatosaurus (a) sample and a juvenile cow (b). The laminar arrangement of the vascular canals results from their circumferential arrangement, parallel to the periosteal surface. The closer view of the junevile cow in (b) shows a radial canal (white arrow), which will result in a more plexiform organization.

FBL is deposited in a form of laminae. In sauropod, quantification of the laminae thickness has shown to be rather independent of the age of the animal, at about 5 laminae/mm (Sander and Tuckmantel 2003). One lamina is about 200µm thick. The cortical bone apposition has been studied and measured of 1-20µm per day. The apposition rate measured decreased with age and is similar to those of large mammals.

3.2 Bone growth and remodeling

The growth in length of sauropod bone is provided by endochondral growth setting up by cartilage (Figure 1.4). Basically, the bone grows in length by division of chondrocytes (cells of cartilage) and subsequent secretion of extracellular matrix. Vascularization is very dense in young juvenile sauropod, which will ensure a high quantity of bone tissue essential for a long growth in diameter. The growth in diameter around the diaphysis occurs by deposition of FBL bone beneath the periosteum (de Ricqles 1975, Francillon-Vieillot et al. 1990).

In sauropods contrary to mammals, there are no secondary ossification centers (Haines 1942), which develop at the end of the epiphysis of long bones. These “primitives” epiphysis are characteristic of indefinite growth animals (de Buffrenil and Mazin 1992). Details of epiphyseal structures (Rimblot-Baly et al. 1995, Schwarz et al. 2007) show indeed precise adaptations to active longitudinal growth even at large body size and to support heavy strains in the case of adult bones.

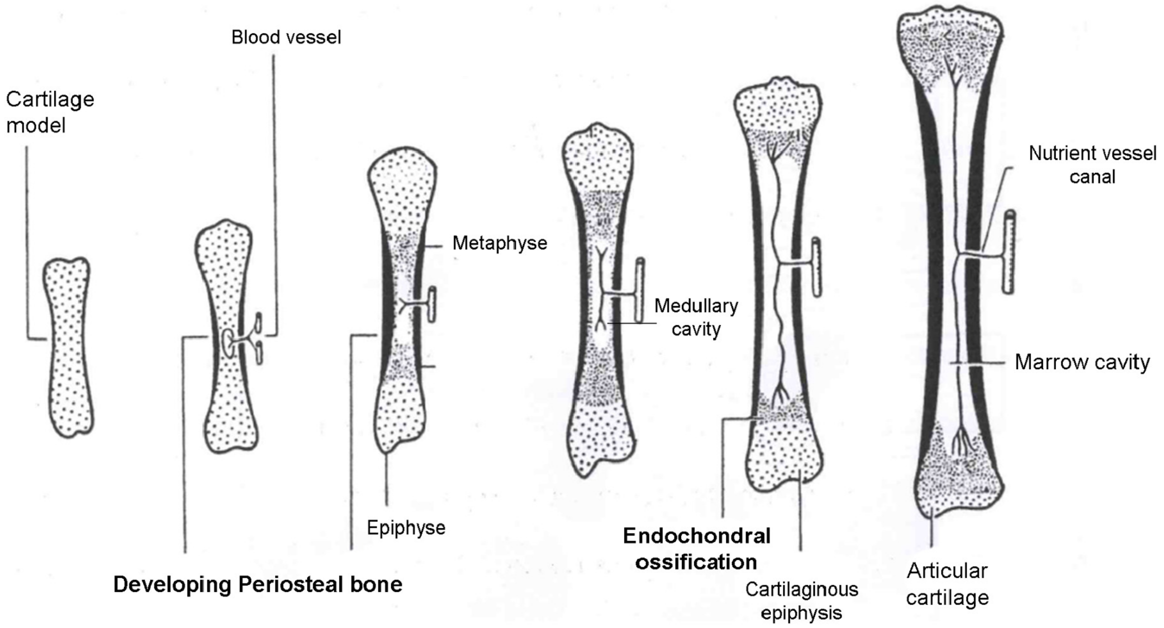

Figure 1.4 Diagram growth stages in a long bone with primary center of ossification. The cartilage model will growth in length by division of chondrocytes. On the periphery of the cartilage, periosteal bone grows with development of the perichondrium by new chondroblasts. It will result in a compact bone. In the metaphyse, cartilage is replaced by endochondral bone. The cartilage in the epiphysis will be replaced by porous bone (with vascular canals) known as trabecular bone. Modified from Francillon-Vieillot et al. (1990).

In all saurischian investigated, as in large mammals (de Ricqlès et al. 1991), the primary bone tissue deposited is changes into a secondary (haversian) bone tissue. This resorption and remodeling process appears early in the ontogeny and starts at the medulary cavity. It is not limited to the endosteal margin but can spread through the whole thickness of the cortex (Curry 1999, Sander 2000, Klein and Sander 2008). This Haversian tissue is considered to be high metabolic signal (de Ricqlès 1983). Figure 1.5 explains how the remodeling and the formation of secondary lamellar bone takes place. The primary bone tissue is eroded by osteoclasts. Subsequent osteoblasts filled these erosion cavities by forming new concentric lamellar bone, called secondary osteons. These secondary osteons are easily recognized by their cementing line, their distinguishable cylindrical layers and their longitudinal orientation (for more details see Francillon-Vieillot et al. 1990, Dumont et al. 2011, Sander et al. 2011b).

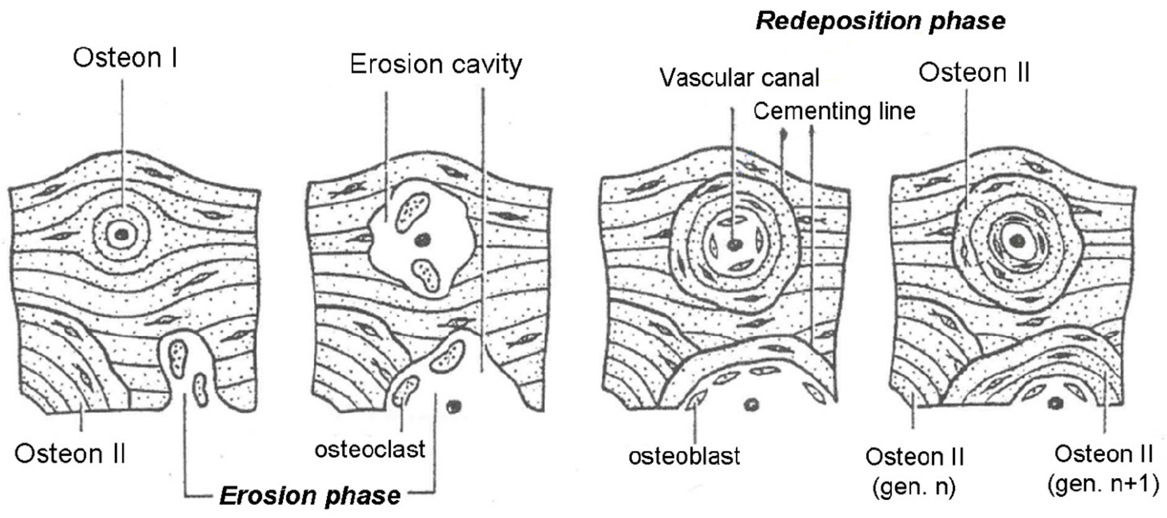

Figure 1.5: Diagram of remodeling/formation of secondary (haversian) bone. This involves two processes. 1) Bone resoprtion where osteoclast resorb the surface of the bone (Howship´s lacunae). 2) Bone redeposition with lamellar deposition bone centripetally by osteoblasts. This bone remodeling is always linked with the presence of cement line.

This remodeling may be linked with three phenomena: i) bone reshaping during ontogeny to acquire the perfect adult morphology structure (Enlow 1963), ii) physiological and histological demand of calcium and phosphorium (Amprino 1948, 1967), iii) response to physical and mechanical constraints (Frost 1988)

Throughout ontogeny, FBL is not only remodeled but also indicates a significant decrease in bone deposition in both groups' sauropod and mammal. The cortical bone becomes avascular and parallel fibered and LAGs (lines of arrested growth) are formed at its periosteal side. This is called an external fundamental system (EFS). But these LAGs were only observed late in ontogeny (Sander 2000, Klein and Sander 2008).

3.3 Sauropod long bone history

Basal sauropodomorph have similar histological pattern than more derived sauropods. The prosauropod *Plateosaurus* bone tissue consists of zones of FBL with alternating annuli of lamellar bone and lines of arrested growth (Chinsamy 1993, Sander and Klein 2005). FBL was already present in the earliest sauropodomorph ancestors (for more details see Stein 2010). Early sauropodomorph present growth marks, rarely present in sauropods (Sander et al. 2000, Klein and Sander 2008). The loss of growth marks in sauropod indicates growth rate acceleration compared to prosauropod, as well as the loss of developmental plasticity (where bone growth is influenced by external environmental factors like climate and food availability) (Sander and Klein 2005).

4 Diagenesis

After death, diagenesis occurs (Karkanas et al. 2000); dinosaur bones have been subjected to a multitude of physical, chemical, and biological processes, all of which are poorly understood. An understanding of fossil preservation is primordial since fossils are used to provide information concerning morphology and paleobiology. Various chemical studies of bones are also used intensively to provide information on paleodiet (Lambert et al. 1985, Tütken 2011), paleoclimate, physiology (e.g. Kolodny et al. 1996, Ambrose et al. 1997, Cerling and Harris 1999, Lee-Thorp and Sponheimer 2003, Sponheimer et al. 2006, Croft and Anderson 2008). Diagenesis has many consequences: it can affect bone histology, bone porosity, protein content, the crystallinity of the apatite, and the bone’s content of chemical elements and compounds in general (e.g. Bell et al. 1996; Berna et al. 2004; Elliott and Grime 1993, Hedges and Millard 1995, Nielsen-Marsh and Hedges 2000; Reiche et al. 2003, Trueman et al. 2004; Turner-Walker and Jans 2008). These studies imply the assumption that the isotopic signature is preserved in biomineralized samples. Thus, for studying fossils it is necessary to know the way leading to preservation and it is imperative to be aware of the alterations that a fossil underwent.

4.1 Diagenetic changes in the fossil bone

Since the 20th century it is generally accepted that microstructural features in dinosaur bones, such as primary and secondary osteons and osteocyte lacunae are well preserved, even if secondary mineral deposition in bone voids or pore spaces are observed. De Ricqlès (1980), who performed studies on thin sections, first suggested the concept of molecule-by-molecule replacement of bone tissue without changes in the bone tissue structure. Organic substances, such as collagen, decompose after burial, but the inorganic (mineral) substances, mainly carbonated hydroxyapatite ($Ca_5(PO_4)_3(OH)$), are more resistant and generally preserved with only slight changes. Substitution commonly takes place, and the hydroxyapatite becomes fluorapatite ($Ca_5(PO_4)_3F$), with the fluorine replacing the hydroxyl group. An increase in crystallinity (Bartsiokas and Middleton 1992, Sillen and Parkington 1996) is also observed and often correlates to the collagen loss (Person et al. 1995, Sillen and Parkington 1996). This is a crucial point for further biomechanical considerations since it’s the mutual interaction between collagen and mineral that determines the mechanical performance of the bone.

Assumptions are also complicated by the fact that the crystals are generally considered to be larger in fossil bones (Tuross et al. 1989, Reiche et al. 2002, Trueman et al. 2004).

Because of the change of crystallinity, collagen loss and mineral density, it is impossible to apply techniques such as tension or compression tests, normally used in material sciences or in biological mechanical testing. With all these changes encountered by the bone, it is hard to interpret the results obtained from this kind of natural testing. Turner-Walker and Parry (1995) already mentioned the loss of mechanical strength in archaelogical bones, directly link by an increase of porosity. In 2010, Olesiak et al. applied nanoindentation comparing modern and fossil bone. Even if their results indicate a general preservation of anisotropy, the mechanical properties of fossilized bone were significantly altered during diagenesis. These two papers show a high variability of strength values, majorly affected by difference of global preservation of the bone samples from different geological sites (or even from one bone to an other bone from one same site).

After burial for millions years, it is generally accepted that little of organic phase is retained in sauropod bones. The mineral component of the bone, crystals of hydroxyapatite may stay basically unchanged for a certain time. The arrangement of the tiny crystals may stay unchanged as the porosity of the skeletal material becomes filled by exogenous minerals. The general microstructure and histology (e.g. osteons morphology, distinction between woven and lamellar bone, structure up to level 2 in Figure 1.1) can remain essentially unchanged in fossils.

The organization of the crystals is induced by the spatial organization of collagen fibrils. Mostly apatite crystals are lying parallel to them (Weiner and Traub 1986, Traub et al. 1989, Weiner et al. 1991, Landis et al. 1993, 1996). This organization is basically remained, even after removal of the organic part of the bone (i.e. collagen fibrils), as seen under polarized light. However, it was noticed, that HAP crystals are submitted to changes after fossilization. Chemical analyses of fossil bone for example indicate that they are richer in fluorine content compare to modern bone. It is generally assumed that fluor is trapped and substituted by hydroxyls to form true fluorapatite. The trapping properties of various heavy elements are noteworthy. It was noticed for example that uranium, located in fossil bone as uranyl ions, has a high affinity to carbonated hydroxyapatite (Dumont et al. 2011). In most of cases, fossil bone material is a calcium rich apatite with various ions including fluorine.

The size of crystals in fossil bone of various animals is known to be diverse. With diagenesis it was stated that this size is increasing by addition of ions and increased according to the absolute values of the geological age (Paine 1937). However ontogenically young fossils are sometimes known to have larger grains apatite crystal than much older one.

4.2 Exceptional preservation

Thought preservation of collagen has been demonstrated in some archeological bones (Wyckoff et al. 1963), it was generally accepted that this organic component is not remained in older fossil bones. But since few years the work of Schweitzer et al. demonstrate that dinosaur bone in specific conditions can be really well preserved, as revealed by conservation of numerous biomolecule in a *Tyrannosaurus rex* bone and recently in an hadrosaur (Schweitzer et al. 1997, 2009) and also some soft tissues with cells preserved (Schweitzer 2005, 2007). Macromolecular resolution of fossilized muscle made of fibrous proteins has been also reported by Martill (Martill 1990). Muscle fibers were replaced by phosphate in which individual crystallites are less than 100nm. As the crystallite orientation was controlled by the orientation of structural proteins, the muscle morphology is preserved with molecular resolution though the original organic molecules decayed. Recently Mc Namara et al. reported organic residue (Mc Namara et al. 2006) and fossilized musculature (Mc Namara et al., 2010) with preservation of ultracellular details in 18Myrd old amphibians. All these results, observed thanks to new advanced techniques like electron microscopy combined with EDX or transmission electron microscopy or spectrometry, prove that preservation of tissue can be a common state.

5 Objectives and approaches

Most of previous works on bone structure of fossil bones performed in paleohistology was based on optical microscopy to obtain assumptions on evolutionary trait histories, evolution or ecology of fossil animal. So far very little work was focused on the nanostructure or their biomechanics (Turner-walker et al. 1995, Olesiak et al. 2010) due to the factors discussed above. For a few years, the craze of understanding the formation and the properties of the bone shows a wide spread area in different domains: medicine, bioengineering (transplant and hip join replacement). To attain this goal, modern investigation techniques used in materials science are currently being applied to characterize the structure of each phase at every hierarchical level of bone (Weiner and Wagner 1998). The use of different microscopic methods, such as scanning and transmission electron microscopy, as well as diffraction techniques, enables an understanding of bone structure and crystallographic texture.

In the framework of this thesis, the hypothesis that sauropod bones are structured in a superior high-strength material compare to mammal bone, will be test. The objectives of the present work are therefore the following: (1) Understand the diagenesis processes and observe if the signals or preservation of the sauropod fossils are different from the micro- to the nanostructure of the bone. This goal will be accomplished using advanced characterization techniques. (2) Investigate the hierarchial structure of Jurassic sauropod long bones by (i) characterizing the evolution of crystal size (aspect ratio and size distribution) with the growth of the giant animal and rely the size of the crystals with biomechanical aspects of the bone, (ii) studying the crystallographic orientation and its evolution with growth and progressive remodeling of the sauropod cortical bone.

In order to attend these objectives different experiments were handled in this work. Preservation of fossil bone was investigated in two different ways. Elements mapping by synchrotron X-Ray fluorescence were used for the first time in a fossil material and compared to traditional techniques like SEM-EDX (Chapter 3). Different complementary techniques were used for studying three sauropod bones from the Morrison Formation until the lowest hierarchical level (Chapter 4). Crystallographic investigations (size and orientation) were studied using two different complementary techniques X-Ray diffraction (Chapter 5) or direct observations in TEM (Chapter 7). In Chapter 5, general textures of sauropod bone were conducted by X-Ray diffraction measurements to follow the general crystallographic orientation in their cortical. In Chapter 6, measurements of crystal size of sauropod, subfossil and recent bone were conducted by X-Ray diffraction and TEM. Supplementary qualitative investigations were made in TEM to obtain direct observations of fossil apatite crystal orientation in FBL and secondary lamellar bone (Chapter 7). Assumptions of bone biomechanics are also evocated in this last chapter.

The different results are discussed in their respective chapters; the most important findings are summarized in chapter 8, together with the conclusions obtained from this work.

References

Alexander, R. McN. 1989. Dynamics of dinosaurs and other extinct giants. Columbia University Press, New York, 167 pp.

Ambrose, S. H., Butler B. M., Hanson D. B., Hunter-Anderson R. L., Krueger H. W. 1997 Stable isotopic analysis of human diet in the Marianas Archipelago, Western Pacific. American. Journal of Physical. Anthropology. 104: 343–361.

Amprino, R. 1947. La structure du tissu osseux envisagée comme expression de différences dans la vitesse de l´acroissement. Archives de Biologie 58: 315-330.

Amprino, R. 1948. A contribution to teh functional meaning of teh substitution of primary and secondary bone tissue. Acta Anatomica 5: 291-300

Amprino, R. 1967. Signification fonctionelle du remaniement osseux. Journal of Medical Montpellier 2: 104-108.

Anderson, J. F., Hall-Martin, A., Russell, D. A. 1985. Long-bone circumference and weight in mammals, birds and dinosaurs. Journal of Zoology 207: 53–61.

Bartsiokas, A. and Middleton, A.P. 1992. Characterization and Dating of Recent and Fossil Bone by X-Ray-Diffraction. Journal of Archaeological Science, 19(1): 63- 72.

Beck, T.J., Oreskovic, T.L., Stone, K.L., Ruff, C.B., Ensrud, K., Nevitt, M.C. 2001. Structural adaptation to changing skeletal load in the progression toward hip fragility: the study of osteorotic fractures. Journal of bone mineral research 16: 1108-1119.

Bell, L.S., Skinner, M.F. and Jones, S.J. 1996. The speed of post mortem change to the human skeleton and its taphonomic significance. Forensic Science International 82(2): 129-140.

Berna, F., Matthews, A. and Weiner, S. 2004. Solubilities of bone mineral fromarchaeological sites: the recrystallization window. Journal of Archaeological Science 31(7): 867-882.

de Buffrénil, V., Mazin, J.M. 1992. Contribution de l´histologie osseuse à l´interprétation paléobiologique du genre Placodus Agassiz, 1833 (Reptilia, Placodontia). Revues Paleobiologiques 11: 397-407.

Cerling T. E., Harris J. M. 1999. Carbon isotope fractionation between diet and bioapatite in ungulate mammals and implications for ecological and paleoecological studies. Oecologia 120: 347–363.

Chinsamy, A. 1993 Bone histology and growth trajectory of the prosauropod dinosaur Massospondylus carinatus (Owen). Modern Geology 18: 319–329.

Cowin 2002. Bone biomechanics Handbook. CRC Boca Raton Informa Healthcare

Croft, D.A., Anderson, L.C. 2008. Locomotion in the extinct notoungulate Protypotherium. Palaeontologia Electronica, 11(1): 20.

Cui, F.-Z., Li, Y., Ge, J. 2007. Self assembly of mineralized collagen composites. Materials science and engineering R 57: 1-27.

Currey, J.D. 1960. Differences in the blood supply of boen of different histological types. Quarterly Journal of Microscopical Science 101(3): 351-370.

Currey, J.D. 1962. The histology of the bone of a prosauropod dinosaur. Paleontology 5: 238-246.

Currey, J. D. 1968. The adaptation of bones to stress. Journal of Theoretical Biology 20: 91–106.

Currey, J. D. 1984. *The* Mechanical Adaptation of Bones. Princeton University Press, Princeton.

Currey, J.D. 1988. The effect of porosity and mineral content on the Young´s modulus of elasticity of compact bone. Journal of Biomechanics 21(2): 131-139.

Currey, J.D. 2002. Bones: Structures and Mechanics. Princeton University Press, Princeton, NJ

Curry, K.A. 1999. Ontogenetic histology of Apatosaurus (dinosaurian, sauropoda): New insights on growth rates and longevity. Journal of vertebrate paleontology 19(4): 654-665.

Curry Rogers, K., Erickson, M. 2005. Sauropod Histology: Microscopic Views on the Lives of Giants. In: The Sauropods: Evolution and Paleobiology (K. Curry Rogers and J. A. Wilson, eds.). University of California Press, Berkeley: 303-326.

Elliott, T.A., Grime, G.W. 1993. Examining the diagenetic alteration of human bone material from a range of archaeological burial sites using nuclear microscopy. Nuclear Instruments and Methods in Physics Research Section B 77(1-4): 537- 547.

Enlow, D.H., Brown, S.O. 1956. A comparative histological study of fossil and recent bone tissue. Part I, Texas Journal of Science 8: 405-483.

Enlow, D.H., Brown, S.O. 1958. A comparative histological study of fossil and recent bone tissue. Part III, Texas Journal of Science 10: 187-230.

Enlow, D.H. 1963. Principles of bone remodeling. Thomas, Ch. C(ed., Springfield, Illinois, 131p.

Eppell, S.J., Tong, W., Katz, J.L., Kuhn, L., Glimcher, M.J. 2001. Shape and size of isolated bone mineralites measured using atomic force microscopy. Journal of Orthopaedic Research 19: 1027–1034.

Francillon-Vieillot, H., de Buffrénil, V., Castanet, J., Géraudie, J., Meunier, F. J., Sire, J. Y., Zylberberg, L., de Ricqlès, A. 1990. Microstructure and mineralization of vertebrate skeletal tissues. *In* Carter, J. G. (ed.). Skeletal Biomineralization: Patterns, Processes and Evolutionary Trends, Vol. 1. Van Nostrand Reinhold, New York: pp. 471–530.

Fratzl, P., Weinkamer, R. 2007. Nature's hierarchical materials. Progress in Materials Science 52: 1263–1334.

Frost, H.M. 1988. Vital biomechanics: proposed general concepts for skeletal adaptationd to mechanical use. Calcified Tissue International 42: 145-156.

Gunga, H-C., Suthau, T., Bellmann, A., Stoinski, S., Friedrich, A., Trippel, T., Kirsch, K., Hellwich, O. 2008. A new body mass estimation of Brachiosaurus brancai Janensch, 1914 mounted and exhibited at the Museum of Natural History (Berlin, Germany). Fossil Record 11: 33-38.

Haines, W.R. 1942. The evolution of epiphyses in the long bones of tetrapods. Journal of Anatomy 72: 323-343.

Handschin, R.G., Stern, W.B. 1995. X-ray diffraction studies on the lattice perfection of human bone apatite (Crista iliaca). Bone 16: 355–363.

Hedges, R.E.M. Millard, A.R. 1995. Bones and Groundwater - Towards the Modeling of Diagenetic Processes. Journal of Archaeological Science 22(2): 155-164.

Karkanas, P., Bar-Yosef, O., Goldberg, P., Weiner, S. 2000. Diagenesis in prehistoric caves: the use of minerals that form in situ to assess the completeness of the archaeological record. Journal of Archaeological science 27: 915-929.

Kim, H.-M., Rey, C., Glimcher, M.J. 1995. Isolation of calcium–phosphate crystals of bone by non-aqueous methods at low temperature. Journal of Bone Mineral Research 10: 1589–1601.

Klein, N., Sander, P.M. 2008. Ontogenetic stages in the long bone histology of sauropod dinosaurs. Paleobiology 34(2): 247-263.

Kolodny, Y., Luz, B., Sander, M., and Clemens, W.A., 1996. Dinosaur bones: Fossils or pseudomorphs? The pitfalls of physiology reconstruction from apatitic fossils. Paleogeography, Paleoclimatology, Paleoecology 126: 161–171.

Lambert, J.B., Vlasak, S., Simpson, Szpunar, C.B., Buikstra, J.E. 1985. Bone diagenesis and dietary. Journal of Human evolution 14(5): 477–482.

Landis, W.J., Song, M.J., Leith, A., McEwen, L., McEwen, B.F. 1993. Mineral and organic matrix interaction in normally calcifying tendon visualized in three dimensions by high-voltage electron microscopic tomography and graphic image reconstruction. Journal of Structural Biology 110: 39–54.

Landis, W.J., Hodgens, K.J., Arena, J. Song, M.J., Mc Ewen, B.F. 1996. Structural relations between collagen and mineral in bone as determined by high voltage electron microscopic tomography. Microscopy research and technique 33: 199-202.

Lee-Thorp, J. and Sponheimer, M., 2003. Three case studies used to reassess the reliability of fossil bone and enamel isotope signals for paleodietary studies. Journal of Anthropological Archaeology 22(3): 208-216.

Martill, D.M. 1990. Macromolecular resolution of fossilized muscle tissue from an elopomorph fish. Nature. 346*:* 171–172

McNamara, M.E., Orr, P.J., Kearns, S.L., Alcalá, L., Anadón, P., Peňalever-Mollá, E., 2006. High-fidelity organic preservation of bone marrow in ca. 10 Ma amphibians. Geology 34: 641–644.

McNamara, M., Orr, P. J., Kearns, S. L., Alcala, L., Anadon,P., Penalver-Molla, E. 2010.Organic preservation of fossil musculature with ultracellular detail.Proceedings of the Royal Society B 277: 423–427

Meulen, van der, M.C.H., Jepsen, K.J., Mikic, B. 2001. Understanding bone strength: size isn´t everything. Bone 29(2): 101-104.

Nielsen-Marsh, C.M., Hedges, R.E.M., 2000. Patterns of Diagenesis in Bone I: The Effects of Site Environments. 27(12): 1139-1150.

Olesiak, S., Sponheimer, M., Eberle, J.J., Oven. M.L., Ferguson, V.L. 2010. Nanomechanical properties of modern and fossil bone. Palaeogeography, Palaeoclimatology, Palaeoecology 289: 25-32.

Paine, G. 1937. Fossilization of bone. American Journal of Science 234: 148-157.

Person, A., Bocherens, H., Saliege, J.F., Paris, F., Zeitoun, V., Gerard, M. 1995. Early Diagenetic Evolution of Bone Phosphate: An X-ray Diffractometry Analysis. Journal of Archaeological Science 22(2): 211-221.

Pritchard, J. J. 1956. General histology of bone. *In* Bourne, G. H. (ed.). The Biochemistry and Physiology of Bone. Academic Press, New York: pp 1–25.

Reiche, I., Vignaud, C., Menu, M. 2002. The crystallinity of ancient bone and dentine: new insights by transmission electron microscopy. Archaeometry 44 (3): 447–459.

Reiche, I., Favre-Quattropani, L., Vignaud, C., Bocherens, H., Charlet, L., Menu, M.A. 2003. A multi-analytical study of bone diagenesis: the Neolithic site of Bercy (Paris, France). Measured Sciences Technology 14: 1608-1619.

Reilly DT, Burstein AH. 1974. The mechanical properties of compact bone. The Journal of bone and joint surgery 56: 1001-1022.

Reilly DT, Burstein AH. 1975. The elastic and ultimate properties of compact bone tissue Journal of Biomechanics 8: 393–405

Rho, J.-Y., Kuhn-Spearing, L., Ziuopos, P. 1998. Mechanical properties and the hierarchical structure of bone. Medical Engineering and Physics 20: 92–102.

de Ricqlès, A. 1975. Recherches paléohistologiques sur les os longs des tétrapodes VII Sur la classification, la signification fonctionnelle et l´histoire des tissus osseux des tétrapodes. Première partie : structures. Annales de Paleontologie (Vertébrés) 61 : 51-129.

de Ricqlès, A. 1980. Tissue structures of dinosaur bone. Functional significance and possible relation to dinosaur physiology. In Thomas, D. K. & Olson, E. C. (eds.). A Cold Look at the Warm-Blooded Dinosaurs. Westview Press, Boulder: pp. 103–140.

de Ricqlès, A. 1983. Cyclical growth in the long limb bones of a sauropod dinosaur. Second Symposium on Mesozoic Terrestial Ecosystems, Jadwisin 1981. Acta Paleontologica Polonica 28(1-2): 225-232.

de Ricqlès, A., Meunier, F.-J., Castanet, J., Francillon-Vieillot, H. 1991. Comparative microstructure of bone. *In* Hall, B. K. (ed.). Bone, Vol. 3: Bone Matrix and Bone Specific Products. CRC Press, Boca Raton: pp. 1–78.

Rimblot-Baly, F., de Ricqlès, A., Zylberberg, L. 1995. Analyse palohistologique d´une série de croissance partielle chez Lapparentosaurus madagascariensis (Jurassique moyen): essai sur la dynamique de croissance d´un dinosaur sauropode. Annales de Paléontologie 81(2): 49-86.

Sander, P. M. 2000. Longbone histology of the Tendaguru sauropods: implications for growth and biology. Paleobiology 26: 466–488.

Sander, P. M., Tückmantel, C. 2003. Bone lamina thickness, bone apposition rates, and age estimates in sauropod humeri and femora. Palaeontologische Zeitschrift 77:161–172.

Sander, P.M., Klein, N. 2005. Developmental plasticity in the life history of a prosauropod dinosaur. Science 310: 1800-1802.

Sander, P. M, Andrassy, P. 2006. Lines of arrested growth and long bone histology in Pleistocene large mammals from Germany: what do they tell us about dinosaur physiology? Palaeontographica Abt. A 277: 143–159.

Sander, P.M., Christian, A., Clauss, M., Fechner, R., Ge, C.T., Griebeler, E.-M., Gunga, H.-C., Hummel, J., Mallison, H., Perry, S.F., Preuschoft, H., Rauhut, O.W.M., Remes, K., Tütken, T. Wings, O., Witzel, U. 2011a. Biology of the sauropod dinosaurs: the evolution of gigantism. Biological Reviews 86(1): 117-155.

Sander, P. M., Klein, N., Stein, K., Wings O. 2011b. Sauropod bone histology and its implications for sauropod biology.. *In* N. Klein, K. Remes, C. T. Gee, and P. M. Sander, eds. Biology of the Sauropod Dinosaurs: Understanding the Life of Giants. Life of the Past (series ed. Farlow, J.). Indiana University Press, Bloomington. Pp. 276-302

Schwartz, D., Wings, O., Meyer, C.A. 2007. Super sizing the giants: first cartilage preservation at a sauropod dinosaur limb joint. Journal of geological society, 164: 61-65.

Schweitzer, M.H., Johnson, C., Zocco, T.G., Horner, J.R., Starkey, J.R. 1997. Preservation of Biomolecules in Cancellous Bone of Tyrannosaurus rex. Journal of Vertebrate Paleontology 17(2): 349-359.

Schweitzer, M.H., Wittmeyer, J.L., Horner, J.R., Toporski, J.K. 2005. Soft-tissue vessels and cellular preservation in Tyrannousaururs rex. Science 307: 1952-1955.

Schweitzer, M.H., Wittmeyer, J.L:, Horner, J.R. 2007. Soft tissue and cellular preservation in vertebrate skeletal elements from the cretaceous to the present. Proccedings of the Royal Society B 274: 183-197.

Schweitzer, M.H., Zheng, W., Organ, C.L., Avci, R., Suo, Z., Freimark, L.M., Lebleu, V.S., Duncan, M.B., Vander Heiden, M.G., Neveu, J.M., Lane, W.S., Cottrell, J.S., Horner, J.R., Cantley,L.C., Kalluri,R., Asara, J.M. 2009. Biomolecular characterization and protein sequences of the campanian hadrosaur B. Canadensis. Science 324: 626-631.

Seebacher, F. 2001. A new method to calculate allometric length-mass relationships of dinosaurs. Journal of Vertebrate Paleontology 21: 51-60.

Sevostianov, I., Kachanov, M. 2000. Impact of the porous microstructure on the overall elastic propeties of the osteonal cortical bone. Journal of Biomechanics 33: 881-888.

Shawn Davison, K., Siminoski, K. Adachi, J.D., Hanley, D.A., Goltzman, D., Hodsman, A.B., Josse, R., Kaiser, S., Olszynski, W.P., Papaioannou, A., Ste Marie, L:-G., Kendler, D.L., Tenenhouse, A., Brown, J.P. 2006. Bone strength: the whole is greater than the sum of its parts. Seminars in Arthritis and Rheumatism 36(1): 22-31.

Sillen, A., Parkington, J., 1996. Diagenesis of bones from Eland's bay cave. Journal of Archaeological Science, 23(4): 535-542.

Sponheimer, M., Passey, B.H., de Ruiter, D.J., Guatelli-Steinberg, D., Thure E. Cerling, T.E, Lee-Thorp, J.A., 2006. Isotopic Evidence for Dietary Variability in the Early Hominin Paranthropus robustus. Science, 314(5801): 980-982.

Su, X., Sun, K., Cui, F.Z., Landis, W.J. 2003. Organization of apatite crystals in human woven bone. Bone 32: 150-162.

Tanck, E., Homminga, J., van Lenthe, G. H., Huiskes, R. 2001.Increase in bone volume fraction precedes architectural adaptationin growing bone. Bone 28: 650–654.

Tong, W., Glimcher, M.J., Katz, J.L., Kuhn, L., Eppell, S.J., 2003. Size and shape of mineralites in young bovine bone measured by atomic force microscopy. Calcified Tissue International 72: 592–598.

Traub, W., Arad, T., Weiner, S. 1989. Three-dimensional ordered distribution of crystals in turkey tendon collagen fibers. Proceedings of National Academy of Sciences 86: 9822-9826.

Trueman, C.N.G., Behrensmeyer, A.K., Tuross, N., Weiner, S. 2004. Mineralogical and compositional changes in bones exposed on soil surfaces in Amboseli National Park, Kenya: diagenetic mechanisms and the role of sediment pore fluids. Journal of Archaeological Science 31: 721–739.

Turner, C.H. 2002. Biomechanics of bone: determinants of skeletal fragility and bone quality. Osteoporosis international 13: 97-104.

Turner-Walker, G., Parry, T.V. 1995. The tensile strength of archaeological bone. Journal of Archaeological science 22: 185-191.

Turner-Walker, G., Jans, M., 2008. Reconstructing taphonomic histories using histological analysis, Palaeogeography, Palaeoclimatology, Palaeoecology 266: 227–235.

Tuross, N., Behrensmeyer, A.K., Eanes, E.D., Fischer, L.W. 1989. Molecular preservation and crystallographic alterations in a weathering of wildebeest bones. Applied Geochemistry 4: 261–270.

Tütken, T. 2011. The diet of sauropod dinosaurs: implications of carbon isotope analysis on teeth, bones, and plants. Pp. 57-79. In N. Klein, K. Remes, C. T. Gee, and P. M. Sander, eds. Biology of the Sauropod Dinosaurs: Understanding the Life of Giants. Life of the Past (series ed. Farlow, J.). Indiana University Press, Bloomington.

Upchurch, P. 1998. The phylogenetic relationships of sauropod dinosaurs. Zoological Journal of the Linnean Society of London 124: 43–103.

Weiner, S., Traub, W. 1986. Organization of hydroxyapatite crystals within collagen fibrils. FEBS 206(2): 262-266.

Weiner, S., Arad, T., Traub, W., 1991. Crystal organization in rat bone lamellae. FEBS Letters 285 (1): 49–54.

Weiner, S., Traub, W. 1992. Bone structure: from angstoms to microns. The FASEB journal 6: 879-885.

Weiner, S., Arad, T., Sabanay, I., Traub, W. 1997. Rotated plywood structure of primary lamellar bone in the rat: orientations of the collagen fibril arrays. Bone 20: 509–514.

Weiner, S., Wagner, H. D. 1998. The material bone: structure-mechanical function relations. Annual Review of Materials Science 28: 271–98.

Wilson, J. A. 2002. Sauropod dinosaur phylogeny: critique and cladistic analysis. Zoological Journal of the Linnean Society of London 136: 217–276.

Wolff, J. 1892. Das Gesetz der Transformation der Knochen. Hirschwald, Berlin.

Wyckoff, W.G. Wagner, E., Matter P., Doberenz A.R. 1963. Collagen in fossil bone, Proceedings of the National Academy of Science**.** 5: 215–218.

Ziv, V., Wagner, H.D., Weiner, S. 1996. Microstructure-microhardness relations in parallel-fibered and lamellar bone. Bone 18 (5): 417-428.

Chapter 2 Material and Methods

1 Material

The material investigated here is mostly based on long bones core drilling sections (Stein and Sander 2009) of *Apatosaurus sp.* (Figure 2.1). The sauropods come from the Morrison Formation in USA. These samples were chosen according to firsthand studies of Sander, 2000 and Klein and Sander 2008, because they represent an ontogenetic stage series describing really well the different histological stage (Table 2.1). For more details, refer to Klein and Sander (2008).

The sauropod samples were compared with different mammals or other fossils animals' bone.

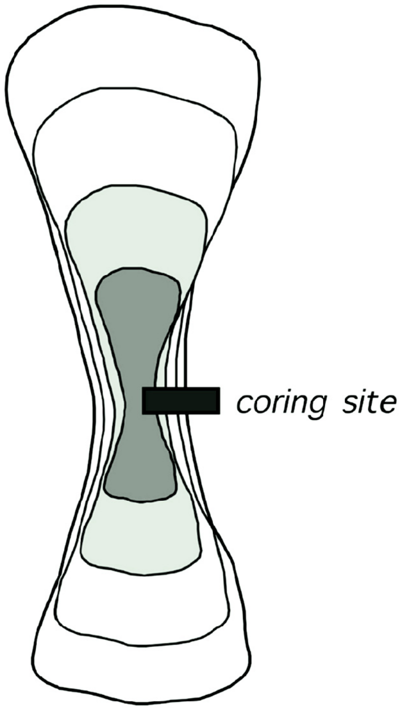

Figure 2.1: Schematic drawing illustrating the core drilling for obtaining histological samples. The appositional growth of a sauropod long bone is marked by 4 different growths. The optimal sampling location is positioned at the midshaft of the bone, recording the complete growth record (from Stein and Sander 2009, Sander et al. 2011,)

Table 2.1: Taxa studied, bone type, specimen number, locality, and the chapter where the samples are evocated.

Taxon	Bone	Specimen no.	Locality	Study
Apatosaurus sp. [1]			Morrison Formation, USA	
Apatosaurus sp.	Humerus	OMNH 1278	Kenton Quarry	Chapter 6,7,8
Apatosaurus sp.	Femur	OMNH 1279	Kenton Quarry	Chapter 6,7,8
Apatosaurus sp.	Femur	BYU 681-11940	Cactus Park	Chapter 7,8
Apatosaurus sp.	Femur	BYU 601-17328	BYU locality 601	Chapter 6,7,8,9
Apatosaurus sp.	Femur	SMA 0014	SMA Howe Ranch	Chapter 8
Apatosaurus sp.	Femur	OMNH 4020	Kenton Quarry	Chapter 8
Sauropoda indet.[2] previously assigned to *Barosaurus africanus* (see Remes 2009)			Tendaguru, Africa	
Sauropoda indet.	Humerus	MFN Ba IX 94	Upper Transitional Sands	Chapter 8
Sauropoda indet.	Humerus	MFN Ba XI a 7	Upper Transitional Sands	Chapter 8
Sauropoda indet.	Femur	MFN Ba Ki 4	Upper Transitional Sands	Chapter 8, 9
Sauropoda indet.	Tibia	MFN Ba Ki 5	Upper Transitional Sands	Chapter 8
Brachiosaurus brancai	Femur	MFN Br XV	Upper Saurian Marls	Chapter 5
Comparison material				
Bison priscus[3]	Tibia	FKBiRs		Chapter 7,8
Equus sp. [4]		MQB 48516	Rhein-Herne Ship channel, Germany	Chapter 8, 9
Ceratopsian indet.			Collection Bonn	Chapter 7
Giraffa camelopardalis	Humerus	5834A	Collection Hamburg, Zoo animal	Chapter 7
Struthio camelus	Femur	K Str 1	Farm, Germany	Chapter 7
Elephas maximus	Humerus	8057	Collection Hamburg, Zoo animal	Chapter 7

Alligator mississipiensis	Femur	K Kr 26	Rockefeller Wildlife Refuge, Louisiana, USA	Chapter 7

[1] The histology of this material was described in Klein and Sander (2008)
[2] The histology of this material was described in Sander (2000)
[3]. The histology of this material was described in Tütken (2003)
[4] The histology of this material was described in Sander and Andrassy (2006)
Collections acronyms: BYU = Museum of Paleontology of Brigham Young University, Provo, Utah, USA, MFN = Museum für Naturkunde, Berlin, Germany; MQB = Museum Quadrat, Bottrop, Germany; OMNH = Sam Noble Oklahoma Museum of Natural History, Norman, Oklahoma, USA, SMA = Sauriermuseum Aathal, Aathal, Switzerland.

2 Energy dispersive techniques: EDX and X-Ray fluorescence

Secondary signals arise from the interaction of sample with an electron beam (Figure 3.2). Many of these signals are used in analytical electron microscopy, providing chemical information and many other details about the material being studied. Signals generated during the interaction between the probe (the electron beam) and the specimen can be classified in two categories because they are the result of either elastic or inelastic scattering of the electrons. In the first case, the energy of the incident electrons is conserved. In contrast, during the inelastic scattering process, the energy of the incident electrons is transferred. Elastic scattering leads to diffraction contrast in TEM, and it is directly related to the nature of crystal lattice defects present in the sample (grain boundaries and other microstructural features). Secondary electrons are produced when the incident electrons knock out loosely bound conduction electrons. Because of their low energy, these secondary electrons (<50 eV) can only escape from a thin subsurface layer with a thickness of about 10 nm. The intensity of the detected signal depends on the angle between the beam and the specimen. These two factors mean that the secondary electron signal provides the highest topographic resolution. Secondary electrons are usually used in SEM to visualize the specimen. The backscattered electron (BSE) signal is produced in SEM by elastically scattered electrons, deflected through angles of 0° to 180° by atoms within the specimen. Those scattered by angles greater than 90° can reemerge from the specimen surface and still retain a high level of energy. Under similar operating conditions, the BSE signal will be produced from a larger volume of the sample than the secondaryelectron signal and has a lower topographical resolution. The BSE signal can also be used to give qualitative compositional information in heterogeneous samples. Phases consisting of heavy elements (high atomic number) will backscatter electrons more strongly than those with light elements (low atomic number), thus emitting a more intense signal and appearing brighter.

Electrons that lose energy during the interaction with the sample may eject lower-energy secondary electrons and X-rays. The X-rays emitted will have a characteristic energy that is unique for the element from which they originate, and their intensity is proportional to the concentration of the element. This analytical technique, called energy dispersive X-ray spectroscopy (EDS or EDX), is commonly used for determining qualitative element composition in a specific material. It is a technique complementary to observations made with BSE. Whereas BSE imaging displays compositional contrast (resulting from a difference in atomic numbers), EDS allows for the identification of particular elements and their relative proportion in the sample.

The major difference between spectroscopy techniques XRF and EDS is only the type of the ionizing radiation, which in XRF is a high-energy X-ray beam, in standard EDS is an electron beam. By analyzing and quantifying the energy of the characteristic radiation, the elements can be identified (qualitative analysis), but element ratios for both mass and element percentages can be also calculated (quantitative analysis). The spectroscopy methods also allow for the identification of specific minerals; however, some care must be taken because of the lack of adequate standards and reduced energy resolution of available detectors.

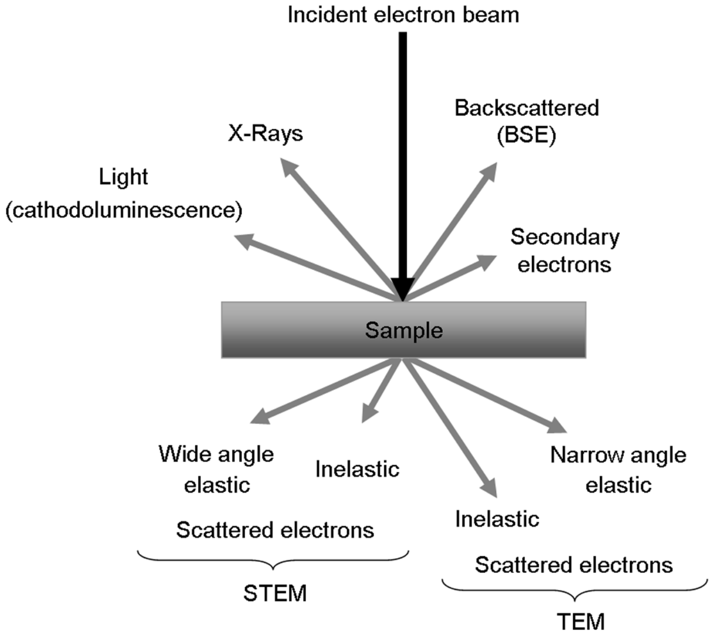

Figure 2.2: Signals generated during interaction of an electron beam with a sample: Most of the signals can be detected in Scanning Electron Microscopy and Transmission Electron Microscopy. The directions shown for each signal do not always represent the physical direction of the signal; they only indicate in a relative manner where the signal is the strongest or where it is measured.

Synchrotron micro-X-Ray Fluorescence (SR-μ XRF) was also employed here. The synchrotron radiation is a source emitting brilliant beams of light by moving electrons through a strong magnetic field. The use of this radiation instead of high-energy X-Rays results in higher resolution and improves the detection limit (Chapter 3)

3 X-ray diffraction

X-Ray diffraction is a non-destructive analytical method, widely used in material science. It reveals crystallographic, chemical and physical information of a structure. X- Rays are produced by the interaction of an electron beam with the sample (Figure 3.2).
The principle of X-Ray diffraction (for more details see Warren 1990), which is the basis for texture characterization and EDX or other chemical composition methods are presented below.

3.1 Bragg diffraction and phase analysis

A monochromatic beam incident on a crystal is diffracted by the crystallographic lattice planes (defined by Miller indices, *hkl*) if they satisfy Bragg’s law:
$2d \sin \theta = \lambda$, (1) where d is the distance between diffracting crystallographic planes, λ is the wavelength of the incident radiation, and θ is the diffraction angle measured between the incoming beam and the reflecting crystallite planes.

The diffraction angle is also the angle formed between the detector (which registers the amount of reflected radiation as the number of incoming photons or neutrons) and the reflecting planes. A diffraction spectrum is obtained by recording the reflected intensities for gradually increasing angles θ. An example of a diffraction spectrum is shown in Fig. 2.3b, in which the intensity of the reflected radiation is plotted as a function of twice the diffraction angle (2 times θ). When Bragg’s law is satisfied—or, in other words, when a suitable combination of d and θ satisfying equation (1) occurs—a peak of intensity is generated, indicating that a greater amount of radiation is diffracted by the sample. The peaks observed in a diffraction spectrum are called *hkl* (or Bragg) reflections because each one of them corresponds to crystallographic lattice planes of different (*hkl*) indices. On the basis of the equation above, the interplanar distance d between two planes of atoms aligned in the same direction can be evaluated by measuring the diffraction angle θ. Different mineral phases are usually characterized by different interplanar distances. Therefore, by studying a whole spectrum of diffraction, different mineral phases present in a material can be identified, as exemplified in the case of apatite and calcite in Fig. 2.3b. Assuming that the crystallographic structures of the constituent minerals or other crystalline materials are known (hexagonal for apatite and orthorhombic for calcite), the individual peaks can be assigned to their corresponding crystallographic planes (for more details, see e.g. Randle & Engler 2000).

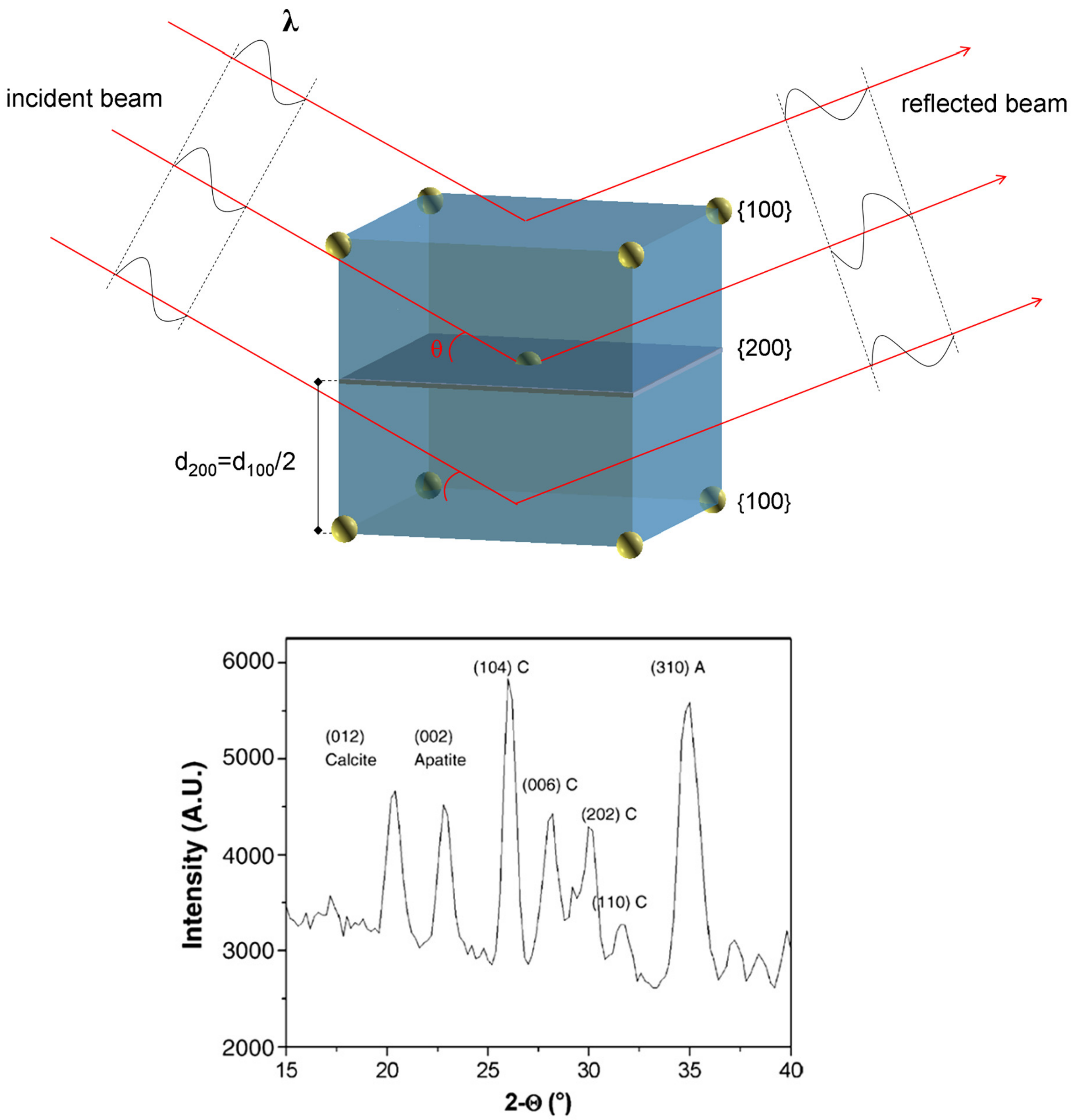

Figure 2.3: Principle of Bragg diffraction. Beams with identical wavelength and phase approach a crystalline solid and are scattered off different atoms within it. The lower beam traverses an extra length of $2d\sin\theta$. Constructive interference occurs when this length is equal to an integer multiple of the wavelength of the radiation.
b. Example of diffraction spectrum of a sauropod long bone (*Brachiosaurus brancai*, MFN J 12, right humerus, 170.0 cm). The diffraction spectrum shows the different peaks corresponding to apatite (A) and calcite (C) with corresponding (*hkl*) reflections (from Pyzalla et al. 2006).

3.2 Crystal size determination

The X-Ray diffraction spectrum can be used to determine the apparent crystallite using the Scherrer equation (Scherrer, 1918; Klug and Alexander, 1974; Cullity, 1978):

$$\varepsilon = \lambda / (FWHM \cdot \cos\theta)$$

where ε is the apparent crystallite size, λ is the wavelength of the X-rays, and θ is the Bragg angle. The full width at half maximum FWHM corresponds to the width of the peak, measured at the half intensity of the peak (Figure 3.4). True crystallite size "*t*" is obtained through the shape factor *K* (known also as the Scherrer constant):

$$t = K\varepsilon$$

which can vary between approximately from 0.9 to 2.2, depending on the shape of the crystallite (Klug and Alexander, 1974). For the calculation of the real crystallite size from peak broadening, the choice of the *K* factor is crucial. *K* = 0.9 was commonly used in studies of bone crystallites even though this value applies to cubic crystals (Chipera and Bish, 1991; Ziv and Weiner, 1994). The combined XRD and TEM investigations of Ziv and Weiner (1994) on rat bones show, however, that *K* = 2 leads to a better agreement of crystallite length values determined by the XRD and TEM. An application of these two methods is shown in chapter 8.

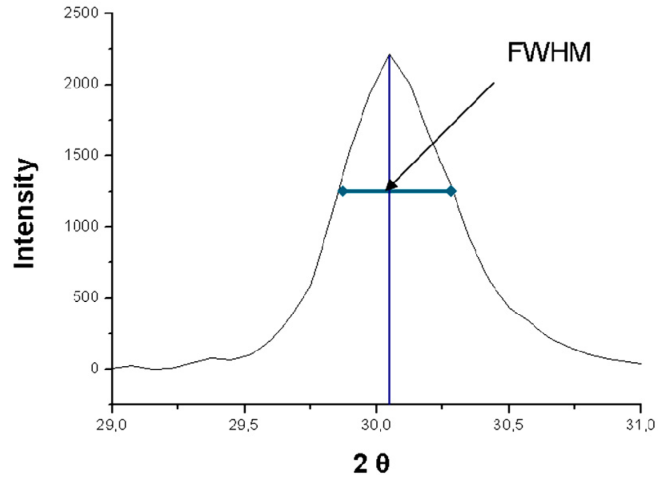

Figure 2.4: Isolated peaks from a diffractogramm with the illustration of the FWHM. As seen on the illustration the FWHM correspond to the width of the half of the peak.

X- Ray diffraction is also the basis of the next technique described.

4 Texture analysis

The crystallographic orientation of apatite (or any other crystallographic phase) with respect to specific directions in a bone can be obtained by performing pole figure measurements.

A pole figure is a graphic representation of the distribution of a specific group of crystal planes in a material with respect to a reference coordinate system. Therefore, a single pole figure exists for each set of (*hkl*) planes of a certain mineral phase. If we consider, for example, the spectrum in Figure 2.3, a pole figure can be obtained for the (002) and (310) apatite planes. It is important to start by defining the reference coordinate system in which the orientation of crystallographic planes is described from the bone's crystal structure.

An example of the definition of a reference coordinate system is given in Figure 2.5a. Here, the coordinate system is defined by axis LD (longitudinal direction) along the long axis of the bone, axis TD (transverse direction), and axis ND (normal direction), all of which are perpendicular to each other. The orientation of a specific group of apatite crystallites belonging to a given family of crystallographic planes in the reference coordinate system can be determined by measuring the intensity of the corresponding Bragg peak in several different directions in space. This is easily achieved if the detector is positioned at the expected θ angle, for example $2\theta = 23°$ in Figure 2.3 in the case of (002) planes of the hexagonal apatite.

By means of a monochromatic beam, the intensity recorded by the detector (number of incoming photons or neutrons) will be proportional to the number of crystal planes fulfilling the Bragg condition. By tilting the bone by the angle α (with regard to the diffraction plane determined by the incoming and scattered beams) and rotating it around the ND axis by the angle β, a different intensity is recorded. The visualization of the results is usually done by plotting the intensities as a function of tilt angles α (radial) and β (azimuthal) in a so-called stereographic projection (Figure 2.5c).

The principle of stereographic projection is explained in Figure 2.5b, based on a hexagonal bone apatite crystal. The (001) crystallographic direction of the crystal in the bone system is produced by the angles α and β, and it intersects the surface of the sphere at the pole P'. Because the representation of intensity in a 3D space is difficult, the equatorial plane of the sphere is used for this by projecting the pole P' onto this plane. The stereographic projection P of the pole (001) is given by the intersection of the equatorial plane and the line connecting pole P' with the south pole of the sphere. Given that the LD– ND axis plane is the diffraction plane, the apatite crystallite can be brought into diffracting position by rotating it by the angles α and β. In a similar way, we can obtain the pole figures for (101) poles of the apatite crystallites in a bone matrix.

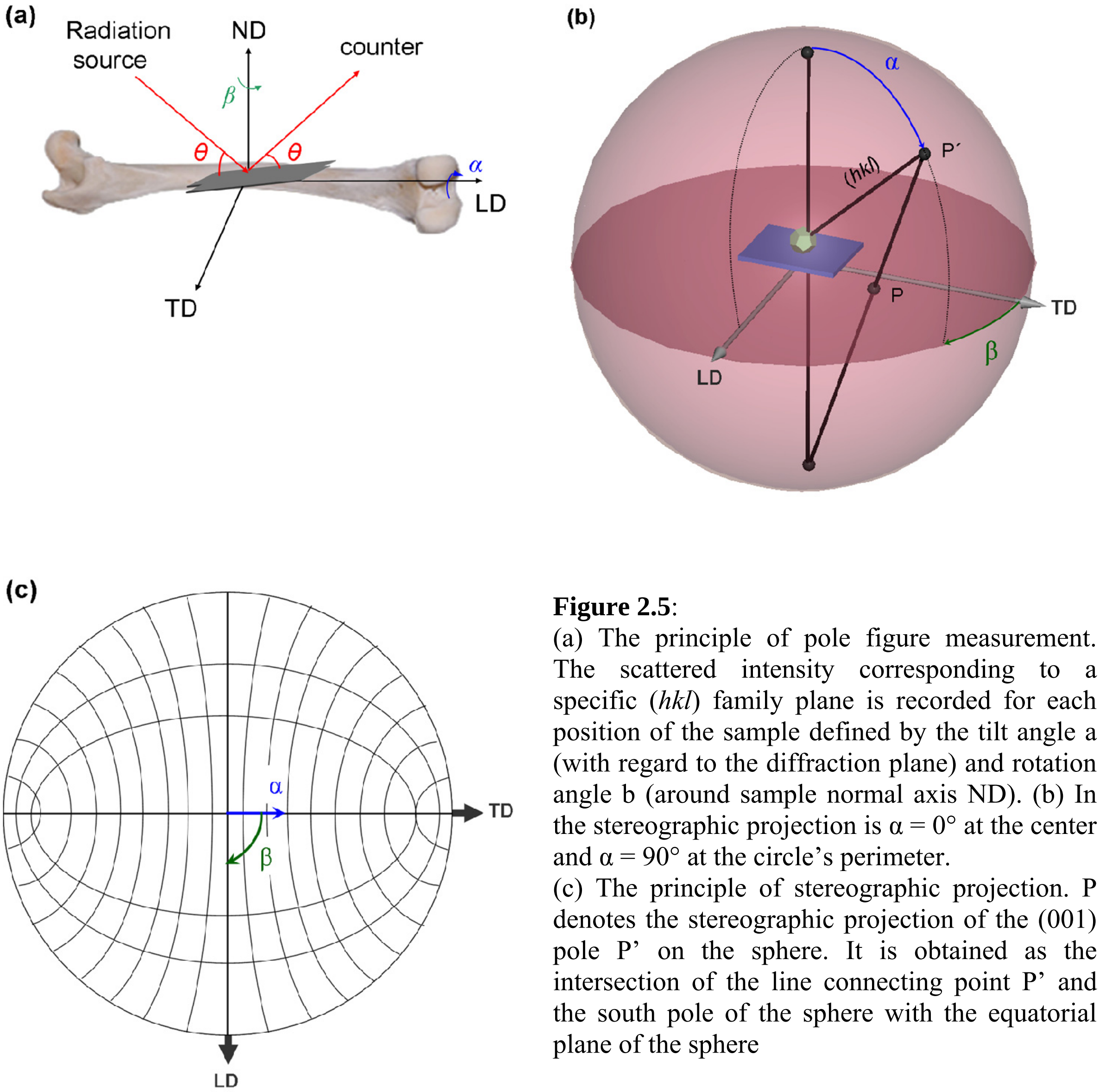

Figure 2.5:
(a) The principle of pole figure measurement. The scattered intensity corresponding to a specific (*hkl*) family plane is recorded for each position of the sample defined by the tilt angle a (with regard to the diffraction plane) and rotation angle b (around sample normal axis ND). (b) In the stereographic projection is α = 0° at the center and α = 90° at the circle's perimeter.
(c) The principle of stereographic projection. P denotes the stereographic projection of the (001) pole P' on the sphere. It is obtained as the intersection of the line connecting point P' and the south pole of the sphere with the equatorial plane of the sphere

If the crystallites' orientation is completely random, the intensity will be uniformly distributed all over the equatorial plane (each point has the same value). If a preferred orientation of (*hkl*) planes is present, then the intensity will be concentrated in a certain area, permitting easy recognition of the orientation of diffracting (*hkl*) planes in the sample. The degree of orientation is quantified by the texture strength, which usually is given as a multiple of the intensity of the random distribution (m.r.d., multiple of random distribution). A higher m.r.d. number means a stronger texture and a higher degree of parallel arrangement in the crystallites in a given direction (for more information, see e.g. Randle & Engler 2000).

5 Transmission electron microscopy (TEM)

In TEM in contrast to optical microscopy and SEM scanning electron microscopy, the image is formed by an electron beam that is transmitted through a thin, transparent sample that is less than 100 nm thick (Figure 2.6a). The most important characteristic of TEM is that it combines information from the real space of an object —at excellent resolution—with information from the reciprocal space of the object (electron diffraction pattern). TEM is a local area analysis technique and is an essential tool for characterizing fine bone structure—for example, the morphology of bone apatite crystals and their local preferred orientations as detected by a specific area electron diffraction pattern. By inserting a selected area aperture (bigger area aperture for information about orientation of few crystals, and smaller area aperture for information about pattern of one specific crystal) and tilting the sample with respect to the incident beam, a diffraction pattern is obtained and recorded using a CCD camera. The reciprocal lattice and orientation of the crystal can be mapped in three dimensions. By studying the diffraction spots, the Bravais lattice and symmetry planes present in the crystal structure can be determined (see example in Figure 2.6b and 2.6c)

In our study, all TEM specimens were extracted and further thinned to the desired thickness by means of a focused ion beam system (Sugiyama & Sisegato 2004). TEM has rarely been used in studies of fossil bone structure (e.g., Zocco & Schwartz 1994; Hubert et al. 1996), despite its routine use in biology and materials science. Characterization of the extremely small apatite crystals (nanometer range) requires an instrument with ultimate resolution. The study of fossil bones by TEM permits for the characterization of the size, shape, and arrangement of bone apatite particles. Moreover, phase identification also becomes possible through electron diffraction images from specific regions. The results, however, should be interpreted carefully because the chemical composition of the bone may have been modified by diagenesis, which influences the interatomic distances. Minerals produced by diagenesis should also be recognized and identified.

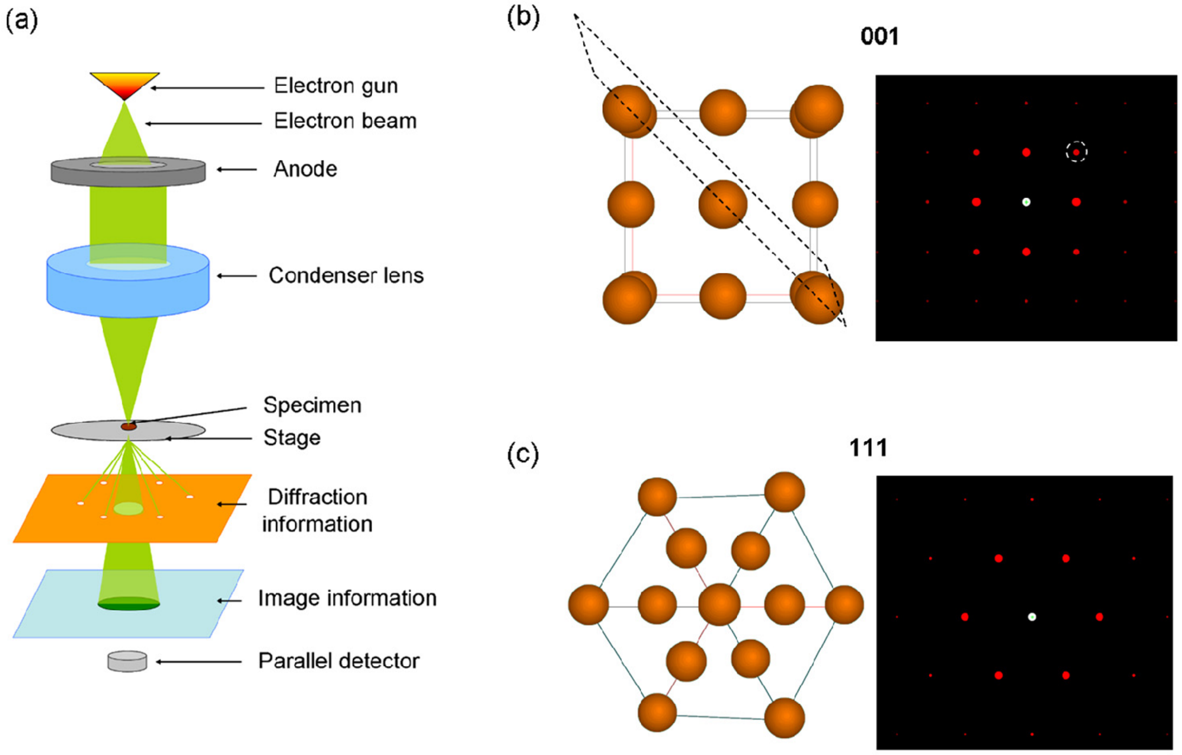

Figure 2.6: (a) TEM instrument illustration with the electron beam passing through the sample, providing images of the specimen as well as diffraction information (spots or circles) on a camera. (b) and (c) examples of diffraction spots obtained for a cubic sample in two different directions 001 and 111. In (b), the diagonal plane illustrated in the model correspond to the red point surround by dashed line on the diffraction pattern. These models were obtained by software JEMS, electron microscopy simulation (Version 3.1512, 2007, Stadelman)

Transmission Electron Microscopy (TEM) studies were performed in a JEOL 2200FTEM/STEM microscope operating at 200kV. Cross-section specimens for TEM analyses were prepared by using a gallium source JEOL JEM-9320 Focused Ion Beam (FIB) system operating at 30kV. The procedure for TEM specimen preparation is illustrated in Figure 2.7. This technique was the first time applied for fossil samples. The first step is called "Rough milling" where the sample, protected by a carbon layer is cut in the sample. The lamella is then removed from the sample and placed on the TEM sample holder (Figure 2.7b and 2.7d). The samples will be then thinned down to approximately 100 nm before being inserted to the microscope.

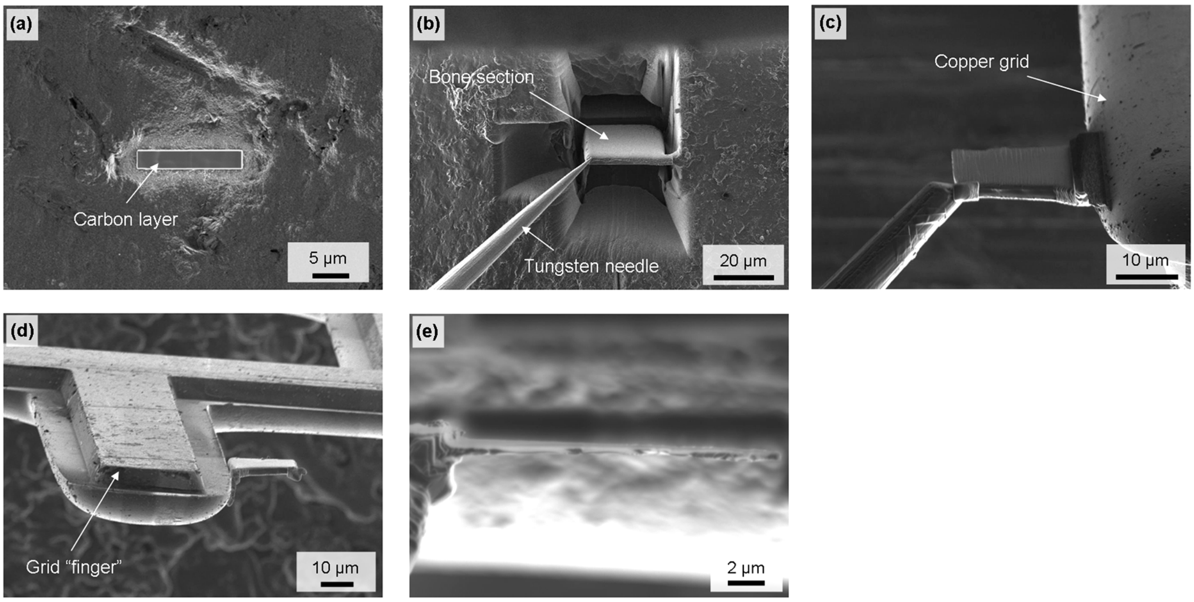

Figure 2.7: FIB lift out technique applied in fossil bone preparation: A carbon layer is deposited where the lamellar will be prepared. The lamella is cut out from the bone. It is picked up with a micromanipulator arm (b). It is fixed to a grid (c) and (d). The thickness of the lamella is reduced to about 150 nm (e). The lamella is ready for TEM (images giving by the courtesy of Dr. Aleksander Kostka)

FIB preparation started to be intensively used for preparation of biomaterials and have already demonstrated its advantage (Hayashi et al. 1998, Volkert et al. 2004, Nalla et al. 2005, Jantou et al. 2009), compared with traditional methods to preserve better the original structure of the specimen. For example, the characteristic periodic contrast, name banding associated with the collagen fibrils is clearly visible in Figure 2.8a in a longitudinal TEM prepared by this technique, without previous need for chemical staining like for ultramicrotomed sections. In Figure 2.8b, needle crystals of cow bone can be easily recognized and diffraction pattern analyzed.

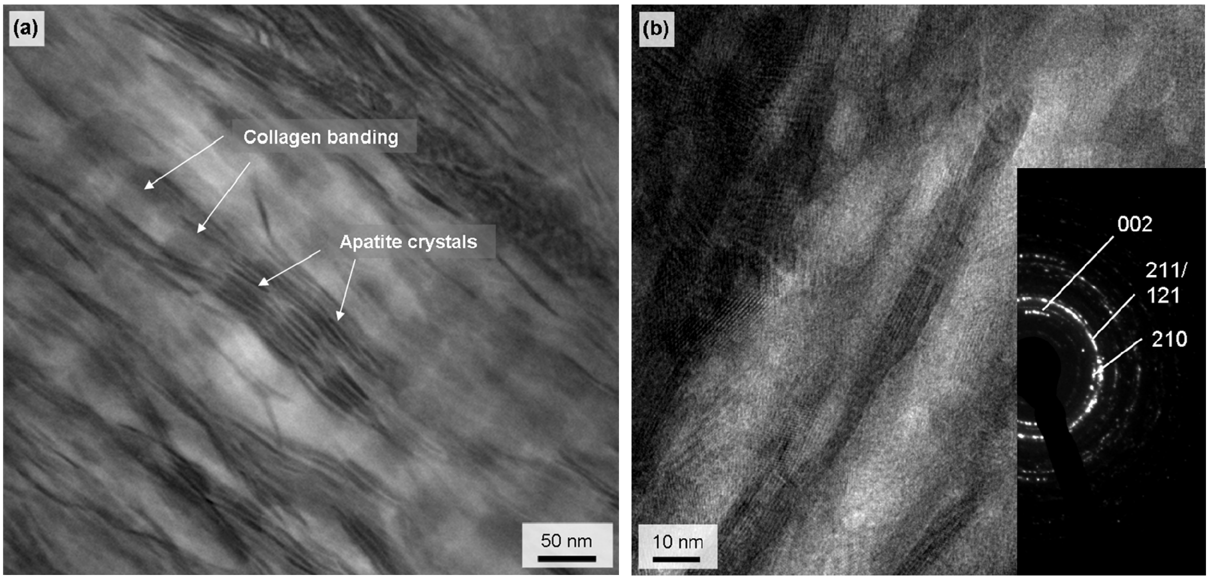

Figure 2.8: (a) STEM FIB sections of a cow bone in a longitudinal plane. The type-I collagen banding (roughly 60 nm period) characteristic of bone material can easily be distinguished, with the apatite crystals associated. (b) TEM section of apatite crystal in the same bone with the diffraction pattern associated. It is composed of rings (diffraction of group of crystals). The symmetry plane can be determined, measuring the distance to the center. The two arcs 002 shows that the crystals are mostly oriented with their c-axis parallel to the bone axis.

Dealing with TEM, biological materials and powerful electron beam, possible electron damage should be discussed. The first damage, easily recognized is the one caused by the heat of the electron beam in a long exposition on the sample. The crystals look coarsened and washed out (Figure 2.9 and 2.10a), like previously observed by Hong et al. (2009). Some voids could form due to the “boiling” and destruction of the material (Figure 2.9, Bres et al. 1991). No phase transformations or second crystallization was observed. Beam damages were essentially observed and increase with the use of the STEM mode (Figure 2.10b), where the beam is scanning slowly and “sweeping” the sample.

Because biomaterial samples are sensitive to the electron beam of transmission microscope, the artefacts were considered in this thesis and avoided, especially for the crystal size measurements.

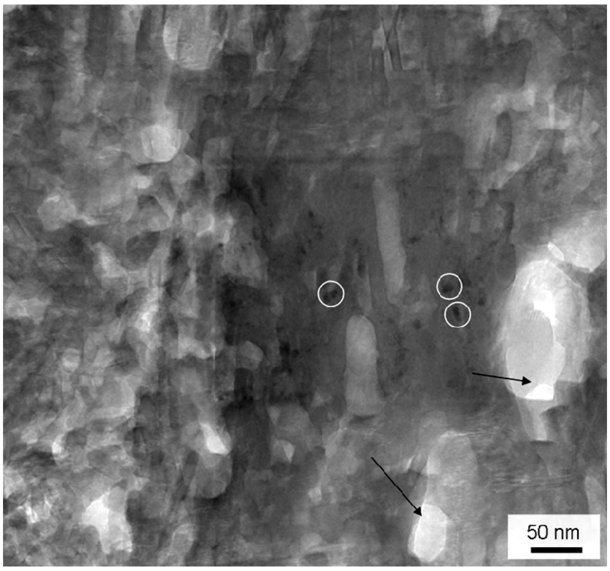

Figure 2.9: Damage observed in TEM lamellar in STEM mode after extended electron beam exposition. Crystals coarsened are observed on the left part giving a frog aspect to the picture. Electron beam also caused formation of voids (black arrows) that are due to destruction of the bone matter. Some blacks spots (white circles) are also observed.

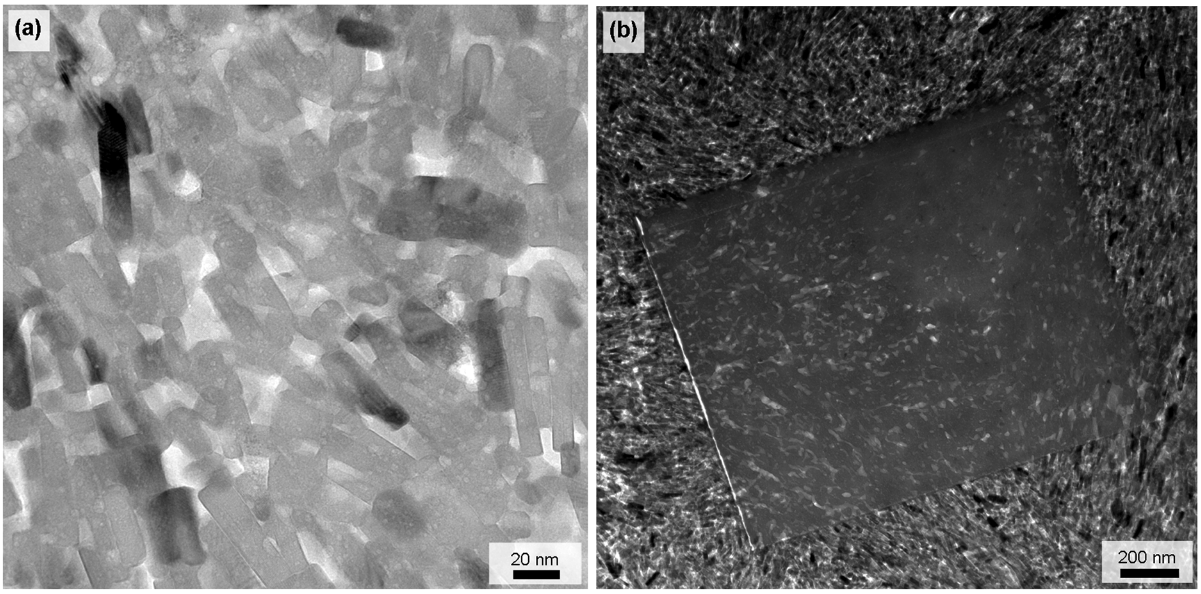

Figure 2.10: Example beam damage (after 120s of beam exposition) in sauropod bones made intentionally for illustration purpose. The crystals are noticed to be coarsened and washed out. An appearance of in-situ boiling of the material is observed due to the heat of the beam (a). Most of damages were observed in STEM where the electron beam is scanning the sample. In (b), a rectangular area of washed out material is experimented after a long scanning.

The characteristics of each method, used in the present work are sum up in the Table 2.2 below. The acquisition of the date for each method depend on the resolution of the results demand by the worker. All methods have both advantages and disadvantages.

Table 2.2: Characteristics (measurement details and data ontained) of the principal methods used in this present thesis. (Prep.=preparation).

Methods	Measurement details	Results
SEM	• Bulk sample: polished or fractured • Prep. not needed • Acquisition: fast	• Microstructure analysis • Chemical analysis with EDX • Crystallographic orientation in a low resolution (µm)
X-Ray diffraction	• Powder or bulk sample • Prep. not needed • Acquisition: variable (depending on the resolution and quality of the data)	• Chemical phase analysis • Crystal size: - good statistics - distibution of crystal size impossible. Average crystal size obtained.
Texture	• Bulk sample • Prep. not needed • Acquisition: time variable depending on the statistics of the result	• Crystallographic orientation analysis Qualitative and quantitative • good statistics
TEM	• Bulk sample • Prep. needed with FIB, slow process • Acquisition slow	• crystallographic orientation: qualitative • Crystal size: statistics relied on the number of the crystals measured (usually lower than the X-ray diffraction method) • Chemical analysis with EDX • Phase analysis precise with diffraction pattern

References

Bres, E.F., Hutchison, J.L., Senger, B., Voegel, J.C. Frank, R.M. 1991. HREM study of irradiation damage in human dental enamel crystals. Ultramicroscopy 35: 305-322.

Chipera, S.J., Bish, D.L. 1991. Applications of X-ray diffraction crystallite size/strain analysis to Seismosaurus dinosaur bone. Advances in X-ray Analysis 34, 473–482.

Cullity, B.D. 1978. Elements of X-Ray Diffraction, 2nd ed. Addison-Wesley Publishing Company, Reading, MA.

Dumont, M., Borbély, A., Kostka, A., Sander, P. M., Kaysser-Pyzalla, A. 2011. Characterization of sauropod bone structure. Pp. 150-170. *In* N. Klein, K. Remes, C. T. Gee, and P. M. Sander, eds. Biology of the Sauropod Dinosaurs: Understanding the Life of Giants. Life of the Past (series ed. Farlow, J.). Indiana University Press, Bloomington.

Klein, N., Sander, P.M. 2008. Ontogenetic stages in the long bone histology of sauropod dinosaurs. Paleobiology 34 (2): 247–263.

Klug, H.P., Alexander, L.E. 1974. X-Ray Diffraction Procedures for Polycrystallite and Amorphous Materials, second ed. John Wiley and Sons, New York.

Hayashi, Y., Yaguchi, T., Ito, K., Kamino, T. 1998. High-resolution electron microscopy of human enamel sections prepared with focused ion beam system. Scanning 20(3): 234-235.

Hong, S.I., Hing, S.K., Wallace, J.M., Kohn, D.H. 2009. Ultrastructural observations of electron irradiation damage of lamellar bone. Journal of Material Science: Materials in Medicine 20: 959-965.

Hubert, J.F., Panish, P.T., Chure, D.J., Prostak, K.S. 1996. Chemistry, microstructure, petrology, and diagenetic model of Jurassic dinosaur bones, Dinosaur National Monument, Utah. Journal of Sedimentary Research 66 (3): 531–547.

Jantou, V., Turmaine, M., West, G.D., Horton, M.A., McComb, D.W. 2009. Focused ion beam milling and ultramicrotomy of mineralized ivory dentine for analytical electron microscopy. Micron 40: 495-501.

Nalla, R.K., Portera, A.E., Daraio, C., Minor, A.M., Radmilovic, V., Stach, E.A., Tomsia, A.P., Ritchie, R.O. 2005. Ultrastructural examination of dentin using focused ion-beam cross-sectioning and transmission electron microscopy. Micron 36: 672–680.

Pyzalla, A.R., Sander, P.M., Hansen, A., Ferreyro, R., Yi, S.-B., Stempniewicz, M., Brokmeier, H.-G. 2006. Texture analyses of sauropod dinosaur bones from Tendaguru. Materials Science and Engineering A 437: 2-9.

Randle, V., Engler, O. 2000. Introduction toTexture Analysis: Macrotexture, Microtexture and Orientation Mapping. Gordon and Breach Science Publishers, London.

Reyes-Gasga, J., Garcia-Garcia, R., Brès, E. 2009. Electron beam interaction damage and reconstruction of hydroxyapatite. Physica B 404: 1867-1873.

Sander, P.M. 2000. Long bone histology of the Tendaguru sauropods: implications for growth and biology. Paleobiology 26 (3): 466–488.

Sander, P.M., Andrassy, P. 2006. Lines of arrested growth and long bone histology in Pleistocene large mammals from Germany: what do they tell us about dinosaur physiology? Palaeontographica A 277: 143–159.

Scherrer, P. 1918. Bestimmung der Grösse und der inneren Struktur von Kolloidteilchen mittels Röntgenstrahlen. Nachr. Ges. Wiss. Göttingen 26: 98–100.

Stein, K., Sander, P.M. 2009. Histological core drilling: a less destructive method for studying bone histology, pp69-80 in Brown, M.A., Kane, J.F., Parker, W.G. (eds.), Methods in fossil preparation: Prooceedings of the first Annual Fossil Preparation and Collections Symposium.

Sugiyama, M., Sisegato, G. 2004. A review of focused ion beam technology and its applications in transmission electron microscopy. Journal of Electron Microscopy 53: 527-536.

Tütken T. 2003. Thesis, published. Die Bedeutung der Knochenfrühdiagenese für die Erhaltungsfähigkeit in vivo erworbener Element- und Isotopenzusammensetzungen in fossilen Knochen. University of Tübingen. 343p.

Volkert, C.A., Busch, S., Heiland, B., Dehm, G. 2004. Transmission electron microscopy of fluorapatite-gelatine composite particles prepared using focused ion beam milling. Journal of Microscopy-Oxford 214: 208–212.

Ziv, V., Weiner, S. 1994. Bone crystal sizes: a comparison of transmission electron microscopic and X-ray diffraction line with broadening techniques. Connective Tissue Research 30: 165–175.

Zocco, G.Z., Schwartz, H.L. 1994. Microstructural analysis of bone of the sauropod dinosaur Seismosaurus by transmission electron miscroscopy. Palaeontology 37 (3): 493–503.

Chapter 3 Diagenesis at the microstructural level

1 Introduction

Fossilized bones are the remnants of sauropod dinosaur cadavers that are available today to provide most information about sauropod organism. Diagenesis (Karkanas et al. 2000), which is the alteration of the bone that appears during burial and fossilization, may affect bone histology, bone porosity, protein content, the crystallinity of the bone apatite, carbonate content, and the bone's content of chemical species in general. The extent of diagenesis mainly depends on direct environmental conditions such as groundwater and sediment composition, soil hydrology and pH, redox potential and temperature, mechanical pressure, biological factors, and particle transport (Reiche et al. 2003).

During bone fossilization apatite replaces the structural protein collagen. The new apatite is incorporated into the bone by external Ca and P, which are transported into the bone via diffusion processes (Pfretzschner et al. 2000). While µm-scale structures of the bone often appear well preserved, early diagenetic pseudomorphosis of bone apatite crystallites can impede the recovery of in-vivo compositional, trace element, and isotope data from fossil bone (Kolodny et al. 1996, Hubert et al. 1996).

Different experimental approaches have been applied to studying and identifying diagenetic processes (Elliott and Grime 1993). Chemical analyses and atomic absorption spectroscopy allow the determination of Sr and Ba contents (Samoilov et al. 1996), but these methods have the disadvantages of being destructive and offering at best a coarse spatial resolution. Among non destructive analysis methods (including e.g. XRF and X-Ray microprobe), electron probe micro-analysis offers a spatial resolution in the µm and sub-µm range, but seems to have an high sensitivity for elements accessible in eth energy range making difficult the quantification of elements such as Sr, U, Ba, and Zn, which are often encountered in fossilized bones (Elliott and Grime 1993, Pfretzschner et al. 2004). Compare to the two already mentioned techniques XRF and X-Ray microprobe, electron probe technique does not require any surface preparation. However, X-ray micro-fluorescence (µ-XRF) analyses are allow semi-quantitative mapping of elements (Z >14) with a local resolution in the order of some µm (depending on the X-ray optics in use) and have been frequently used for studies of archaeological bones (Carvalho et al. 2004). While most research on diagenetic effects on bone has been conducted on archaeological bones, which typically are fully mineralised, here the element distribution is investigated in fossil sauropod dinosaurs buried roughly 140-150 millions years ago (Romer 2001). Using energy dispersive X-ray analyses in the SEM and µ-XRF, the distribution of chemical elements in the fossilized bones is studied with high local resolution. The aim of the combination of these methods is an assessment of the diagenetic effects in sauropod long bones both on a macroscopic and a microscopic scale.

2 Experimental details

2.1 Material

This investigation focuses on sauropod long bones, mainly because they have an exceedingly simple morphology that is largely the product of appositional growth (Sander 2003) and also because they are by far the most abundant in the famed Tendaguru sauropod fauna from Africa from Upper Jurassic (Romer 2001). These sauropod bones excavated in Tendaguru from 1909 to 1912 are today housed in the *Museum für Naturkunde* of the Humboldt-Universität Berlin (Janensch 1914, 1950, 1961; Heinrich 1999). 15mm diameter cores were drilled from the narrowest part of the diaphysis, details are provided in Sander (2003). Afterwards the cores were cut in half along their longitudinal axis. The specimens obtained are half-cylinders that cover the whole bone cortex from the cancellous bone in the center to the primary fibrolamellar bone on the outside. For the analyses, the half core was ground using SiC paper, polished using diamond paste (1µm size) on felt plate. The sample was then cleaned with alcohol.

We started our analysis of the element composition of the sauropod fossil bones by choosing a core taken from specimen no. BrXV, which is a left femur of *Brachiosaurus brancai*, 219 cm in length (Janensch 1961), excavated from the Tendaguru beds. Based on palaeohistological studies (Sander 2003), the femur BrXV belonged to an individual that was still growing. Figure 1 gives an overview of this long bone cortex. The area investigated is located in the white part, between the cancellous bone and the periosteal bone. In this area, the Haversian system, lamellae, and canaliculi appear well preserved (Figure 3.1c)

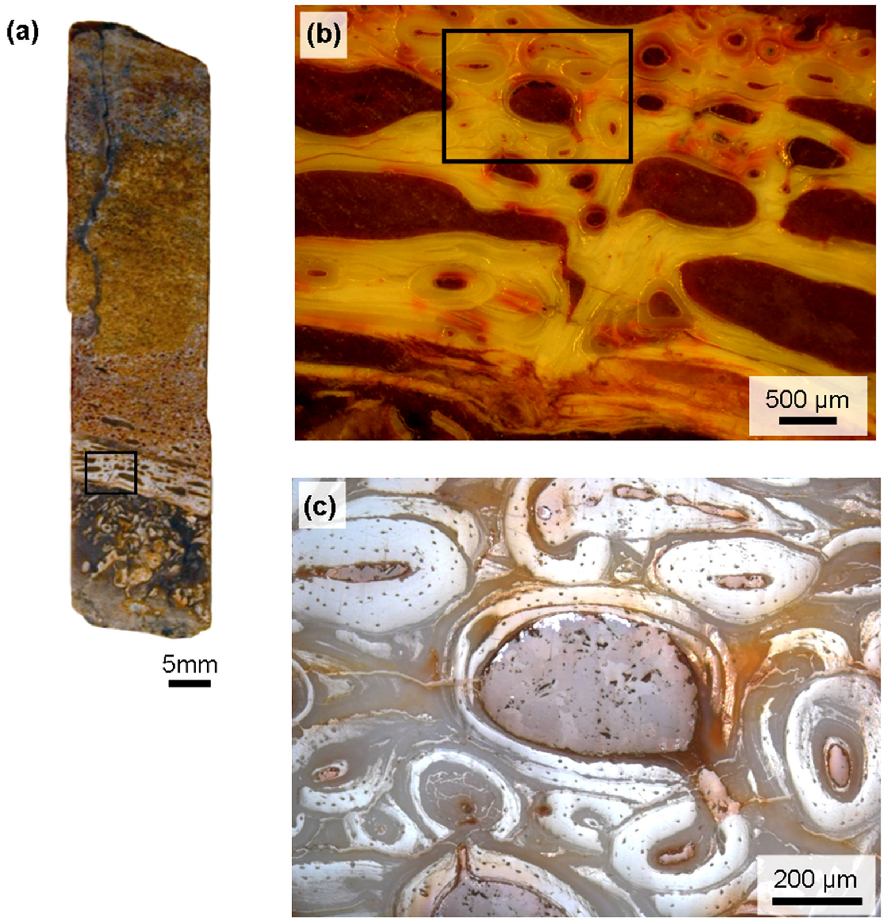

Figure 3.1: Optical micrographs of the sample (BrXV, *Brachiosaurus brancai*, mature individual, femur, femur length 219 cm) a. Overview of the bone cortex. b.,c. Closer view of the area of interest

2.2 Energy Dispersive X-ray Analyses in the Scanning Electron Microscope (SEM-EDX)

SEM/EDX investigations were carried out on Philips XL30 tungsten filament electron microscope operating at 15kV and equipped with EDAX EDS system. The EDX-analyses were performed on uncoated samples. After the EDX-analyses a thin gold layer was sputtered onto the sample surface in order to improve the quality of the secondary electron (SE) and the backscattered electron images (BSE). The element distribution maps obtained by EDX in the SEM reveal the element distribution in a semi-qualitative way: the brighter an area appears in a map for a specific element, the higher is the element concentration.

2.3 Synchrotron Micro-X-ray Fluorescence Analysis (µ-XRF)

Synchrotron radiation induced micro-X-ray fluorescence analysis (SR-µ-XRF) in confocal geometry was carried out at the micro focus end-station at HASYLAB, beamline L, Hamburg, Germany (Janssens et al. 2004). The primary X-ray beam was monochromatized at 17keV by a Ni/C multilayer monochromator and focused by a polycapillary half-lens onto the sample. A second polycapillary half-lens was installed in front of a silicon drift detector (SDD) in order to realize the confocal measurement geometry. By overlapping the focal spots of the two X-ray optic elements a well defined micro-volume was achieved from which the fluorescence radiation was detected. Scanning a 4µm thick Au foil and a 4µm wire, the detection volume at an energy of the Au-Lα line (9.7 keV) was determined to be $20x14x22\mu m^3$ (lateral x height x depth). In the present experiment the 3D capabilities of confocal SR-µXRF were exploited to inhibit unwanted contribution of deeper sample layers (sample thickness ~5mm) to the X-ray fluorescence spectra. In order to enable a comparison of the XRF results with data from the other imaging techniques a confocal µ-XRF area scan was performed in the first layer of the sample. Fluorescence spectra were recorded at 68 x 46 pixels using a step-size of 10µm in each direction and a counting time of 5s per pixel. Net intensities for each pixel were obtained by AXIL fitting (AXIL Tools in QXAS version by IAEA, (Vekemans et al. 1994)) and normalization to 100mA ring current and correction for detector dead time. Element maps were generated by converting the intensity data to 8-bit grayscale images using a scaling from 0 (black) to the maximum counts (white) for each detected element.

3 Results

3.1 EDX Analysis in the Scanning Electron Microscope.

The topographic features visible in the scanning electron microscope (SEM) image are visible also in the EDX maps of Ca, C, Mg, Na, P, Si, and O (Figure 3.2) The vascular canal contains a higher Ca, C, and O concentration than the fossil bone tissue (the bone tissue originally consisted of hydroxyapatite $Ca_{10}(PO_4)_6(OH)_2$). It reveals the presence of calcium carbonate $CaCO_3$ in the vascular canal.

In contrast, the fossil bone apatite contains more P, Si, Mg, and Na than the vascular canal. Since P was not detected in the calcium carbonate, the P distribution reveals very clearly the remnants of the apatite. Thus, the dark areas in the P EDX map reveal details such as cracks introduced by diagenetic processes, e.g. in the lamellae surrounding the vascular canal. A closer view is presented in Figure 3.2; compared with the optical micrograph it is noticed that the crack (blue arrow on the picture) show lack of P.

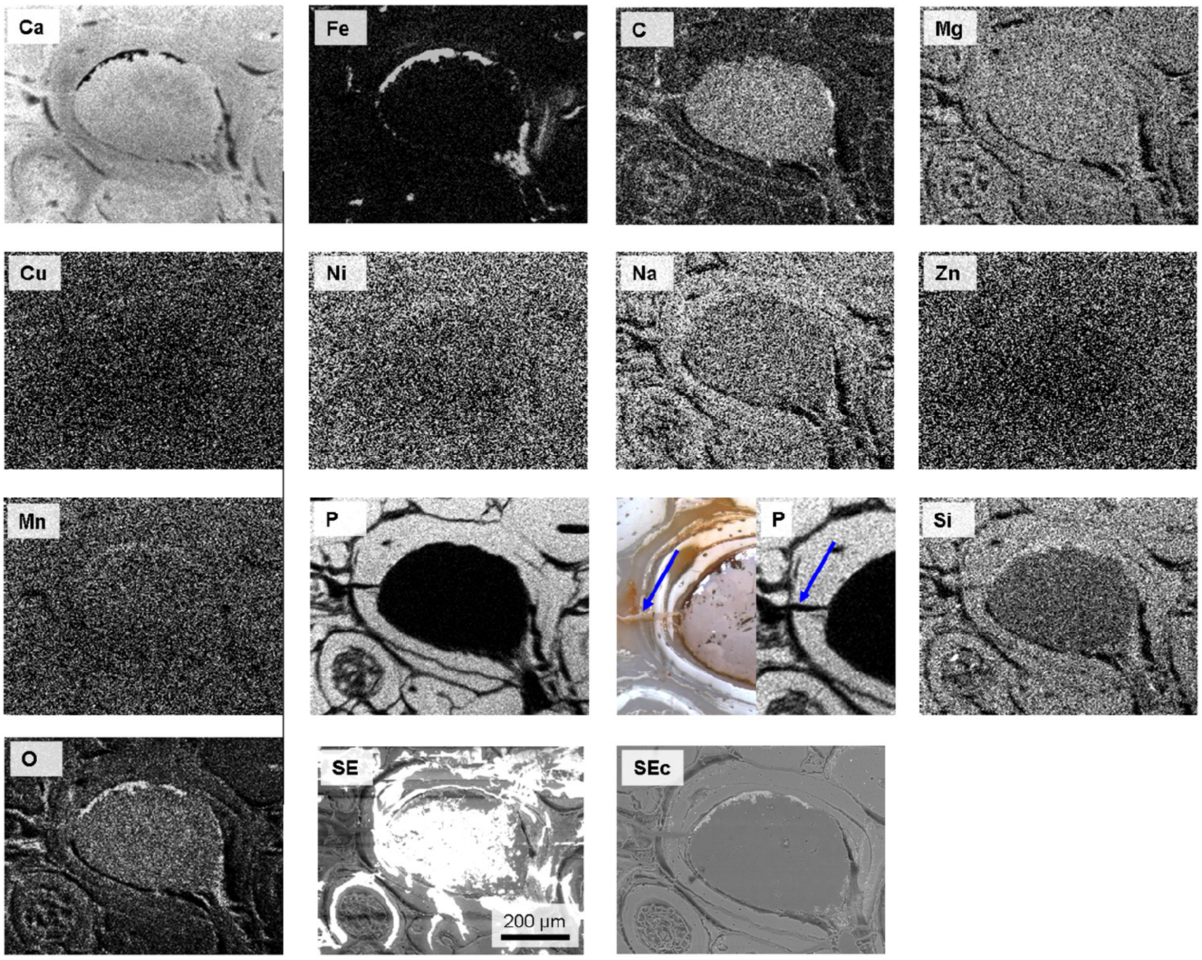

Figure 3.2: SEM EDX element distribution maps of area of interest (in Figure 5.1c). Elements Ca: calcium, Fe: iron, C: carbon, Mg: magnesium, Cu: copper, Ni: Nickel, Na: sodium, Zn. Zinc, Mn: manganese, P: phosphorous, Si: silicon, O: oxygen.

Comparing the P, Ca and Fe EDX-maps reveals Fe enrichment at the interface between the vascular canal and the former apatite. In these areas with high iron content, both Ca and P contents are low. The Fe enrichment is accompanied by a substantial O enrichment, revealing the formation of iron oxides in these pore spaces. Also the Si, Mn, and Ni contents are higher in these regions than within the calcium carbonate and the apatite.

3.2 SR-µ - X-ray Fluorescence Analysis (SR-µ-XRF)

The element distribution maps obtained with high spatial resolution using synchrotron radiation µ-XRF similar to the EDX-analyses in the SEM reveal a qualitative image of the element distribution (Figure 3.3). For each element a scaling was performed with respect to the minimum and the maximum intensities obtained in the spectra collected over the sampled area. The dark areas in the plots for each element correspond to regions where we measured low XRF intensities, on the contrary an increasing brightness corresponds to higher intensities in the XRF spectra and thus to an enrichment in the respective element. Besides element distribution maps obtained for Ca, Fe, Cu, Ni, Zn, and Mn, where SEM EDX maps could be measured, μ-XRF maps were determined for Co, Cr, V, Pb, U, Sr, Y, and As.

Even more clearly than the EDX maps the μ-XRF maps show the Ca distribution and thus the localization of the calcium carbonate within the vascular canal of the bone, in the cracks and between different lamellae surrounding the vascular canal. The calcium carbonate in addition to Ca, C, and O only contains Mn and a low amount of Sr.

Compared to the calcium carbonate the former apatite contains a significantly higher Sr concentration. The μ-XRF distribution map of Sr in the former apatite compares well with the U distribution. The Zn distribution in the former apatite also appears similar to the Sr and U distribution. In both the U and the Sr map the calcium carbonate filled crack and the calcium carbonate filled rims between the lamellae are visible, which were also observed in the SEM EDX-maps.

Fe, Co, Cr, Cu, Ni, V, Zn, Mn, Pb, and As show relative maximum values in the same locations at the interface between the calcium carbonate and the former apatite. The local maximum values of the Fe concentration determined by μ-XRF coincide with those determined by SEM – EDX.

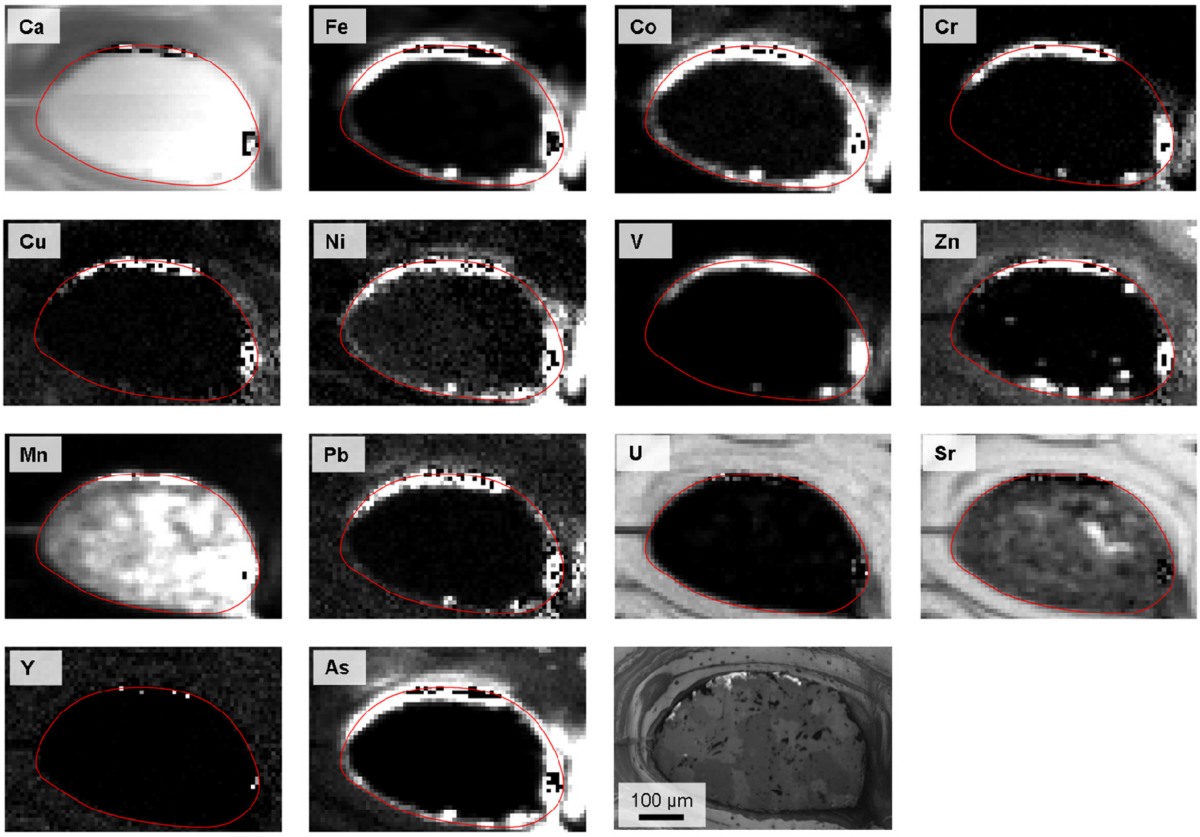

Figure 3.3: µ-XRF element distribution maps of area of interest (in Figure 5.1c).). Elements Ca: calcium, Fe: iron, Co: cobalt, Cr: chromium, Cu: copper, Ni: Nickel, V: Vanadium, Zn. Zinc, Mn: manganese, Pb: lead, U: uranium, Sr: stromtium, Y: yttrium, As: arsenic.

4 Discussion

4.1 EDX Analysis in the SEM

This technique is a fast and far more easily accessible tool for semi-quantitative analyses (C, O and other light elements cannot be quantified reliably. However, this drawback can be overcome using WDX-analysis in a microprobe SEM) at the sample surface. By mapping the X-ray intensity of various chemical elements, their distribution can be related to the fossil microstructure. The EDX–maps of the P distribution directly reveal radial micro-cracks in the lamellae of the former vascular canals. The formation of radial micro-cracks can be attributed to diagenetic processes (Behrensemeyer 1978). The micro-cracks form early during diagenesis due to internal stresses during the replacement of collagen by apatite (Pfretzschner 2000). The radial micro-cracks according to (Bell 1990, Pfretzschner 2000) have an important role during the diagenetic process, since they open additional pathways for diffusion in the Haversian bone and thus they contribute significantly to recrystallization and crystal growth of the former hydroxyapatite in the bone. In addition to radial micro-cracks, polygonal crack networks are also visible in the EDX-map of the element P (Figure 3.2). These polygonal cracks supposedly appear later during the diagenetic process due to external pressure on the fossil (Pfretzschner 2000).

4.2 Synchrotron µ-XRF Analysis

Synchrotron µ-XRF analysis here was applied for first time to characterize the element distribution in fossil bones. It provides a map of the element distribution with a spatial resolution comparable to those offered by EDX in the SEM, but due to its higher detection level in the order of a few ppm, the distribution of elements such as U, Sr, Pb, and As can be determined, which are of particular interest for dietary indicators (Parker and Toots 1980, Rheingold et al. 1983, Ezzo 1994,Safont et al. 1998). Compared to XRF using laboratory X-ray sources (Ferreyro et al. 2006) synchrotron µ-XRF provides a substantially higher spatial resolution and lower detection limits (in the range of ng/g). The combination of synchrotron XRF analyses with EDX analyses in the SEM provides a very clear differentiation between original and diagenetically- formed apatite and pore-filling minerals such as calcium carbonate or iron oxides, because P as well as U and Sr as minerals with an affinity to bone are almost exclusively present in the apatite.

4.3 Element Distribution in Sauropod Dinosaur Bones

A comparison of the element concentrations in the sauropod bone fossils basically indicates agreement with earlier investigations on archaeological bones (Lambert et al. 1985, Reiche et al. 2003), showing that Ca, Na, K, and Pb are lower in the excavated samples (they leach out) and Fe, Mn, and Al are enriched in the excavated samples.

Except for Fe, on a macroscopic level the distribution of elements in the sauropod bone investigated appears fairly homogeneous.

Fe, Mn: Compared to modern bone, the fossilized sauropod femur shows a significantly higher Fe and Mn content. Both the SEM-EDX and the µ-XRF element maps show that Fe and Mn apparently have a very similar spatial distribution, and a similar correlation of Fe and Mn was shown by PIXE microprobe investigations of archaeological human bones (Boscher-Barre 1992). Elliott and Grime (Elliot and Grime 1993) found Mn concentrated within the bone in patterns that correspond to the bone's small pore and canaliculi structures while Fe more typically filled the larger pores in the bone matrix such as Haversian canals. The combined occurrence of Fe, Mn, Cr, V, Si, and O in the fossilized sauropod bones reveals that an oxide seam formed at the interface between the vascular canals and the former hydroxyapatite. Mn, besides being incorporated into the oxides, is known as a contaminant of the calcium carbonate from soil solution (Reeder and Grams 1987). A same tendency can be observed as well in TEM (Chapter 4). Mostly iron oxides inclusions are noticed in small pores and osteocyte canalicular structures.

Enrichment of Fe in fossil bones has been observed previously by (Lambert et al. 1985, Karkanas et al. 2000). The distribution of Fe, which mainly covers the inner surface of the voids created by the degeneration of organic parts, might indicate that the iron oxides formed at an early stage of the diagenetic process. The voids are indeed are the most accessible places where iron oxides is developed first (Pfretzschner 2004). Later in the stage of diagenesis, the oxides filled the radial cracks or the cement line of secondary osteons (Pfretzschner 2000, 2001). Our observations in SEM-EDX or μ-XRF do not indicate such an extend of iron inclusions, but a limitation in the inner surface of osteons.

Sr, U: Sr and U are two elements incorporated in the hydroxyapatite. Sr substitutes Ca in hydroxyapatite (Parker and Toots 1980) and thus is mainly present in the fossilized former hydroxyapatite, but not exclusively present as earlier reported by (Ezzo 1994). U is incorporated into the bone as complexes of the Uranyl ion by diffusion and subsequent adsorption (Millard et al. 1995). The U decrease towards the medullar cavity might indicate that part of it leached out during the diagenetic process.

Mg, Na: Light chemical species such as Mg and Na appear to be homogeneously distributed within the fossilised bone in contrast to previous studies on archaeological bones where Mg and Na were shown to leach out of the bone (Parker and Toots 1980, Reiche et al. 2003). This homogeneous distribution is attributed to the long time available for diffusion.

Ca: According to (Karkanas et al. 2000), in the presence of calcium carbonate the pH of the bones is controlled by the pH of the waters entering the bone, which in turn prevents the apatite from being dissolved. Thus the incorporation of large amounts of calcium carbonate in the sauropod fossil bones is an indication that most of the original apatite has been conserved.

5 Conclusions

μ-X-ray fluorescence analyses using synchrotron radiation determined the preferential location of elements within the sauropod fossils. The analyses allowed a qualitative determination of the element distribution on the level of a few 100 μm^2. Additional EDX analyses in the SEM provided information about the distribution of elements with lower atomic number Z.

The combination of the different analysis techniques revealed that although seemingly unaffected at the histological level, the sauropod fossils endured strong diagenetic changes. Element maps of P obtained by SEM and element maps of Sr and U obtained by µ-XRF reveal the location of the remnants of the apatite of sauropod bone and show micro-cracks introduced by diagenesis. Both methods show that diagenetic minerals filled these micro-cracks and also the vascular canals of the bones.

The concentration and distribution of the trace elements in the sauropod bones reveals that even in case of these extraordinary large fossils strong diagenetic changes occurred, which render conclusions about the abundance of trace elements in the living bones of sauropods extremely difficult.

References

Behrensemeyer, A. K. 1978: Taphonomic and ecologic information from bone weathering: Paleobiology 4: 150–162.

Bell, L. S. 1990. Palaeopathology and diagenesis: An SEM evaluation of structural changes using backscattered electron imaging. Journal of Archaeological Science 17: 85–102.

Boscher-Barre, N., Trocellier, P., Deschamps, N., Dardenne, C., Blondiaux, J., Buchet, L. 1992. Nuclear micropore study of trace element in archeological bones, Journal of Trace Microprobe Technique 10: 77–90.

Carvalho, M. L., Marques, A. F., Lima, M. T., Reus, U. 2004. Trace elements distribution and post-mortem intake in human bones from Middle Age by total reflection X-ray fluorescence. Spectrochimica Acta, B At. Spectrosc. 59: 1251–1257.

Elliott, T. A., Grime, G. W. 1993. Examining the diagenetic alteration of human bone material from a range of archaeological burial sites using nuclear microscopy. Nuclear Instruments and Methods in Physics Research B 77: 537– 547.

Ezzo, J. A. 1994. Putting the chemistry back into archaeological bone chemistry analysis: Modeling potential paleodietary indicators. Journal of Anthropological Archaeology 13: 1–34.

Ferreyro, R., Zoeger, N., Cernohlawek, N., Jokubonis, C., Koch, A., Streli, C., Wobrauschek, P., Sander, P. M., Pyzalla, A. 2006. Determi- nation of the element distribution in sauropod long bones by micro- XRF. Advances in X-Ray Analysis 49: 230–235.

Heinrich, W.-D. 1999. The taphonomy of dinosaurs from the Upper Jurassic of Tendaguru, Tanzania East Africa, based on field sketches of the German Tendaguru expedition 1909–1913. Mitteilungen aus dem Museum für Naturkunde in Berlin, Geowissenschaftliche Reihe 2: 25– 61.

Hubert, J. F., Parish, P. T., Chure, D. J., Prostak, K.S. 1996. Chemistry, microstructure, petrology, and diagenetic model of Jurassic dinosaur bones, Dinosaur National Monument, Utah. Journal of Sedimentary Research 66: 531–547.

Janensch, W. 1914. Übersicht über die Wirbeltierfauna der Tendaguruschichten, nebst einer kurzen Charakterisierung der neu aufgeführten Arten von Sauropoden. Archives für Biontologie 3: 81–110.

Janensch, W. 1950. Die Skelettrekonstruktion von *Brachiosaurus brancai*. Palaeontographica 7: 97–103.

Janensch, W. 1961. Die gliedmaszen und gliedmaszengürtel der sauropoden der Tendaguru-Schichten. Palaeontographica 7: 177–235.

Janssens, K., Proost, K., Falkenberg, G. 2004. Confocal microscopic X-ray fluorescence at the HASYLAB microfocus beamline: Characteristics and possibilities, Spectrochimica Acta, Part B 59: 1637–1645.

Karkanas, P., Bar-Yosef, O., Goldberg, P., Weiner, S. 2000. Diagenesis in prehistoric caves: The use of minerals that form *in situ* to assess the completeness of the archaeological record. Journal of Archaeological Science 27: 915–929.

Kolodny, Y., Luz, B., Sander, M., Clemens, W. A. 1996. Dinosaur bones: fossils or pseudomorphs? The pitfalls of physiology reconstruction from apatitic fossils. Palaeogeography, Palaeoclimatology, Palaeoecology 126: 161–171.

Lambert, J. B., Vlasak Simpson, S., Szpunar, C. B, Buikstra, J. E. 1985. Bone diagenesis and dietary analysis. Journal of Human Evolution 14: 477– 482.

Millard, A. R, Hedges, R. E. M. 1995. The role of the environment in uranium uptake by buried bone. Journal of Archaeological Science 22: 239–250.

Parker, R. B., Toots, H. 1980. Fossils in the Making: Vertebrate Taphonomy and Paleoecology, edited by Behrensmeyer, A. K. and Hill, A. P. University of Chicago, Chicago, pp. 197–207.

Pfretzschner, H.-U. 2000. Microcracks and fossilization of Haversian bone. Neues Jahrbuch für Mineralogie 216: 413–432.

Pfretzschner, H.-U. 2001 Pyrite in fossil bone. Neues Jahrbuch für Geologie und Paläontologie 220 (1): 1–23.

Pfretzschner, H.-U. 2004. Fossilization of haversian bone in aquatic environments. Comptes Rendus Palevolution 3: 605-616.

Reeder, R. J., Grams, J. C. 1987. Sector zoning in calcite cement crystals: Implications for trace element distributions in carbonates. Geochimica Cosmochimica Acta 51: 187–194.

Reiche, I., Favre-Quattropani, L., Vignaud, C., Bocherens, H., Charlet, L., Menu, M. 2003. A multi-analytical study of bone diagenesis: the Neolithic site of Bercy Paris, France. Measurement Science and Technology 14: 1608–1619.

Rheingold, A. L., Hues, S., Cohen, M. N. 1983. Strontium and zinc content in bones as an indication of diet. Journal of Chemical Education 60: 233–234.

Romer, R. L. 2001. Isotopically heterogeneous initial Pb and continuous 222Rn loss in fossils: The U-Pb systematics of *Brachiosaurus brancai* Geochimica Cosmochimica Acta 65: 4201–4213.

Safont, S., Malgosa, A., Subira, M. E., Gibert, J. 1998. Can trace elements in fossils provide information about palaeodiet? International Journal of Osteoarchaeology 8: 23–37.

Samoilov, V., Benjamini, Ch. 1996. Geochemical features of dinosaur remains from the Gobi Desert, South Mongolia. Palaios 11: 519–531.

Sander, P.M. 2000. Longbone histology of the Tendaguru sauropods: Implications for growth and biology. Paleobiology 26: 466–488.

Tükten, T., Pfretzschner, H.-U., Vennemann, T. W., Sun, G., Wang, Y. D. 2004. Paleobiology and skeletochronology of Jurassic dinosaurs: Implications from the histology and oxygen isotope compositions of bones, Palaeogeography Palaeoclimatology Palaeoecology 206: 217–238.

Vekemans, B., Janssens, K., Vincze, L., Adams, F., Van Espen, P. 1994. Analysis of X-ray spectra by iterative least squares AXIL: New developments. XRay Spectrometry 23: 278–285.

Chapter 4 Multiscale analysis of diagenesis of *Apatosaurus* bones with emphasis on TEM technique

1 Introduction

Fossil bones have been used as proxies for palaeoecological and environmental studies (Parker and Toots 1970, Lambert et al. 1982, Bocherens et al. 1994, Kohn et al 1999). But dealing with fossil samples, modification during diagenesis process need to be considered. For a few years, an increase of multidisciplinary methods have been applied to investigate these alterations and to understand the transformations undergone by bone during fossilization (Lee-Thorp and Van der Merwe 1991, Kolodny et al. 1996, Pfretzchner 1998, Nielsen-Marsh and Hedges 2000a, 2000b, Hedges 2002). These methods have their limits: in the resolution, in their application (destructive method) or they show limitations for determining elemental composition. Most of them (e.g. X-ray diffraction, proton induced X-ray emission (PIXE), infrared spectroscopy) demonstrate that the original chemistry of the bone apatite is significantly altered by the diagenesis, with exchange of ions in the apatite lattice. Three different changes are well known: (1) the replacement of the cations of apatite $Ca_5(PO_4)_3OH$ by alkalines or other transitional cations; (2) the substitute of phosphate group by a carbonate group; (3) the exchange of hydroxyl group with fluorine (fluoritization) (Hubert et al. 1996, Trueman 1999). Important infillings of secondary mineral phases are also common to appear in the pores of the bone (Hubert et al. 1996, Zocco and Schwartz 1994, Kolodny et al. 1996, Elorza et al. 1999). As Kohn in 1999 (Kohn et al. 1999) already mentioned, the recognition of secondary minerals or direct modification of apatite bone is important to understand the chemistry of biogenic apatite for paleobiological and paleoclimate features inferences. Indeed, identification and characterization of secondary infillings in fossil bone can help to distinguish diagenetic processes and depositional environments; their crystallization being mostly influenced by environment or water flood.

The understanding of the influence of diagenesis on bone structure at the nanolevel is still challenging (Reiche et al 2003). Different and combined approaches like PIXE, an X-Ray fluorescence method is used for microsized dimensions. Quantification or imaging resolution is still in improvement: Goodwin et al. (2007) decreases the resolution by registering quantitatively chemical composition of dinosaur bone at 1.5 μm diameter beam with PIXE method. Combined with synchrotron radiation, a scale range of some micrometer can be also reached (Dumont et al. 2009).

In the present work use of focused ion beam technique enabled good quality TEM specimens from carefully selected regions. The analytical TEM (good diffraction contrast coupled with EDX information) provided important knowledge about local structure and chemistry of fossilized bone. So far it was not used extensively in paleontology (Zocco and Schwartz 1994, Hubert et al. 1996, Reiche et al. 2002, 2003) and was partially due to the difficulty of sample preparation. Use of focused ion beam, makes the preparation easier and more reliable. Limits of this method reside in the weak ability of the EDX to quantify light elements ($Z<14$) (Kuisma-Kursula 2000).

Three Apatosaurus samples from the Morrison Formation (Colorado, USA) were analysed in this study using the transmission electron microscopy (TEM) to characterize microstructure of the fossilized bones. TEM diffraction technique supported by the Energy Dispersive X-ray (EDX) spectroscopy was used for determining elemental composition and crystal structure from nanoareas. Coupled with X-ray diffraction analysis and SEM-EDX, investigations focused on the micro and nano-scale microstructural and complementary results are described. Chemical composition of fossil bone was quantified and secondary minerals and clays minerals that formed in the natural pores of the bones were identified in situ. It provides informations about diagenesis in dinosaur bones from the Morrison Formation and possibly interprets the different taphonomic processes.

2 Experimental details

2.1 Material

Three different samples of Apatosaurus sauropod coming from Morrison Formation (Upper Jurassic, USA) were studied. They consist of drill core sections of midshaft of cortex long bones (Klein and Sander 2008, Stein and Sander 2009). These samples were analyzed in TEM and selected for their feature observed. This formation has yielded with one of the richest fauna of dinosaur fossils (Foster 2007). It covers a large area from Wyoming to Colorado. Two samples come from continental geological bed (Schultz 1972) of Kenton Quarry: a humerus (OMNH 01278) and a femur (OMNH 01279). The third sample femur BYU 601 17328 has been found in BYU locality 601. Through this study we will keep the signatures of the specimens as following: OMNH 01278, OMNH 01279 and BYU 601 17328.

The sauropod sample were compared with two subfossil mammal samples: a bison *Bison priscus* (FKBiRS) and an horse *Equus sp.* (MQB 48516, Rhein-Herne Ship Channel, Germany, already described in Sander and Andrassy 2006).

2.2 X-ray diffraction

XRD measurements were performed by a Bruker D (diffractometer equipped with a graphite monochromator using CoKα radiation (λ=1.789 Å). The measurements were recorded over the 2θ range of 20°-80°with a step size of 0.075°.

2.3 Scanning electron microscopy (SEM)

Specimens for SEM were prepared via grinding and polishing. SEM investigations were carried out with Jeol JSM-6500F SEM operated at 15 kV, tungsten filament instrument. The microscope is equipped with EDAX-TSL EBSD system.

2.4 Transmission electron microscopy (TEM)

The TEM samples of sauropod were prepared using an Jeol JEM-9320 Focused Ion Beam (FIB) instrument operating at 15 kV. Compare to previous, traditional method, FIB (Munroe) allows high quality TEM sample preparation from specific locations (Nalla et al. 2005, Jantou et al. 2009, Coutinho et al. 2009) and particularly for quantitative work, where a constant thickness is prefered. Furthermore this technique avoids artifacts by chemical staining (Ziv and Weiner, 1994; Eppel et al., 2001) or mechanical deformation by diamond-knife sectioning (Hayashi et al. 1998, Volkert et al. 2004, Nalla et al. 2005, Jantou et al. 2009).

The TEM analyses were carried out using a Jeol Jem-2200FS instrument operating at 200kV and equipped with STEM bright field (BF), High Angle Annular Dark Field (HAADF) and Jeol Energy Dispersive X-ray (EDX) detectors. TEM micrographs were recorded with a Gatan CCD camera and further processed using Gatan Digital Micrograph software (Version 3.8.2).

3 Results

3.1 Bone chemistry results

3.1.1 X-ray diffraction

The three sauropod bones studied were compared with two subfossil mammal bones of *bison* and *horse*. A more pronounced crystallinity is observed in sauropod bones, with sharper peaks, specifically visible for (211), (112) and (300) reflections, in the diffractogram Figure 4.1. Additional peaks are also noticed. When the cortical bone of sample BYU 601- 17328 seems to be only composed by hydroxyapatite, the other two samples OMNH 1278 and OMNH 1279 display secondary minerals of quartz and calcite. Quartz mineral is noticed at 31° in sample OMNH 1278 and OMNH 1279, the intensity is more important for the first sample. Large peaks of calcite have been identified at 32.5 and 35 °(2θ).

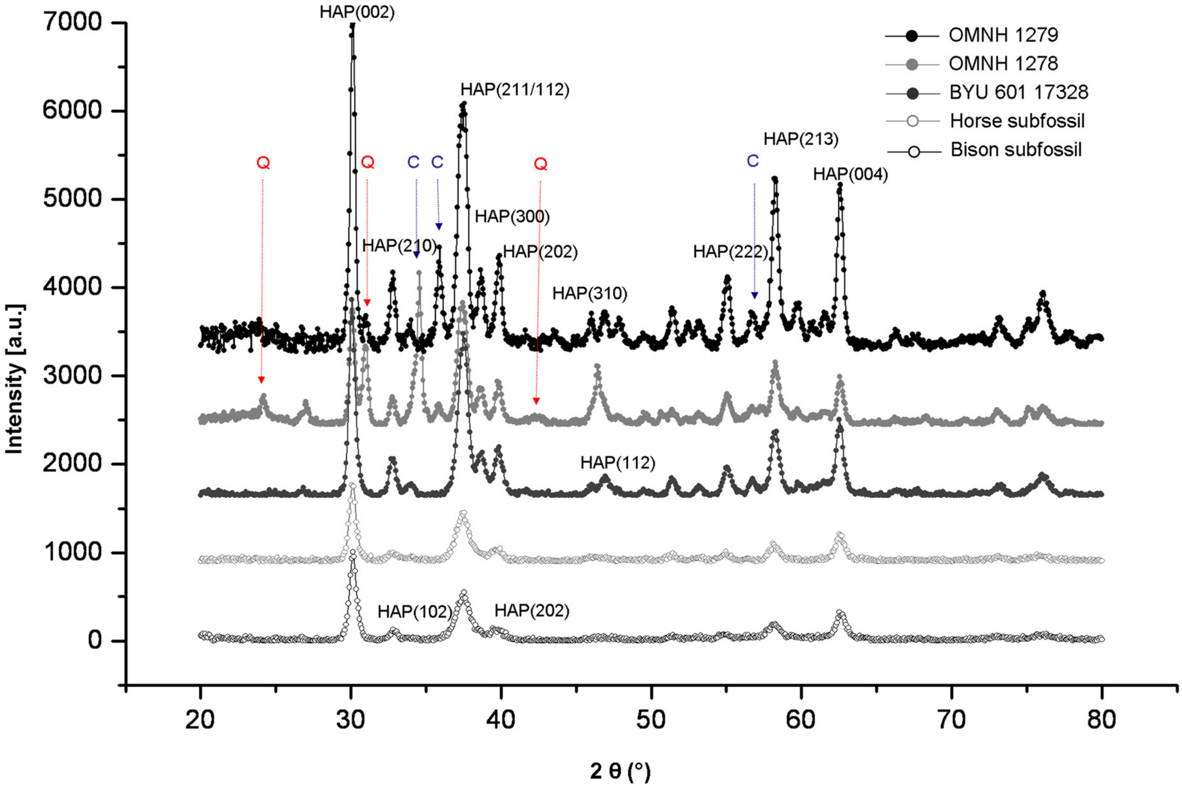

Figure 4.1: Diffractograms of bone obtained by X-Ray diffraction with principal reflections of hydroxyapatite crystals. The peaks for sauropod samples (full circle) present sharper peaks compared to subfossil bones. The subfossil bones present also overlapping of some reflections (i.e. between 112, 300) due to smaller crystal size observed in these samples. Sample OMNH 1278 and OMNH 1279 display additional peaks from minerals different from hydroxyapatite corresponding respectively to quartz (Q) and calcite (C). The sample BYU 601-17328, apart from sharper peaks is a single phase specimen.

3.1.2 SEM

SEM-EDX analyses were performed in the fibrolamellar (FBL) bone of the cortex of the three samples (Table 4.1).

Table 4.1: Concentration (wt. %) of elements of the samples studied.

	C	O	F	Na	Mg	Al	Si	P	S	Ca	Fe	Total
OMNH 1278	12,7	36,4	2	0.4	0.3	0.8	3.7	13.2	0.7	29.5	0.3	100
OMNH 1279	11.3	32.6	1.8	0.4	1.8	0.9	1.8	14.3		32	2.4	100
BYU 601-17328	9.6	25.7	1.8	1.0	0.5	0.05	0.2	17.9	1.3	39.9	1.8	100

Table 4.1 shows the chemical composition of cortical bone of the samples studied. The three samples are composed of around 2% of fluor and have then a francolite composition. They are roughly sharing the same composition with ~30 to 40% of calcium and ~15% of phosphorous. The sample BYU 601-17328 registered the highest calcium concentration in its bone (around 40%). The sample OMNH 1279 has high concentrations of Mg, Al and Fe (>2%). High concentration of silicon can be noticed in the sample OMNH 1278. Whereas in the sample BYU 601-17328, a non negligible percent of iron and sulfurr are both present.

3.1.3 TEM

EDX analyses on the same samples were performed by TEM. The concentrations were registered in the crystallites that are forming the bone apatite. The results are presented in the Table 4.2.

Table 4.2: Measured element concentrations (wt. %) of the samples studied.

	C	O	F	Na	Mg	Al	Si	P	S	Ca	Fe	Total
Bison subfossil	13 ±2.5	32.6 ±0.6	2.1 ±0.02	0.1				15.6 ±0.03	0.2 ±0.01	35.3 ±2.1	1.2 ±0.01	100
OMNH 1278	18.4 ±2	27.7 ±1.7	3.3 ±0.5					14.7 ±0.4	0.2	35.6 ±1.2	0.1	100
OMNH 1279	9.9 ±1.6	29.65 ±3.6	3.85 ±0.7			0.1	0.1 ±0.1	19 ±2		37.4 ±4.6		100
BYU 601-17328	7.9 ±0.2	28.6 ±1.2	3.3 ±0.7		0.2			17.3 ±0.5	0.8	41.7 ±1.5	0.2	100

Bison subfossil

The subfossil bison sample FK BI RS 1 has an apatite composition with large concentration of Fluor up to 2% weight (several analysis points were made for statistical values). The carbone concentrates at 13% and calcium and phosphorous has respectively ~35% and 15%. Minor elements like sodium Na and suffer S are also noticed but only around 0.1 and 0.2%wt. Iron element has been detected as well with 1.2 %wt.

BYU 601-17328

The sample BYU 601-17328 shows a composition of fluorapatite with high concentration of calcium Ca (~ 42%), carbon C (8%) and phosphorous P (~ 18%) and some fluor F (~ 4%). The fluor, phosphorous and calcium concentrations are little bit higher than in the subfossil sample above. As observed already in SEM-EDX analysis, this sample registered the higher calcium concentration (Table 4.1). The carbon content on the other hand is lower. A trace concentration of sulfur S (< 1%) is also registered, as magnesium Mg and iron Fe. The magnesium and iron were registered in a larger area (0.5x0.5nm) including crystals and matrix. And their low concentrations are in the error limit of the detector

OMNH 1278

In comparison, TEM-EDX of sample OMNH 1278 has also been quantified. In Table 4.2, we can observed that the fossil bone has also fluorapatite in composition with roughly same chemical composition e.g. ~35% of Ca, ~15% of P, ~19% of C and 3.3% of F. Lower concentrations of Ca and P observed are due to the higher concentration of C (value double compare to sample BYU 601-17328). The C concentration comes certainly from contamination of secondary minerals (Calcite) already observed in X-Ray diffraction. For this sample, spectrum collected from the large area (Figure 4.2a) reveal presence of small concentration of iron, which is absent in the apatite crystal (Figure 4.2b). Absence of this authigenic element in the apatite crystal structure suggests its typical fluorapatite composition (Table 4.3B). The data show that the iron detected in the larger area seems incorporated in the matrix of the fossil bone as secondary Fe-bearing phase and not infiltrated in the apatite lattice directly.

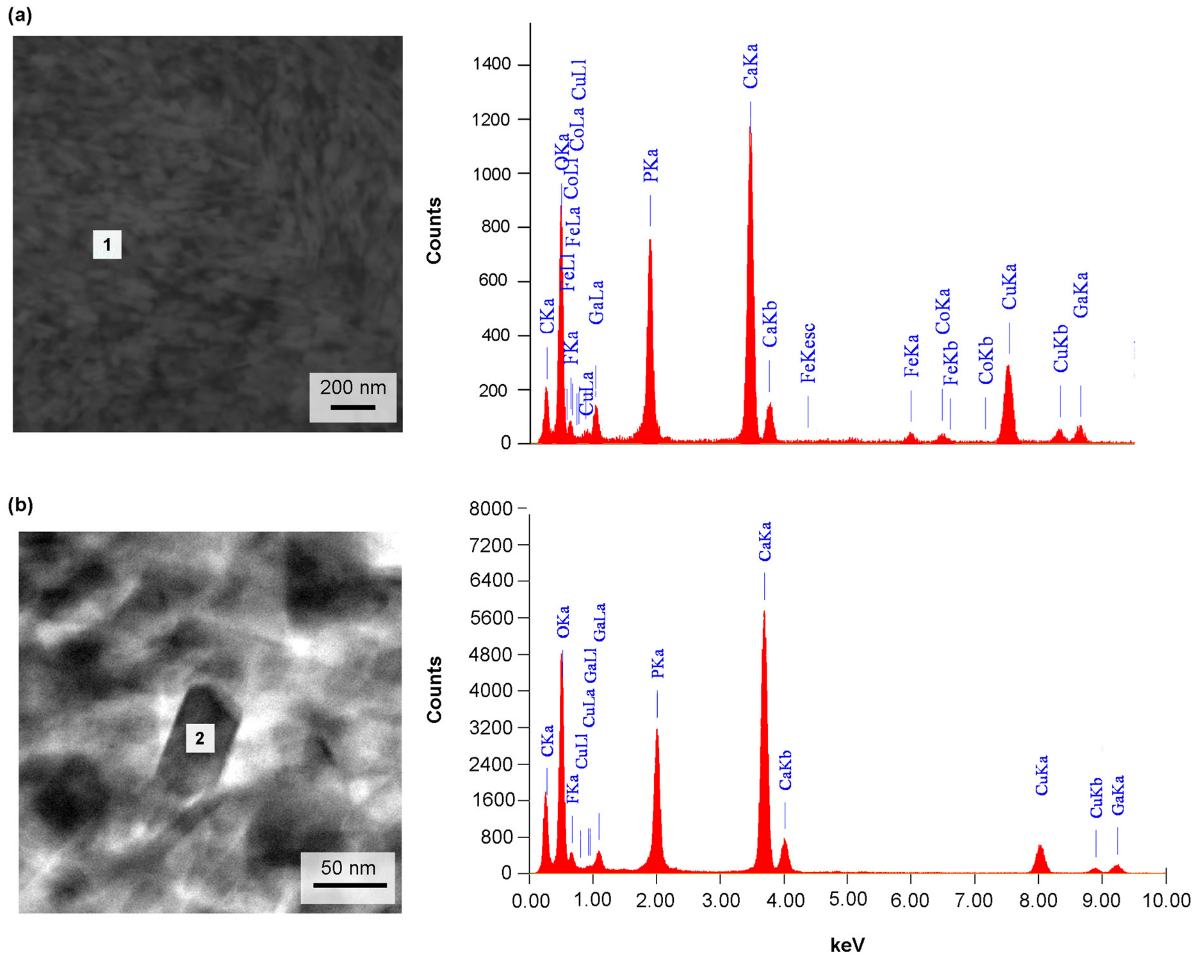

Figure 4.2: Chemical analysis of the regions of the fossil bone of OMNH 1278 consisting of apatite crystals. (a) HAADF STEM micrograph showing the whole area from which the EDX spectrum was obtained. (b) STEM BF highlighting an individual apatite crystal and corresponding EDX spectrum.

Table 4.3: Measured element concentrations (wt. %) in the two area marked in the Figure 4.2

	C	**O**	**F**	**P**	**Ca**	**Fe**	**Total**
A	13.3	25.6	2.5	19.4	36	1.5	100
B	19.87	23.0	2.5	15.2	39.5		100

OMNH 1279

The last sample OMNH 1279 is similar in composition to BYU 601-17320, as already observed in X-Ray diffraction. Its chemical composition is ~38% of Ca, ~20% of P, ~10% of C and 4% of F and some minor traces of Al and Si are also detected.

3.2 Secondary minerals chemistry

3.2.1 OMNH1278

SEM

The SEM-EDX element mapping applied on the sauropod bone OMNH 1278 is presented in Figure 4.3.

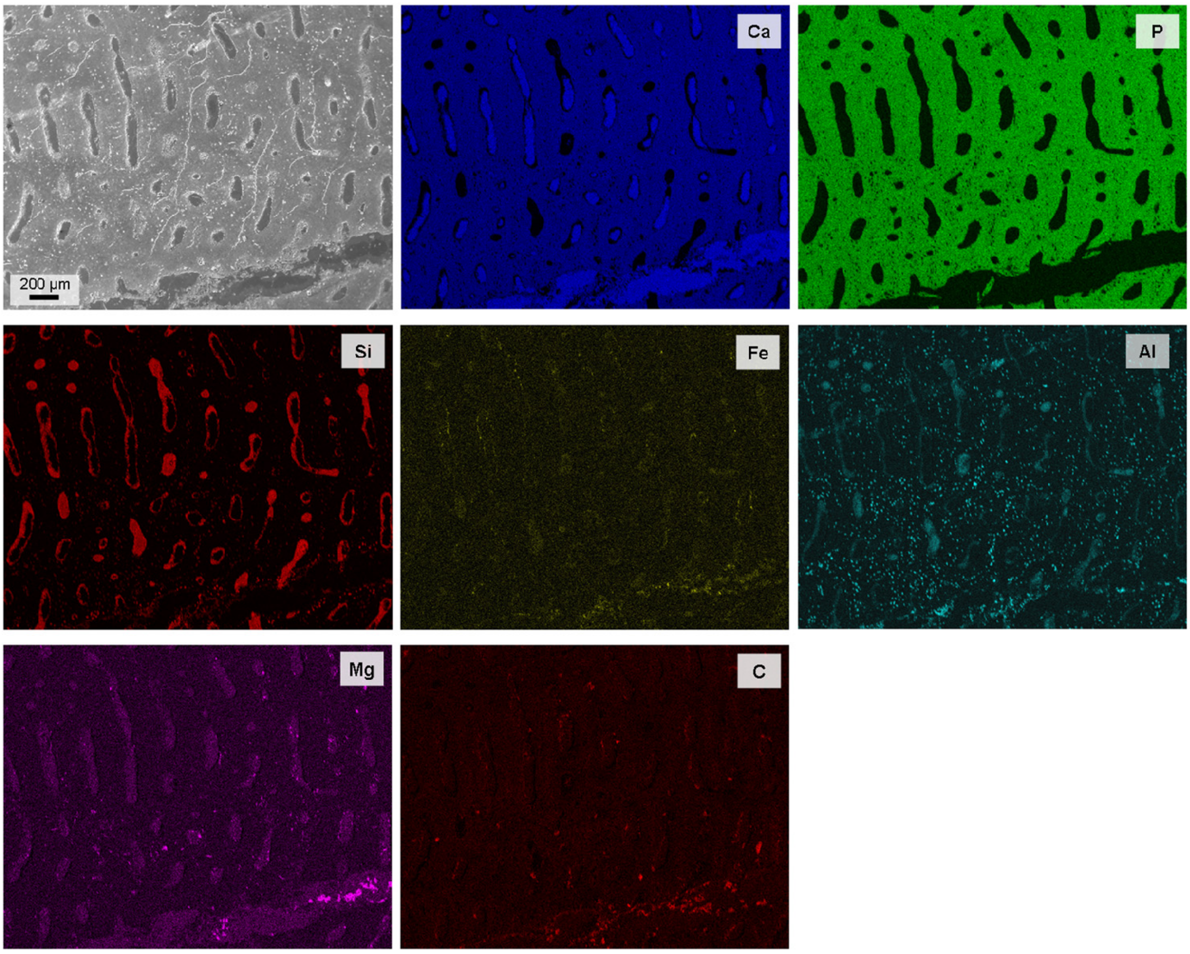

Figure 4.3: Elements map of the FBL bone of OMNH 1278. The SEM picture shows clearly the fibrolamellar (FBL) bone constituting the cortical bone with large lumina and one crack at the lower part of the picture. The bone tissue is easily recognized in the element distribution map of the phosphorous. Elements Ca: calcium, P: phosphorous, Si: silicon, Fe: iron, Al: aluminium, C: carbon, Mg: magnesium.

The bone is easily recognized by phosphorus and calcium maps. Some calcium is also crystallized in the vascular canal (lumina) of the cortex. Silicon is also detectable in the canals, confirming the presence of quartz like observed in the diffractogram in Figure 4.1. Presence of this element could also be an artefact introduced to the sample by polishing with a silicon containing solution. Iron (Fe), carbon (C), calcium (Ca) and magnesium (Mg) have a similar distribution with concentrations in the vascular canal and particularly in the crack in the lower part of Figure 4.4. The aluminium is also concentrated in the canals but mostly seems to be incorporated in the osteocyte lacunae.

TEM

Figure 4.4 shows an element map of the interface region between fossil bone and a vascular canal of the specimen. Apatite crystals are located at the bottom left part of the figure, while two different types of crystals (here visible with different gray-level contrast) fill the vascular canal.

It can be seen that the first phase (big hexagonal prism and right top part of the picture) is composed of silicon and oxygen, corresponding probably to a quartz crystal (SiO_2). Some aluminium is also noticed associated with silicon and oxygen. The “matrix” mineral in the vascular canal seems to consist of typical authigenic phase of calcium carbonate ($CaCO_3$). Some iron – rich inclusions are located at the border of the interface between the bone and the vascular canal. They appear in brighter contrast in the STEM picture in Figure 4.4 (arrows pointing down).

Note that all presented element maps suffer from not uniform thickness of the specimen resulting in a contrast gradient. The left part of presented maps (consisting of apatite crystals) reveal insufficient count of elements, while their right part is thick enough, providing information on the element distribution in different phases crystallized in the vascular canal.
Detailed concentrations (obtained via quantitative analysis) of vascular infillings are presented in figure 4.5 and Table 4.4 associated. Investigations of four different phases, already observed in figure 4.4, are described above. The first phase (marked A in Figure 4.5) is composed essentially of carbon (24%), oxygen (~28%) and calcium (~45%) and probably calcite ($CaCO_3$). Some minor traces of manganese and iron have also been registered. The hexagonal phase B shows also composition of calcite but present a slight absorption of aluminium, silicon and potassium. The phase D is composed of carbon, oxygen and silicon, reflecting probably the signal of a quartz (SiO_2) crystal. We noticed that phases A, B, C display a very unusual high carbon concentration. This could come from the mineral phase it is sitting (calcite) or a probable contamination from the deposition during FIB preparation.

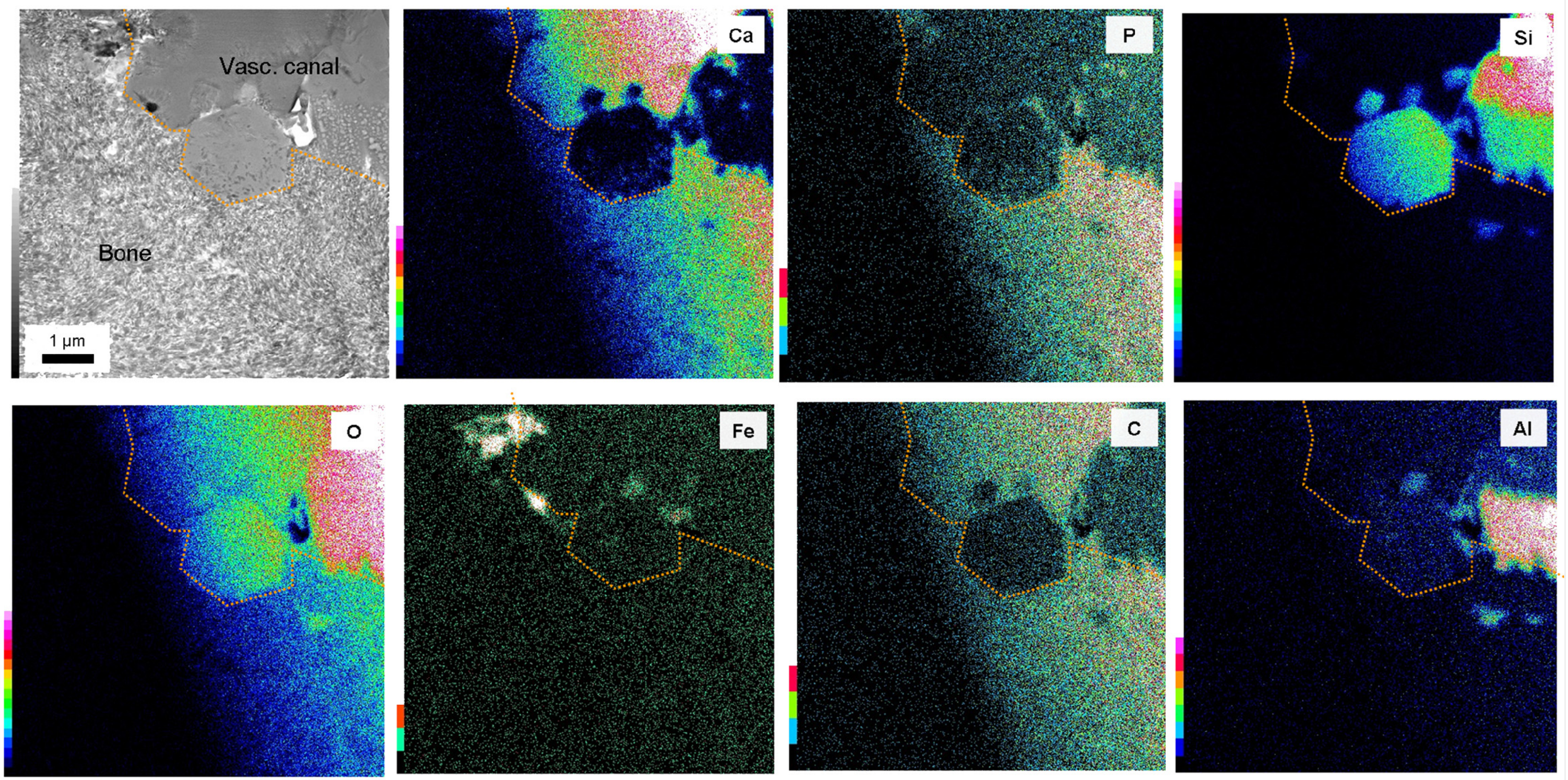

Figure 4.4: Element maps obtained by STEM-EDX of the specimen OMNH 01278 at the interface between the bone tissue and the vascular canal. The interface is marked by a yellow doted line.

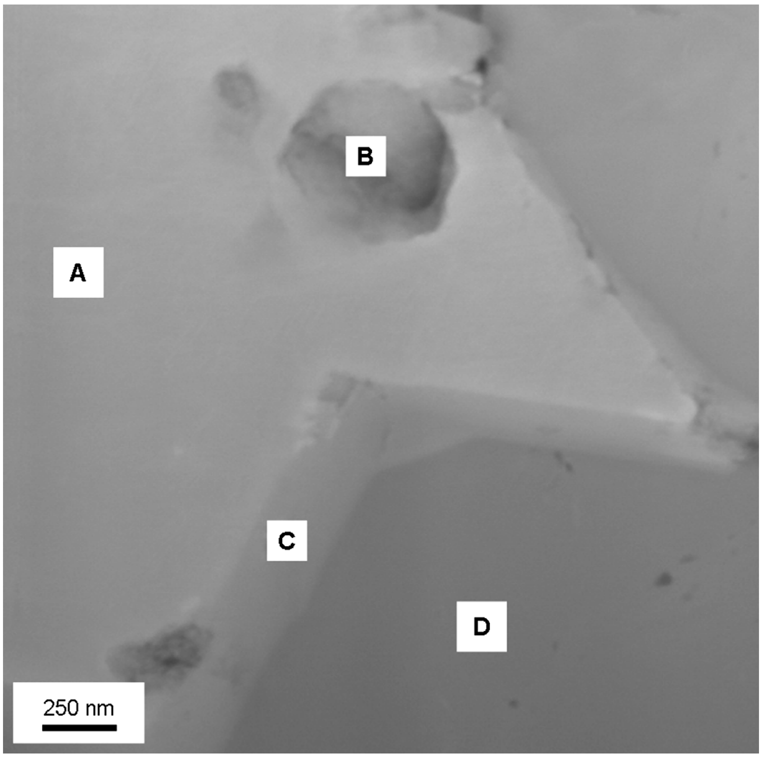

Figure 4.5: STEM DF micrograph of an area situated in the vascular canal of OMNH 01278. Different contrast corresponding to different minerals. Marked squares correspond to quantitative EDX presented in Table 3.

Table 4.4: Measured element concentrations (wt. %) measured at areas marked in the Figure 7.

	C	O	Mg	Al	Si	K	Ca	Fe	Total
A	24.0	27.9	1.2		0.1		45.1	1.3	100
B	19.1	31.4	1.5	6.1	13.5	2.7	21	3.9	100
C	19.4	29.2	0.9	0.1	20.1	0.1	28.7	1.3	100
D	4.9	47.1		0.3	46.5		0.1	0.8	100

Phase identification carried out via combination of EDX (Figure 4.5 and Table 4. 3 results) and selected area electron diffraction analysis (Figure 4.6a-c) reveal that these crystals are calcite III [83607-ICSD] (major fraction) and silicon oxide-quartz [162490-ICSD] respectively. Additionally, small iron – rich inclusions were observed adjacent to the hematite -phase [164814-ICSD] (see an arrow pointing down on Figure 4.6). They are hard to distinguish in the sample (see insert in Figure 4.6) and seem incorporated in the fossil bone matrix (see as well in the element maps in Figure 4.4), compared to the other two minerals which are distinctively formed in the vascular canals.

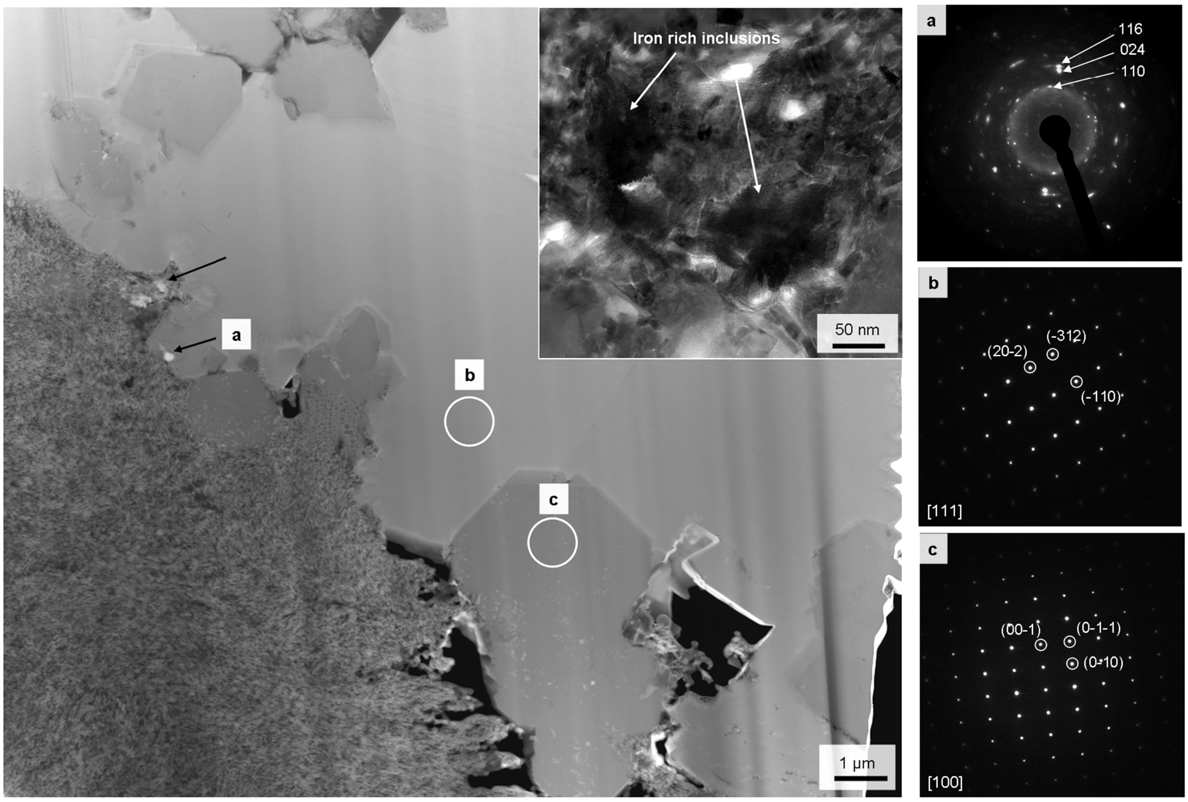

Figure 4.6: Microstructure of the interface region between a fossil bone and a vascular canal of the youngest *Apatosaurus sp.* (specimen OMNH 01278). STEM HAADF micrograph showing the interface between bone tissue and vascular canal and diffraction patterns associated. The a. and arrows pointing down highlight the small iron rich inclusions, seen in details in the insert TEM picture. The a. diffration index an hematite crystal. The diffraction pattern b. corresponds to the calcite matrix. c. corresponds to a quartz crystal. For more details referred to the text. Selected area diffraction patterns acquired using 0.2µm diameter aperture.

3.2.2 OMNH 1279

SEM

The SEM-EDX maps of cortical bone of OMNH1279 are presented in Figure 4.7.

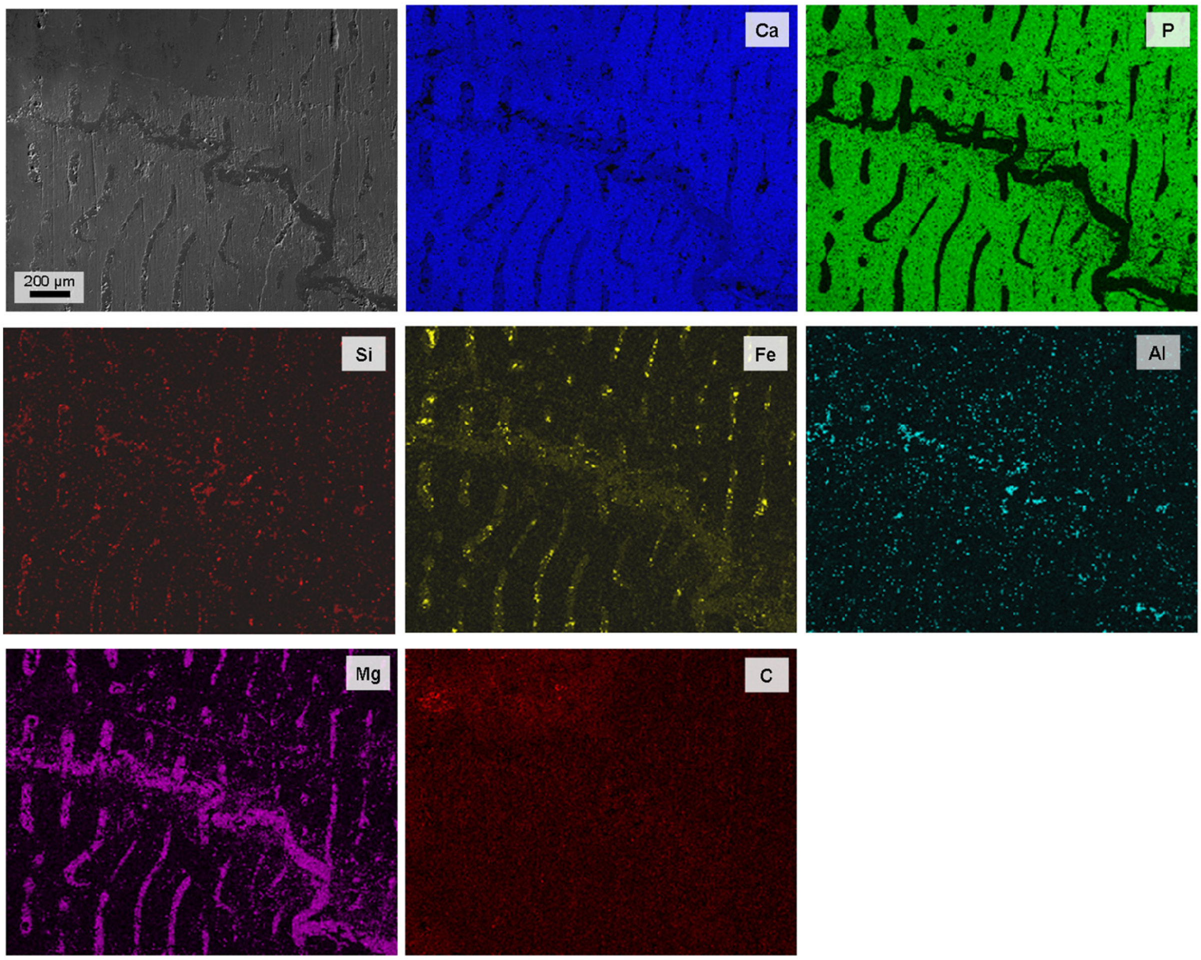

Figure 4.7: Elements map of FBL bone of OMNH 1279. The SEM picture shows clearly the fibrolamellar (FBL) bone constituting the cortical bone with smaller lumina and one crack at the middle part of the picture. The bone is easily recognized in the element map of the phosphorous. Elements Ca: calcium, P: phosphorous, Si: silicon, Fe: iron, Al: aluminium, C: carbon, Mg: magnesium.

A crack appears in the middle of the picture. As for the previous samples, the bone is easily identifiable by Ca and P concentration. The vascular canals contain minerals concentrated in Si, Fe and Mg. The map of C does not show any tendency or more concentrated areas. The map of aluminium indicates that this element is more concentrated in the osteocyte lacunae like in the previous sample OMNH 1278. The crack is filled in majority by Mg.

TEM

Analysis of the interface region between the vascular canal infilling and the fossil bone of sample OMNH 1279 reveal some important diagenetic features: Figure 4.8 shows that the vascular canals are filled with well-crystallized authigenic mineral phases. The crystal formed in the wall of the vascular canal has a fibrous texture (Fig. 4.8b and diffraction pattern associated). It is composed of aluminium silicate, as confirmed by the EDX chemical analysis (Table 4.5).

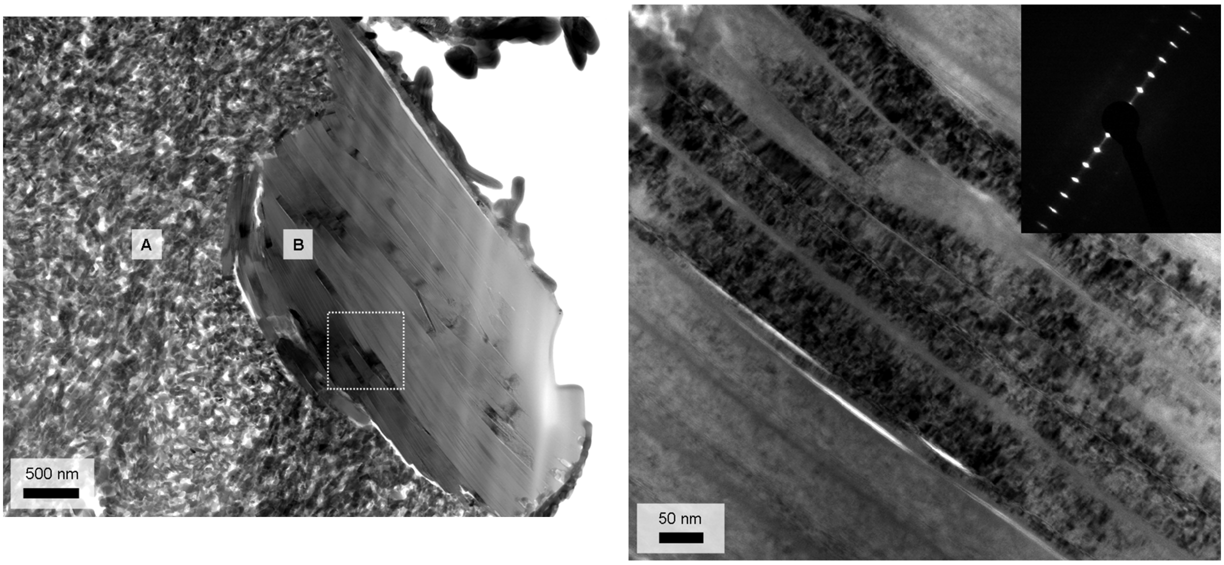

Figure 4.8: **a.** TEM BF micrograph of the sample OMNH 01279 showing the fossil apatite bone (area A) and the osteocyte lacunae (B) filled by mineral deposited by diagenesis. **b.** details of the B crystals the osteocytes (white square in **a.**) and the corresponding diffraction pattern.

Table 4.5: Measured element concentrations (wt. %) of the mineral present in the osteocyte lacunae of sample OMNH 1279 marked B in the Figure 8a.

	C	**O**	**F**	**Al**	**Si**	**P**	**Ca**	**Total**
B		56 ±2.4	1.3	21.2 ±1.0	21.5 ±1.3			100

Unambiguous identification of the crystal structure which filled the osceocyte was carried via a combination of EDX and electron diffraction. Two selected area diffraction patterns at different crystallographic orientation were collected in order to obtain sufficient data (Figure 4.9a, b). Measured interplanar distances, with regard to the EDX composition analysis obtained, both confirmed the recognition of kaolinite crystal ($Al_2Si_2O_5(OH)_4$) (PDF 00-001-0527) with [112] and [310] zone axis respectively.

The kaolinite was the only crystal identified in the sample OMNH 1279.

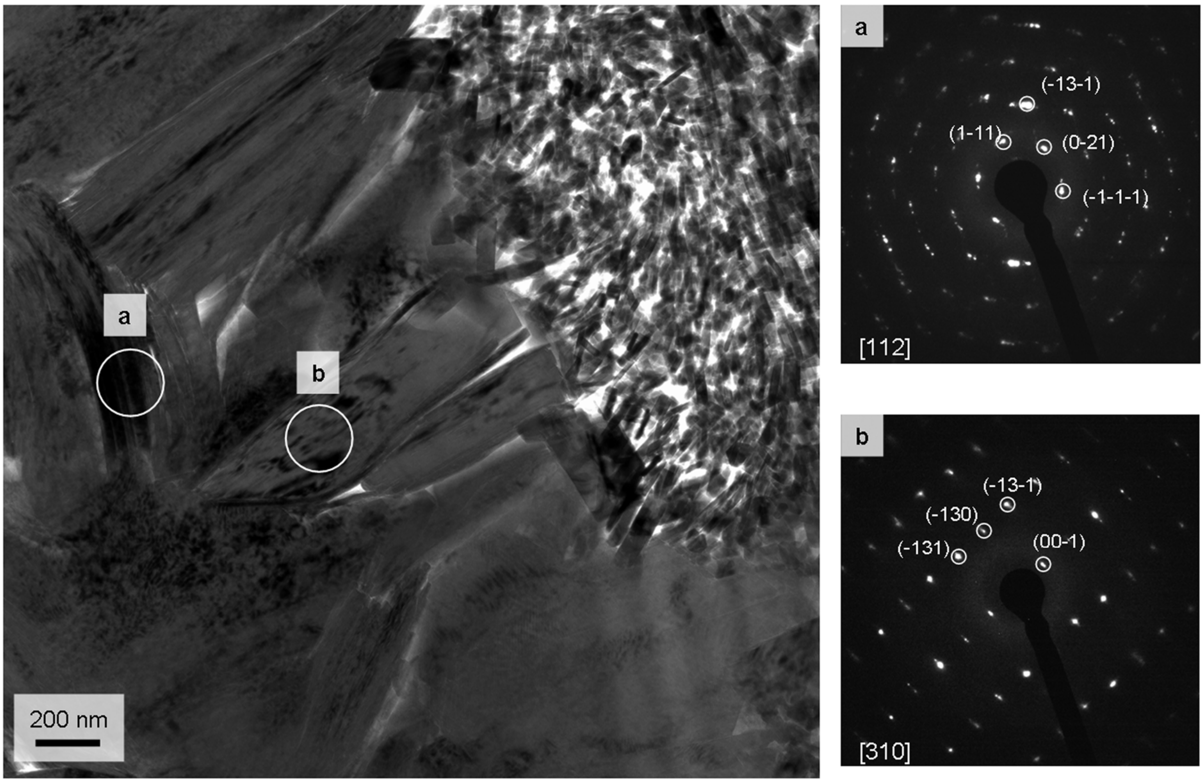

Figure 4.9: TEM BF micrograph obtained in the sample OMNH 1279 showing the interface between a vascular canal and the fossil bone. a and b: diffraction patterns collected from the crystals present in the vascular canal. Both correspond to Kaolinite (PDF 00-001-0527) with [112] (square a) and [310] (square b) zone axis respectively.

3.2.3 BYU 601-17328

SEM

The SEM-EDX was quantified in the secondary osteonal bone for the sample BYU 601-17328, because the canals from the FBL cortical bone were completely filled by lamellar bone and no secondary minerals infillings could have been observed. The secondary osteons are easily recognized by their cement line, appearing in the SEM picture, as bright high reflectance areas. In this sample, radial cracks perpendicular to these cement lines can be noticed in the maps of Ca and P. The vascular canals are filled by minerals rich in carbon. Iron oxides seems to be the most important vascular infilling, it is present in the wall of the vascular canals, in the cracks and in the osteocytes lacunae (like already observed in Dumont et al, 2011). On the other hand, Mg and Al do not show any tendency or particular concentration areas in their respective maps.

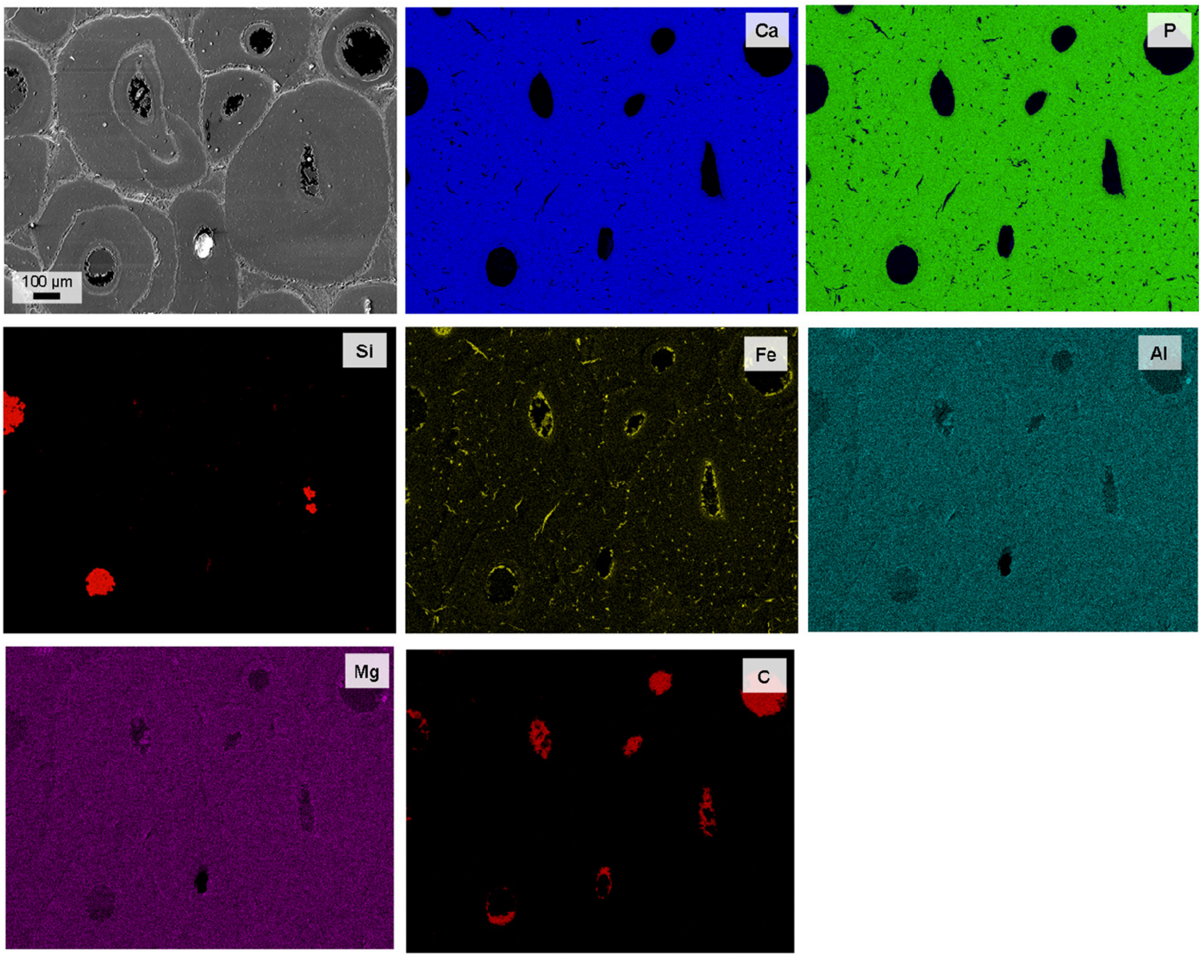

Figure 4.10: Element maps of secondary osteonal bone of BYU 601-17328. The SEM picture shows clearly osteons secondary bone. The bone is easily recognized in the element map of the phosphorous. Elements Ca: calcium, P: phosphorous, Si: silicon, Fe: iron, Al: aluminium, C: carbon, Mg: magnesium.

TEM

Same results were obtained for analysis of the sample in TEM. In Figure 4.11, the sample BYU 601-17328 displays the two areas of interest. The first one defined as the bone is composed of bone apatite crystals and is marked by the letter A. The second dark-grayish area represents osteocytes lacunae (marked B in Figure 4.11) (size from 1 to 5µm). The two different structures can be clearly identified by their contrast and their morphology. The apatite crystals seem to be randomly oriented within entire the observed region. The lacunae appear with much higher contrast as they contain elements of higher atomic Z number (see table 4.6). The insert in Figure 4.11 represents a zoom of the interface between the fossil bone and an osteocyte lacunae. The bone apatite crystals are well visible having a length in the range of 20 to 100 nm. No change in size or morphology of crystals is noticed at this interface between the two structures.

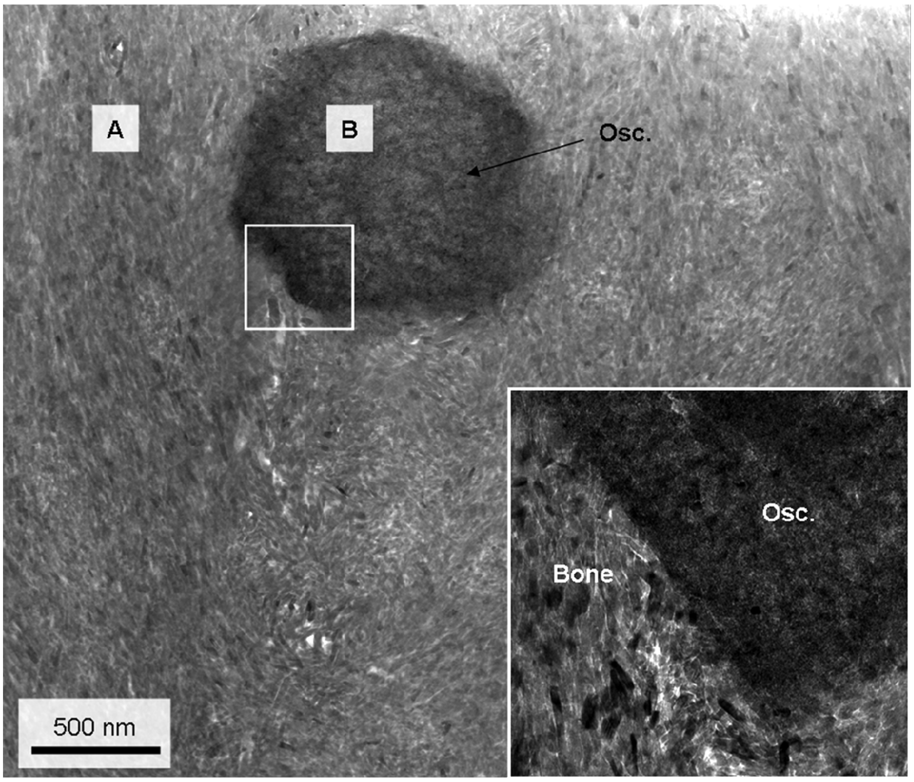

Figure 4.11: STEM BF micrograph of an area of the sample BYU 601-17328 showing the bone (A) formed by apatite crystals and an osteocyte lacunae (B). The zoom insert shows the interface between the fossil bone (presence of apatite crystals) and the osteocyte lacunae (Osc.) filled by diagenetic mineral elements.

The osteocyte lacunae composition (Table 4.6) presents also a trace of fluor (~ 2.5%). But they mainly composed of various diagenetic elements: a high concentration of iron (~ 53%) and also traces (mostly < 2%) of magnesium, aluminium, silicium and sulfur. No trace of manganese was associated with iron occurrence.

Table 4.6: Measured element concentrations (wt. %) in the osteocyte lacunae of sauropod BYU 601-17328 marked in the Figure 6.11

	C	O	F	Mg	Al	Si	P	S	Ca	Fe	Total
B	2.0 ±0.2	33.6 ±0.7	2.5 ±0.2	0.6 ±0.1	0.3 ±0.1	1.3 ±0.1	2.3 ±0.5	0.3	4.4 ±0.8	52.7 ±0.5	100

The chemical analysis presented above is illustrated as well by the elements mapping shown in Figure 4.12. The lacunae display a high concentration of oxygen, iron and fluor. It is clear that the iron atoms do not reside into primary bone apatite crystals.

In Figure 4.12, element mapping confirms that osteocyte lacunae (Oc in the figure) concentrate oxygen, iron and fluor. The fluor seems to be higher in the iron oxide than in the bone matrix. Moreover, the osteocyte reveals an enrichment pattern (minor rings) of calcium and phosphor. It is clear that the iron atoms do not contribute into primary bone apatite crystals.

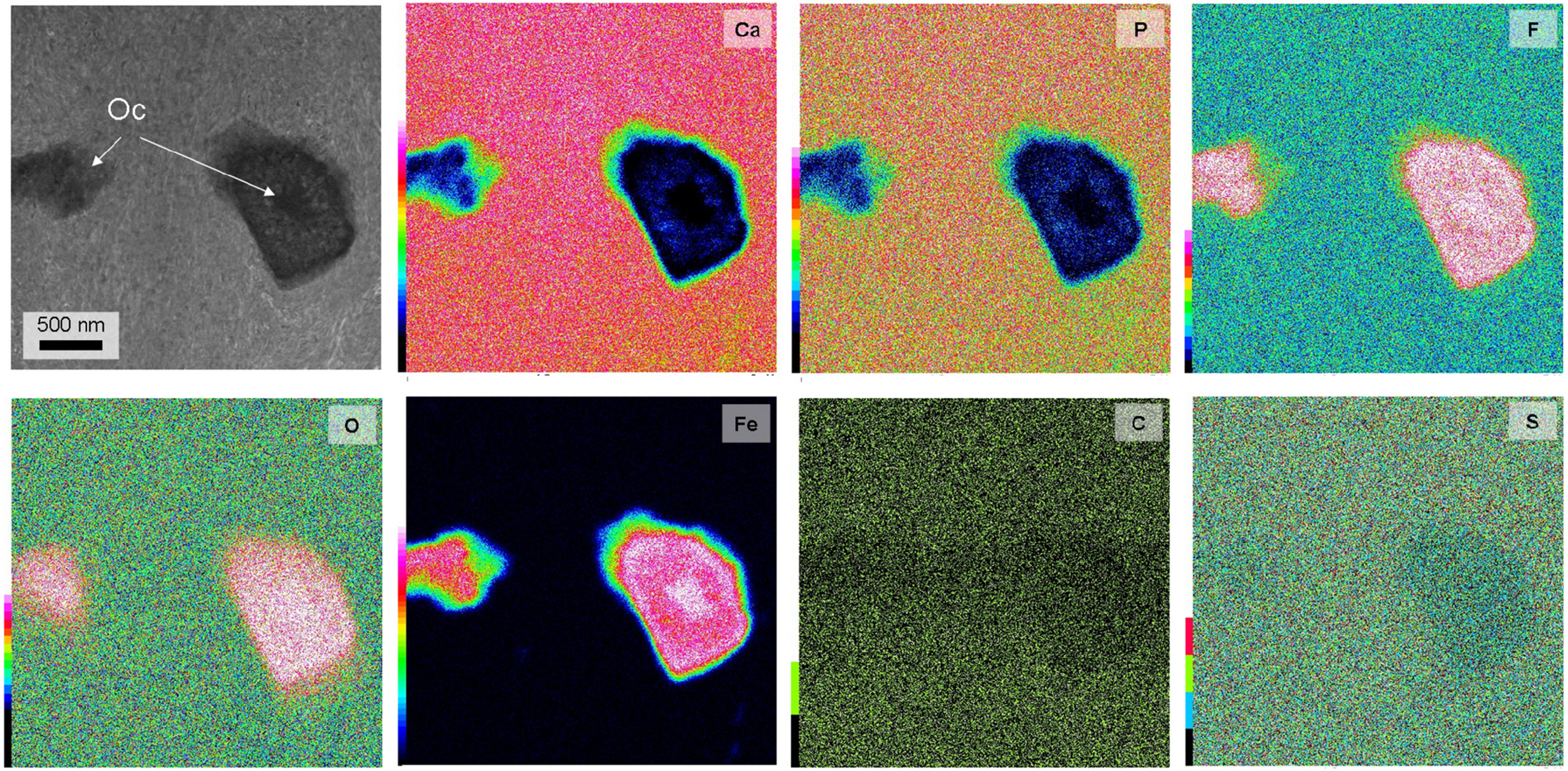

Figure 4.12: Elements maps obtained by EDX on the TEM sample of the sauropod Apatosaurus BYU 601-17328. Oc: osteocyte lacunae surrounded by bone tissue. Brighter color means an higher concentration of the element.

4 Discussion

4.1 Comparison of the technique

Three techniques were complementary used in this study: X-ray diffraction, SEM-EDX and TEM-EDX. X-ray diffraction is a quantitative method for identifying the elements in the fossil bone and the general composition of apatite crystals. The SEM-EDX and TEM-EDX are more qualitative and quantitative methods. When the SEM is coupled with EDX analysis, it is able to observe mineral infillings at the microstructure level, the other technique permits to increase the image resolution distinguishing details at the level of the bone crystals. But both last techniques are limited by the detector resolution: concentrations of light elements ($Z<10$) are usually uncertain. The X-ray diffraction method has its limit: for example during data acquisition it is difficult to only determinate if data point include only fossil bone or fossil bone plus osteocyte lacuane (which are generally filled with second mineral). Analysis on bulk samples are preferred but can not exclude second minerals contamination.

X-ray diffraction results have shown that the three sauropod bones have higher degree of crystallinity compared to the horse and bison subfossil bones (Figure 4.1). This higher crystallinity even known to be higher in fossil bones (Tuross et al. 1989, Nielsen-Marsh 2000a, Roberts et al. 2002, Berna et al. 2004), has failed to be correlated with diagenetetic status or progressively loss of organic material (Hedges et al. 1995, Trueman et al. 2008). Analyses of the X-ray diffractograms have shown that additional peaks of the corresponding fluorapatite appear in sauropod samples. While the sample BYU 601-17328 has quite similar profile compare to the subfossil bone, extra peaks were registered for sample OMNH 1278 and OMNH 1279. They correspond to calcite and quartz mineral. Same results were obtained in SEM-EDX, where these mineral infillings were observed in the element maps (Figure 4.3 and figure 4.7). On the other hand the X-ray diffractogram did not detect iron mineral in the sample BYU 601-17328, when their inclusions were both observed in SEM and TEM (figure 4.11 and figure 4.12). In the same way, it was revealed for the sample OMNH 1278 that secondary minerals infilling was more important and diversified than results obtained in X-ray diffraction and SEM analysis.

On the other hand, bone chemistry analyzes by SEM and TEM techniques have displayed similar results. It was noticed that the sample BYU 601-17328 in SEM has a higher concentration of calcium around 40%, as well as a higher phosphorous concentration (~ 18%) (Table 4.1). EDX-TEM has confirmed the same tendency (Table 4.2).

The different concerned the concentration of fluor, where in TEM it has been registered to be ±1% higher, but this slight increase can reflect error measurement range of the detector. Minor elements are also present in roughly the same range for both methods. For example, sulfur was registered in the sample BYU 601-17328 with a concentration of 1.82% (±0.2), a minor concentration <1% was detected in TEM method. The sample OMNH 1279 displays no iron in TEM, when ~2.5% (±0.8) was registered in SEM. It is difficult to predict if i) these minor concetrations reflect trace elements present in the apatite crystallite composition itself, ii) EDX detector error or elements include in the matrix of the bone (as observed in figure 4.2 for the sample OMNH1278), iii) if the TEM sections did not contain the iron oxide because of the small area size investigated with this method.

4.2 Discussion about diagenesis

The fossil bone apatite of the three samples attests different chemical composition. However they all present some fluor traces: around 2-3% (Table 4.1 and 4.2), indicating modification of the original apatite in francolite (Hubert et al. 1996). The sample BYU 601-17328 presents the highest concentration of calcium of all the samples. The two other samples share the same calcium concentration as the subfossil bison (~35%). Generally all the samples present same chemistry compare to other references (around 35-45 wt% for calcium and 20-30 wt% of phosphorous). The sauropod samples contain some other minor elements like iron, sulfur, aluminium, magnesium and sodium but their concentrations are lower than 1%. The bison subfossil present a really low concentration of iron. Very little iron is incorporated in the bone yet and is mostly considered to be diagenetically of origin (Ezzo 1994).

Secondary minerals clays have been visualized and identified in all the three samples. They crystallized in pore spaces, i.e. vascular canals and osteocyte lacunae (Parker and Toots 1970, Hubert et al. 1996; Pfretzschner 2000a, 2001, Farlow & Argast 2006; Turner-Walker & Jans 2008). The study demonstrates the high variability of diagenesis effect between different site localities, between bone samples from the same locality site and also between different parts of a fossil bone.

The sample BYU 601-17328 (Figure 4.2 and Table 4.1B) and sample OMNH 01278 (figure 4.5) show iron oxides (probably hematite or goethite mineral phase) as pore filling. No pyrite (FeS_2) or any other mineral containing sulfur was detected. Iron oxide have several possible origins: i) primary origin of iron in the bone tissue ii) diagenetic penetration of iron rich water into collagen material (Pfretzchner 2000a, 2000b) iii) late diagenetic oxidization., like already observed previously (in Parker 1966, Parker and Toots 1970, Wings 2004) the iron oxides being weathering products of pyrite (Barker et al. 1997). Some traces of sulfur have already been observed in the trabecular bone of BYU 601-17328 (Dumont et al. 2011), as well in small quantity in this study (Table 4.2 and 4.3). These specific authigenic phases are known to form in aquatic or freshwater alluvial environment. Presence of radial microcracks (sample BYU 601-17328 in Figure 4.10) could confirm aquatic conditions.These cracks mostly appear by water uptake and swelling the bone collagen (Preftzschner 2000a, 2006, Preftzschner and Tütken 2011). But on the other hand, TEM results (not shown in this study) prepared near secondary osteons have lacked these diagenetic infillings, implying heterogeneous preservation in some parts of the bone. It could be postulated as an early stage of diagenesis (Pfretzschner 2004, Tuba et al. 2006) with iron rich water penetration. In the case of the sample OMNH 01278, the hematite inclusions present are mainly a consequence of a later diagenesis.

Even tough of similar provenance, the sample OMNH 01278 and OMNH 01279 have different preservation and different second mineral infillings. The femur OMNH 1279 has displayed crystallization of kaolinite (Figure 4.8 and Figure 4.9) as a clay matrix (Elorza et al. 1999, Piga et al. 2009). Kaolinite usually reflects proximity to the sediment source and deposition in relatively nearshore settings (Ruffel et al. 2002). It is also interpreted as formed during early diagenesis under acidic conditions and related to meteoric waters. Elorza concluded also that kaolinite suggest a climate with seasonal variations of pluviosity (Elorza et al. 1999).

The sample OMNH 01278 (Figure 4.4 and Figure 4.7) on the other hand displays a more diverse secondary mineral crystallization, reflecting more complex diagenetic histories and fluctuations in the Eh-pH regimes (Barker et al. 1997). Some silicon, aluminium, carbonate, calcium, iron oxides identify as quartz, calcium, hematite and probably alumina silicate. These heterogeneities in this bone can be interpreted as a later diagenesis state, as suggested by formation of calcite pyrite or barite. The sample proves that the vascular canal is mostly filled by calcite. No sulfate has been identified. Quartz has also been recognized as well as hematite (Figure 4.6). But the sample displayed also some different and complicated chemical composition (Figure 4.5 and Table 4.4). Even if in general, mixture of these minerals lack unambiguous environmental controls (Wings 2004), it seems that precipitation of both calcite and hematite, as appearing in our sample is only possible under oxidizing conditions (Krumbein and Garrels 1952, Holz and Schultz 1998). The presence of authigenic quartz in bones indicates soluble silica as a component in the groundwater (Wings 2004). But differences with the sample OMNH 01279 suggest different depositional settings.

5 Conclusions

This study has lead to different conclusions:

- TEM coupled with EDX analysis are really good quantitative and qualitative analysis. The advantage of this technique is the direct observation of fossil bone alteration "in-situ", compared to bulk X-Ray diffraction results. It permits also to obtain chemical analysis at the sub-nano and nanolevel of the bone. Associated with diffraction pattern studies, second clay minerals could be identified.
- The three methods are quite well complementary but lack real precise measurement of light elements. Complementary PIXE measurements and synchrotron X-Ray fluorescence could be able to detect these one as well as the trace element, present in the fossil bone.
- The diagenesis of the three samples is quite heterogeneous and reflects different stage of alteration. Between same geological beds (so same burying environmental conditions), it was observed different second mineral crystallization in bone´s pores, reflecting the ambiguity and the complexity of the diagenesis phenomenon.

References

Barker M.J., Clarke, J.B. Martill D.M. 1997. Mesozoic reptiles as diagenetic windows. Bulletin de société géologique de France 168 (5): 535-545.

Berna, F., Matthews, A., Weiner, S. 2004. Solubilities of bone mineral from archaeological sites: the recrystallisation window. Journal of Archeological Science 31: 867–882.

Bocherens, H., Brinkman, D.B., Dauphin, Y., Mariotti, A. 1994. Microstructural and geochemical investigations on Late Createceous archosaur teeth from Alberta (Canada). Canadian journal of earth science 31: 783-792.

Chipera, S. J., Bish, D. L. 1991. Applications of X-ray diffraction crystallite size/stain analysis to *Seismosaurus* dinosaur bone. In *Advances in X-ray analysis* (eds Barrett, C. S., Gilfrich, J. V., Noyan, I. C., Huang, T. C. & Predecki, P. K.) 34: 473–482.

Coutinho, E., Jarmar, T., Svahn, F., Neves, A.A., Verlinden, B., Van Meerbeek, B., Engqvist, H. 2009. Ultrastructural characterization of tooth-biomaterial interfaces prepared with broad and focused ion beams. Dental materials 25: 1325-1337.

Dumont, M., Zoeger, N., Streli, C., Wobrauschek, P., Falkenberg, G., Sander, P.M., Pyzalla, A.R. 2009. Synchrotron XRF analyses of element distribution in fossilized sauropod dinosaur bones. Powder diffraction 24(2): 130-134.

Dumont, M., Borbely, A., Kostka, A., Sander, P.M., Kaysser-Pyzalla, A.R. 2011. Characterization of sauropod bone structure. In Biology of Sauropod dinosaurs: Understanding the life of giants. Ed. N. Klein, K. Remes, C.T. Gee and P.M. Sander. Indiana University Press, Bloomington.

Elorza, J., Astibia, H., Murelaga, X., Pereda-Superbiola, X. 1999. Francolite as a diagenetic mineral in dinosaur and other Upper Cretaceous reptile bones (Lano, Iberian Peninsula): microstructural, petrological and geochemical features. Cretaceous Research 20: 169–187.

Eppell, S. J., Tong, W., Katz J. L., Kuhn, L., Glimcher, M. J.,2001. Shape and size of isolated bone mineralites measured using atomic force microscopy. Journal of Orthopaedic Research 19, 1027-1034.

Ezzo, J.A. 1994 Putting the "chemistry" back into bone chemistry analysis: Modeling potential dietary indicators. Journal of Anthropological Archaeology 13: l-34.

Farlow, J.O., Argast, S. 2006. Preservation of fossil bone from the pipe creek sinkhole (late Negogene, Grant County, Indiana, USA). Journal of the Paleontological Society of Korea 22(1): 51-75.

Foster, J. 2007. Jurassic West: The Dinosaurs of the Morrison Formation and Their World. Indiana University Press. 389pp.

Goodwin, M.B., Grant, P.G., Bench, G., Holroyd, P. A. 2007. Elemental composition and diagenetic alteration of dinosaur bone: distinguishing micron-scale spatial and compositional heterogeneity using PIXE. Palaeogeography, Palaeoclimatology, Palaeoecology 253: 458-476.

Hayashi, Y., Yaguchi, T., Ito, K., Kamino, T. 1998. High-resolution electron microscopy of human enamel sections prepared with focused ion beam system. Scanning 20: 234-235.

Hedges, R.E.M., Millard, A.R., Pike, A.W.G. 1995. Measurements and relationships of diagenetic alteration of bone from three archaeological sites, Journal of Archaeological Science 22: 201–209.

Hedges, R.E.M. 2002. Bone diagenesis: an overview of processes. Archaeometry 44 (3): 319-328.

Holz, M., Schultz, C.L. 1998. Taphonomy of the South Brazilian Triassic herpetofauna: fossilization mode and implicartions for morphological studies. Lethaia 31: 335-345.

Hubert, J. F., Panish, P. T., Chure, D. J., Prostak, K. S. 1996. Chemistry, microstructure, petrology, and diagenetic model of Jurassic dinosaur bones, Dinosaur National Monument, Utah. Journal of Sedimentary Research 66(3): 531-547.

Jantou, V., Turmaine, M., West, G.D., Horton, M.A., McComb, D.W. 2009. Focused ion beam milling and ultramicrotomy of mineralized ivory dentine for analytical electron microscopy. Micron 40: 495-501.

Klein, N., Sander, P.M. 2008. Ontogenetic stages in the long bone histology of sauropod dinosaurs. Paleobiology 34(2), 247-263.

Kohn, M.J., Schoeninger, M.J., Barker, W.B. 1999. Altered states: effects of diagenesis on fossil tooth chemistry, Geochimica Cosmochimica Acta 63: 2737–2747.

Kolodny, Y., Luz, B., Sander, M., and Clemens, W.A. 1996, Dinosaur bones: Fossils or pseudomorphs? The pitfalls of physiology reconstruction from apatitic fossils. Paleogeography, Paleoclimatology, Paleoecology 126: 161–171.

Krumbein, W. C., Garrels, R. M. 1952. Origin and classification of chemical sediments in terms of pH and oxidation reduction potentials. Journal of Geology 60: 1-33.

Kuisma-Kursula, P. 2000. Accuracy, precision and detection limits of SEM–WDS, SEM–EDS and PIXE in the multi-elemental analysis of medieval glass. X-Ray spectrometry 29: 111-118.

Lambert, J.B., Vlasak, S.M., Thometz A.C., Buikstra, J.E. 1982. A comparative study of the chemical analysis of ribs and femurs in Woodland populations. American Journal of Physical Anthropology 59: 289–294.

Lee-Thorp, J. A., van der Merwe, N. J. 1991. Aspects of the chemistry of modern and fossil biological apatites. Journal of Archaeological Science 18: 343–354.

Munroe, P. Principles and applications of Focused Ion Beam milling. Electron Microscope Unit, University of New south Wales, Sydney, NSW 2052.

Nalla, R.K., Portera, A.E., Daraio, C., Minor, A.M., Radmilovic, V., Stach, E.A., Tomsia, A.P., Ritchie, R.O. 2005. Ultrastructural examination of dentin using focused ion-beam cross-sectioning and transmission electron microscopy. Micron 36: 672–680.

Nielsen-Marsh, C. M., Hedges, R. E. M. 2000a. Patterns of diagenesis in bone I: the effects of site environments. Journal of Archaeological Science 27**,** 1139–1150

Nielsen-Marsh, C. M., Hedges, R. E. M. 2000b. Patterns of Diagenesis in Bone II: Effects of Acetic Acid Treatment and the Removal of Diagenetic CO_3^{2-}. Journal of Archaeological Science 27: 1151–1159.

Parker, R.B. 1966. Electron microprobe analysis of fossil bones and teeth. Geological Society of Amerisa Special papers 101:415-416.

Parker, R. B., Toots, H. 1970. Minor elements in fossil bones. Bulletin of the Geological Society of America 81: 925-932.

Pfretzschner, H.U. 1998. Frühdiagenetische Prozesse bei der Fossilisation von Knochen, N. Jahrb. Geol. Paläont. Abh. 210 (3):369–397.

Pfretzschner, H.U. 2000a. Pyrite formation in Pleistocene long bones – a case of very early mineral formation during diagenesis. Neues Jahrbuch für Geologie und Paläontologie - Abhandlungen 217(1): 143–160.

Pfretzschner, H.U. 2000b. Microcracks and fossilization of Haversian bone. Neues Jahrbuch für Geologie und Paläontologie - Abhandlungen 216: 413–432.

Pfretzschner, H.U. 2001. Pyrite in fossil bone. Neues Jahrbuch für Geologie und Paläontologie - Abhandlungen Abh. 220(19): 1–23.

Pfretzschner, H.U. 2004. Fossilization of Haversian bone in aquatic environments. Comptes Rendus Palevol 3: 605–616

Pfretzschner, H.U. 2006. Collagen gelatinization: the key to understand early bone-diagenesis. Palaeontographica A 278:135–148.

Pfretzschner, H.-U., Tütken, T. 2011. Rolling bones – Taphonomy of Jurassic dinosaur bones inferred from diagenetic microcracks and mineral infillings. Palaeogeography, palaeoclimatology, palaeoecology 310: 117-123.

Piga, G., Santos-Cubedo, A., Moya Sola, S., Brunetti, A., Malgosa, A., Enzo, S. 2009. An X-ray Diffraction (XRD) and X-ray Fluorescence (XRF) investigation in human and animal fossil bones from Holocene to Middle Triassic. Journal of Archaeological Science 36(9): 1857-1868.

Reiche, I., Vignaud, C., Menu, M. 2002. The crystallinity of ancient bone and dentine: new insights by transmission electron microscopy. Archaeometry 44(3): 447-459.

Reiche, I., Favre-Quattropani, L., Vignaud, C., Bocherens, H., Charlet, L., Menu, M.A. 2003. A multi-analytical study of bone diagenesis: the Neolithic site of Bercy (Paris, France). Measured Sciences Technology 14: 1608-1619.

Roberts, S.J., Smith, C.I., Millard, A., Collins, M.J. 2002. The taphonomy of cooked bone: Characterizing boiling and its physico-chemical effects, Archaeometry 44: 485–494.

Ruffel, A., McKinley, J.M., Worden, R.H.L. 2002. Composition of clay mineral stratigraphs to other proxy paleoclimate indicators in the Mesozoic of NW Europe. Philosophycal Transactions of the Royal Society A 360: 675-693.

Sander, P.M., Andrassy, P. 2006. Lines of arrested growth and long bone histology in Pleistocene large mammals from Germany: what do they tell us about dinosaur physiology? Palaeontographica A 277: 143–159.

Schultz, G. E. 1972. Vertebrate Paleontology of the Southern High Plains: New Mexico. Geological Society, Annual Field Conference Guidebook 23: 129-133.

Stein, K., Sander, P.M. 2009. Histological core drilling: a less destructive method for studying bone histology, pp69-80 in Brown, M.A., Kane, J.F., Parker, W.G. (eds.), Methods in fossil preparation: Prooceedings of the first Annual Fossil Preparation and Collections Symposium.

Tuba Gy, Kiss, P., Pósfai, M., Mindszenty, A. 2006. Preliminary data on the diagenesis of cretaceous dinosaur bones from the bakony mts, hungary. Acta Mineralogica-Petrographica, Abstract Series 5, Szeged.

Trueman, C.N. 1999. Rare Earth Element Geochemistry and Taphonomy of Terrestrial Vertebrate Assemblages. Palaios 14: 555–568.

Trueman, C.N., Privat, K., Field, J. 2008. Why do crystallinity values fail to predict the extent of diagenetic alteration of bone mineral? Palaeogeography, Palaeoclimatology, Palaeoecology 266: 160-167.

Turner-Walker, G., Jans, M. 2008. Reconstructing taphonomic histories using histological analysis. Palaeogeography, Palaeoclimatology, Palaeoecology 266: 227–235.

Tuross, N., Behrensmeyer, A.K., Eanes, E.D., Fisher, L.W. 1989. Molecular preservation and crystallographic alterations in a weathering sequence of wildebeest bones. Applied Geochemistry 4: 261–270.

Volkert, C.A., Busch, S., Heiland, B., Dehm, G. 2004. Transmission electron microscopy of fluorapatite-gelatine composite particles prepared using focused ion beam milling. Journal of Microscopy-Oxford 214: 208–212.

Wings, O. 2004 Authigenic minerals in fossil bones from the Mesozoic of England: poor correlation with depositional environments. Palaeogeography, Palaeoclimatology, Palaeoecology 204: 15-32.

Ziv, V., Weiner, S. 1994. Bone crystal sizes: a comparison of transmission electron microscopic and X-ray diffraction line with broadening techniques. Connective Tissue Research 30: 165-175.

Zocco, G.Z., Schwartz, H.L. 1994. Microstructural analysis of bone of the sauropod dinosaur *Seismosaurus* by transmission electron miscroscopy. Palaeontology 37(3): 493-503.

Chapter 5 Texture of sauropod bones

1 Introduction

Sauropod dinosaurs were the heaviest animals that ever inhabited the land. Understanding how their weight influenced the mechanical properties of their bones is a particularly interesting, and ongoing research subject (Sander et al. 2010). At the microstructural level, sauropod bone consists predominantly of fibrolamellar (FLB) bone tissue (Sander 2000, Klein and Sander 2008), that is, a core of woven fibrous bone with centripetally deposited lamellar osteonic bone (Enlow & Brown 1956, 1957; de Ricqlès 1980, Francillon-Vieillot et al. 1990, Klein & Sander 2008). As the animal grows, the bone is progressively remodeled by resorption and redeposition of secondary material, such as secondary osteons, which can be easily observed in sauropod bones. According to Wolff´s law, an increase in mechanical anisotropy might be expected for giant animals, where the high loads occurring in specific directions will be mirrored in the arrangement of the collagen architecture. Therefore, during ontogeny these animals most likely made structural adaptations to cope with the massive weight placed on the bones, as exemplified by the reorientation of collagen fiber with remodeled bone. This remodeling was observed to appear much later in the ontogeny of sauropods than in mammals (de Ricqlès 1980, Rimblot-Baly at al. 1995, Klein and Sander 2008).

Bone is generally considered a composite material consisting primarily of hydroxyapatite (HA) nano-crystallites embedded in a fibrous collagen matrix. Its mechanical performance depends on the amount and geometrical organization of the components, including the phase volume fractions, the shape of HA particles, and their spatial distribution and orientation. HA has a hexagonal crystallite structure with anisotropic elastic properties (Katz & Ukraincik 1971), which implies that proper prediction of a bone's macroscopic response to stress requires information on the preferential orientation of the HA crystallites (Wagner and Weiner 1992, Landis 1995). The usual techniques used to characterize the geometrical alignment of HA crystallites are small-angle scattering (Fratzl et al. 1996, Rinnerthaler et al. 1999, Wess et al. 2001, Liu 2010a) and Transmission Electron Microscopy (TEM), although the latter provides only limited, local information (Zocco and Schwartz 1994). Due to alignment of the c-axis with the longest edge of HA particles (Weiner and Traub 1986, Traub et al. 1989, Landis et al. 1996), the distribution of the 002 crystallographic poles is implicitly describing the alignment of crystallites (Bacon et al. 1979, Sasaki et al. 1989) and it can be detected by X-ray or neutron texture measurements. These techniques allow a quantitative assessment of the proportion of crystallites, having a selected crystallographic axis in a given, preferred direction of space.

Several journal articles describe the texture of fossil bones, indicating that HA particles are mainly aligned along the long axis of the bone. Lonardelli et al. (2005) have shown, for example that crystallites of the dinosaur tendon have their c-axes strongly aligned with the tendon direction. Similar results were obtained by Pyzalla et al. (2006) and Dumont et al. (2011) for the long bones of two different sauropods *Brachiosaurus brancai* and *Barosaurus africanus*. These latter results reveal a predominantly 001-fiber texture of HA, the fiber direction coinciding with the long axis of the bones. Variations of texture strength across the bone wall were not significantly large, however it was mentioned that texture components other than the 001 fiber component may also be present. The aim of the current study is therefore, to systematically analyze the degree of preferential orientation of HA crystallites in sauropod cortical bone. Since bone's final structure is a result of functional adaptation, one can expect that primary and remodeled secondary bone show different features according to their different growth strategies (Klein and Sander 2008). Consequently, special attention was given to texture analysis as a function of the ontogenetic stage of the bones, which might allow for the preferential orientation of HA crystallites to be correlated with the weight/age of the animal. In order to assess the impact of diagenesis, the texture of sauropod bones was compared with that of subfossil and recent mammals, crocodiles, and birds. The microstructure of the mammals and the ostrich are similar to that of a sauropod bone (Enlow and Brown 1956, Sander and Andrassy 2006) and as such, they constitute an adequate reference material for comparison.

2 Experimental details

2.1 Material

The material consisted of an ontogenetic series of Apatosaurus from the Morrison Formation, USA. Humerus and femur sections were taken from the middle of the shaft (Klein and Sander, 2008, Stein and Sander 2009). Based on observations of histological features (e.g. growth stop marks, remodeling etc.), the histological ontogenetic stage (HOS) and maturity of each specimen were determined (Klein and Sander, 2008). The *Apatosaurus* samples studied are: a humerus of a juvenile (OMNH1278), femora of two adults (BYU 681 11940 and BYU 601 17328) and a femur of one old animal (OMNH 4020) (Klein and Sander, 2008). The sauropods were compared with a fossil ornithopod or ceratopsian bone sample from the Judith River Formation (Campanian, upper Cretaceous, Kennedy Coulee, Montana, USA), as well with a subfossil tibia of a bison (*Bison sp.*, FK BI RS 1) from the late Pleistocene Rhine River gravels (Germany). Finally, the texture of four recent tetrapod bones was evaluated: the femur of a five year old ostrich (*Struthio camelus*, K Str 1); an eight year old *Alligator mississipiensis* (K Kr 26) from Rockfeller Wildlife Center, Louisiana, USA; the humerus (44.5 cm) of a giraffe *Giraffa camelopardalis* (5834 A); and the humerus (72 cm) of an elephant, *Elephas maximus*.

2.2 X-ray diffraction measurements

The XRD texture measurements were performed on a Seifert ID3000 diffractometer equipped with a graphite monochromator tuned for the CoKα radiation. The texture of HA crystallites in sauropod bones was measured using the 002, 300, 112, and 213 diffraction peaks. For recent bones, due to overlapping between 112 and 300 reflections, the 222 peak was used instead. The difference between fossil and experimentally heated bone is well known in the corresponding literature (Chipera and Bish 1991, Person et al. 1996); Normally the higher crystallinity and higher fluorine content that can be observed in fossil bones tend to sharpen the X-ray diffraction pattern, (Eanes 1965, Tannenbaum and Termine 1965, Bartsiokas and Middleton 1992, Chipera and Bish 1991) splitting the reflections peaks 211, 112, 300 and 202. Incomplete pole figures have been measured by varying the tilt angle ψ from 0° to 65° in 5° steps and the azimuthal angle φ from 0° to 360° in 5°steps. Measurements using an X-ray beam, size of 1.5 mm^2, were done at different points through the cortex, both on the axial and longitudinal sections of the bone. The incomplete pole figures were then used to calculate the orientation distribution function (ODF) of HA utilizing the BEARTEX software (version 3.6, Wenk et al. 1998). The final results are presented in the form of recalculated complete 002 and 300 pole figures, where the pole density is given in multiples of the density corresponding to the random distribution (mrd.) (Wenk and Van Houtte 2004).

3 Results

3.1 Texture of sauropod FBL bone

The recalculated pole figures for the transverse (a) and longitudinal (b) sections of an adult sample (BYU 681 11940; HOS 10 according to Klein and Sander, 2008) are shown in Figure 5.1, for the 002, 300, 222 and 213 poles. The 002 pole figures show high pole density in the center of the figure and an axial symmetry. The 002 pole figure shows a typical 001-fiber texture, that is, the crystallographic 001 and 100 axes are respectively, lying along and rotated symmetrically around the bone's long axis. The maximum pole density of 3.1 mrd indicates that the probability of a non-random distribution of c-axes parallel to born long axis is three times more likely than a random distribution. The 300 pole figure corresponding to the transverse section confirms the 001-fiber texture of HA crystallites, namely that the 100 poles are lying circularly in the center, and symmetrically around the bone's long axis. The 002 pole figure shows maximal density in the south and north areas of the pole figure, confirming that 002 poles are perpendicular to the longitudinal direction of the bone.

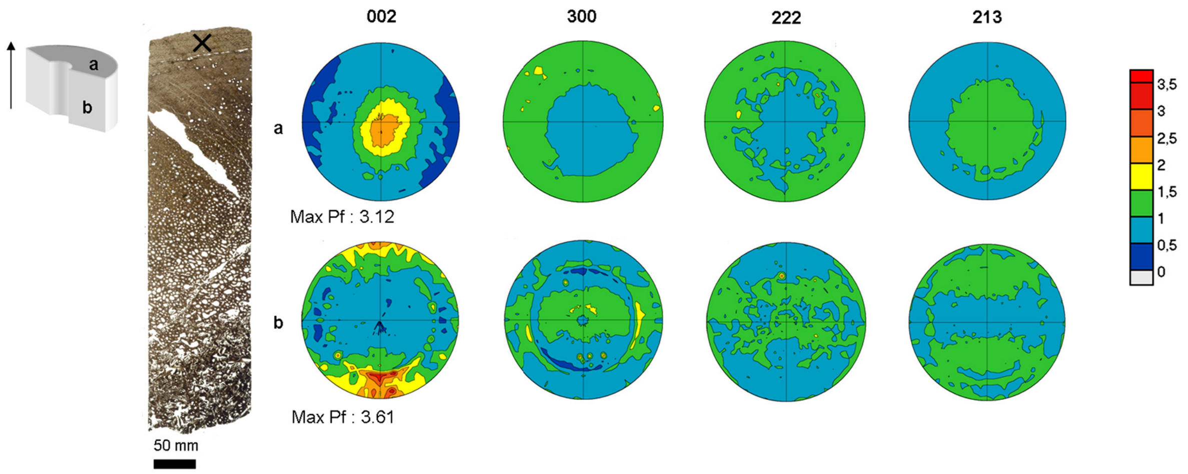

Figure 5.1: Schematic drawing of the bone cortex with transversal (a) and longitudinal sections (b). The bone's long axis is represented by the arrow. Optical micrograph of the transversal section of the sample BYU 681-11940, the black cross marks the location of the texture measurement. Recalculated pole figures corresponding to the two texture measurements performed on the transverse (a) and longitudinal (b) sections of bone. The maximum pole densities are indicated by warm colors meaning that this orientation has a certain density of crystals. The 002 pole figure in the transverse section (a) describes a maximum in the center of the pole. The same result is obtained for the 213 reflection. Whereas the 300 and 222 pole figures are defined by maximums in a circle shape. In the longitudinal section, the 002 and 213 share a similar configuration with a maximum density at the south and north poles. The 300 and 200 reflections describe an off-centered density.

The results observed on the longitudinal section of the bone support the presence of a 001-fiber texture; however, the maximum texture index, in this case, is somewhat higher with 3.6 mrd. The difference of about 0.5 mrd is related to possible fluctuations or error margins in the orientation of HA particles, which has to be taken into account when comparing different samples.

3.2 Texture in other tissue types

Sauropod bone

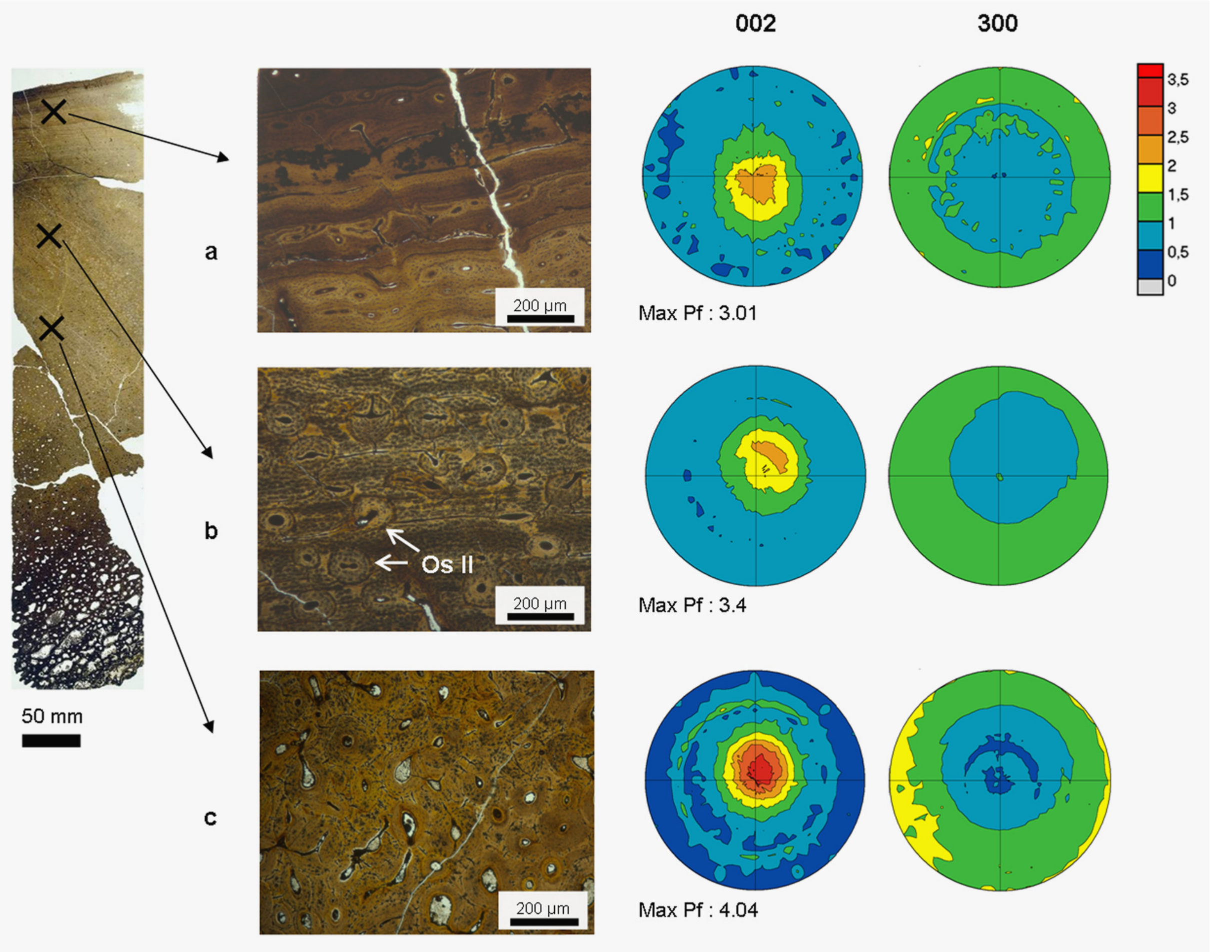

Figure 5.2: Optical micrographs of the transverse section and pole figures characteristic for three different regions in the *Apatosaurus* specimen BYU 601-17328 (Femur, 158 cm, HOS 12). **a.** Measurement from the outer cortex consisting of laminar FLB with primary osteons and a line of arrested growth. **b.** Measurement from the cortex containing scattered secondary osteons (Os II) in laminar FLB. **c.** Measurement from a location with numerous secondary osteons. For the three locations measured, 002 pole figures describe a maximum in the center of the pole, more or less aligned axially. The 300 pole figure describes circular pole density distribution.

Texture measurements were also performed at different points in the bone cortex, in zones with different histologies such as primary or secondary bone. Figure 5.2 shows complete 002 and 300 pole figures obtained at the three different points a, b and c in the cortex of an *Apatosaurus* specimen (BYU 601-17328). The magnified optical micrographs clearly indicate different bone tissue structures at the three points. In the outer cortex, FLB is interrupted by lines of arrested growth (LAGs) (Figure 5.2a). Due to remodeling, progressive changes into secondary bone are characterized by scattered secondary osteons (Figure 5.2b). In the inner part, the remodeling becomes intense as indicated by the dominance of secondary osteons. A comparison of the pole figures indicates the same type of 001-fiber texture throughout the cortex. The texture index, however, shows significant differences, continuously increasing from the FLB (~3 mrd) towards the secondary bone (~4 mrd). In other words, the number of crystallites aligned with the bone's long axis increases with the number of secondary osteons, which results from bone remodeling.

Subfossil bison bone

A bison tibia from the late Pleistocene was compared with sauropod samples (Figure 3). The upper part of the cortex (Figure 5.3a) of the bison tibia is composed of FLB. The middle part consists of FLB with a few secondary osteons filled with diagenetic pyrite material (Figure 5.3b), while the innermost cortex is formed by endosteal lamellar bone as confirmed optical microscopy of bone sections in polarized light (Figure 5.3c). The pole figures corresponding to the outer cortex region shows a rather weak 001 fiber texture. However, the c-pole density has a maximum value near the figure center corresponding to the direction of the bone's long axis. The texture index is low (< 2mrd) and it increases gradually in the remodeled part of the bone (Figure 5.3b and 5.3c). The increase in c-pole density happens in spite of the presence of the diagenetic material pyrite that has filled in secondary osteons and osteocyte lacunae (Tütken, 2003). The pole figures corresponding to the endosteal region are quite different. The maximum intensity of 002 poles spreads over a large region in a direction perpendicular to the bone radius. Correspondingly, the 300 pole figures show maximum pole density at the north and south poles. The 300 pole describes a texture perpendicular to the transversal section.

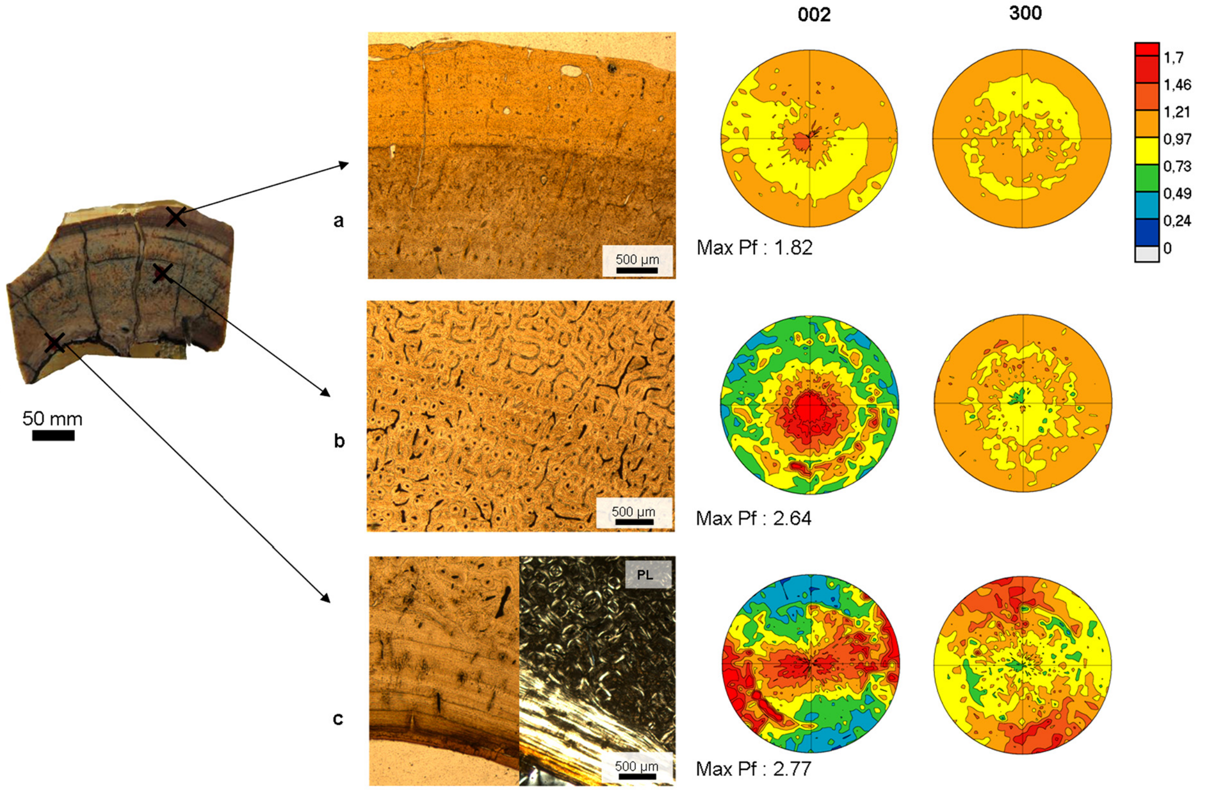

Figure 5.3 Optical micrograph of the transverse section and recalculated 002 and 300 pole figures corresponding to three different locations in the subfossil bison tibia specimen FK BI RS 1. **a.** Outer cortex consisting of FLB, lacking collagen. **b.** Cortical bone with laminar to reticular FLB tissue and a few secondary osteons. **c.** Lamellar endosteal bone in normal light and in polarized light (PL) showing the different crystallographic orientation. The outer and the middle part of the cortex show a maximum pole density in the center of the 002 profiles. The 300 pole figure shows a typical circular symmetry profile. The more inner, endosteal part of the cortex displays a different pole figure configuration: the 002 pole is spread from the west to the east part of the figure and the 300 pole figure has maximal intensity in the north and south poles.

3.3 Texture at different ontogenetic stages

To assess the impact of bone size on ontogenetic development, texture analysis was carried out on the FLB of *Apatosaurus* bone specimens. Figure 5.2 and Figure 5.4 show the results obtained for the cortex of three different sauropods of different HOS (histological ontogenetic stage), a young individual (OMNH 1278, HOS 4) represented by a humerus, 25.8 cm in length, a mature but not fully grown individual (BYU 681-11940, HOS 10) with a femur of 133 cm in length and another mature individual (BYU 601-17328, HOS 12) with a larger femur, 158 cm in length. The ontogenetic series is completed by the fully grown and fully remodeled 180 cm femur (OMNH 4020, HOS-13).

(a)

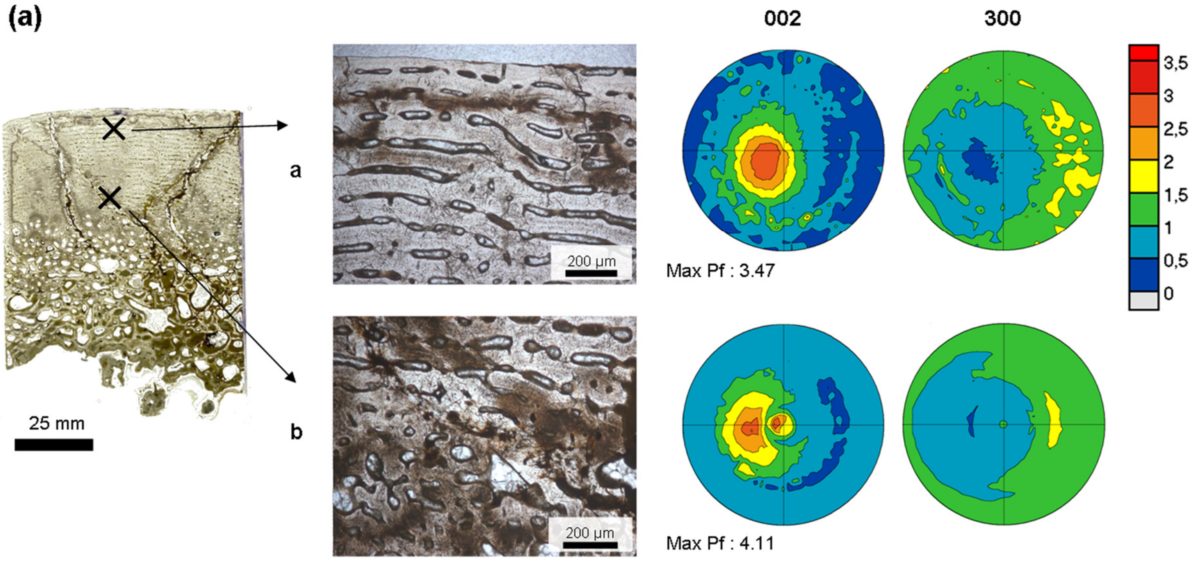
002
300
a
b
25 mm
200 µm
200 µm
Max Pf : 3.47
Max Pf : 4.11
3,5
3
2,5
2
1,5
1
0,5
0

(b)

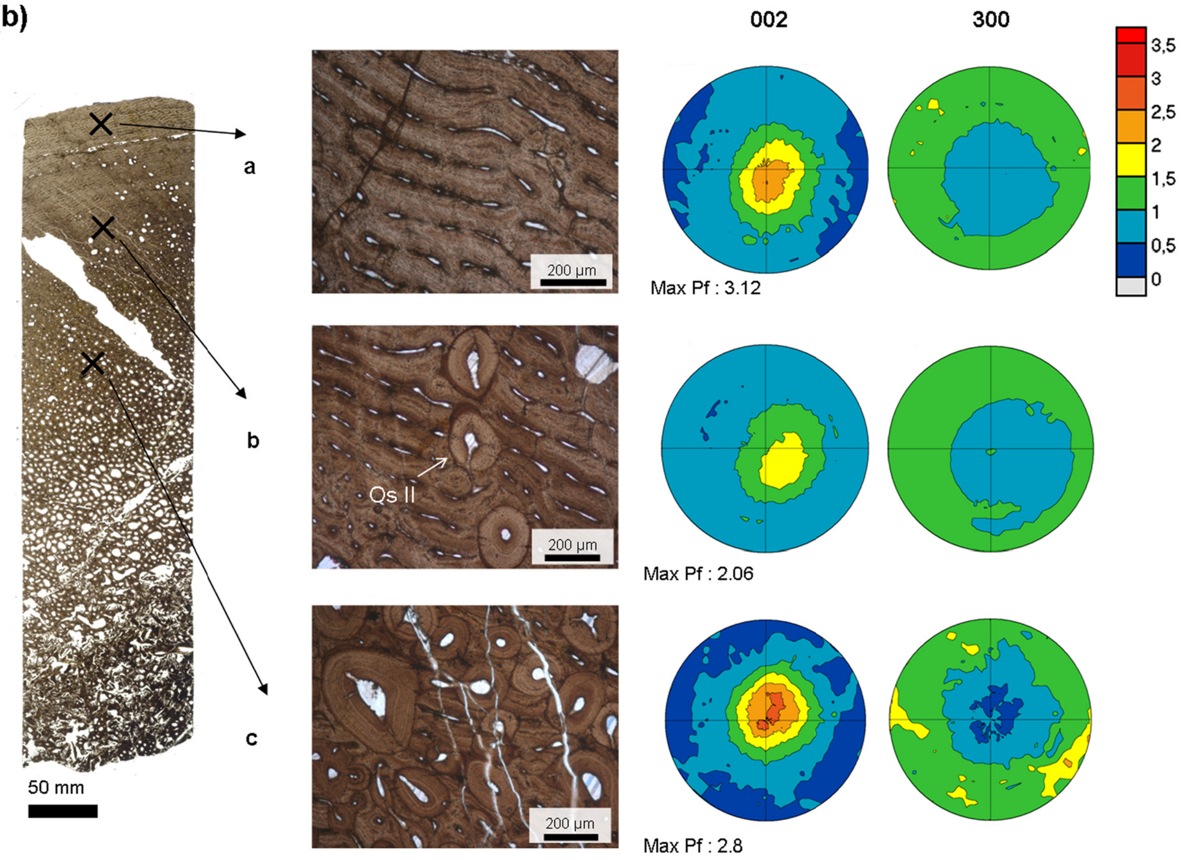
002
300
a
b
c
50 mm
200 µm
Qs II
200 µm
200 µm
Max Pf : 3.12
Max Pf : 2.06
Max Pf : 2.8
3,5
3
2,5
2
1,5
1
0,5
0

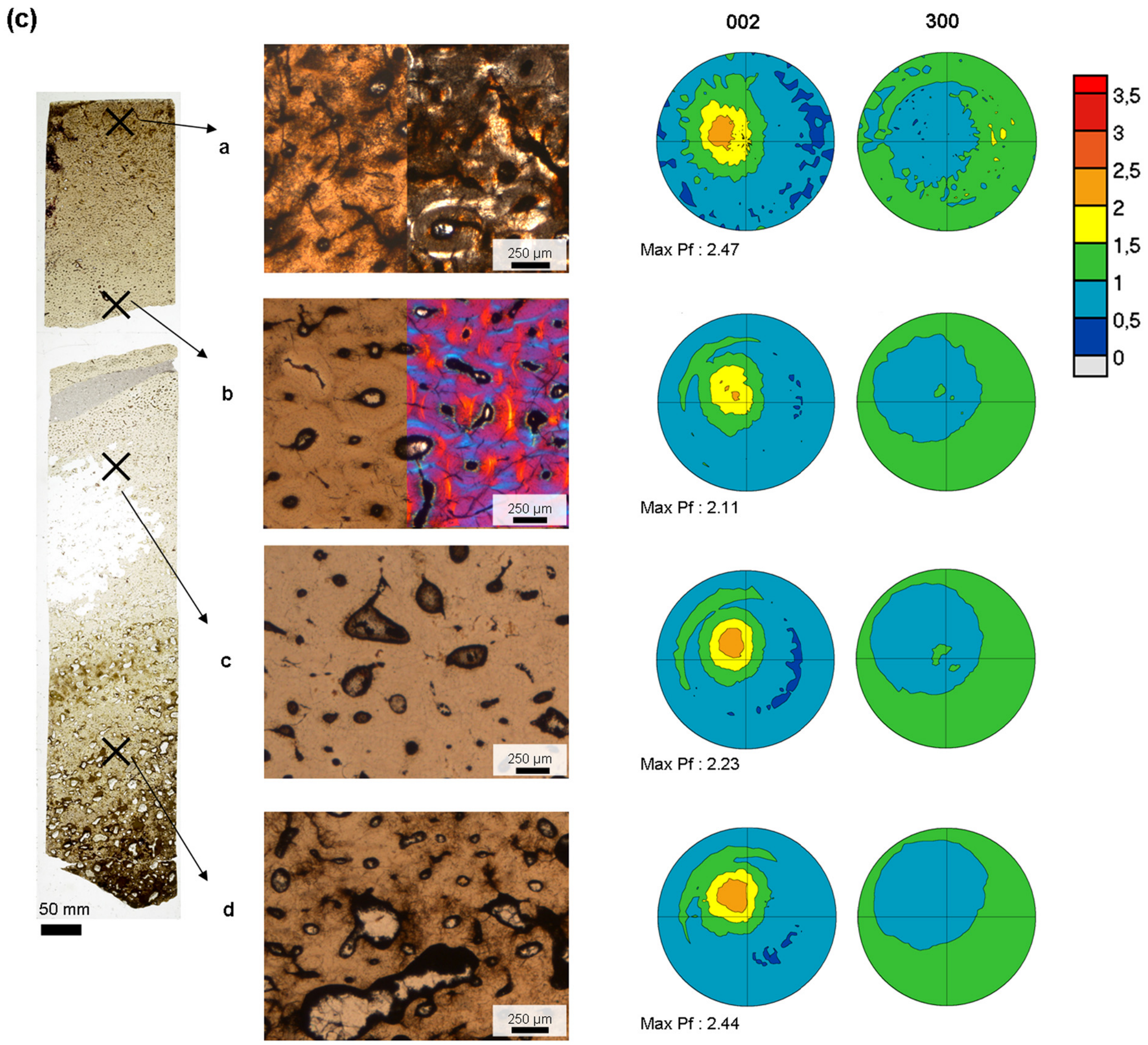

Figure 5.4 A.: OMNH 1278 (HOS 4, 25.8 cm): a. FLB bone of young animal dominated by woven bone, b. FLB with erosion cavities. **B.**: BYU 681-11940 (HOS 10, 133 cm): a. Laminar FLB with distinct primary osteons; b. Laminar FLB showing remodeling activity consisting of scattered secondary osteons (Os II); c. Laminar FLB that is heavily remodeled by large secondary osteons. The right hand side of the figure shows recalculated pole figures at the sample locations. C.: OMNH 4020 (HOS 13, 180 cm): a., b., c., d. Laminar FBL in normal and polarized light (for a. and b.) showing complete remodeling with presence of large secondary osteons. For the four points measured, 002 pole figures describe maximal intensity in the center of the pole, confirming the 001 fiber texture. 300 pole figures exhibit circular intensity at the periphery of the pole.

The juvenile specimen (OMNH 1278) shows characteristic laminar FLB composed mainly of woven/fibrous bone with distinct, wide lumina. Its texture was measured at two points marked by crosses. The outer cortex is characterized by a typical 001-fiber texture with a maximum pole density of about 3.5 mrd. The second point situated deeper in the cortex shows a similar texture but has a somewhat higher texture index. Similar changes in texture are observed through the cortex of the mature sauropod bone (BYU 11940, Figure 5.4B). The cortex is progressively remodeled towards the middle region (point b) with laminar FLB containing primary and secondary osteons. Generally, such regions have larger volumes with higher texture indices. A slight deviation (of about 5°-15°) of pole figure maximum from the bone's long axis can be noticed in Figures 4A and 4B. This could be either due to heterogeneities in the bone microstructure or to misalignment during sample preparation or mounting in the goniometer.

No significant trends were noticed in texture strength either as a function of tissue type, of HOS or remodeling. An average texture index of about 2.5-3 characterizes the majority of the long bones of *Apatosaurus*. Indices show slight variations along the cortex of the bones. For example specimens BYU 681-11940 (HOS 10) (Fig. 4B) and BYU 601-17328 (HOS 13) (Figure 5.2) have a lower texture index of about 2-2.5 mrd in FLB with fewer secondary osteons. The pole density increases in the remodeled section to about 3-3.5 mrd. Although in this case the mrd values vary in primary bone and remodeled bone, the difference of the two fits well within the scatter of the values mentioned for figure 5.1 (3.12 and 3.61 mrd for the transversal and longitudinal directions, respectively).

Comparing the texture in the outer cortex of the three sauropod bones (Figure 5.4 and Figure 5.2) of different HOS (HOS 4, HOS 10, and HOS 12), it is evident that the 001-fiber texture is not only qualitatively but also quantitatively similar in all samples. The highest index of 2.5-3 mrd is shown by the sample with HOS 4 (OMNH 1278) (Figure 5.4A), whereas the adult specimens BYU 601-17328 (HOS 12) (Figure 5.2) and BYU 681-11940 (HOS 10) (Figure 5.4B) are characterized by a pole density of about 2-2.5 mrd. Similar texture strength is seen in the ontogenetically oldest sauropod bone among our material, sample OMNH 4020 (HOS 13) (Figure 5.4C). This bone contains secondary osteons up to the surface of the cortex and is completely remodeled. Its texture strength index has values between 2 and 2.5 mrd.

3.4 Texture of recent animals

To asses the influence of diagenesis, the texture of HA minerals was quantified in bones of a ceratopsian dinosaur, a subfossil bison (Figure 5.3) and four recent species: an alligator (*Alligator mississippiensis)*, an ostrich (*Struthio camelus*), an elephant (*Elephas maximus*, Loxodonta Africana) and a giraffe (*Giraffa camelopardis*).

The ceratopsian was studied as a fossil example to complement the results on sauropods. It is characterized by a 001-fiber texture (Figure 5.5) similar to the sauropod bones, but has lower texture strength of about 2-2.5 mrd. Compared to sauropods, the amount of highly aligned HA crystallites, as described by the area of the corresponding contour bands in the pole figure, is smaller. This means that the texture is not as pronounced as in sauropods, even if the maximum appears at the center of the pole figure. Compared to the subfossil bison sample (FK BI RS 1, Figure 5.3) the ceratopsian dinosaur shows less symmetry but has a similar pole density.

The femora of all four extant animals show the typical 001-fiber texture along the bone's long axis. The maximum texture index as well as the proportion of crystallites aligned along the bone's long axis is lower in the alligator, the ostrich, and the giraffe (around 2 to 2.5) than in the dinosaur bones. Only the elephant shows a higher texture index (3-3.5 mrd), close to the results of sauropods (Figure 5.1, Figure 5.2 and Figure 5.4A, 5.4B). The oldest sauropod OMNH 4020 (HOS 13) shares similar texture indices with those of the alligator, giraffe, and ostrich (around 2 mrd).

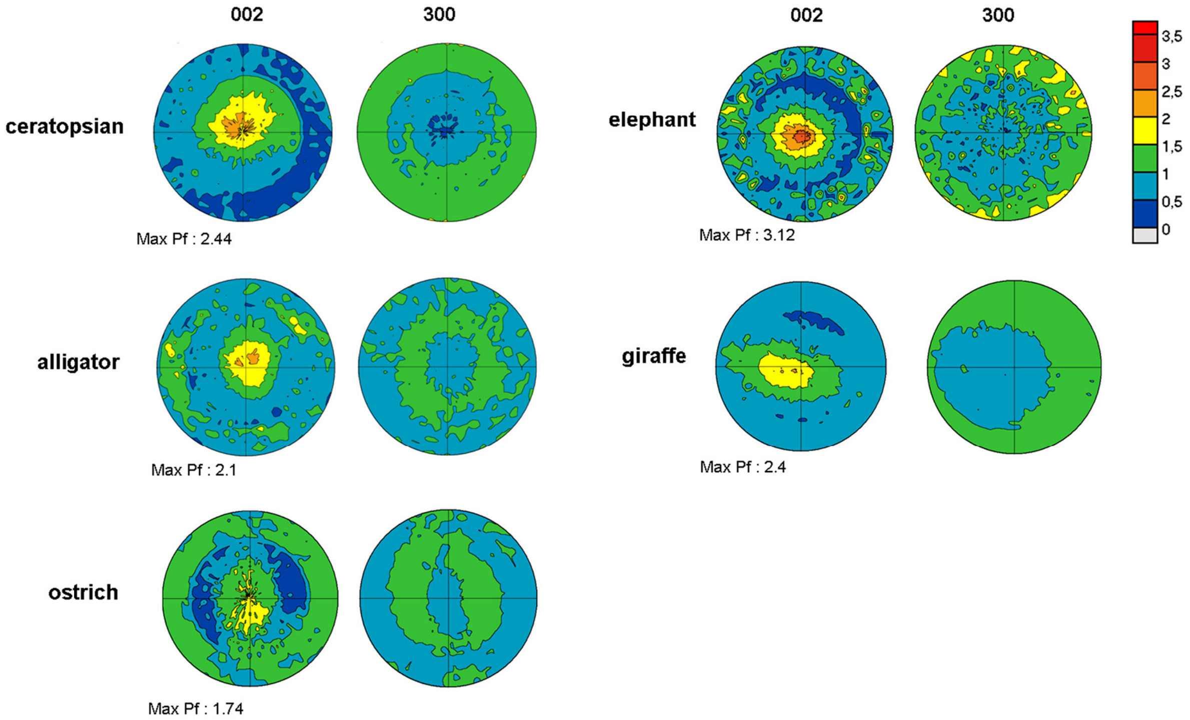

Figure 5.5: Recalculated 002 and 300 pole figures describing the preferred orientation of the HA crystallites in the outer cortex of the undetermined ceratopsian dinosaur and of the extant alligator, ostrich, elephant, and giraffe. The pole figures represent transverse sections. The ceratopsian, the elephant, and the giraffe show the same 002 and 300 pole figure profiles, with maximal intensity in the center and circular symmetry for both reflection profiles, respectively. The pole figure of the giraffe is asymmetric and not quite centered. The elephant displays a higher index, in comparison with the other animals illustrated in the figure. The alligator and the ostrich display identical 002 pole figures and the 300 pole figures show a circular maximal density shifted from the edge to the middle, surrounding the center.

4 Discussion

4.1 Texture of sauropod bone and diagenesis

Crystallographic texture is one of the basic attributes of bone that influences its mechanical properties (Bacon et al 1979, Currey 1984, Sasaki et al. 1991, Nakano et al. 2002, 2008, Liu et al 2010b). Long bones have been preferentially studied as they are subjected only to simple, mechanical, compression load. However, before mechanical properties can be analyzed, diagenetic effects, like the partial recrystallization of apatite minerals, need to be considered to understand its influence on the texture of the bone.

Fossil sauropod and ceratopsian bone, subfossil bison bone and recent tetrapod bones were analyzed for diagenetic effects. The femur of *Apatosaurus* sp. (BYU 681-11940) shows that the crystallographic 001 axis lies along and the 100 axis rotates symmetrically around the bone axis (Figure 5.1). The texture of HA in long bones of recent tetrapods shows the same pattern as sauropod bones; these results are in agreement with literature data on recent mammals (Jackson 1979, Sasaki and Sudoh 1997). Only one study on bovine ankle bones documents a complete rotational freedom of c-axes about the normal surface and no preferential alignment with the long bone axis (Wenk and Heidelbach, 1999), a phenomenon not observed in our study. Majority of literature results clearly indicate that the alignment of HA is kept during the fossilization process. This seems to be in agreement with the model already proposed by Hubert at al. (1996) based on birefringence investigations of crystals already observed using TEM by Zocco and Schwartz 1995. Hubert's model considers a seeded growth of authigenic apatite around original crystallites. This statement is generally accepted in paleohistology where the preservation of structural features is observed (de Ricqlès 1980, Reid 1984).

The texture index of dinosaur samples conforms to previous results of Pyzalla et al. (2006) who also reported values of 3 - 3.5 mrd for a sauropod femur sample. The comparison with subfossil bison (Figure 5.3) and recent tetrapod bones (alligator, ostrich, and giraffe) (Figure 5.5) demonstrates that dinosaur long bones have a higher pole density (~3.5 mrd compared to 2 mrd). Elephant bones have a texture index of about 3-3.5 mrd, similar to that of sauropods. The amount of oriented crystallites in alligator and ostrich bones is lower than those in the long bone of sauropods. This may be due to the fact that their long bones are exposed to smaller loads. As the highest value of Young's modulus (stress divided by the strain) is obtained along the c-axis, therefore the stronger 002 texture means that the elephant femur can carry a higher load per unit cross-sectional area than the femur of the other extant tetrapods, which agrees with their rankings of weight. Since the weight of sauropods and the elephant are quite different, the same reasoning can not be used in interpreting the nearly identical texture strengths of the two animals. It is therefore plausible that diagenesis plays a non-negligible role in establishing the observed texture of the fossil sauropod bones or that texture is not a principal trait to ensure bone strength.

4.2 Texture in different tissue type

Texture with remodeling of the bone

The 001-fiber texture appears to be present in both the primary as well as in secondary bone, both in *Apatosaurus* bones and in the subfossil bison bone. No large variation of the texture index was found across the cortex of sauropods with different HOS and apart from the case of the BYU 601-17328 specimen (Figure 5.2), there was no correlation between texture strength and the number of secondary osteons. The slight differences between primary and secondary bone, as reported by Jackson 1979, seem to be rendered almost negligible by the relatively large scatter of our results for the selected X-ray spot size with an area of about 1.5 mm^2. According to results of Figures 5.2 and 5.4, the texture does not change with the growth of the sauropod. Moreover, no trend (increase /decrease) in the texture index could be observed with the degree of remodeling of the bone (increase in the number of secondary osteons). An increased anisotropy through the secondarily remodeled bone has already been reported by Currey (2002, extant cranes). Riggs et al. (1993a, 1993b) also suggested that secondary osteons replace primary bone under locomotor mechanical circumstances making it more resistant in compression. The collagen fibril orientation becomes more transverse and more efficient in withstanding compressive loads.

This tendency of increased anisotropy with progressive remodeling was not observed when looking at the results for the *Apatosaurus* sample BYU 681-11940 (Figure 5.4B) where the texture index is decreasing in regions with secondary osteons. Similarly, the oldest individual, OMNH 4020, having a fully remodeled bone up to the surface of the cortex, has the lowest texture index for a pole density (2-2.5 mrd).

Secondary osteons are cylindrical structures extending parallel to the bone's long axis, and differences in the degree of orientation of crystallites should be expected. Their presence in the bone could increase texture strength by increasing the density of collagen fibrils oriented along the long axis. However, different morphotypes of secondary osteons (longitudinal, transversal and alternate) are characterized by different collagen fiber orientations (that is, collagen with inorganic particles) (Ascenzi and Bonucci 1976), and therefore have different mechanical properties (Ascenzi and Bonucci 1976, Ascenzi et al. 1994, Martin et al. 1996, Skedros et al. 2009). No distinction between the different types of secondary osteons was made in the present study because previous results demonstrated that a similar fiber texture is observed for all the morphotypes (Ascenzi et al. 1979, Ascenzi et al. 1985, Bigi et al. 1998). No substantial differences in texture have been reported for different stages of osteon calcification (Ascenzi et al. 1985) (where apatite crystallites cover a larger area and collagen fibrils are entirely calcified (Ascenzi et al. 1965)) for longitudinal and alternate osteons. Indeed the fibrils running transversally in longitudinal structures are not revealed by X-Ray diffraction because of their low abundance (Ascenzi et al. 1983, 1985), whereas they are clearly seen on transmission electron micrographs. Usually, longitudinal osteons have a higher degree of orientation than others (Ascenzi et al. 1985). In alternate osteons, fibrils oriented at right angles to the bone axis contribute to the scattering of the X-Ray diffraction. Studies (Martin 1996, Riggs et al 1993a and 1993b, Skedros et al. 2009) indicate the higher texture index obtained for the sauropods and elephant is probably due to a larger amount of longitudinal osteons or at least the support of one preferential osteon morphotype due to the mechanical demands on the bones of these heavily loaded animals.

Particular case of Bison tibia bone

In our study only one specimen displayed a different pattern from the 001-fiber texture. This is the endosteal lamellar bone forming the inner part of the bison cortex (Figure 5.3c). This lamellar bone shows the existence of a different HA population with a pole density similar to that of the 001-fiber. The 002 poles of this second population are mainly oriented in the hoop direction (perpendicular to the bone's long axis and bone radius). This is consistent with observations in polarized light (Figure 3c). The existence of HA particles with 002 poles perpendicular to the bone's long axis had already been noticed by Nightingtale and Lewis (1971) as well as by Sasaki et al. (1991, 1989). Their observations were made for a cow femur with the X-Ray diffraction technique. The endosteal lamellar bone in the bison tibia is probably due to a different mechanical loading that induces a different stress distribution in the bone. The role of this lamellar endosteal bone is presently not well understood (Weiner 1997, 1999), being mainly considered as a bone tissue that prevents micro-crack propagation (Nyman et al. 2005). The gradual tilting and rotating of mineralized collagen fibrils (Giraud Guille 1988, Ziv et al. 1996a) provides nearly isotropic properties, permitting the bone to withstand a variety of multiaxial loads (Ziv et al. 1996b). Endosteal lamellar bone was considered to be formed where higher bending occurred (rat tibia in Turner et al. 1994, and mouse ulna in Lee et al. 2002). Sauropod long bones do not form this lamellar endosteal bone (Sander 2000, Klein and Sander 2008, Sander et al. 2011) possibly because they are only loaded under compression and not under bending as suggested by studies by Witzel (e.g., Sverdlova and Witzel 2010). Their study does not state that a biomechanical signal is the only factor of endosteal lamellar bone formation; other explanations are included.

5 Conclusions

Texture analysis of the orientation of HA crystallites in fossil sauropod long bones, a subfossil bison long bone, and the long bones of the four recent tetrapods indicates that the texture of sauropod bone is qualitatively similar to recent animals. The c-axis crystallographic orientation is preserved and the texture in *Apatosaurus* is maintained throughout ontogeny, without significant change in the texture index during remodeling of the bone. The dominating 001 texture may indicate, however, that the major mechanical load is via compression rather than tension or bending. Contrary to expected differences the texture strengths of *Apatosaurus* and elephant are the same, indicating a possible influence of diagenesis on the texture in fossil specimens. Also, the statistical error (of about 0.5 mrd) of the maximum texture index may be the result of diagenesis in sauropod bones. This can hinder the discovery of small differences that may exist in dinosaur bones as a function of HOS or tissue type.

In recent animals, weight correlates well with the texture strength in bones, suggesting that the collagen in compact bones of heavier animals has a higher degree of orientation.
The preferential crystal alignment with higher stress in the bone has been already concluded. Conclusions in (Bacon and Griffiths 1985, Bacon and Goodship 1991, Sasaki et al. 1989, Fratzl et al. 1992, Weiner et al. 1999) have shown that in many long bones, the c-axes of mineral crystals are aligned with longitudinal axis of the bone. This was implied by observations made by Paterson, (1973): in some inorganic minerals, crystals grow in a direction parallel to principal stress. The effect of diagenesis is difficult to predict but according the hypothesis above could lead to significant decrease in the texture strength of sauropod bones.

Texture measurements could help further research concerning the osteon morphotypes and their mechanical influence. As suggested by Martin et al. (1996), Riggs et al. (1993a, 1993b) and Skedros et al. (2009, 2010, 2011), the different osteon morphotypes are the results of bone adaptation to different loading conditions. For example, osteons which present mostly transverse or longitudinally oriented fibers are assumed to have a higher resistance in tension than those having alternate lamellae (Ascenzi and Bonucci 1967, 1968, Skedros et al. 2009).

References

Ascenzi, A., Bonucci, E., Bocciarelli, D. S. 1965. An electron microscope study of osteon calcification. Journal of Ultrastructure Research 12: 287-303.

Ascenzi, A., Bonucci, E. 1967. The tensile properties of single osteons. Anatomical Record 158: 375–86.

Ascenzi A., Bonucci E. 1968. The compressive properties of single osteons. Anatomical Record 161: 377–91.

Ascenzi, A., Bonucci. E. 1976 Relationship between ultrastructure and "pin test" in osteons. Clinical Orthopaedics and Related Research 121: 275-294.

Ascenzi A., Bonucci E., Generalli P., Ripamonti A., Roveri N. 1979. Orientation of apatite in single osteon samples as studied by pole figures. Calcified Tissue International 29: 101-105.

Ascenzi, A., Bigi, A. Koch, M. H. J., Ripamonti, A., Roveri N. 1985. A low angle X-ray diffraction analysis of osteonic inorganic phase using synchrotron radiation. Calcified Tissue International 37: 659–664.

Ascenzi, A., Benvenuti, A. 1986. Orientation of collagen fibers at the boundary between two successive osteonic lamellae and its mechanical interpretation. Journal of Biomechanics, 19(6): 455-463.

Ascenzi, A., Baschieri, P., Benvenuti A. 1994. ‘The torsional properties of single selected osteons. Journal of Biomechanics 27: 875–884.

Bacon, G. E., Bacon, P. J., Griffiths, R. K. 1979. The study of bones by neutron diffraction. Journal of Applied Crystallography 10: 124 –126.

Bacon, G.E., Griffiths, R. K. 1985. Texture, stress and age in the human femur. Journal of Anatomy 143: 97–101.

Bacon, G.E., Goodship, A.E. 1991. The orientation of the mineral crystals in the radius and tibia of the sheep and its variation with age. Journal of Anatomy 179: 15-22.

Bartsiokas, A., Middleton, A.P., 1992. Characterization and dating of recent and fossil bone by X-Ray diffraction. Journal of’Archaeologica1 Science 19: 63-72.

Bigi, A., Cacchioli, A., Fichera, A. M., Gabbi, C., Koch, M. H. J., Ragionieri, L., Ripamonti, A., Roveri, N. 1998. X-ray diffraction and polarizing optical microscopy investigation of the structural organization of rabbit tibia. Journal of Biomedical Materials Research 41(2): 289-295.

Chipera, S.J., Bish, D.L. 1991. Applications of X-ray diffraction crystallite size/strain analysis to *Seismosaurus* dinosaur bone. Advances in X-Ray analysis 34: 473-482.

Currey, J.D. 1984. The mechanical adaptations of bones. Princeton University Press, Princeton, NJ

Currey, J. D. 2002. Bones: Structure and Mechanics. Princeton University Press, Princeton.

Currey, J. D. 2003. Many adaptations of the bone. 2003. Journal of biomechanics 36: 1487-1495.

Dumont, M., Borbély, A., Kostka, A., Sander, P. M., Kaysser-Pyzalla, A. 2011. Characterization of sauropod bone structure. Pp. 150-170. *In* N. Klein, K. Remes, C. T. Gee, and P. M. Sander, eds. Biology of the Sauropod Dinosaurs: Understanding the Life of Giants. Life of the Past (series ed. Farlow, J.). Indiana University Press, Bloomington.

Eanes, E.D. 1965. Effects of fluoride on human bone apatite crystals. Annals of the New York Academy of Sciences 131: 727.

Enlow, D. H. and Brown, S. O. 1956. A comparative histological study of fossil and recent bone tissues, part 1. Texas Journal of Science 8: 405–443.

Enlow, D. H. and Brown, S. O. 1957. A comparative histological study of fossil and recent bone tissues, part 2. Texas Journal of Science 9: 186–214.

Francillon-Vieillot, H., de Buffrénil, V., Castanet, J., Géraudie, J., Meunier, F. J., Sire, J. Y., Zylberberg, L., de Ricqlès, A. 1990. Microstructure and mineralization of vertebrate skeletal tissues. *In* Carter, J. G. (ed.). Skeletal Biomineralization: Patterns, Processes and Evolutionary Trends, Vol. 1. Van Nostrand Reinhold, New York: pp. 471–530.

Fratzl, P, Groschner M, Vogl G, Plenk Jr H, Eschberger J, Fratzl-Zelman, N. 1992. Mineral crystals in calcified tissues: a comparative study by SAXS. Journal of Bone Mineral Research 7: 329–34.

Fratzl, P., Schreiber, S., Boyde, A. 1996. Characterization of bone mineral crystals in horse radius by small-angle X-Ray scattering. Calcified Tissue International 58(5): 341-346.

Giraud-Guille, M.M. 1988. Twisted plywood architecture of collagen fibrils in human compact bone osteons. Calcified Tissue International 42: 167-180.

Hubert, J.F., Panish, P.T., Chure, D.J., Prostak, K.S. 1996 Chemistry, microstructure, petrology, and diagenetic model of Jurassic dinosaur bones, Dinosaur National Monument, Utah Journal of Sedimental Research 66:531-547

Jackson, S. 1979.The fibrous structure of bone determined by x-ray diffraction. Journal of Biomedical Engineering 1: 121-122.

Katz, J.L., Ukraincik, K., 1971. On the anisotropic elastic properties of hydroxyapatite, Journal of Biomechanics 4(3): 221-227.

Klein, N., Sander, P.M., 2008. Ontogenetic stages in the long bone histology of sauropod dinosaurs. Paleobiology 34(2): 247-263.

Landis, W. J. 1995. The strength of a calcified tissue depends in part on the molecular structure and organization of its constituent mineral crystals in their organic matrix. Bone 16: 533-544.

Landis, W.J., Hodgens, K.J., Song, M.J., McEwen, B.F. 1996. Structural relations between collagen and mineral in bone as determined by high voltage electron microscopic tomography. Microscopy research and technique 33: 192-202.

Lee, K.C., Maxwell, A., Lanyon, L.E. 2002. Validation of a technique for studying functional adaptation of the mouse ulna in response to mechanical loading. Bone 31(3): 407-412.

Liu, Y. 2010a. Mineral crystal alignment in mineralized fracture callus determined by 3D small-angle X-ray scattering. Journal of Physics Conference Series 247.

Liu, Y., Manjubala, I., Schell, H., Epari, D., Roschger, P., Duda, G.N. Fratzl, P. 2010b. Size and habit of mineral particles in bone and mineralized callus during bone healing in sheep. Journal of Bone and Mineral Research 25 (9): 2029–2038.

Lonardelli, I., Wenk, H.-R., Luterotti, L., Goodwin, M. 2005. Texture analysis from synchrotron radiation images with the Rietveld method: dinosaur tendon and salmon scale. Journal of Synchrotron Radiation 12: 354–360.

Martin, R.B., Gibson, V.A., Stover, S.M., Gibeling, J.C., Griffin, L.V. 1996. Osteon structure in the equine third metacarpus. Bone 19: 165–71.

Nakano T., Kainara K., Tabata Y., Nagata N., Enomoto S., Marukawa E., Umakoshi Y. 2002. Unique alignment and texture of biological apatite crystallites in typical calcified tissues analyzed by microbeam X-Ray diffractometer system. Bone 31(4): 479-487.

Nakano, T., Tabata, Y., Umakoshi, Y. 2008. Texture and bone reinforcement. Encyclopedia of Materials: Science and Technology: 1-8.

Nightingale, J.P., Lewis, D. 1971: Pole figures of the orientation of apatite in bones. Nature 232: 334-335.

Nyman, J.S., Reyes, M., Wang, X. 2005. Effect of ultrastructural changes on the toughness of bone. Micron 36: 566-582.

Paterson, M.S. 1973. Nonhydrostatic thermodynamics and its geological applications. Reviews of Geophysics and Space Physics 11: 355–389.

Person, A., Bocherens, H., Mariotti, A., Renard, M. 1996. Diagenetic evolution and experimental heating of bone phosphate. Palaeogeography, Palaeoclimatology, Palaeoecology 126: 135-149

Pyzalla A.R., Sander, P.M., Hansen A., Ferreyro R., Yi S.-B., Stempniewicz M., Brokmeier H.-G. 2006. Texture analyses of sauropod dinosaur bones from Tendaguru. Materials Science and Engineering A 437: 2-9.

Reid, R. E. H. 1984. The histology of dinosaurian bone and its possible bearing of dinosaurian physiology. Symposium of the Zoological Society of London 52: 629–663.

de Ricqlès, A. 1980. Tissue structures of dinosaur bone. Functional significance and possible relation to dinosaur physiology. *In* Thomas, D. K. & Olson, E. C. (eds.). *A Cold Look at the Warm- Blooded Dinosaurs.* Westview Press, Boulder: pp. 103–140.

Riggs, C.M., Lanyon, L.E., Boyde, A. 1993a. Functional associations between collagen fibre orientation and locomotor strain direction in cortical bone of the equine radius. Anatomy and embryology 187: 231-238.

Riggs, C.M., Vaughan, L.C., Evans, G.P., Lanyon, L.E., Boyde, A. 1993b. Mechanical implications of collagen fiber orientation in cortical bone of the equine radius. Anatomy and Embryology 187: 239-248.

Rimblot-Baly, F., De Ricqlès, A., Zylberberg, L. 1995. Analyse paleohistologique d´une série de croissance partielle chez Lapparentosaurus madagascariensis (Jurassique moyen): essai sur la dynamique de croissance d´un dinosaure sauropode. Annales de Paléontologie 81(2): 49-86.

Rinnerthaler, S., Roschger, P., Jakob, H.F., Nader, A., Klaushofer, K., Fratzl, P. 1999. Scanning small angle X-Ray scattering analysis of human bone sections. Calcified Tissue International 64(5): 422-429.

Sander, P.M. 2000. Long bone histology of the Tendaguru sauropods: implications for growth and biology. Paleobiology 26 (3): 466-488.

Sander, P. M., Andrassy, P. 2006. Lines of arrested growth and long bone histology in Pleistocene large mammals from Germany: what do they tell us about dinosaur physiology? Palaeontographica Abt. A 277: 143–159.

Sander, P.M., Christian, A., Clauss, M., Fechner, R., Ge, C.T., Griebeler, E.-M., Gunga, H.-C., Hummel, J., Mallison, H., Perry, S.F., Preuschoft, H., Rauhut, O.W.M., Remes, K., Tütken, T. Wings, O., Witzel, U. 2010. Biology of the sauropod dinosaurs: the evolution of gigantism. Biological Reviews 86(1): 117-155.

Sander, P. M., Klein, N., Stein, K., Wings O. 2011. Sauropod bone histology and its implications for sauropod biology. Pp. 276-302. *In* N. Klein, K. Remes, C. T. Gee, and P. M. Sander, eds. Biology of the Sauropod Dinosaurs: Understanding the Life of Giants. Life of the Past (series ed. Farlow, J.). Indiana University Press, Bloomington.

Sasaki, N., Matsushima, N., Ikawa, T., Yamamura, H., Fukuda, A. 1989. Orientation of bone mineral and its role in the anisotropic mechanical properties of bone. Transverse anisotropy. Journal of Biomechanics 22: 157–164

Sasaki, N., Ikawa, T., Fukuda, A. 1991. Orientation of mineral in bovine bone and the anisotropic mechanical properties of plexiform bone. Journal of Biomechanics 24: 57–61.

Sasaki, N., Sudoh, Y. 1997. X-ray pole figure analysis of apatite crystals and collagen molecules in bone. Calcified Tissue International 60: 361-367.

Skedros, J.G., Mendenhall, S.D., Kiser, C.J., Winet, H. 2009. Interpreting cortical bone adaptation and load history by quantifying osteon morphotypes in circularly polarized light images. Bone 44: 392–403.

Skedros, J.G., Kiser, C.J., Mendenhall, S.D. 2010. A weighted osteon morphotype score outperforms regional osteon percent prevalence calculations for interpreting cortical boen adaptation. American Journal Of Physical Anthropology 144 (1): 41-50.

Skedros, J.G., Kiser, C.J., Keenan, K.E., Thomas, S.C. 2011. Analysis of osteon morphotype scoring schemes for interpreting load history: evaluation in the chimpanzee femur. Journal of Anatomy 218: 480-499.

Stein, K., Sander, P. M. 2009. Histological core drilling: a less destructive method for studying bone histology. *In* Brown, M. A., Kane, J. F. & Parker, W. G. (eds.). Methods in Fossil Preparation: Proceedings of the First Annual Fossil Preparation and Collections Symposium.

Su, S.C., Skedros, J.G., Bachus, K.N., Bloebaum, R.D. 1999. Loading conditions and cortical bone construction of an artiodactyl calcaneus. The journal of Experimental Biology 202: 3239-3254.

Sverdlova, N.S., Witzel, U. 2010. Principles of determination and verification of muscle forces in the human musculoskeletal system: Muscle forces to minimise bending stress. Journal of Biomechanics 43(3): 387-396.

Tannenbaum, P.J., Termine, J.D. 1965. Statistical analysis of the effect of fluoride on bone apatite. Annals of the New York Academy of Sciences 131: 743.

Traub, W., Arad, T., Weiner, S. 1989. Three dimensionnal ordered distribution of crystals in turkey tendon collagen fibers. Proceedings of National Academy of Science 86: 9822-9826.

Trueman, C. N., Tuross, N. 2002 Trace elements in recent and fossil bone apatite. Reviews in mineralogy and geochemistry 48:489-521.

Tütken, T. 2003. Thesis, published. Die Bedeutung der Knochenfrühdiagenese für die Erhaltungsfähigkeit in vivo erworbener Element- und Isotopenzusammensetzungen in fossilen Knochen. University of Tübingen. 343p.

Turner, C.H., Forwood, M.R., Rho, J.-Y., Yoshikawa, T., 1994. Mechanical loading threshold for lamellar and woven bone formation. Journal of bone and mineral research 9(1): 87-97.

Wagner, H.D., Weiner, S. 1992. On the relationship between the microstructure of bone and its mechanical stiffness. Journal of Biomechanics 25:1311–1320.

Weiner, S., Traub, W. 1986. Organization of hydroxypatite crystals within collagen fibrils. FEBS 206(2): 262-266.

Weiner, S., Arad, T., Traub, W. 1997. Rotated plywood structure of primary lamellar bone in the rat: orientations of the collagen fibril arrays. Bone 20 (6): 509-514.

Weiner, S., Traub, W., Wagner, H.D. 1999. Lamellar bone: structure–function relations. Journal of Structural Biology126: 241–55.

Wenk, H. R., Matthies, S., Donovan, J., Chateigner, D. 1998. BEARTEX : a Windows-based program system for quantitative texture analysis, Journal of. Applied Crystallography 31: 262–269.

Wenk, H.-R., Heidelbach, F. 1999. Crystal alignment of carbonated apatite in bone and calcified tendon: results from quantitative texture analysis. Bone 24(4): 361-369.

Wenk, H.-R., Van Houtte, P. 2004. Texture and anisotropy. Report on progress in physics 67: 1367-1428.

Wess, T., Alberts, I., Hiller, J., Drakopoulos, M., Chamberlain, A. T., Collins, M. 2001. Microfocused small angle X-ray scattering reveals structural features in archaeological bone samples: detection of changes in bone mineral habit and size. Calcified Tissue International 70: 103-110.

Ziv, V., Wagner, H.D., Weiner, S. 1996a. Microstructure–microhardness relations in parallel-fibered and lamellarbone. Bone 18: 417–428.

Ziv, V., Sabanay, I., Arad, T., Traub, W., Weiner, S. 1996b. Transitional structures in lamellar bone. Microscopy Research and Technique 33: 203–213.

Zocco, T.G., Schwartz, H. L. 1994. Microstructural analysis of bone of the sauropod dinosaur *Seismosaurus* by transmission electron microscopy. Palaeontology 37: 493-503.

Chapitre 6 Size and size distribution of apatite crystals in sauropod fossil bones

1 Introduction

Bone has a hierarchical structure composed of different structural units at different size scales (Weiner and Traub, 1992). These units work in concert to perform different functions and especially to impart good mechanical properties to the bone (Rho et al., 1998; Weiner and Wagner, 1998; Currey, 2002). At the nanometer level, bone is generally considered as a composite material formed by inorganic apatite crystallites embedded in an organic matrix (Weiner and Price, 1986; Wagner and Weiner, 1992; Weiner and Traub, 1992). Most of the studies at this level describe the fibrillar nature of the bone matrix and focus on determining the orientation and organization of the fibers (collagen fibrils and the associated mineral particles) (Sasaki et al., 1991; Wagner and Weiner, 1992; Akiva et al., 1998; Sasaki and Sudoh, 1997). These geometrical parameters have been determined by X-ray or neutron small angle scattering (Fratzl et al., 1996, 1997) or texture analysis (Wenk and Heidelbach, 1999), and have also been characterized for sauropod bones (Pyzalla et al., 2006).

Mechanical models of bone (Ji and Gao, 2004, 2006; Dubey and Tomar, 2009) consider the structure at the nanometer level as a composite material made up of mineral particles embedded in a collagen matrix. A relevant question is whether the size and shape of apatite particles in bone is optimal with regard to mechanical properties. In metal–matrix composites for example, load transfer from the matrix to the reinforcing phase is known to be more effective for particles that have a higher aspect ratio (the ratio between the longer and shorter dimension of the particle) and are aligned with their longest axis parallel to the external load (Christman et al., 1989). Because of their gigantism (Sander et al., 2010) and the high load that their bones were exposed to, sauropods constitute an interesting model to address this effect. However, dealing with fossil bones, the problem of preservation state of the crystallites also needs to be considered. It is generally recognized that the microstructure of fossil bones is quite well preserved. However, only a few studies deal with the preservation of fossil bone at the nanostructure level. It was suggested (Tuross et al., 1989; Reiche et al., 2002; Trueman et al., 2004) that the apatite crystallite size in fossil bone increases during diagenesis, especially in the direction of the longest axis of the crystallite, and that fossil bone crystallites show a more needle like morphology resulting from the dissolution and recrystallization of the original platelet shape (Glimcher, 2006).

Less research has been carried out on the size of apatite crystallites in the cortical bone of recent animals, most of the data having been obtained for lamellar bone (Landis et al., 1993; Rho et al., 1998). Less attention (Handschin and Stern, 1995; Kuhn et al., 2008) has also been given to the systematic study of crystallite size at different growth stages of the same animal. Besides diagenetic effects, ontogenetic change could also explain the controversial interpretation of crystallite sizes found in the literature (Kimet al., 1996;Glimcher, 1998; Hassenkamet al., 2004).

Direct and indirect methods of size determination show a large discrepancy, and sample preparation usually introduces artifacts as well. For the last 20 years, several methods have been used to quantify bone crystallite size and shape. These are: atomic force microscopy (AFM) (Eppell et al., 2001; Tong et al., 2003; Hassenkam et al., 2004), small angle X-ray scattering (SAXS) (Fratzl et al., 1996, 1997; Rinnerthaler et al., 1999; Paris et al., 2000; Fratzl, 2003), X-ray diffraction (XRD) (Jackson et al., 1978; Ziv and Weiner, 1994) and transmission electron microscopy (TEM) (Ziv and Weiner, 1994; Kim et al., 1996). In this study we use the last two methods with the aim of showing that their combination provides a reliable basis for crystallite size quantification in spite of the experimental difficulties involved (Ziv and Weiner, 1994). The effect of diagenesis on the nanostructure of the bones is also discussed.

2 Experimental details

2.1 Material

The specimens studied are listed in Table 1 and include sauropod, subfossil mammal and recent mammal bones. The sauropod material was obtained by core drilling at a prescribed location in the middle of the shaft of the large long bones humerus and femur (for details see Sander, 2000; Klein and Sander, 2008). The Apatosaurus series originates from different localities in the Morrison Formation (Late Jurassic, North America). The indeterminate sauropod samples are from the Tendaguru bed (Late Jurassic, Tanzania). This material was formerly assigned to Barosaurus africanus (Janensch, 1961; Sander, 2000) and probably belongs to diplodocid sauropods (Remes, 2009).

The investigations were carried out on the fibrolamellar bone that formed the principal part of both sauropods and mammals' cortical bone (Enlow and Brown, 1956, 1957; Ricqlès de, 1980; Francillon-Vieillot et al., 1990; Klein and Sander, 2008). The results obtained were compared with literature data.

Table 6.1 Taxa studied, bone type, histological study number, bone length, locality

Taxon	Bone	Specimen no.	Bone length (cm)	Adult length [%]	Locality
***Apatosarus* sp.** [1]					Morrison Formation, USA
Apatosaurus sp.	Humerus	OMNH 1278	25.8	22	Kenton Quarry
Apatosaurus sp.	Femur	OMNH 1279	34	19	Kenton Quarry
Apatosaurus sp.	Femur	BYU 681-11940	133	74	Cactus Park
Apatosaurus sp.	Femur	BYU 601-17328	158	88	BYU locality 601
Apatosaurus sp.	Femur	SMA 0014	164	91	SMA Howe Ranch
Apatosaurus sp.	Femur	OMNH 4020	180	100	Kenton Quarry
Sauropoda indet.[2] previously assigned to *Barosaurus africanus* (see Remes 2009)					Tendaguru, Africa
Sauropoda indet.	Humerus	MFN Ba IX 94	64	62	Upper Transitional Sands
Sauropoda indet.	Humerus	MFN Ba XI a 7	80	78	Upper Transitional Sands
Sauropoda indet.	Femur	MFN Ba Ki 4	120	79	Upper Transitional Sands
Sauropoda indet.	Tibia	MFN Ba Ki 5	84	86	Upper Transitional Sands
Bison priscus	Tibia	FKBiRs			
Equus sp. [3]		MQB 48516			Rhein-Herne Ship channel, Germany

[1] The histology of this material was described in Klein and Sander (2008)
[2] The histology of this material was described in Sander (2000)
[3] The histology of this material was described in Sander and Andrassy (2006)
Collections acronyms: BYU = Museum of Paleontology of Brigham Young University, Provo, Utah, USA, MFN = Museum für Naturkunde, Berlin, Germany; MQB = Museum Quadrat, Bottrop, Germany; OMNH = Sam Noble Oklahoma Museum of Natural History, Norman, Oklahoma, USA, SMA = Sauriermuseum Aathal, Aathal, Switzerland.

2.2 X-ray diffraction

Bulk and powder bone samples were analyzed in a Bruker D8 diffractometer equipped with a graphite monochromator and tuned for Co–Kαradiation. The powder samples were prepared by grinding up bulk bone material using a mortar and pestle (Bish and Post, 1989; Chipera and Bish, 1991). X-ray diffractogramswere recorded over the 2θ range of 20°–80° with a step size of 0.075°. All spectrawere checked for the presence of contaminating minerals. The full width at half maximum (FWHM) of principal reflections corresponding to apatite crystalliteswere measured after background subtraction. Considering that strain broadening is negligible, the crystallite size was determined fromthe Scherrer equation (Scherrer, 1918; Klug and Alexander, 1974; Cullity, 1978):

$$\varepsilon = \lambda / (FWHM \cdot \cos\theta)$$

where ε is the apparent crystallite size, λ is the wavelength of the X-rays, and θ is the Bragg angle. True crystallite size "*t*" is obtained through the shape factor *K* (known also as the Scherrer constant):

$$t = K\varepsilon$$

through the shape factor *K* (known also as the Scherrer constant) that can vary between approximately 0.9 to 2.2, depending on the shape of the crystallite (Klug and Alexander, 1974). For the calculation of the real crystallite size from peak broadening, the choice of the *K* factor is crucial. *K* = 0.9 was commonly used in studies of bone crystallites even though this value applies to cube-shaped crystals (Chipera and Bish, 1991; Ziv and Weiner, 1994). The combined XRD and TEM investigations of Ziv and Weiner (1994) on rat bones show, however, that *K* = 2 leads to a better agreement of crystallite length values determined by the two methods.

The broadening of X-ray diffraction peaks is generally related to both crystal size and internal lattice imperfection induced by structural disorder or lattice defects (Chipera and Bish, 1991). The broader the peak, the smaller and/or more strained is the crystal. The main difference between peak broadening induced by small crystallite size and lattice strain resides in their diffraction order dependency (Warren and Averbach, 1950). A strain-free spherical crystal for example leads to peak widths proportional to cos(θ) (i.e. decreasing with the diffraction angle θ). In contrast, a large crystal containing lattice defects leads to a diffraction pattern where the FWHM of the peaks increases with diffraction angle. The diffraction patterns of powder and bulk samples show some differences due to anisotropic shape of the crystallites and their preferred orientation in the bone (Sasaki and Sudoh, 1997). Surprisingly, powder specimens revealed enhanced microstrain effects probably introduced during powder preparation, a conclusion also obtained by Danilchenko et al. (2002) (Figure 6.1). All peaks corresponding to apatite particles were indexed, but only four of them, the 002, 004, 300, and 310 reflections, were considered for crystallite size evaluations. The 002 and 004 reflections yield the crystallite length along the crystallographic c-axis, while the 300 and 310 reflections allow the determination of crystal width perpendicular to the c-axis. A small microstrain broadening component in bulk specimens is indicated by the systematic difference between the crystallite lengths determined from the 002 reflection compared to 004 reflections (see Figure 6.1 and 6.3). However, the difference is small except for the powder specimens. A similar conclusion is given by the Williamson–Hall plot of the half-widths (Williamson and Hall, 1953) showing only a scatter in the data and no increasing trend of FWHM as a function of the magnitude of the diffraction vector. For these reasons strain broadening of bulk specimens was neglected. The FWHM values considered for crystal size analysis were corrected for instrumental broadening as suggested by Klug and Alexander (1974). The error of crystallite sizes was obtained from the error of the FWHM provided by the curve fitting program Peakfit (Peakfit, 3.0, Jandel Scientific Software, San Rafael, CA).

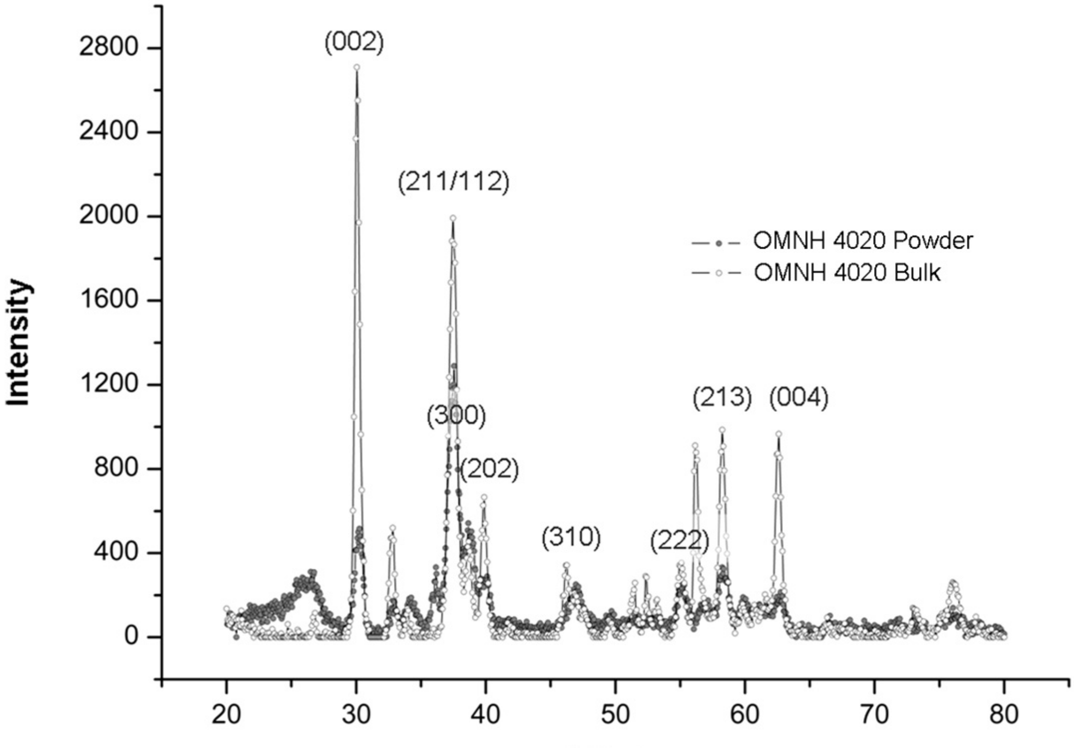

Figure 6.1. Diffractograms of the powder and bulk OMNH 4020 samples.

2.3 TEM

Longitudinal sections of primary cortical bone tissue were carefully cut parallel to the long axis of sauropod long bones and were analyzed by TEM. Samples were all prepared with the same orientation, parallel to the surface of the cortex. The specimens were prepared by FIB using a Jeol Jem-9320 system operating at 30 kV. Prior to ion beam cutting, the specimens were mechanically polished and sputter coated in gold. The areas selected for study were free of cracks or openings in the bone, indicators of a possible diagenetic contamination (Zocco and Schwartz, 1994; Hubert et al., 1996; Reiche et al., 2002). Additionally, one TEM specimen was prepared from the lamellar bone of a secondary osteon (sample MFN Ba Ki 5). The FIB technique is well known in materials science, but its application for biomaterial sample preparation is relatively new (Nalla et al., 2005; Porter et al., 2005; Jantou et al., 2009). A clear advantage of FIB over ultramicrotomy is that the preliminary chemical preparation (i.e. dehydration, embedding and section flotation) is eliminated, so the partial mineral loss due to dissolution (Ziv and Weiner, 1994; Eppell et al., 2001) or growth of crystallites is avoided. The TEM analysis was carried out using a Jeol Jem-2200FS microscope operating at 200 kV. Images were recorded with a Gatan CCD camera and further processed using Gatan Digital Micrograph software (Version 3.8.2).

The apatite crystallites selected for quantification of their shape were those fulfilling the criteria specified by Ziv and Weiner (1994), namely: separated crystallites, for which the entire periphery was visible, or partially overlapping crystallites, where at least three edges were visible and maximum dimensions could be determined (Figure 6.2). For each bone studied, approximately 100 crystallites were measured. Mean values and standard deviations for these data were calculated, statistical differences were examined using a *t*-test and the corresponding P values reported ($P<0.05$ was considered statistically significant).

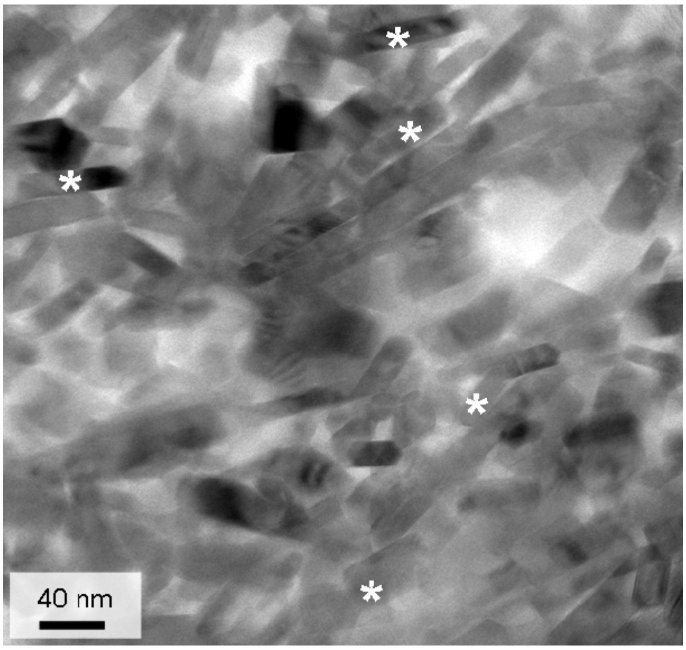

Figure 6.2. TEM Bright Field (BF) micrograph showing the crystals in the cortical bone of an *Apatosaurus* sample (OMNH 1278). The asterisks indicate crystals selected for measurement.

3 Results

3.1 X-Ray diffraction

The mineral apatite has a hexagonal crystallographic structure with the [001] crystallographic direction aligned along the length of the crystals (Jackson et al., 1978; Weiner et al., 1991; Landis et al., 1993; Landis, 1995; Ziv et al., 1996a,b). Based on this structure, crystallite length was determined from the 002 reflection, while the crystallite width was determined from the size corresponding to the 300 reflection.

Results of the X-ray diffraction in bulk samples indicate that crystallite size increases with geologic age and thus degree of fossilization (Figure 6.3). The apparent crystallite sizes exhibit the same trend for all samples with an increase from the 300 direction towards the 002 (Figure 6.3). In subfossil mammal bone (unknown age) (black and white pattern in the graph), only a small increase of apatite crystallite size compared to recent bone (Elk bone) is observed. For example crystallite size in recent bone is approximately 10–15 nm but 20–25 nm for the subfossil mammal bone. The crystallite size range of heated elk bone is similar to that in subfossil mammals. The 002 reflections have different crystal sizes for recent and subfossil bones. The heated elk bone does not have a bigger crystal size compared to non-heated bone and the subfossil horse and bison have crystal lengths smaller than recent bones (<15 nm). Ranging from 20 nm to 45 nm, dinosaur bones have larger crystallite lengths compared tosubfossil mammal bones. An increase in all crystallographic directions is observed for sauropod samples.

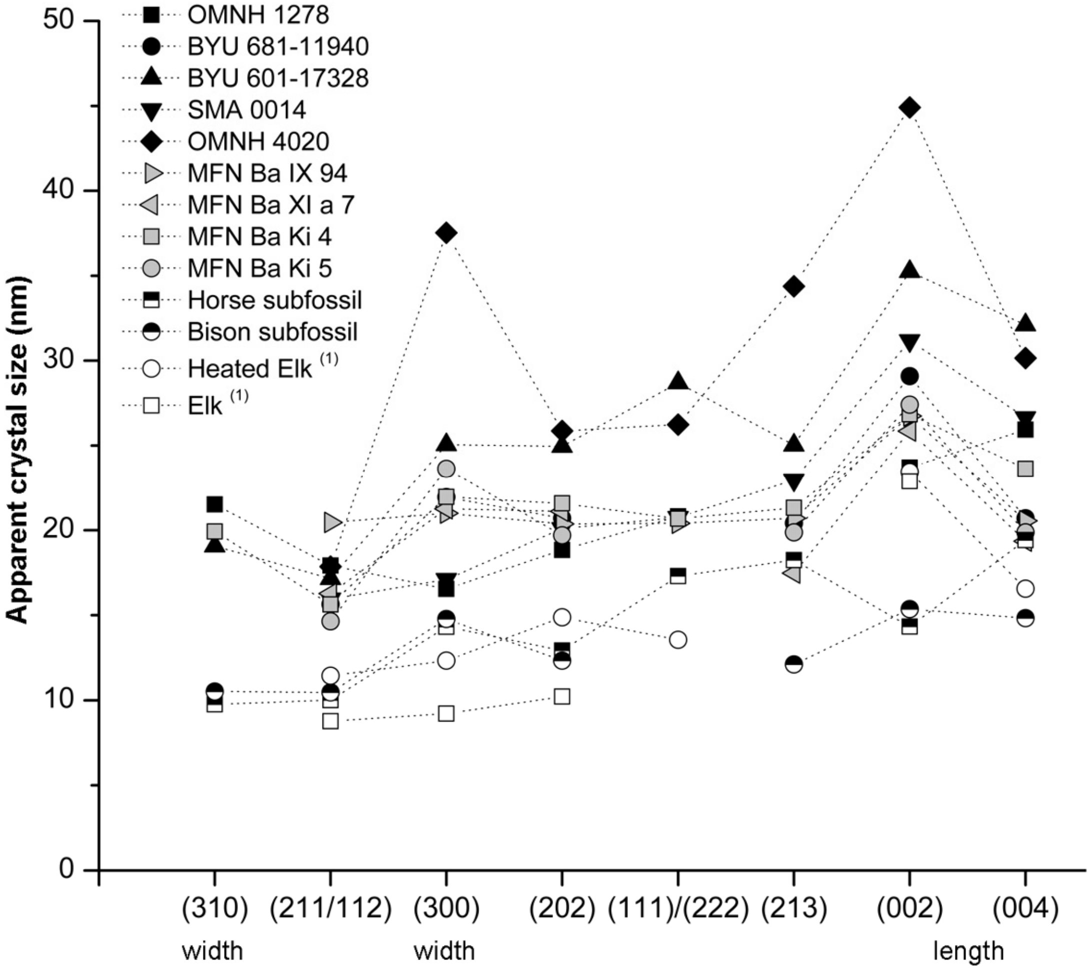

Figure 6.3. The apparent apatite crystallite size in fossil sauropod bone and subfossil bison and horse bone obtained by Eq. (1) from different Bragg reflections. This is compared to values for fresh elk and heated elk bone taken from Chipera and Bish (1991) indicated by $^{(1)}$ in the figure. The dotted lines do not represent any physical or crystallographic link. Note that crystallite dimensions increase with degree of fossilization. See Table 1 for identity of the specimens.

Relatively small differences were found among the indeterminate sauropod specimens from Tendaguru (gray color pattern in Figure 6.3). These samples all come from the same bed (Upper Transitional Sands) and correspond to the same approximate ontogenetic stage (Table 6.1). The results indicate that either diagenesis had exactly the same effect on these samples, or the effect is small and the original state of the crystallites is quite well preserved. In contrast, two other samples originating from the same locality (OMNH 1278 and OMNH 4020 from Kenton Quarry; Table 1), have a larger difference in crystallite size in both the (002) and (300) crystallographic directions. The smaller crystallites occur in sample OMNH

1278, which is from a juvenile because it shows histologic ontogenetic stage (HOS) 4 of Klein and Sander (2008) whereas the bulk sample OMNH4020 is from a very large adult of HOS 13 and has larger crystallites. This is suggestive of an increase in crystallite size with individual growth (Tuross et al., 1989; Ziv and Weiner, 1994; Handschin and Stern, 1995; Boskey, 2003). In Figure 6.4 apatite crystallite size determined from the 002 and 300 reflections as a function of sauropod bone length was plotted. No significant increase in crystallite size is observed. The largest apatite crystallites were found in the largest sauropod individual, Apatosaurus OMNH 4020 (Table 1), which biases the trend.

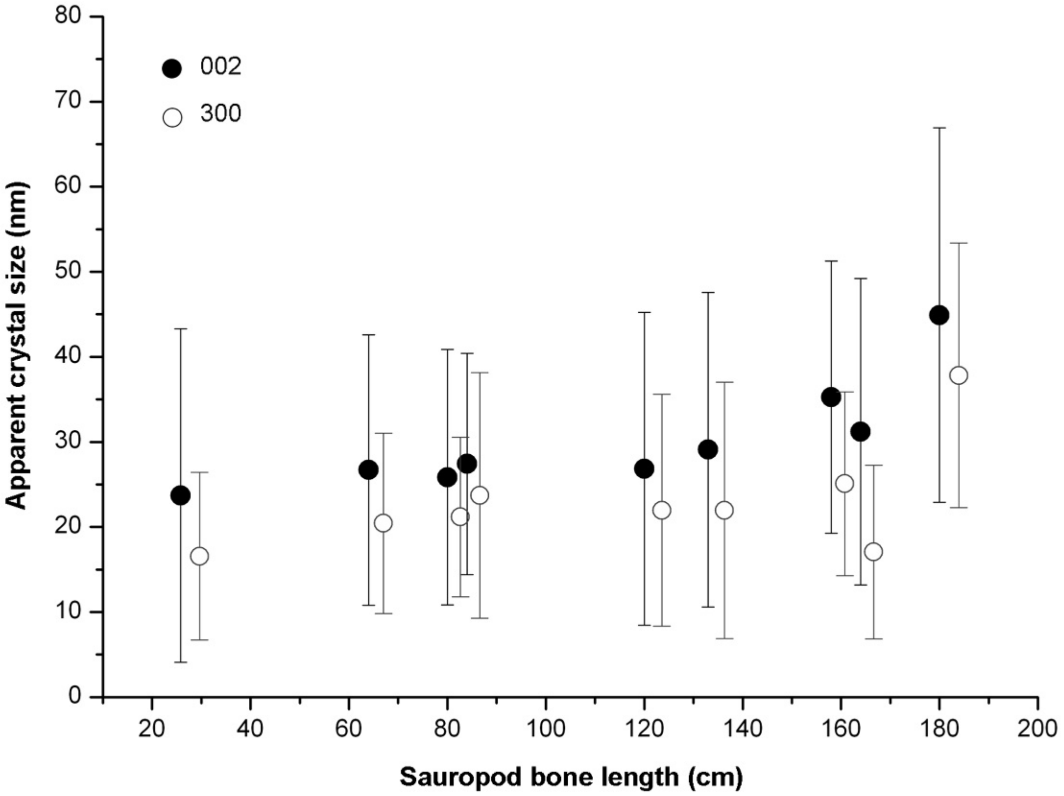

Figure 6.4. Apparent crystallite dimensions evaluated from the 300 and 002 reflections versus sauropod bone length. The samples plotted correspond to the *Apatosaurus* sp. and Sauropoda indet. specimens listed in Table 1. The 300 reflections correspond to the width and the 002 reflection represent the length of the crystallite.

3.2 TEM

The TEM investigations focused on five sauropod samples: two juvenile Apatosaurus specimen OMNH 1278 and OMNH 1279, Apatosaurus specimen BYU 601-17328, and the two Sauropoda indet. specimens MFN Ba Ki 4 and MFN Ba Ki 5. The size distributions of crystallites for these samples are presented in Figure.6.5, Figure 6.7, Tables 6.2 and 6.3.

Length and width of the crystallites

The distributions (Figure 6.5a to d) of crystallite length in sauropod bones have modal and average values ranging from 60 nm through 100 nm, which are larger than values characteristic of recent mammal bone. Most specimens in Figure 6.5f to h are characterized by a relatively narrow distribution of crystallite width, with a mode of around 10–15 nm. The exception is the juvenile Apatosaurus OMNH 1278 (Figure 6.5e), which shows a large spread of values from 10–50 nm. The sample MFN Ba Ki 4 also has a small fraction of crystallites with widths superior to 40 nm. In totality, however, only a small number of crystallites with widths in the 40–50 nm range have been observed (5–10%), which might be an indication that the crystallites are wellpreserved. Figure 6.5e to h may also suggest that crystallite shape in the juvenile Apatosaurus OMNH 1278 is different (a wide distribution of width/thickness values would suggest platelet-shaped crystallites, too) from crystallite shape in mature Apatosaurus bones (narrow distribution, characteristic for needle shaped crystallites). Due to overlapping of crystallites, tilting experiments of the sample in the TEM could not answer this question, which requires further investigation.

Table 6.2 summarizes the TEM results. Statistical analysis (ANOVA, significance level $p<0.05$) indicates that the average crystallite lengths and widths in the four analyzed samples are different. Exceptions include samples BUY 601-17328 and MFN Ba Ki 5 with almost identical width distributions (Figure 6.5f and h), and those of MFN Ba Ki 4 and MFN Ba Ki 5 for the aspect ratio.

Table 6.2. Mean length, width and aspect ratio (l/w) of apatite crystallites in sauropod bones as measured in TEM images.

Specimen	Length [nm]	Width [nm]	Aspect ratio	n (number of crystallites)
OMNH 1278	88.31 (±25.07)	24.32 (±11.15)	4.14 (±2.18)	120
BUY 601-17328	59.33 (±14.9)	12.24 (±3.26)	5.18 (±1.9)	150
MFN Ba Ki 5	71.06 (±27.53)	12.57(±4.77)	6.11 (±2.79)	70
MFN BAKi 5 (O^{II})*	78.85 (±22.36)	18.06(±10.16)	5.28 (±2.75)	180
MFN Ba Ki 4	96.55 (±26.25)	18.26 (±14.42)	7.07 (±3.39)	80

Collections acronyms: BYU = Museum of Paleontology of Brigham Young University, Provo, Utah, USA, MFN = Museum für Naturkunde, Berlin, Germany; OMNH = Sam Noble Oklahoma Museum of Natural History, Norman, Oklahoma, USA.

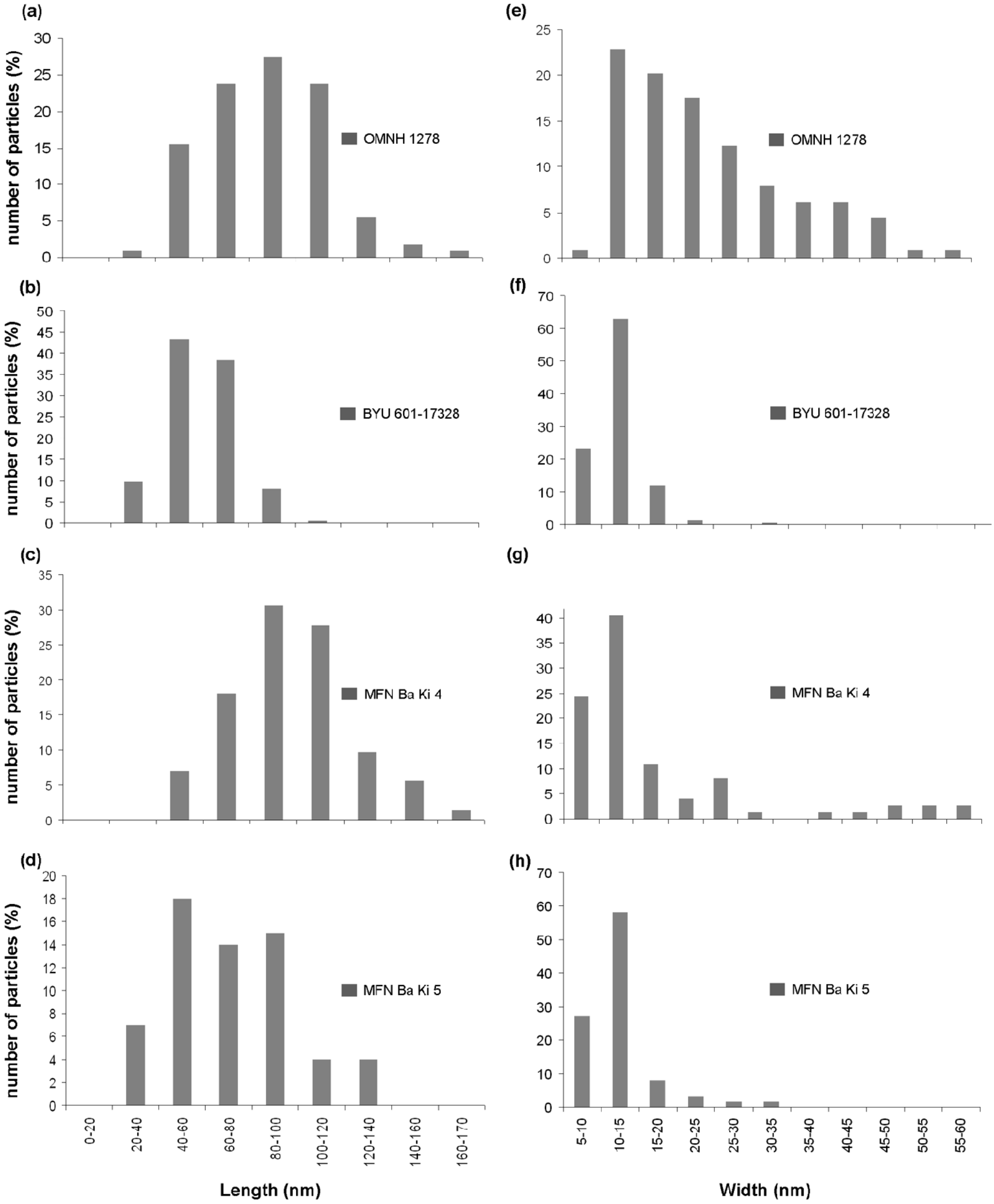

Figure 6.5. (a) to (d) Histograms of crystals length; (e) to (h) Histograms of crystallite width for the sauropods sample studied. See Table 1 and Table 2 for identify of the specimens.

Two TEM samples were prepared from specific areas of specimen MFN Ba Ki 5, one from the primary bone (woven bone tissue) and another from a secondary osteon.We observed that the apatite crystallites are slightly bigger and more elongated in the secondary osteon, but only the results for the width/thickness are statistically different (two paired ANOVA, significance level $p<0.05$). The aspect ratio of crystals in secondary osteons is smaller than that inwoven bone (statistically different in a two paired ANOVA test). This indicates that apatite crystallites in woven bone might be smaller than in mature lamellar bone.

Crystallites aspect ratio

The geometrical parameter describing the shape of apatite crystallites is the aspect ratio. Data obtained by TEM (Table 6.2 and Figure 6.6) indicate that the aspect ratio is much higher in sauropod bones compared to recent bones in which it is about 1.7 to 2 (Trueman et al., 2004). The ratio is different for all the samples, excepting two sauropods MFN Ba Ki 4 and MFN Ba Ki 5.

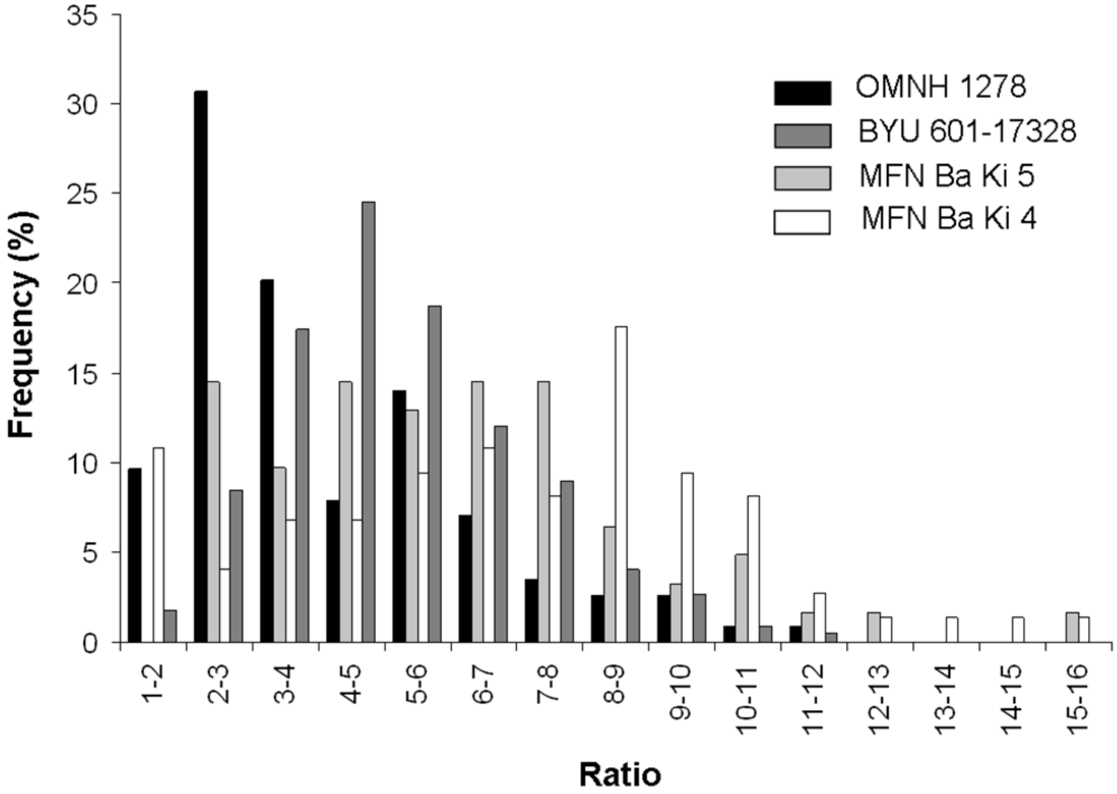

Figure 6.6. Histogram of the aspect ratio of apatite crystallites in four sauropod specimens.

The apatite crystallites in adult Apatosaurus and Barosaurus specimens have higher aspect ratios compared to juvenile Apatosaurus (OMNH 1278, OMNH 1279). For the two other Barosaurus samples a different trend is observed: the sample MFN Ba Ki 5 (a tibia 84 cm in length) corresponds to a bone of 86% adult length, hence to a bigger individual than the sample MFN Ba Ki 4 (a femur 120 cm in length, 79%adult length). Longer bones have crystallites with larger mean aspect ratio: approximately 6 in MFN Ba Ki 5 and of about 7 in MFN Ba Ki 4. This difference does not seem to be due to ontogenetic stage but related to absolute bone length.

Crystallite size through the cortex

To test the effect of diagenesis on crystallite size in fossil bone, samples through the cortex of OMNH 1279 specimen were prepared. Samples A, B, C were respectively taken from the periosteal to the endosteal part of the cortex bone. This allows testing if crystallite size in woven bone is changing from deeper and older layers compared to superficial and younger layers of bone tissue.

The results are presented in Table 6.3 and graphs 6.7a and 6.7b. Crystallite length distribution is unimodal with an average value around 60-80 nm (Figure 6.7a). Crystallite width has mean values around 20 nm for all the samples; however, its distribution has a large spread of up to 40 nm (Figure 6.7b). This large spread was already observed for the younger humerus sample OMNH 1278 (Table 6.2 and Figure 6.5e). Statistical analysis indicates that crystallite lengths are different for the three samples. Crystallite widths and aspect ratios are identical for samples A and C (Figure 6.7b), but different for sample B. Both periosteal and endosteal parts of the cortex seem to be very similar, while sample B from the middle part has larger crystals (in both length and width dimensions).

Table 6.3. Mean length, width and aspect ratio (l/w) of apatite crystallites in sauropod sample OMNH 1279, as measured in TEM pictures. Three TEM samples were prepared from the border periosteal of the cortex (sample A), from the middle (sample B) and from the endosteal part (sample C)

Specimen	Length [nm]	Width [nm]	Aspect ratio	n (number of crystallites)
Sample A	63.93 (±23.5)	20.20(±13.49)	3.9 (±2.05)	550
Sample B	89.52 (±28.22)	23.37 (±14.42)	4.82 (±2.48)	510
Sample C	69.38 (±26.56)	19.92 (±10.68)	4.06 (±1.96)	657

Collections acronyms: OMNH = Sam Noble Oklahoma Museum of Natural History, Norman, Oklahoma, USA.

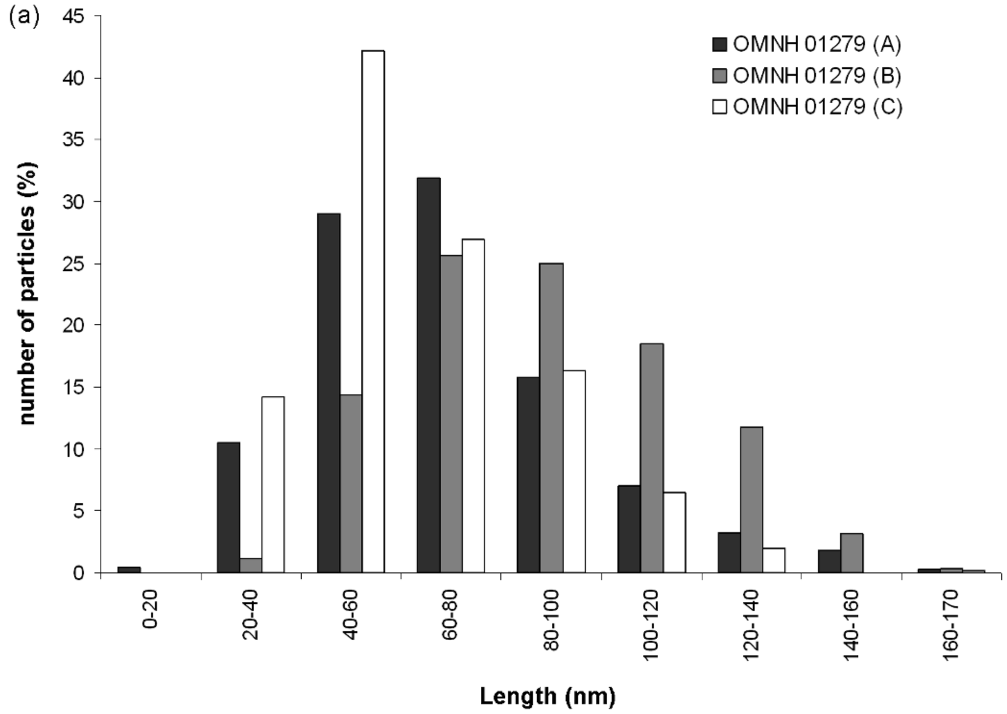

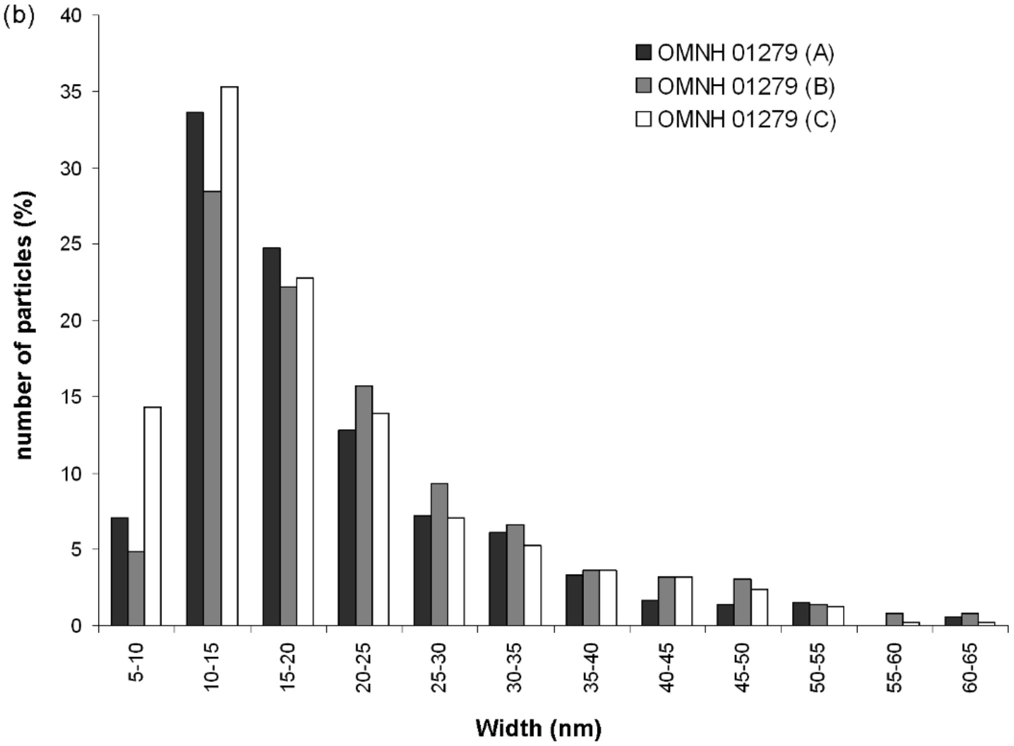

Figure 6.7: Histograms of crystal length (a) and width (b) for the three different samples prepared in the sauropod OMNH 1279. See Table 3 and text for more details.

4 Discussion

4.1 Comparison of XRD and TEM results

The XRD and TEM techniques used to characterize crystallite dimension yield different results. This requires comments about the possible sources of discrepancy between the results obtained

(i) Counting of crystallites on TEM micrographs was done manually for the most contrasted and isolated particles, i.e. crystallites (in which the periphery is well-defined). Due to the small number of particles counted (~100 particles/sample) it is expected that TEM results have larger errors than XRD.

(ii) The FWHM of XRD peaks is proportional to crystallite volume, thus the mean size determined from XRD corresponds to the most representative particle in terms of volume (Chiche et al. 2008). The distribution of crystallite's linear size and their length/width has been determined using TEM. Therefore, the two evaluation methods do not necessarily give identical results.

(iii) The main uncertainty of the particle size determined by XRD is, however, related to the unknown shape of the crystallites and the associated Scherrer constant *K*. Based on TEM micrographs, it is obvious that crystallite shape is elongated and has a reasonably large aspect ratio. An acceptable agreement between crystallite lengths obtained by XRD and TEM is obtained if one chooses $K = 2$ for the 002 reflection (as proposed by Ziv and Weiner, 1994) (Figure 6.8a). However adiiferent $K = 1$ leads to a similar good agreement for the width/thickness determined from the 300 reflections (Figure 6.8b). This does not mean, however, that these *K* values are universally applicable for the characterization of apatite crystallites.

(iv) The broadening of XRD peaks, used to quantify the average crystallite size, can be influenced by other factors like instrumental profile (corrected in this study), different types of microstrain, temperature factors, etc., that can lead to an underestimation of crystallite size.

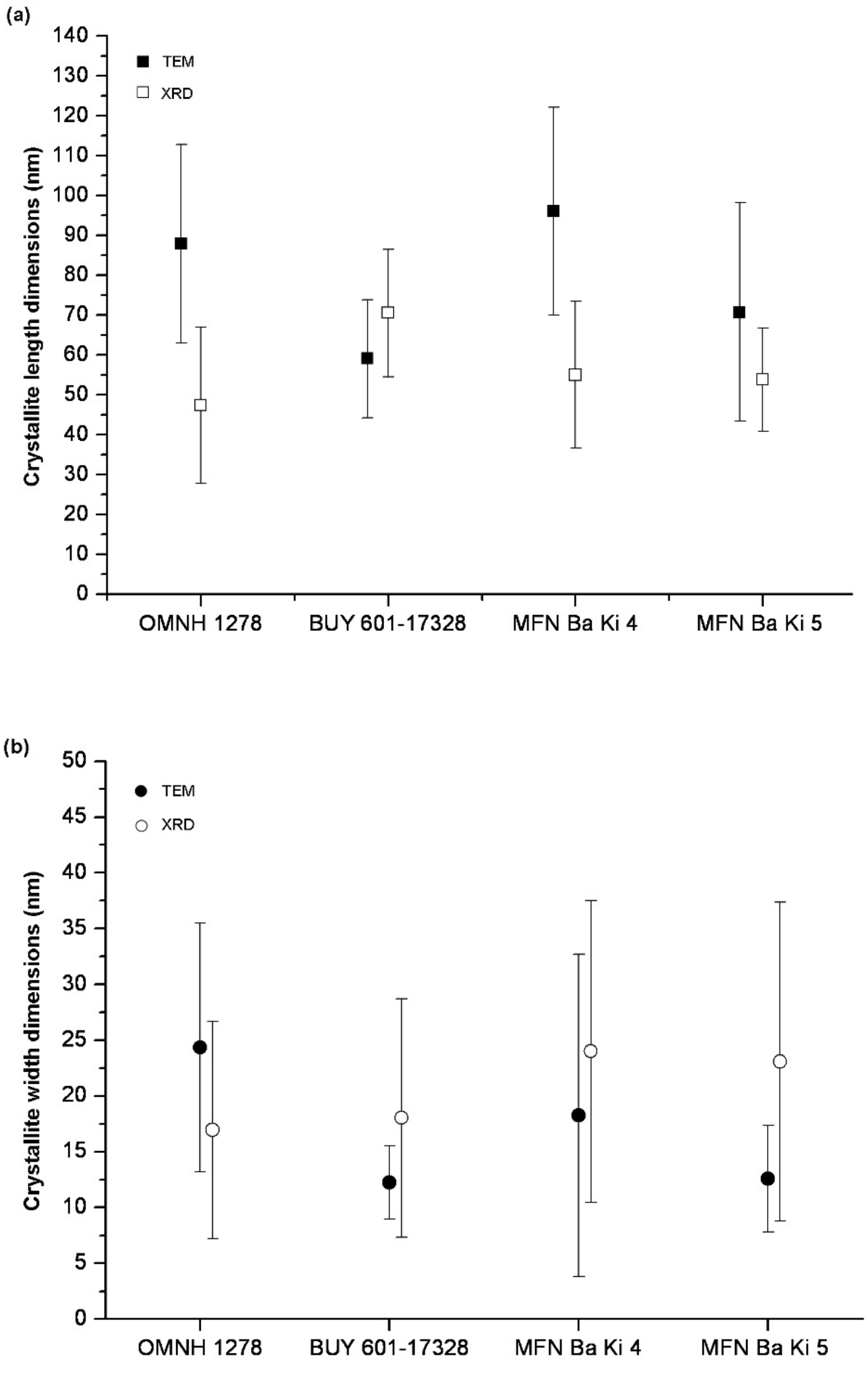

Figure 6.8. Comparison of the mean crystallite length (a) and mean width/thickness (b) obtained by XRD and TEM techniques.

The two methods used in this work thus mainly have a complementary character, and no conclusions should be drawn from their comparison. Both techniques have advantages and disadvantages. X-ray diffraction and the corresponding Scherrer equation give an average apparent crystallite size characteristic for a relatively large bone volume. Determination of the true size, however, is impeded by the unknown shape factor K. TEM, in contrast, allows the precise determination of the size of individual crystallites, but only on a local scale. The limited number of measurements permitted by TEM due to the time-consuming sample preparation leads to a relatively high uncertainty in the results. Since the TEM image shows a projection of the crystallites on a plane perpendicular to the electron beam, the crystallite size obtained by this method should be considered as a minimum value. The relative orientation of crystallites with regard to the direction of the incident electron beam can, therefore, influence the mean crystal size and size distribution. Since all the analyzed samples have been prepared in exactly the same way, (longitudinal sections parallel to the bone cortex limit) and the specimens were tilted in the TEM by about ±20° for evaluations, we assume that the results are not influenced by eventual minor differences in orientation of crystallites with regard to the incidence of the electron beam.

4.2 Crystal size in fossil and recent bone

Our XRD and TEM results show that the apatite crystals in fossil bone are larger than in recent mammal bone. The length distribution of crystallites in sauropod fossils has a mode of around 60-100 nm, whereas bones of mature (4-8 year) bovines have a mean length of about 27.3 nm and 15.8 nm width (Kim et al., 1995; Eppel et al., 2001) and of about 32 nm long in rabbit, ox, and human bones (Jackson et al., 1978). However, it is not apparent from their papers if they analyze the crystallite size of primary or secondary bone. Landis et al. (1995) also found large crystallites in calcifying tendon by high-voltage electron microscopic tomography with 170 nm in length, 30-45 nm in width and 4-6 nm in thickness.

A general increase in size of each crystallographic direction for fossil bone was already mentionned by Tuross et al. (1989) and Trueman et al. (2004). Our results are in agreement with a crystallite size for Diplodocus hallorum (previously known as Seismosaurus hallorum, Lucas et al., 2004) of 35.2 nm in the (300) direction and 63.1 nm in the (002) direction obtained by Chipera and Bish (1991). Chipera and Bish also show that heating modern bone specimens at 400 °C for 35 days to simulate the diagenetic processes results in a small increase of the crystallite size along {002} and {300} crystallographic directions (Figure 6.3). Bacon et al. (1979) investigated the effects of short term heating, but found no significant crystallite growth. Recent publications have also emphasized the effect of low temperature annealing, which has the same consequence on apatite crystallite size as diagenesis (Hiller et al., 2003; Lebon et al., 2008; Lebon et al., 2010). They indicate, however, a fast alteration of the crystallites when the annealing temperature rises above 500 °C.

According to Trueman et al. (2004) the mean crystallite length in recent mammal bones is around 40 nm and is characterized by a wide range from 10 nm to 100 nm. They attributed the higher values to a post mortem increase, as already established in other studies (Tuross et al., 1989; Zocco and Schwartz, 1994; Reiche et al., 2002). The crystallite size in subfossil mammals studied in this work also falls into this range but they have smaller lengths compared to elk and heated elk bone (Chipera and Bish, 1991). However, crystallite length in subfossil mammal bone can reach more than 100 nm in special geochemical environment, such as waterlogged areas (Reiche et al., 2002). The authors provide two explanations of the diagenesis processes: one possibility is the wash-out of the small crystallites and the second is the dissolution and re-precipitation of the small crystallites yielding an overall increase in average crystallite size.

A possible variation of crystal size due to diagenesis has been analyzed. The results (Table 6.3 and Figure 6.7) suggest that crystallite size distributions are similar through the cortex. Statistical analyses have confirmed that crystallite size is different throughout the bone cortex. The sample B, located in the middle part of the cortex has larger crystals. Crystallites of samples A and C are not different in their width. The results are difficult to interpret. It seems that the width of crystals is the same in newer periosteal bone and deeper older bone. The length of the crystals is larger in older bone in agreement with the general observations for diagenesis (see discussion in Section 4.3 below). However, the middle part of the cortex has much longer crystals than the extremes of the cortex, which might be due to diagenesis.

TEM investigations by Eppell et al. (2001) show a bimodal distribution of crystallite sizes, which they have attributed to artifacts produced during sample preparation (i.e. chemical alteration, reaction of the mineral particles with aqueous solution, etc.). Considering the fact that the distribution of the crystal sizes obtained in present TEM investigations for sauropod bones led to unimodal distributions, it is likely that the preparation of TEM lamellae by FIB reduces the risk of preparation artifacts. This is in agreement with conclusions of Volkert et al. (2004) and Nalla et al. (2005), stating that the FIB technique better preserves the original structure of the specimen compared to conventional preparation. They mention, however, that electron beam irradiation causes some damage to the structure of the bone. Hong et al. (2009) have shown that mineral crystallites of lamellar bone become coarsened after electron irradiation (continuous diffraction rings became spotty and the contrast between rings and background become sharper). Recently Reyes-Gaya et al. (2009) have also shown that longer interaction with the electron beam can damage the crystal structure of hydroxyapatite.

4.3 Crystal size and biomechanical aspects of the bone

The primary aim of our study was to determine if mineral crystallite size is related to mechanical properties of sauropod bone. Contrary to the results for recent animals (Bonar et al., 1983; Bertazzo et al., 2006; Roberts et al., 1992) the XRD and TEM results (Figure 6.4 and Table 6.2) do not show any systematic increase of the width and the length through ontogenetic stages of sauropod bone. It must be noted, however, that the sample, which shows the largest crystal dimensions, OMNH 4020, corresponds to an old Apatosaurus with the cortical bone consisting only of secondary osteons. This may reflect the presence of larger crystals in secondary osteons (as previously observed in Su et al., 2003), and observed for the sample MFN Ba Ki 5 (Table 6.2). We must also admit that the Kenton Quarry specimens and in particular OMNH 4020 have been diagenetically affected by a postmortem fungal attack, which may alter the original nanostructure of the bone. These hypotheses could also explain the larger crystallite dimensions of this sample and the increase of crystal size with bone size observed in this study.

Bones from young, recent animals usually have a broader distribution of crystallite widths (Tong et al., 2003), sometimes even a bimodal one. Based on the higher rate of remodeling, bone of young animals contains a mixture of new and old crystals. At full maturity the bone will present thinner crystallites (Eppell et al., 2001; Tong et al., 2003). The newly deposited crystallites can change the mechanical properties at the maximal content of mineral phase. Our results (Figure 6.5, Figure 6.7, Tables 6.2, and 6.3) show that the average crystallite size in young sauropods (humerus OMNH 1278 and femur OMNH1279) has a much wider distribution than that in the femora of adult sauropods, similar to the case for recent animals. This large spread of crystallite sizes also coincides with observations of Hubert et al. (1996) for Apatosaurus bone and Zocco and Schwartz (1994), who mention that larger crystallites (i.e. broader distribution) occurs along crack areas and openings in the bone. For TEM investigations such areas with cracks and visible diagenetic material have been avoided. The much broader distribution of crystallite width/thickness in young specimens should, therefore, be related to the age of the specimen. Evidently, diagenetic effects cannot be neglected (the two samples are coming from the same locality), but in this case it is difficult to explain why diagenesis is not similar for adult and young specimens.

As stated by Boskey (2003, 2007) a mixture of larger and smaller crystallites usually provides a more efficient response to load. Boskey based this hypothesis on the observation of older and osteoporotic animal models, both of which tend to fracture more easily. Their crystallite size distribution is narrower and the mean is shifted towards larger values. Similar trends were demonstrated by XRD, TEM and AFM for bone crystallites isolated from mammals of different ages (Bonar et al., 1983; Roberts et al., 1992; Handschin and Stern, 1995; Tong et al., 2003; Kuhn et al., 2008). It is known that fracture toughness of the bone is not only influenced by crystallite size but also by its density. Low bone density reduces the fracture load due to a smaller concentration of the reinforcing phase in the collagen matrix. On the other hand, larger particles contain more defects (e.g. flows), therefore being more prone to fracture. It is, however, difficult in the case of bone to predict which effect is primordial. For equal concentration of minerals a wider size distribution has better fracture properties.

Apatite crystallites of sauropod bones have a high aspect ratio with a mean value around 5. This is higher than the aspect ratio of crystallites in recent mammals and Turkey tendons (Heywood et al., 1990) (about 2) as well as in subfossil mammals (about 3–5; Trueman et al., 2004). This result agrees with the hypothesis that sauropod bones might have a higher load-bearing capacity due to the higher aspect ratio of the consisting mineral particles. The aspect ratios of the two juvenile sauropods OMNH 1278 and OMNH 1279 (Tables 6.2 and 6.3) are not different. However, the aspect ratio does not correlate with the cortex bone length or even length of the adult (provided by the study of Klein and Sander, 2008). For example, according to this hypothesis sample BYU 601-17328 (at 88% maximal bone length) should have higher aspect ratio. But the highest aspect ratio is obtained for the Sauropoda indet. MFN Ba Ki 4 (mean aspect ratio of 7.07) (at 79% maximal bone length) followed by the femur MFN Ba Ki 5 (at 86% maximal bone length). This emphasizes that the higher aspect ratio can be the result of diagenesis impeding an unequivocal conclusion.

5 Conclusions

Based on XRD and TEM investigations of sauropod bones the following conclusions regarding the size and shape of the apatite crystallites in dinosaur fossil bone can be drawn:

- Apatite crystallite size is larger in fossil sauropod bone than in subfossil and recent mammal bone.
- Crystal size in sauropod dinosaur bones does not correlate with age (bone length) as previously shown for recent animals.
- Crystallites in fossil sauropod bones have higher aspect ratio than crystallites in recent mammals and subfossil bones. For sauropods the aspect ratio appears to increase with bone length and/or ontogenetic age.
- The distribution of the crystallite's width/thickness is wider in young sauropod bones than in bones from adults, suggesting that younger animals had a mixture of recently formed and mature crystallites. However, this conclusion is based on a small data set and requires further confirmation.

References

Akiva, U., Wagner, H.D., Weiner, S. 1998. Modelling the three-dimensionnal elastic constants of parallel-fibred and lamellar bone. Journal of Materials Science 31, 1497–1509.

Bacon, G.E., Bacon, P.J., Griffiths, R.K. 1979. The orientation of apatite crystals in bone. Journal Applied of Crystallography 12: 99–103.

Bertazzo, S., Bertran, C.A., Camilli, J.A. 2006. Morphological characterization of femur and parietal bone mineral rats at different ages. Key engineering materials 309: 11–14.

Bish, D.L., Post, J.E. 1989. Modern powder diffraction. In: Ribbe, P.H. (Ed.), Reviews in Mineralogy, volume 20. The Mineralogical Society of America, Washington.

Bonar, L.C., Roufosse, A.H., Sabine, W.K., Grynpas, M.D., Glimcher, M.J. 1983. X-ray diffraction studies of the crystallinity of bone mineral in newly synthesized and density fractionated bone. Calcified Tissue International 35: 202–209.

Boskey, A. 2003. Bone mineral crystal size. Osteoporosis International 14 (5): 16–21.

Boskey, A., 2007. Mineralization of bones and teeth. Elements 3: 385–391.

Chiche, D., Digne, M., Revel, R., Chanéac, C., Jolivet, J.-P. 2008. Accurate determination of oxide nanoparticle size and shape based on X-ray powder pattern simulation: application to Boehmite AlOOH. Journal of Physical Chemistry C 112: 8524–8533.

Chipera, S.J., Bish, D.L. 1991. Applications of X-ray diffraction crystallite size/strain analysis to Seismosaurus dinosaur bone. Advances in X-ray Analysis 34: 473–482.

Christman, T., Needleman, A., Suresh, S. 1989. An experimental and numerical study of deformation in metal–ceramic composites. Acta Metallurgica 37 (11): 3029–3050.

Cullity, B.D. 1978. Elements of X-Ray Diffraction, 2nd ed. Addison-Wesley Publishing Company, Reading, MA.

Currey, J.D. 2002. Bones: Structures and Mechanics. Princeton University Press, Princeton, NJ.

Danilchenko, S.N., Kukharenko, O.G., Moseke, C., Protsenko, I., Yu., Sukhodub, L.F., Sulkio- Cleff, B. 2002. Determination of the bonemineral crystallite size and lattice strain from diffraction line broadening. Crystal Research and Technology. 37 (11): 1234–1240.

Dubey, D.K., Tomar, V. 2009. Role of hydroxyapatite crystal shape in nanoscale mechanical behavior of model tropocollagen–hydroxyapatite hard biomaterials. Materials Science and Engineering C 29: 2133–2140.

Enlow, D.H., Brown, S.O. 1956. A comparative histological study of fossil and recent bone tissues, Part 1. Texas Journal of Science 8: 405–443.

Enlow, D.H., Brown, S.O. 1957. A comparative histological study of fossil and recent bone tissues. Part 2 Texas Journal of Science 9: 186–214.

Eppell, S.J., Tong, W., Katz, J.L., Kuhn, L., Glimcher, M.J. 2001. Shape and size of isolated bone mineralites measured using atomic force microscopy. Journal of Orthopaedic Research 19: 1027–1034.

Francillon-Vieillot, H., de Buffrénil, V., Castanet, J., Géraudie, J., Meunier, F.J., Sire, J.Y., Zylberberg, L., de Ricqlès, A. 1990. Microstructure and mineralization of vertebrate skeletal tissues. In: Carter, J.G. (Ed.), Skeletal Biomineralization: Patterns, Processes and Evolutionary Trends, vol. 1. Van Nostrand Reinhold, New York, pp. 471–530.

Fratzl, P. 2003. Small angle scattering in material science—a short review of application in alloys, ceramics and composite material. Journal of Applied Crystallography 36: 397–404.

Fratzl, P., Schreiber, S., Boyde, A. 1996. Characterization of bone mineral crystals in the horse radius by small-angle X-ray scattering. Calcified Tissue International 58: 341–346.

Fratzl, P., Jakob, H.F., Rinnerthaler, S., Roschger, P., Klaushoffer, K. 1997. Position resolved small-angle X-ray scattering of complex biological materials. Journal of Applied Crystallography 30: 765–769.

Glimcher, M.J. 1998. The nature of the mineral phase in bone: biological and clinical implications. In: Avioli, L.V., Krane, S.M. (Eds.), Metabolic Bone Disease and Clinically Related Disorders. Academic Press, San Diego, pp. 23–50.

Glimcher, M.J. 2006. Bone: Nature of the calcium phosphate crystals and cellular, structural, and physical chemical mechanisms in their formation. In: Sahai, N., Schoonen, M.A.A. (Eds.), Medical Mineralogy and Geochemistry: Reviews in Mineralogy and Geochemistry, 64, pp. 223–282.

Handschin, R.G., Stern, W.B. 1995. X-ray diffraction studies on the lattice perfection of human bone apatite (Crista iliaca). Bone 16: 355–363.

Hassenkam, T., Fantner, G.E., Cutroni, J.A.,Weaver, J.C., Morse,D.E.,Hansma, P.K. 2004.High resolution AFM imaging of intact and fractured trabecular bone. Bone 35 (4): 4–10.

Heywood, B.R., Sparks, N.H.C., Shellis, R.P., Weiner, S., Mann, S. 1990. Ultrastructure and crystal growth of biogenic and synthetic apatites. Connective Tissue Research 25 (2): 103–119.

Hiller, J.C., Thompson, T.J.U., Evison, M.P., Chamberlain, A.T., Wess, T.J. 2003. Bone mineral change during experimental heating: an X-ray scattering investigation. Biomaterials 24: 5091–5097.

Hong, S.I., Hong, S.K., Wallace, J.M., Kohn, D.H. 2009. Ultrastructural observation of electron irradiation damage of lamellar bone. Journal of Materials Science: Materials in Medecine 20: 959–965.

Hubert, J.F., Panish, P.T., Chure, D.J., Prostak, K.S. 1996. Chemistry, microstructure, petrology, and diagenetic model of Jurassic dinosaur bones, Dinosaur National Monument, Utah. Journal of Sedimentary Research 66 (3), 531–547.

Jackson, S.A., Cartwright, A.G., Lewis, D. 1978. The morphology of bone mineral crystals. Calcified Tissue Research. 25: 217–222.

Janensch, W. 1961. Die Gliedmaßen und Gliedmaßengürtel der Sauropoden der Tendaguru-Schichten. Palaeontographica 3 (Supplement 7): 177–235 Band.

Jantou, V., Turmaine, M., West, G.D., Horton, M.A., McComb, D.W. 2009. Focused ion beam milling and ultramicrotomy of mineralised ivory dentine for analytical transmission electron microscopy. Micron 40: 495–501.

Ji, B., Gao, H. 2004. Mechanical properties of nanostructure of biological materials. Journal of the Mechanics and Physics of Solids 52: 1963–1990.

Ji, B., Gao, H. 2006. Elastic properties of nanocomposite structure of bone. Composites Science and Technology 66: 1212–1218.

Kim, H.-M., Rey, C., Glimcher, M.J. 1995. Isolation of calcium–phosphate crystals of bone by non-aqueous methods at low temperature. Journal of Bone Mineral Research 10: 1589–1601.

Kim, H.-M., Rey, C., Glimcher, M.J. 1996. X ray diffraction, electron microscopy and Fourier Transform Infrared Spectroscopy of apatite crystals isolated from chicken and bovine calcified cartilage. Calcified Tissue International 59: 58–63.

Klein, N., Sander, P.M. 2008. Ontogenetic stages in the long bone histology of sauropod dinosaurs. Paleobiology 34 (2): 247–263.

Klug, H.P., Alexander, L.E. 1974. X-Ray Diffraction Procedures for Polycrystallite and Amorphous Materials, second ed. John Wiley and Sons, New York.

Kuhn, L.T., Grynpas, M.D., Rey, C.C., Wu, Y., Ackerman, J.L., Glimcher, M.J. 2008. A comparison of the physical and chemical differences between cancellous and cortical bone mineral at two ages. Calcified Tissue International 83: 146–154.

Landis, W.J. 1995. The strength of a calcified tissue depends in part on the molecular structure and organization of its constituent mineral crystals in their organic matrix. Bone 16 (5): 533–544.

Landis, W.J., Song, M.J., Leith, A., McEwen, L., McEwen, B.F. 1993. Mineral and organic matrix interaction in normally calcifying tendon visualized in three dimensions by high-voltage electron microscopic tomography and graphic image reconstruction. Journal of Structural Biology 110: 39–54.

Lebon, M., Reiche, I., Fröhlich, F., Bahain, J.-J., Falguères, C. 2008. Characterization of archaeological burnt bones: contribution of a new analytical protocol based on derivative

FTIR spectroscopy and curve fitting of the ν1ν3 PO4domain. Analytical Bioanalytical Chemistry 392: 1479–1488.

Lebon, M., Reiche, I., Bahain, J.-J., Chadefaux, C., Moigne, A.-M.-, Fröhlich, F., Sémah, F., Schwarcz, H.P., Falguères, C. 2010. New parameters for the characterization of diagenetic alterations and heat-induced of fossil bone mineral using Fourier transform infrared spectrometry. Journal of Archaeological Science 37: 2265–2276.

Lucas, S.G., Herne, M.C., Heckert, A.B., Hunt, A.P., Sullivan, R.M. 2004. Reappraisal of Seismosaurus, a late Jurassic sauropod dinosaur from New Mexico. Geological Society of America Abstracts with Programs 36 (5): 422.

Nalla, R.K., Porter, A.E., Daraio, C., Minor, A.M., Radmilovic, V., Szach, E.A., Tomsia, A.P., Ritchie, R.O. 2005. Ultrastructural examination of dentin using focused ion-beam cross-sectioning and transmission electron microscopy. Micron 36: 672–680.

Paris, O., Zizak, I., Lichtenegger, H., Roschger, P., Klaushofer, K., Fratzl, P. 2000. Analysis of the hierarchical structure of biological tissues by scanning X-ray scattering using a micro-beam. Cellular and Molecular Biology 46: 993–1004.

Porter, E.A., Nalla, R.K., Minor, A., Jinschek, J.R., Kisielowskia, C., Radmilovic, V., Kinney, J.H., Tomsia, A.P., Ritchie, R.O. 2005. A transmission electron microscopy study of mineralization in age-induced transparent dentin. Biomaterials 26: 7650–7660.

Pyzalla, A.R., Sander, P.M., Hansen, A., Ferreyro, R., Yi, S.-B., Stempniewicz, M., Brokmeier, H.-G. 2006. Texture analyses of sauropod dinosaur bones from Tendaguru. Materials Science and Engineering A 437: 2–9.

Reiche, I., Vignaud, C., Menu, M. 2002. The crystallinity of ancient bone and dentine: new insights by transmission electron microscopy. Archaeometry 44 (3): 447–459.

Remes, K. 2009. Taxonomy of Late Jurassic diplodocid sauropods from Tendaguru (Tanzania). Fossil Record 12 (1): 23–46.

Reyes-Gaya, J., Garcia-Garcia, R., Bre, E. 2009. Electron beam interaction and damage and reconstruction of hydroxyapatite. Physica B 404: 1867–1873.

Rho, J.-Y., Kuhn-Spearing, L., Ziuopos, P. 1998. Mechanical properties and the hierarchical structure of bone. Medical Engineering and Physics 20: 92–102.

de Ricqlès, A. 1980. Tissue structures of dinosaur bone. Functional significance and possible relation to dinosaur physiology. In: Thomas, D.K., Olson, E.C. (Eds.), A Cold Look at the Warm-Blooded Dinosaurs. Westview Press, Boulder, pp. 103–140.

Rinnerthaler, S., Roschger, P., Jakob, H.F., Nader, A., Klaushofer, K., Fratzl, P. 1999. Scanning small angle X-ray scattering analysis of human bone sections. Calcified Tissue International 64: 422–429.

Roberts, J.E., Bonar, L.C., Griffin, R.G., Glimcher, M.J. 1992. Characterization of very young mineral phases of bone by solid state 31 phosphorus magic angle sample spinning nuclear magnetic resonance and X-ray diffraction. Calcified Tissue International 50: 42–48.

Sander, P.M. 2000. Long bone histology of the Tendaguru sauropods: implications for growth and biology. Paleobiology 26 (3): 466–488.

Sander, P.M., Andrassy, P. 2006. Lines of arrested growth and long bone histology in Pleistocene large mammals from Germany: what do they tell us about dinosaur physiology? Palaeontographica A 277: 143–159.

Sander, P.M., Christian, A., Clauss, M., Fechner, R., Gee, C.T., Griebeler, E.-M., Gunga, H.-C.,Hummel, J., Mallison, H., Perry, S.F., Preuschoft, H., Rauhut, O.W.M., Remes, K., Tütken, T., Wings, O., Witzel, U. 2010. Biology of the Sauropod Dinosaurs: The Evolution of Gigantism. Biological Reviews of the Cambridge Philosophical Society 1–43.

Sasaki, N., Sudoh, Y. 1997. X-ray pole figure analysis of apatite crystals and collagen molecules in bone. Calcified Tissue International 60: 361–367.

Sasaki, N., Ikawa, T., Fukuda, A. 1991. Orientation of mineral in bovine bone and the anisotropic mechanical properties of plexiform bone. Journal of Biomechanics 24 (1): 57–61.

Scherrer, P. 1918. Bestimmung der Grösse und der inneren Struktur von Kolloidteilchen mittels Röntgenstrahlen. Nachr. Ges. Wiss. Göttingen 26: 98–100.

Su, X., Sun, K., Cui, F.Z., Landis, W.J. 2003. Organization of apatite crystals in human woven bone. Bone 32: 150–160.

Tong, W., Glimcher, M.J., Katz, J.L., Kuhn, L., Eppell, S.J. 2003. Size and shape of mineralites in young bovine bone measured by atomic force microscopy. Calcified Tissue International 72: 592–598.

Trueman, C.N.G., Behrensmeyer, A.K., Tuross, N., Weiner, S. 2004. Mineralogical and compositional changes in bones exposed on soil surfaces in Amboseli National Park, Kenya: diagenetic mechanisms and the role of sediment pore fluids. Journal of Archaeological Science 31: 721–739.

Tuross, N., Behrensmeyer, A.K., Eanes, E.D., Fischer, L.W. 1989. Molecular preservation and crystallographic alterations in a weathering of wildebeest bones. Applied Geochemistry 4: 261–270.

Volkert, C.A., Bush, S., Heiland, B., Dehm, G. 2004. Transmission electron microscopy of fluorapatite-gelatine composite particles prepared using focused ion beam milling. Journal of Microscopy-Oxford 214: 208–212.

Wagner, H.D., Weiner, S. 1992. On the relationship between the microstructure of bone and its mechanical stiffness. Journal of Biomechanics 25: 1311–1320.

Warren, B.E., Averbach, B.L. 1950. The effect of cold work distortion on X-ray patterns. Journal of Applied Physics: 21: 595.

Weiner, S., Price, P.A. 1986. Disaggregation of bones into crystals. Calcified Tissue International 39: 365–375.

Weiner, S., Arad, T., Traub, W. 1991. Crystal organization in rat bone lamellae. FEBS Letters 285 (1): 49–54.

Weiner, S., Traub, W. 1992. Bone structure: from angstroms to microns. The FASEB Journal 6: 879–885.

Weiner, S., Wagner, H.D. 1998. The material bone: structure–mechanical function relations. Annual Review of Materials Science 28: 271–298.

Wenk, H.-R., Heidelbach, F. 1999. Crystal alignment of carbonated apatite in bone and calcified tendon: results from quantitative texture analysis. Bone 24 (4), 361–369.

Williamson, G.K., Hall, W.H. 1953. X-ray line broadening from filed aluminium and wolfram. L'elargissement des raies de rayons x obtenues des limailles d'aluminium et de tungsteneDie verbreiterung der roentgeninterferenzlinien von aluminiumund wolframspaenen. Acta Metallurgica. 1 (1): 22–31.

Ziv, V., Weiner, S. 1994. Bone crystal sizes: a comparison of transmission electron microscopic and X-ray diffraction line with broadening techniques. Connective Tissue Research 30: 165–175.

Ziv, V., Wagner, H.D., Weiner, S. 1996a. Microstructure–microhardness relations in parallel-fibered and lamellar bone. Bone 18: 417–428.

Ziv, V., Sabanay, I., Arad, T., Traub, W., Weiner, S. 1996b. Transitional structures in lamellar bone. Microscopy Research and Technique 33: 203–213.

Zocco, G.Z., Schwartz, H.L. 1994. Microstructural analysis of bone of the sauropod dinosaur Seismosaurus by transmission electron miscroscopy. Palaeontology 37 (3): 493–503.

Chapter 7 Nanostructural analysis of primary and secondary bone

1 Introduction

Sauropod compact bones are constituted of fibrolamellar (FBL) bone, like mammals (Enlow and Brown 1956, 1958; de Ricqlès 1968, Rimblot-Baly et al. 1995, Sander and Andrassy 2006). The matrix of the bone is formed rapidly by deposition of woven tissue around vascular canals, which are filled centripally by lamellar bone during the growth of the animal (for more details see Francillon-Vieillot 1990). This bone tissue is interpreted by Amprino (1948) as fast deposited bone tissue. During the life of the sauropods remodeling of the bone appears. Formation of this haversian tissue was mostly interpreted as a reshaping of the bone, muscle attachment, aging or mineral storage (Amprino 1948, 1967, Enlow 1963, Reid 1984, Martin and Burr 1989). Moreover, biomechanical implications of remodeling have also been explored (see for example Currey 1959, Hert et al. 1965, Burr et al. 1985, Vincentelli and Grigorov 1985, Rho et al. 1999). It is possible that many of these conjoint factors are responsible for the structure of secondary bone in the tissue (Currey 2002). Curry in 1999 conjectured that due to the heavy mass of sauropods the haversian tissue formed by accretional lamellar bone can provide mechanical stiffness against large compressive loads.

The organization of the two principal bone tissue primary and secondary bone have consequences on mechanical adaptations of cortical bone. Little is known about organization of the woven fibered bone (Su et al. 2003); extensive studies are available about the structure of lamellar bone (work of Ascenzi, Riggs, Weiner et al. 1999). There are two models regarding the structure of these lamellae. The first concluded in a rotated plywood structure (see for example Giraud-Guille 1988, Weiner et al. 1998), while the second model (Marotti 1993) assumes a structure of alternate rich and poor collagen lamellae. Nowadays the first hypothesis is globally admitted. The models are based on mammals and specifically human bones samples. Studies of sauropod bones should provide us hints for this model.
The crystallographic orientation measurements given by the texture data (Chapter 7) have shown that the (001) direction of the crystals is the principal texture of long bones of sauropod or other recent animals. During ontogeny, growth and remodeling of the bone this texture is kept. Electron microscopic investigations of primary and secondary bone will provide us insight of the ultrastructure and crystallographic orientations of these two tissues.

The present chapter presents TEM investigations on the organization, the size and shape of apatite crystals in sauropod bones (lacking of collagen), based on which we expect to obtain some light on their original structure. Comparison with recent and subfossil mammals is made and evolution of the organization of primary and cortical bone with age is also discussed. Crystal size was already evocated in Chapter 8. Two major observations were made. First in the woven primary bone and secondly in the lamellar bone constituting the secondary bone.
As the cylindrical growth of sauropod long bones occurs principally by outer periosteal new bone deposition and endosteal resorption, the bone from endosteal and periosteal surface exhibits different stages of maturation (Enlow 1963). The study of the crystallographic orientation and size from periosteal to endosteal bone will give us hints of possible differences during bone´s growth.

Observations of sauropod cortical nanostructure show that lamellar bone composing the secondary osteons is by far more complex than the woven bone, as noticed already for recent mammals. The work expands the results to biomechanical aspects of published data.

2 Experimental details

2.1 Material

Specimens studied include subfossil and recent mammal bone (horse and cow respectively) as well as Apatosaurus sp. (see experimental part of chapter 6 to 8 for more details).
The sample of fresh cow bone was placed in a solution of trichloroethylene until all the organic tissue has been removed (approximately 24 hours). Then it was rinsed and put in 95% ethanol and dried in vacuum. The sample was then fractured by hand and coated with gold. The fossil and subfossil samples were mechanically polished using diamond paste and sputter coated with gold.

2.2 SEM

Samples were examined in a SEM Jeol JSM-6490 equipped with tungsten filament. Higher magnification pictures were made in a Jeol JSM-6500F microscope equipped with a field emission electron gun. A cow sample has been investigated in SEM.

2.3 TEM

Lamellar sections of subfossil horse and sauropod samples were prepared by FIB for TEM investigation, in the longitudinal direction of the bone axis. All samples were prepared with same orientation parallel to the periosteal surface of the bone cortex (Figure 7.1). TEM analyses were carried out using a Jeol JEM-2200FS microscope operating at 200 kV. Images were recording with a Gatan CDD camera and further processed using Gatan Digital Micrograph software (Version 3.82). Further quantitative evaluations were made using the Image J software (version 1.6.5, available online in http://rsbweb.nih.gov/ij/index.html).

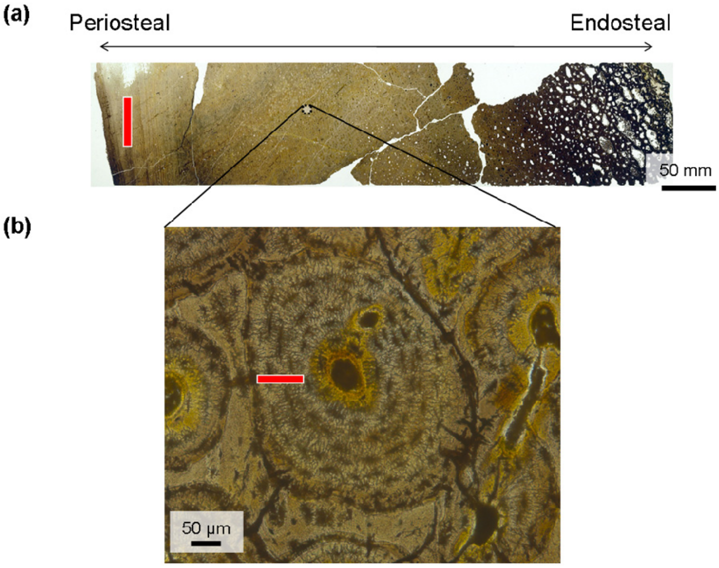

Figure 7.1: Illustration of the orientation of the thin sections prepared in TEM. (a) Optical micrograph of the Apatosaurus (BYU 601-17328), both periosteal and endosteal side are indicated by the arrow. The red square (not to scale) represents the orientations of the TEM sections prepared in the sample. In (b), display a secondary osteon with its thin section (not to scale) prepared. The TEM lamellae in secondary osteon were prepared perpendicular to the cement line of secondary osteon, as illustrated in the figure.

3 Results

3.1 SEM Results

SEM micrograph of fractured cow bone is illustrated in Figure 7.2. It evidences the different structure of two tissue types. Woven bone is clearly identified by a smooth and compact texture (black arrow on Figure 7.2a), while the surface of the lamellar bone appears rougher (white arrow on Figure 7.2a). The insert (Figure 7.2b) shows precisely this typical lamellar structure made up of collagen fibers of different orientations. Thinner lamellae with fairly smooth surface (1-2 µm thick) are succeeded by thicker lamellae with rough surface (2-3 µm thick). The lamellae are highlighted on Figure 1b by dashed lines. The thinner lamella describes a lineation parallel to the plane of the lamellar boundaries and is interpreted as transversal lamellae (Reid 1986, Ziv et al 1996a). The thicker lamellae are present in sublayers (numbered from 1 to 5) (Figure 7.2c) where the orientation of collagen fibers changes gradually forming a rotate plywood pattern (Giraud-Guille 1988, Weiner and Traub 1992, Weiner et al. 1997, 1999).

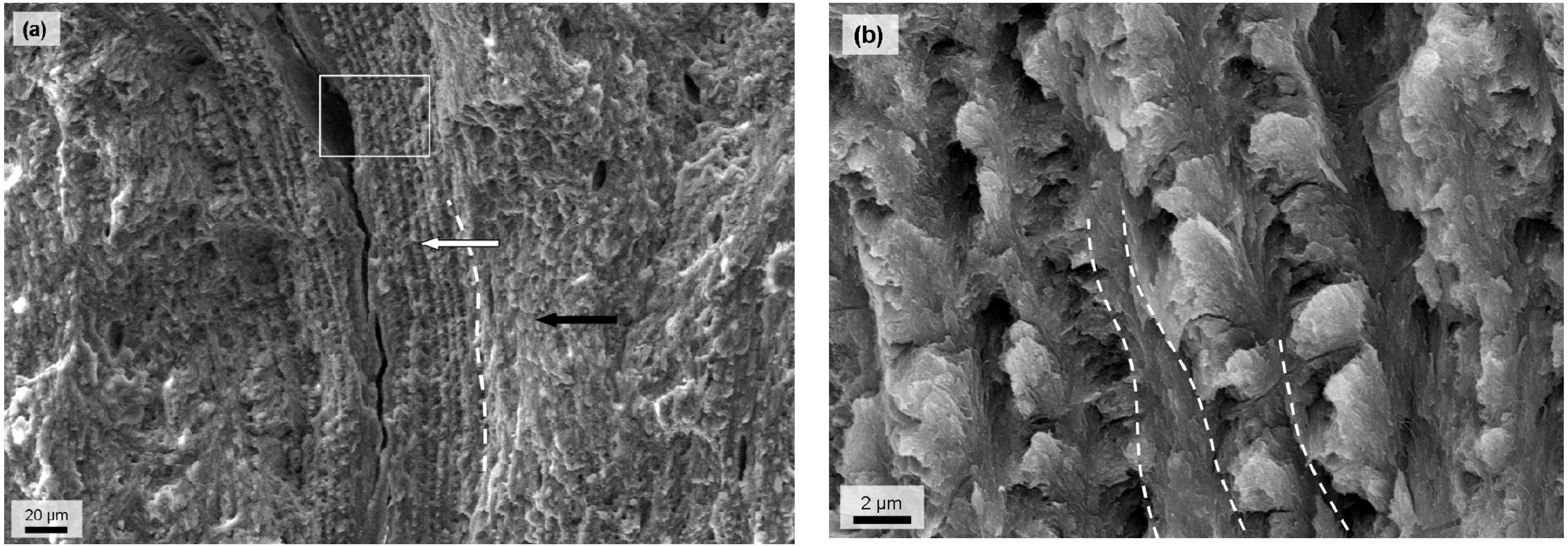

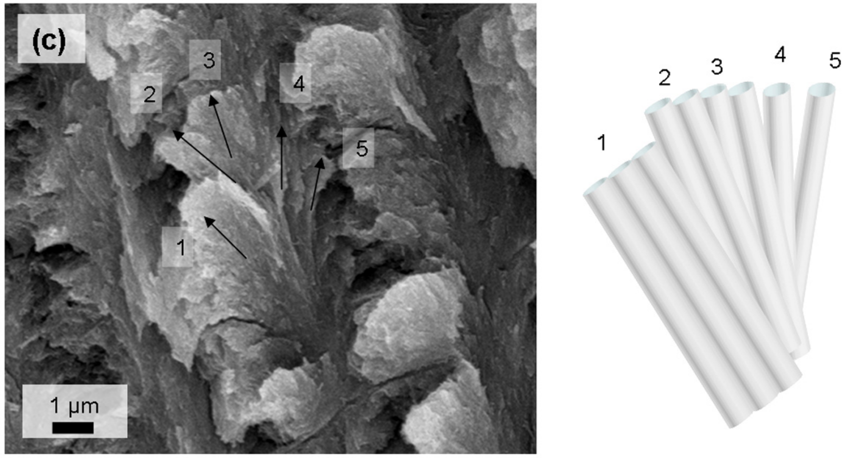

Figure 7.2: (a). SEM micrograph of the fractured surface of a recent cow bone. The two types of bone tissue can be easily recognized and identified (dashed lines). The rough surface corresponds to the woven bone tissue composing to the matrix of mammal (black arrow). The layered surface corresponds to the lamellar bone formed around osteons (white arrow). (b) Zoom corresponding to the white box in (a). The dashed lines indicate the succession of different lamellae in the structure. The lamella with rough surface texture is embraced by two other smooth lamellae (one is indicated on the left of the lamellae). The packing of the fibrils in the center lamellae shows a well developed layered structure (c). The layers have different orientations with regard to each other (indicated by arrows and numbers). 5 different sublamellae are noticed here (picture modified from Dumont et al. 2011)

3.2 TEM results

3.2.1 Primary bone

Organization of the crystals

Longitudinal TEM sections from the endosteal and periosteal surfaces of the subfossil horse bone were prepared. It can be observed that the collagen is preserved in the subfossil bone, as seen by its typical banding (marked in Figure 7.4b for example) observable under microscopy.

Figure 7.2 and 7.3 sum up observations made at the periosteal and endosteal surface of the subfossil horse cortex, respectively. In the sample adjacent to the endosteal surface the collagen fibers were more organized than at the periosteal surface (Figure 7.4). The spatial disorganization of collagen fibers is visible near the osteocyte lacunae (Figure 7.3b), where the diffraction pattern clearly illustrates circle rings. Otherwise both regions described associated diffractions patterns with the characteristic 002 arc texture. Preferential crystallographic orientation (texture) is stronger, however, at the endosteal part compared to the periosteal part (Figure 7.4b). This is related to the organization of the collagen fibrils which are more disordered in the latter (Figure 7.3a). This difference has been already reported by Su et al. (Su et al. 2003). The fibrils at the endosteal part of the bone are more densely packed and changed to a more ordered arrangement (Su et al. 1997)

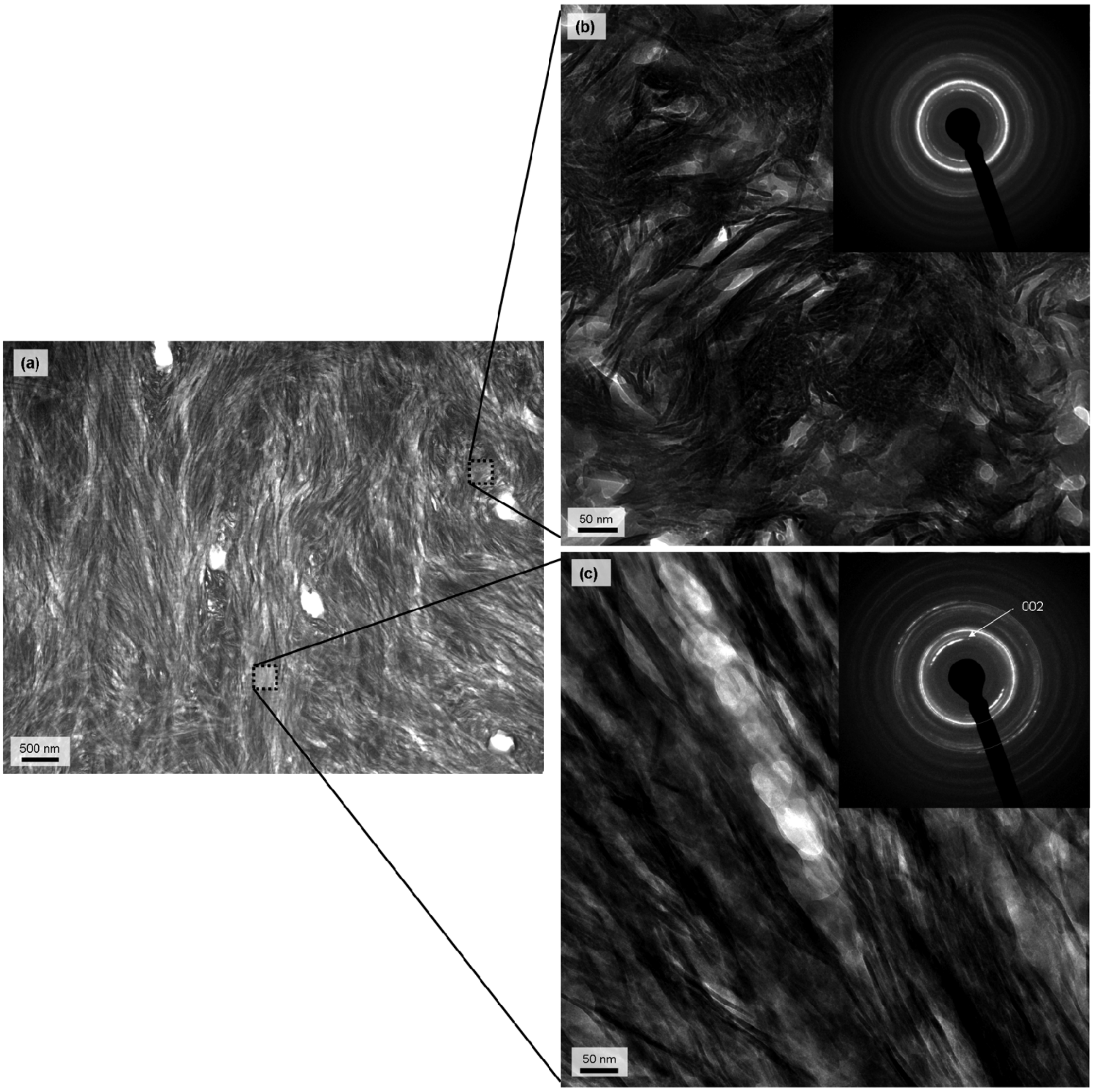

Figure 7.3: Sample A in the periosteal side of the of subfossil horse cortex bone. (a) STEM micrograph. The sample A show a less regular organization of collagen fibrils. Some of the fibers (b) display fibered bundles, when others have a parallel organization (c). The diffraction patterns associated with the TEM picture (b and c) confirm this statement. The pores are due to artifacts of the sectioning of the osteocytes lacunae.

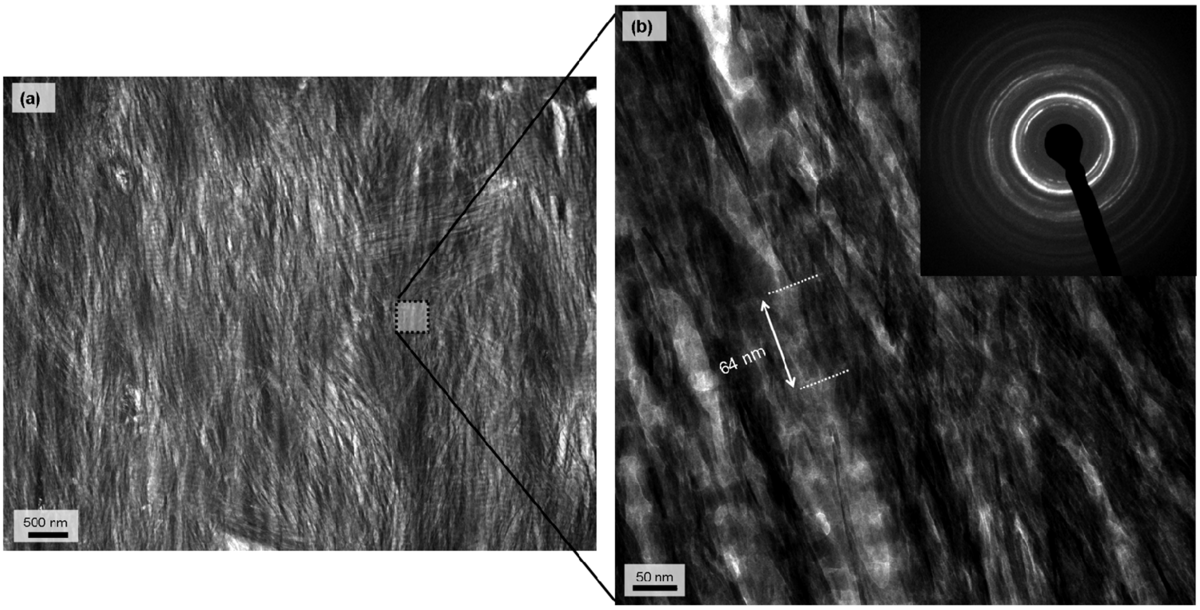

Figure 7.4: Sample B in the periosteal side of the of subfossil horse cortex bone. (a) STEM micrograph. The sample B shows a parallel collagen fibers structure. The TEM micrograph in B display well organized collagen and mineral particles, which are parallel to each other. The collagen fibril is well noticed by the typical band patterning with a periodicity of around 67 nm. The diffraction pattern displays a 002 texture (well marked inner arc).

Crystal size

Crystal size was measured in samples from both the periosteal and endosteal part of the cortex. The results are presented in Table 7.1.

Table 7.1: Mean crystal length and width at the periosteal and endosteal surface part of the bone. Around 340 crystallites have been counted for both samples.

	Sample A (periosteal part)	Sample B (endosteal part)
Length	58.3 ± 15.3	53.3 ± 16.1
Width	4.3 ± 1.4	4.2 ± 1

Apatite crystal lengths are slightly larger in the sample from the periostal surface (newer bone) compared to the endosteal part (older bone). Statistical *t*-test indicates that the mean lengths are significantly different ($p < 0.05$). There is, however, no difference between crystal widthsin the periosteal and endosteal part.

Sauropod sample

Contrary to subfossil horse sample, where it was noticed that the periosteal surface has more distorted crystals, no differences in the orientation of the crystal are observed in TEM between newer (periosteal) bone and older (endosteal) bone. In agreement with light microscopy the periosteal bone consists of rather organized fiber bundles. The fibers are mainly parallel to each other although fibrils interweaving at small angles can be seen. No cementing lines bridging fibrils are visible like in lamellar bone. Concerning the size of the crystals no difference between periosteal and endosteal part of the cortex of sauropod bone (see Chapter 6 for sample OMNH 1279, Table 6.3 and Figure 6.7) has been noticed. Interpretation of the results is rendered difficult due to possible diagenesis and lack of collagen which could be misleading in our interpretations.

3.2.2 Lamellar bone

Organization of the crystals

The secondary lamellar bone present in the secondary osteons of sauropod bone has a more complex organization than woven bone tissue. It is known to have a different organization of fibrils arrays arrangement, where woven bone is known to be arranged in fiber bundles poorly oriented, and lamellar bone formed by parallel fibers with each fibril have different orientations between each other. The plywood like structure as already described (see for example Giraud-Guille 1988, Weiner and Traub 1992, Weiner et al. 1997, Weiner and Wagner 1998) has received increasing interest because of its abundance in the nature (in marine crustacean shells Lowenstam and Weiner 1992, Giraud-Guille 1998, in teleost scales Bigi et al. 2001). Giraud- Guille (1988 and Figure 7.4) pointed out that many structures and crystallographic orientations observed are mainly misinterpretations that arise from different orientations of TEM sample sections. For example this led to the incorrect interpretation of collagen fibrils having arc-like curvature (see Figure 7.5 and Figure 7.9). Basically, the plywood-like structure observed in lamellar bone has fibril arrays oriented orthogonally to each other.

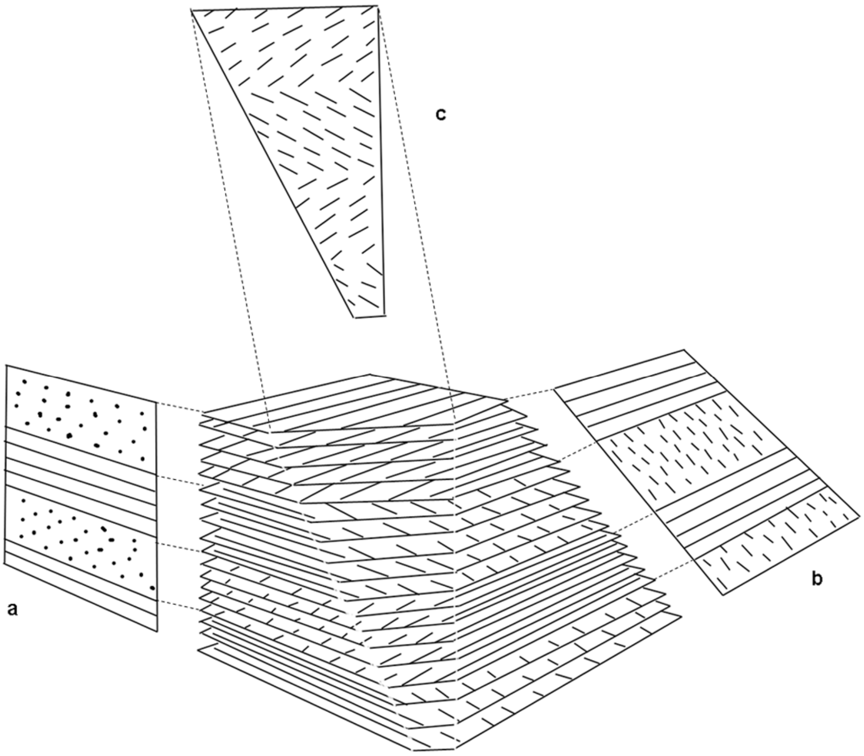

Figure 7.5: Orthogonal plywood. The diagram represents parallel planes. On each planes the lines correspond to orientation of collagen fibrils. The orthogonal plywood is characterized by two directions perpendicular to each other (angle of 90°). Section a., shows a transverse cut. The fibrils appear as long segments and dots. The sections b. and c. are oblique. Section b. shows alternation of long segments and shorter segments perpendicular to each other. Section c. shows the herring bone pattern (Franck et al. 1955) with a zigzag aspect of collagen fibrils (modified from Giraud-Guille, 1988).

The different sections have been investigated in the lamellar bone of the sauropod sample. The collagen fibrils are not preserved, however, the TEM images indicate that the orientation of apatite crystals is maintained during fossilization (Trueman and Tuross 2002, Chapter 6 of this thesis) keeping the original structural organization.

Figure 7.6 is a STEM micrograph of lamellar bone observed in *Apatosaurus* lamellar osteonal bone. Crystal bundles with different orientation can be observed. Most crystals are located in irregular bands (collagen fibril bands), lying parallel to each other. Figure 7.6 illustrates these different aspects. Abrupt changes in crystals' orientation are noticed, which are highlighted by white dashed lines. In these local areas, the crystals are lying obliquely or randomly oriented with regard to each other. An example of strong orientation change is visible in the Figure 7.7.

Figure 7.6: STEM micrograph of *Apatosaurus* bone BYU 601-17328 showing the general organization of crystals in the fossil lamellar bone. The crystals are generally aligned parallel to each other. Some areas, highlighted by dashed line show crystals with a random orientation distribution. (similar to observations of Giraud-Guille (1988)).

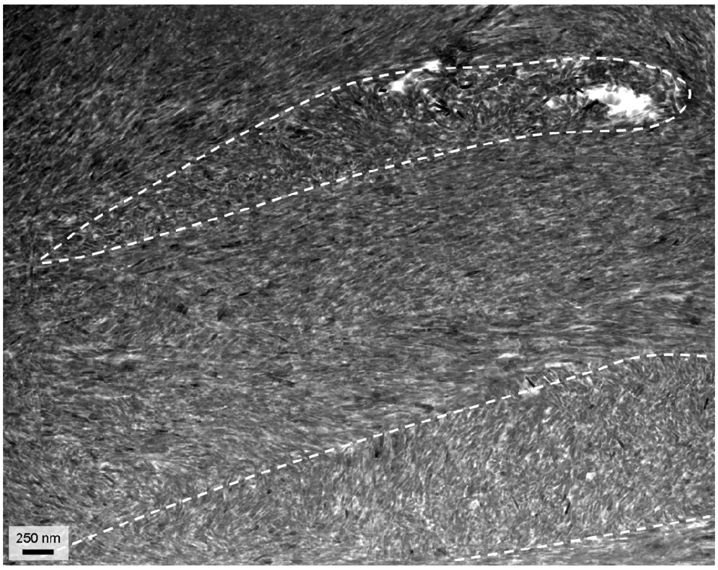

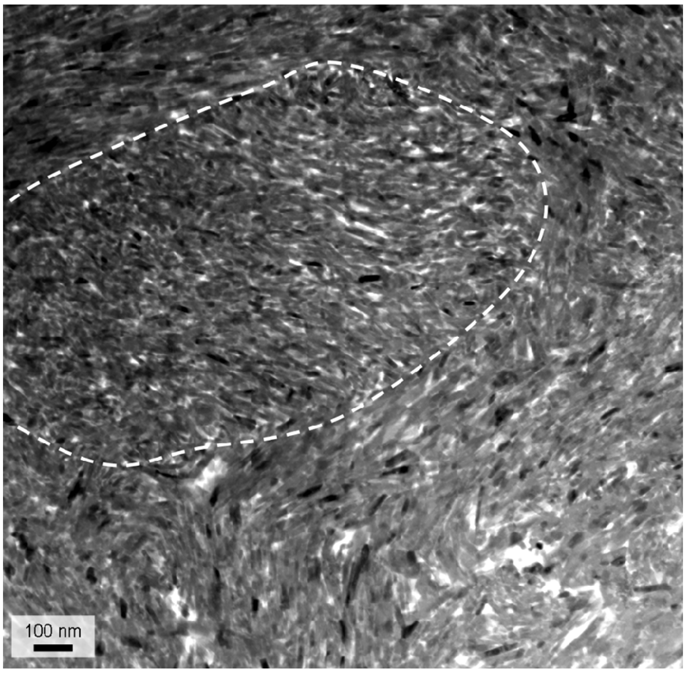

Figure 7.7: TEM micrograph showing the abrupt change in apatite crystals orientation. Zoom in an area where the orientation of the crystals changed abruptly compared to the matrix where crystals are oriented parallel to each other and plane with the section.

The general organization of osteon nanostructure is visible in Figure 7.8. Boundaries between successive bands are indicated by dashed lines. The central band in the figure presents crystals oriented parallel to each other. The other adjacent bands are recognized as interlamellar cementing zone (Ascenzi et al. 1965) by their different structure and crystal organization. The crystals are distributed randomly and oriented differently to each other. This is more evident in Figure 7.9 where the crystallographic diffraction patterns attest the strong texture (alignment) observed in the lamellar unit (Figure 7.9b) and its lack in the interlamellar zone (Figure 7.9a). The boundaries between lamellar units are not straight but undulate. This pattern corresponds to an oblique section of Figure 7.5b. The randomly distributed crystals in the cementing zone are probably some disorder introduced by sectioning or diagenesis.

According to the TEM micrographs the thickness of the lamellar unit varies from 200nm to up to 500nm in the osteon, whereas in the interlamellar cementing zone measure can reach 300nm. No evidence of change of width of interlamellar cementing zone with increase of calcification has been found as previously noticed by Ascenzi et al. (1965).

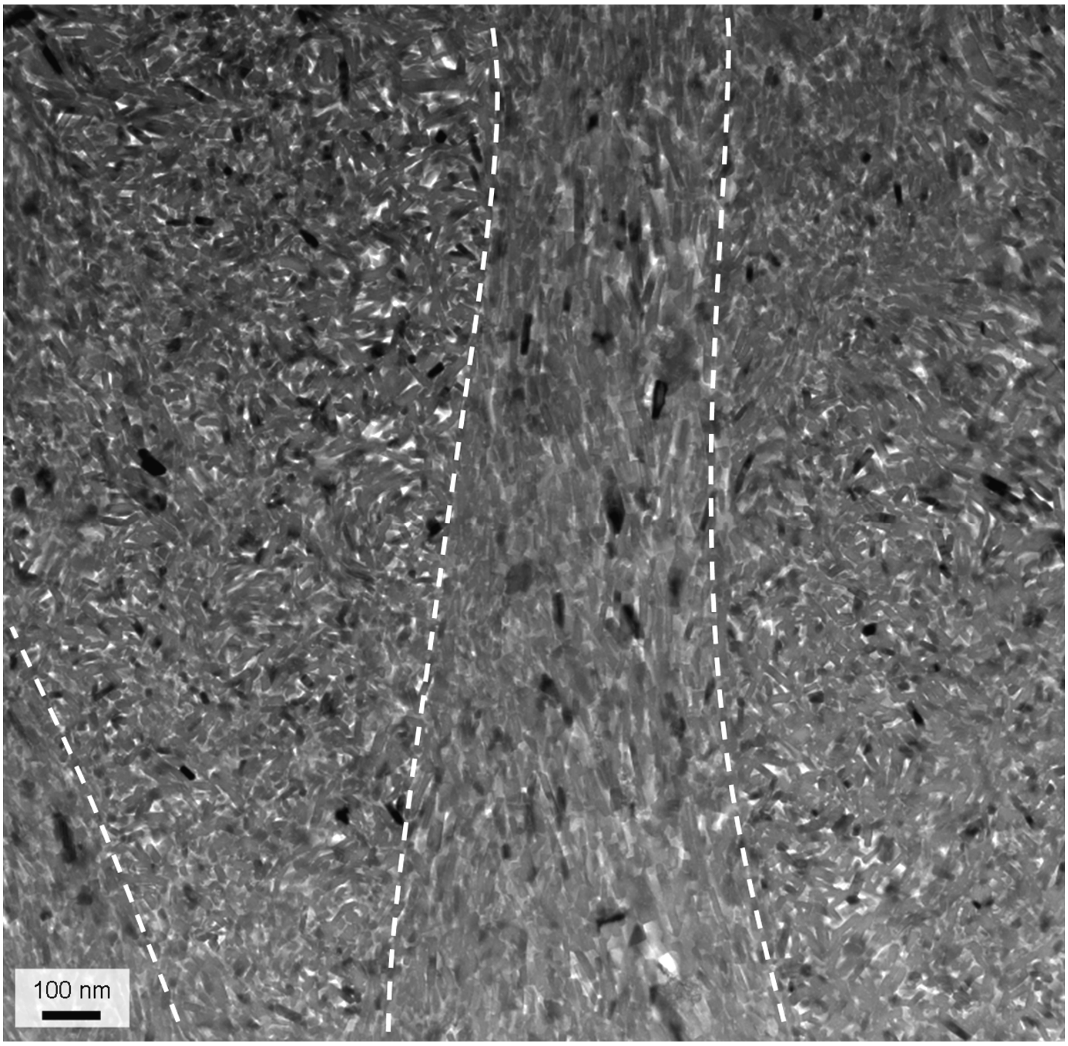

Figure 7.8: TEM micrograph of lamellar bone of Apatosaurus BYU 601-17328. Bands of crystals lying in the plane of the section and parallel to each other are emphasized by white dashed lines. These are separated by bands where crystals cut and make various angles oblique to the principal band with parallel crystal. The disordered zones are named “interlamellar cementing zone”.

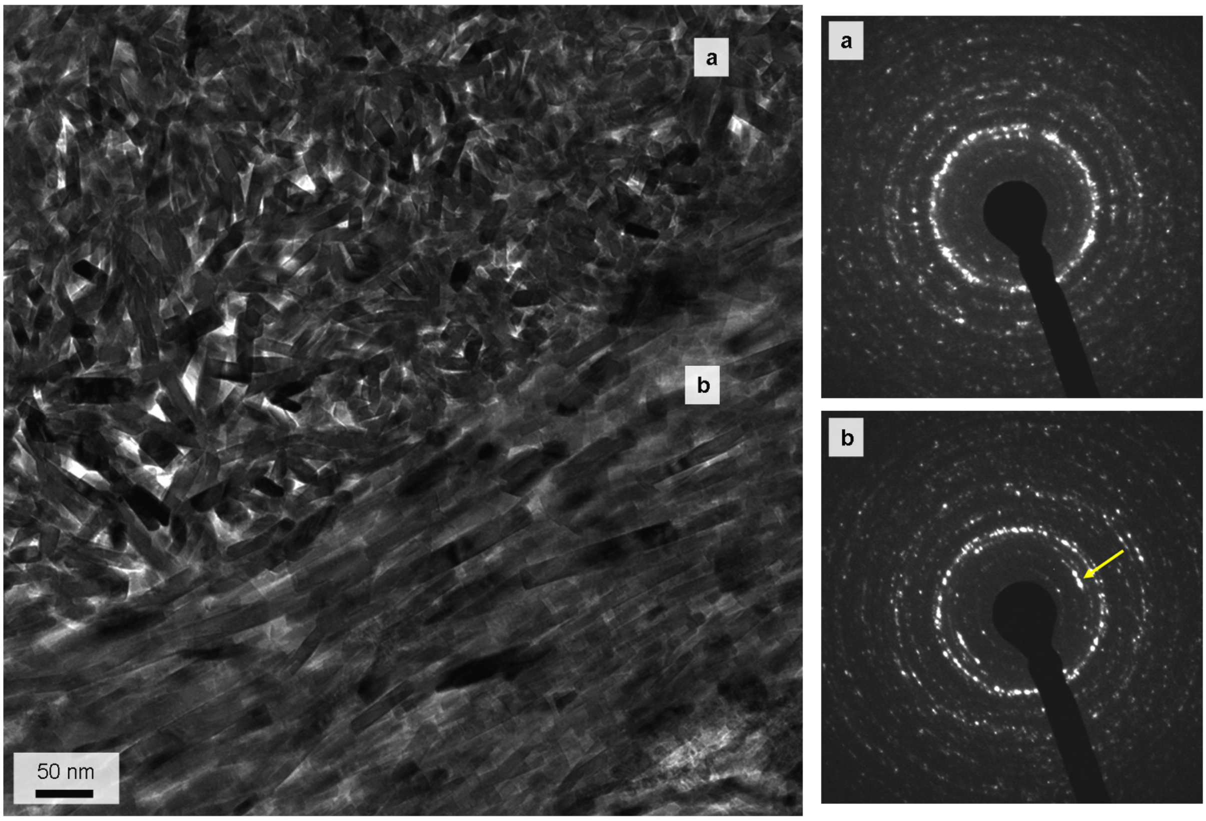

Figure 7.9: TEM micrograph emphasizing the alignment and disorder of apatite crystals orientation. The upper part describes the area where crystals are oriented randomly. The diffraction pattern associated a. does not show any arcs thus any preferential orientation of the crystals. In area b. at the lower part of the figure, crystallites are oriented longitudinally and parallel to each other with their c-axis. This texture is confirmed by the diffraction pattern registered. Diffraction arcs (indicated by the yellow arrow) corresponding to the 002 reflections appear perpendicular to the alignment direction.

This view of lamellar structure observed in sauropod bone confirms the orthogonal plywood model observed in mammals bone (human bone in Giraud-Guille (1988), rat bone in Weiner et al. (1999) and mice bone in Rubin et al. (2004)), with layers of collagen fibrils aligned in the plan of the section and those aligned at intermediate and close to perpendicular orientations. The arc- like pattern (Figure 7.10) and herring bone pattern (Figure 7.11) are usually interpreted as disorder due to the different orientation of the sectioned bone, even if a special care during sample preparation of longitudinall sections has been done.

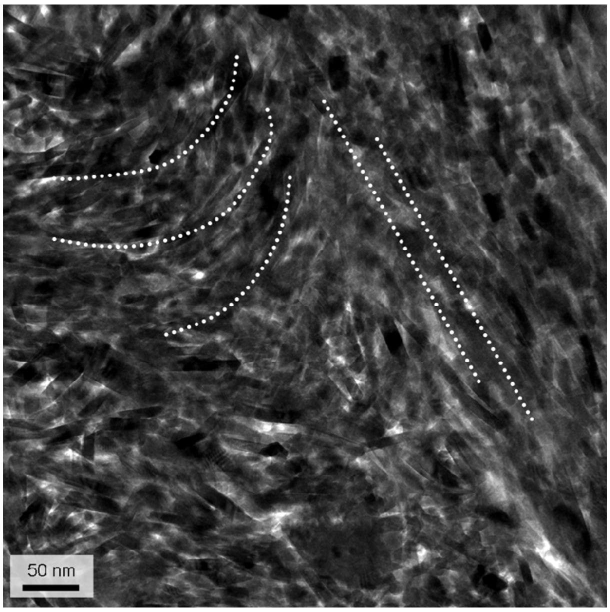

Figure 7.10: TEM micrograph of the lamellar bone of *Apatosaurus* BYU 601-17328. The dotted lines indicate the different orientations suggested by the arrangement of the apatite crystals. A phenomenon of arc pattern is noticed as previously observed by Giraud-Guille (1988), Ziv et al. (1996a) and Yamamoto et al. 2000, corresponding to a twisted plywood structure.

Other misinterpretation of crystallites arrangement is illustrated in Figure 7.10 showing a herring-like bone pattern (Franck et al. 1955, Figure 7.4c). Crystals are forming an angle of 65° with a zigzag aspect. The figure shows only two lamellar bands.

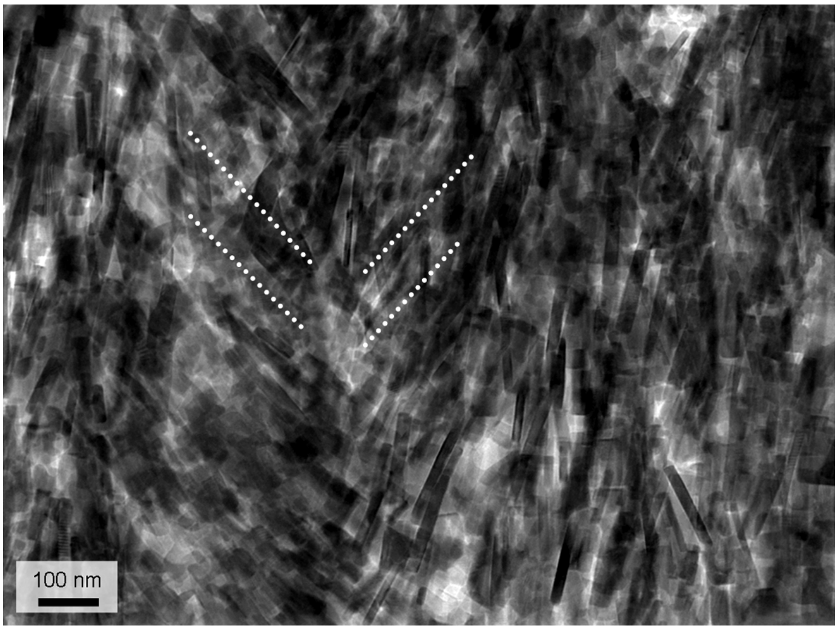

Figure 7.11: STEM micrograph of apatite crystals organization showing herring bone pattern (see c. in Figure 9.5) in lamellar bone of a sauropod indeterminate Ba KI 4. The typical zigzag configuration can be seen with large crystals which form an angle of roughly 65°

Crystallographic orientation

Because of particular interest, the orientation angle between adjacent crystallite bundles was investigated. Different areas of the section of sample BYU 601-17328 were examined. Packs of parallel crystals are interpreted as fingerprints of the early collagen fibril arrays in the fossil bone. The different angles described by different parallel crystal bundles were quantified according to Weiner et al. (1997). Figures 7.12a and 7.12b show TEM micrographs describing different successive crystals orientation. In Figure 11a the three distinct packets of crystals are oriented progressively counterclockwise (with regard to arrow 1). Contrary to Weiner et al. (1997) (see Figure 7.14a) no differences in the thickness of the arrays could be noticed, probably due to the lack of remaining collagen. The measurements of the angles are done between each arrays of parallel crystals.

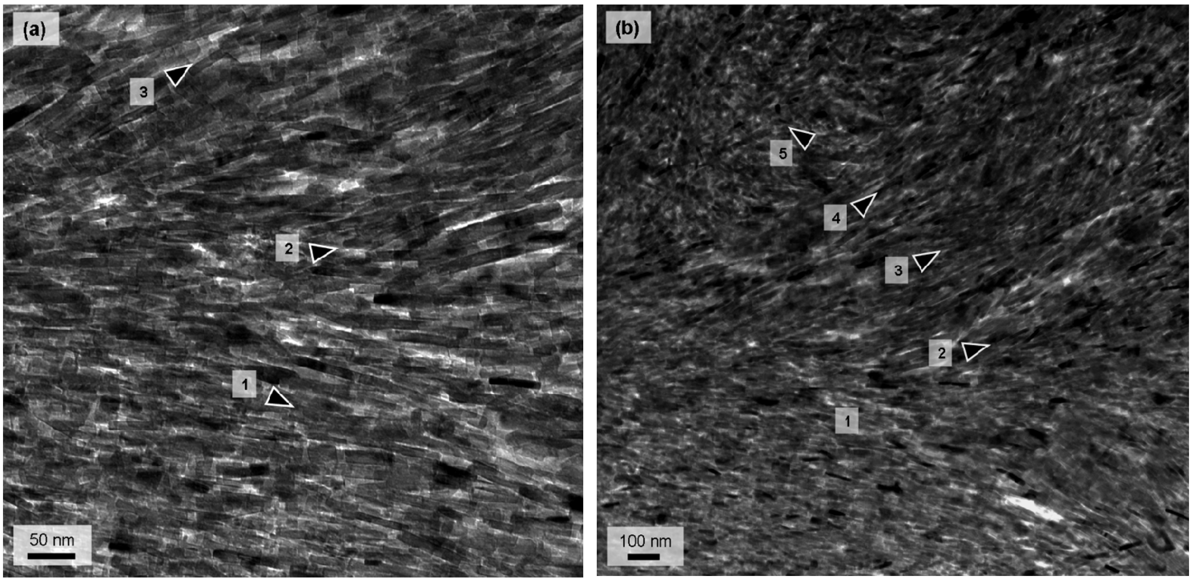

Figure 7.12: (a) TEM micrograph of lamellar osteonal bone in sauropod fossil (BYU 601-17328) showing crystal bundles with different orientation. Three different arrays of parallel crystals are visible on the micrograph (arrowheads marking their direction). The angles measured between nearby bundles are 30° (between 1 and 2) and 12° (between 2 and 3). (b) Second TEM micrograph with 5 units. The angles measured consecutively are 39° (between 1 and 2), 10° (between 2 and 3), 11° (between 3 and 4), and 115° (between 4 and 5).

The histograms of the measured angles are shown in Figures 7.13a and 7.13b, which correspond to the two TEM lamella noted A and B. We notice that there is no significant difference between distributions measured on the two different sections of the same sample (according to a *t*- test they are not statistically different, $p<0.05$). In a previous work Weiner et al. (1997) have found a bimodal distribution with major peak at 30° and a minor peak at 70° (Figure 7.14a). Present measurement shows only a distribution with major peak at 25°. The larger extension of the distribution to large angles (angles >70°) could suggest a bimodal distribution. The second peak observed by Weiner et al. (1997) at 70° was not observed for the sauropod lamellar bone. The minor peak observed at 70° in Weiner work has described the angular relationship between thinner fibrils. Due to the impossibility to differentiate the thickness of crystallite bundles in the sauropod bone such a detailed analysis of nearby orientations was not possible.

Crystal size

Crystal sizes in primary and secondary bone for the indeterminate sauropod sample MFN BaKi5 were measured (see Table 6.2 in chapter 6). The crystals in secondary osteonal bone were slightly larger and more elongated than in primary bone. The crystal sizes were only stastical different for width/thickness measurements.

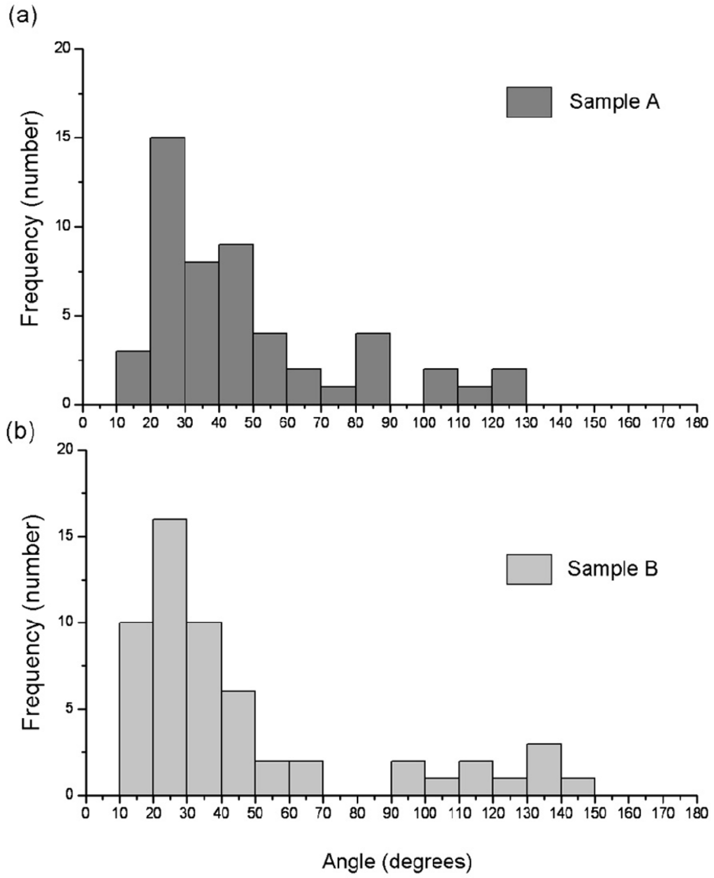

Figure 7.13: Histogram showing the distribution of angles between adjacent arrays of parallel crystal bundles in two different TEM lamellae (a) and (b). Both samples show similar distributions.

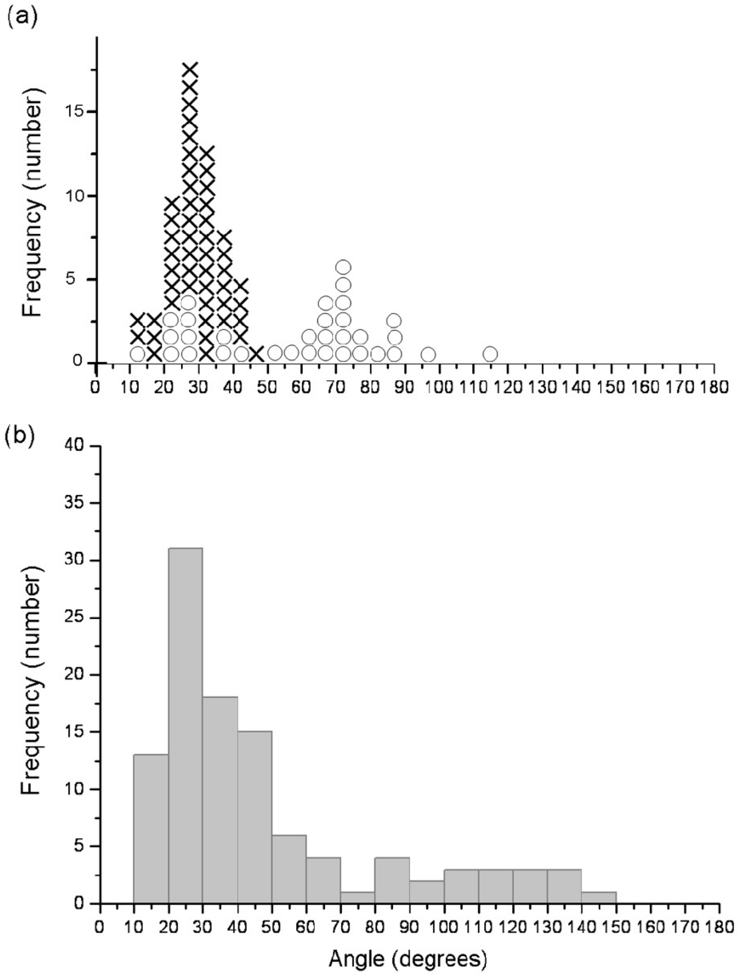

Figure 7.14: Histogram showing the measured angles between adjacent arrays of parallel collagen fibrils in a rat bone (modified from Weiner et al. 1997) (a). The cross is indicates adjacent arrays composed of thicker fibrils. The circle designates the angles when one of the arrays is composed of thinner fibrils. (b) Histogram showing the measured angles between groups of parallel crystals from two samples (A and B, cf. Figure above) of sauropod bone (BYU 601-17328). No distinction between thin and thicker groups can be made.

4 Discussion

4.1 Organization of primary bone

The woven primary bone was investigated in both recent mammals and sauropod bone. The results show that there are differences in crystal organization between periosteal and endosteal part of the cortex. Several disorganized and loosely packed fiber bundles were observed at the periosteal surface of the subfossil horse (Figure 7.2a), even though the bone shows the presence of a slight 002 texture (arcs in the diffraction pattern of Figure 7.2a). Sample B from the endosteal older layers of cortical bone has more regular collagen fibers with clear crystallographic texture (Figure 7.2b), where collagen periodicity is well marked (Figure 7.3).

Such differences were observed for both fetal human and young rat femora (Su et al. 2003, Bertazzo et al. 2006). Newly deposited woven bone at the periosteal surface has more interweaven and dispersed collagen fibrils organization (Ascenzi et al. 1967).

Cylindrical growth of long bones occurs principally by formation of new bone at the periosteal surface and resorption at the endosteal one. Therefore, the bone at two surfaces exhibits different stages of maturation (Enlow 1963). As apatite crystals grow with maturity of the bone (Handschin and Stern 1995, Bertazzo et al. 2006, Kuhn et al. 2008), larger crystals in the deeper layer of the cortex should be expected. Here the bone becomes denser and more compact with age. Deposition of new bone at the periosteal surface should lead to smaller crystals (Tong et al. 2003). In other words, larger crystals are formed from the merger of the smaller plaques present in the mineral phase from younger animals; the arrangement of mature animal's bone is becoming more compact with larger and denser structure. Our results (Table 7.1) in the horse cortex are conflicting with this hypothesis: longer crystals are noticed in the periosteal surface of the horse cortex bone. The difference noticed in crystal size results could be, however, due to a biased evaluation of crystal size range by TEM (Hassenkam et al 2004 and chapter 6). The experiment should be repeated with a larger sampling set (different part of the bone and different samples). Our comparison for sauropod bone (OMNH 1279, chapter 6: Table 6.3 and Figure 6.7) indicates that crystal size varied through the cortex of the bone. Larger crystals were noticed in the middle of the cortex when smaller sizes were measured in both endosteal and periosteal surfaces. This unexpected result can be also due to diagenetic effects. It seems also likely that crystal size varies in the same range from periosteal and endosteal bone for fast growth animals like sauropods. However, further experiments are needed before conclusions can be drawn about crystallite size gradients in fast or slow growing bone of different animals.

4.2 Organization of secondary lamellar bone

Present TEM observations show that osteonal bone of fossil sauropod samples describe the twisted plywood model of bone lamellar structure (Giraud-Guille 1988, Ziv et al. 1996a and Weiner et al. 1997, Yamamoto et al. 2000), i.e. periodic rotation fibrils resulting in alternating lamellar pattern. The second model (Marotti 1993, 1996) proposes that lamellar bone is made up of alternating layers of rich and poor collagen with highly interwoven arrangement of fibers. Even if collagen is not preserved in fossil sauropod bone, crystals and collagen are intimately linked; no difference of crystal density was spotted between different successive lamellae, as expected in Marotti´s model. Investigated sauropod fossil bones do not show this systematic alternation. It was assumed by Yamamoto et al. (2000), that the observations of Marotti could have been an artifact due to preparation.

As observed, lamellar bone organization is complex and individual lamellae are made of sublayers of varying thickness (Figure 9.8 and 9.9) that could also vary in different bone types of the same species (Weiner et al 1997, 1999) as well as with orientation collagen (Figure 7.9). Misleading in interpretation of the structure (like arc-like curvatures) could easily be made arise by different oblique sections (Figure 7.10 and 7.11). The angle distribution between parallel crystals packets agreed with previous results of Weiner et al. (1997): it demonstrated that sub-layers of the lamellar unit are on the average rotated progressively by 30°. The fifth 120° sublayer (called back flip layer (Weiner et al. 1997)) can be as well noticed in Figure 7.11b, agreeing with the rotate plywood model too as indicated in Figure 7.15.

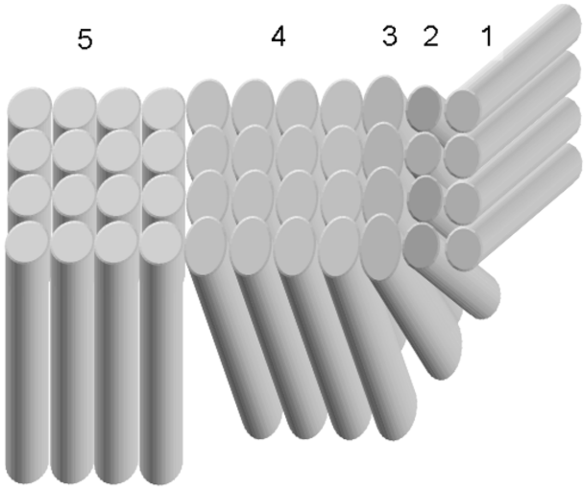

Figure 7.15: Schematic illustration of five sub-layers observed in the lamellar unit of lamellar bone (modified from Weiner et al. 1997). The different thickness of sub-layers drawn here correspond to observations in baboon tibia (Liu et al. 2000).

Mammals and sauropods seem to have the same rotate plywood structure. Indeed our results agree with different angles orientation already described for recent animals (Weiner et al. 1997, 1999). Variations of the relative thickness of the sublayers could however be expected. Considering the model and previous observations (Weiner et al. 1999, Liu et al. 1999), sublayers 5 and 4 are thicker (Figure 7.15). Weiner et al. (1999) suggest that different thickness could be a mirror of adaptation to specific functions. Such observations are hard to distinguish in the sauropod bone, by difficulty of discerning thickness differences. However, it is pretty clear that the sublayer 5 in Figure 7.12b is thicker than the third or the second one. This different sublayer thickness could occur in areas of tension and compression. This hypothesis of collagen fiber distribution in function of mechanical properties corroborates studies of Riggs et al. (1993) and Skedros et al. (1996, 2006). Observations by circularly polarized light indicate density differences between transverse and longitudinal collagen fibers in accordance with the different mechanical loading to which they are exposed. Weiner and Wagner 1998 inferred that the osteoblasts integrate the mechanical signals and form sublayers of varying thickness.

4.3 Biomechanical aspects of primary and secondary lamellar bone

Fibrolamellar bone (Enlow and Brown 1956, 1958; de Ricqlès 1975, 1977; Francillon-Vieillot et al. 1990) developed in sauropod and mammals, has been designated as fast growing bone with high metabolic rate(de Ricqles 1975, 1980, 1983, Sander and Klein 2005, Sander and Clauss 2008, Sander et al. 2010). During remodeling this FBL tissue is replaced by secondary osteons formed exclusively in lamellar bone. Both tissues are considered in this study as biomechanically linked. But other relation with age or element mobilization is not excluded.

The two structures show different organization that leads to different mechanical properties. Currey (1959) compared tensile strength of primary and haversian bone of cow samples. His results show that haversian bone has a lower tensile strength than primary one. But as already suggested (chapter 7) long bones of sauropods seem to be mainly adapted to compressive loads (Sverdlova and Witzel 2010). Results of compressive loading tests show an increase of strength in younger primary bone with increase in mineralization level (Hert et al. 1965). But Currey (2002) suggested in the other way that woven bone is mostly inferior to lamellar bone in its mechanical properties and concluded that a bone made only of woven bone tissue will produce FBL as a mechanical response. Resorption (called rebuilding in their paper) causes a decrease in mechanical strength while progressive lamellar refilling will stabilize little by little the weakness of the structure. In entire tests made so far, it is basically assumed that woven bone has better strength properties than secondary bone (Reilly et al. 1974, Currey 2002); the strength of primary bone were the same or even higher than for secondary (Haversian) bone. It was noticed by de Ricqlès (1980) that in Haversian bone, because of the high percentage of cement substance and structural discontinuities by formation of cylinder osteons, the mechanic resistance is lower than primary periostic bone. Martin and Ishida (1989) on the other hand, compared plexiform and osteonal bone and concluded that the latter bone tissue is weaker because of its smaller fraction of longitudinally oriented collagen fibers.

Woven fibered structure shows fibrils arranged into bundles, loosely packed and poorly oriented. Sauropod fossil bones have shown as well crystals which seem to be randomly oriented. This disordered structure result in isotropic properties. Woven bone is formed basically after fracture or in other pathologic circumstance, i.e. situations where a fast bone deposition is required (Currey 2002). The plywood like structure presented in lamellar bone is more complex. Ziv et al. (1996b) measured microhardness values in circumferential lamellar bone of rat tibia. Their results clearly revealed anisotropy with highest values in direction perpendicular to the long axis. The rotated plywood structure with this gradual tilting and rotation results in a material that is more isotropic (Weiner et al. 1998) and it was suggested that it implies a better adaptation to withstand compressive forces in many direction.

It was also assumed that secondary osteons are basically limiters for crack propagation due to their longitudinal scattered directions (Ascenzi and Bonnucci 1976, Martin and Burr 1989, Martin et al. 1998). But this structure could also have a mechanical advantage for accommodating large compressive loads. Evans and Vincetteli (1974) have already noticed a positive correlation between compressive strength and the percentage of osteons regardless of their collagen fiber orientation. They suggested that osteons tend to increase compressive strength. In addition to these observations differences in the strength of transverse, alternate or longitudinally oriented collagen in osteons formed under specific loads has been found. They observed a positive correlation between compressive strain and percentage of cross-sectional area with light (transverse) osteons. Ascenzi and Bonucci reported indeed that these different osteon morphotypes have different elastic modulus in compression: the alternating type of osteon showing the greater elastic modulus of 7.4GPa (Ascenzi and Bonnuci 1968, 1976, 1977, Ascenzi and Benvenutti 1986). These results were confirmed by polarized light observations (Riggs et al. 1993, Skedros et al. 1996, 1997). Globally their results indicate that a longitudinal arrangement osteons presents the better ultimate tensile strength and modulus of elasticity compare to the two others osteons morphotypes.

5 Conclusions

The current study of the nanostructure of primary and secondary bone of sauropod has lead to different conclusions:

- In TEM, both woven primary bone and secondary lamellar bone have different crystallographic organizations in sauropod bone, identical to subfossil mammals. Woven primary bone present disorganized fiber bundles, which become more ordered in endosteal surface of the bone. However it was observed that a 002 texture is present in both surface (endosteal and periosteal) of the compact bone in subfossil and sauropod bone (see Chapter 5).
- Our results have shown that the crystal is not necessarily increasing from the periosteal (newer bone) to the endosteal (older bone) of compact woven bone, contrarily to recent hypothesis published. This could be due to biased of measurement of the crystal size by TEM method (Dumont et al 2011, Chapter 6), diagenesis effect or biased rising by the small sampling investigated.
- Structures observed in secondary lamellar bone of sauropod concede with twisted plywood model described by Giraud-Guille (1988) and Weiner et al. (1997).
- Biomechanical aspects of both structures have been disccused. Previous research has shown that woven bone has higher strength than secondary bone. But it seems probable that the general organization of lamellar bone observed in secondary osteons conferred to the structure a more longitudinal arrangement, better for resisting compressive loads.

References

Amprino, R. 1948. A contribution to the functional meaning of the substitution of primary bone by secondary bone tissue. Acta Anatomica 5: 291-300.

Amprino, R. 1967. Signification fonctionnelle du remaniement osseux. Journal Medical de Montpellier 2: 105-109.

Ascenzi, A., Bonucci, E., Bocciarelli, D.S. 1965. An electron microscope study of osteon calcification. Journal of ultrastructure research 12: 287-303.

Ascenzi, A., Bonucci, E., Bocciarelli, S. 1967. An electron microscope study on primary periosteal bone. Journal of ultrastructure research 18: 605-618.

Ascenzi, A., Bonucci, E. 1968. The compressive properties of single osteons. Anatomical Research 161: 377-391.

Ascenzi, A., Bonucci, E. 1976. Mechanical similarities between alternate osteons and cross-ply laminates. Journal of biomechanics 9(2): 65-71.

Ascenzi, A., Bonucci, E. 1977.An investigation of the mechanical anisotropy of the alternately structured osteons. Calcified Tissue Research 22, supp.1: 553-555.

Ascenzi, A., Benvenuti, A. 1986. Orientation of collagen fibers at the boundary between two successive osteonic lamellae and its mechanical interpretation. Journal of Biomechanics 19(6): 455-463.

Bertazzo, S., Bertran, C.A., Camilli, J.A. 2006. Morphological characterization of femur and parietal bone mineral of rat at different ages. Key Engineering Materials 309-311: 11-14

Bigi, A., Burghammer, M., Falconi, R., Koch, M.H.J., Panzavolta, S., Riekel, C., 2001. Twisted plywood pattern of collagen fibrils in teleost scales: an x-ray diffraction investigation. Journal of structural biology 136: 137-143.

Burr, D.B., Bruce Martin, R., Schaffler, M.B., Radin, E.L. 1985. Bone remodeling in response to in vivo fatigue microdamage. Journal of biomechanics 18(3): 149-200.

Currey, J.D. 1959. Differences in tensile strength of bone of different histological types. Journal of Anatomy 93: 87-95.

Currey, J.D. 2002. Bones: Structures and Mechanics. Princeton University Press, Princeton, NJ

Curry, K.A. 1999. Ontogenetic histology of Apatosaurus (dinosaurian, sauropoda): New insights on growth rates and longevity. Journal of vertebrate paleontology 19(4): 654-665.

Dumont, M., Borbély, A., Kostka, A., Sander, P.M., Pyzalla, A.R., 2011. Characterization of sauropod bone structure. In Biology of the sauropod dinosaurs: Understanding the life of giants (ed. N.Klein, K.Remes, C.T.Gee and P. M.Sander). Indiana University Press, Bloomington.

Enlow, D.H., Brown, S.O. 1956. A comparative histological study of fossil and recent bone tissue. Part I, Tex. J. Sci. 8 : 405-483.

Enlow, D.H., Brown, S.O. 1958. A comparative histological study of fossil and recent bone tissue. Part III, Tex. J. Sci. 10: 187-230.

Enlow, D.H., 1963. Principles of bone remodeling. Ch.C. Thomas (ed), p131. (Springfield, Illinois).

Evans, F.G., Vincentelli, R. 1974. Relations of the crompressive properties of human cortical bone to histological structure and calcification. Journal of Biomechanics 7: 1-10.

Francillon-Vieillot, H., de Buffrénil, V., Castanet, J., Géraudie, J., Meunier, F. J., Sire, J. Y., Zylberberg, L., de Ricqlès, A. 1990. Microstructure and mineralization of vertebrate skeletal tissues. *In* Carter, J. G. (ed.). *Skeletal Biomineralization: Patterns, Processes and Evolutionary Trends, Vol. 1.* Van Nostrand Reinhold, New York: pp. 471–530.

Frank, R., Frank, P., Klein, M., Fontaine, R. 1955. Microscopie ectronique de l'os humain. Archives Anatomie Microscopique et de Morphologie Experimentale 44: 191-206.

Giraud-Guille, M.M., 1988. Twisted plywood architecture of collagen fibrils in human compact bone osteons. Calcified Tissue International 42: 167-180.

Giraud-Guille, M.M., 1998. Plywood structures in nature. Current opinion in solid state and materials science 3 (3): 221-227.

Handschin, R.G., Stern, W.B., 1995. X-ray diffraction studies on the lattice perfection of human bone apatite (Crista iliaca). Bone 16: 355–363.

Hassenkam, T., Fantner, G.E., Cutroni, J.A., Weaver, J.C., Morse, D.E., Hansma, P.K. 2004. High resolution AFM imaging of intact and fracture trabecular bone. Bone 35(4): 4-10.

Hert, J., Kucera, P., Vavra, M., Voleuik, V. 1965. Comparison of the mechanical properties of both primary and Haversian bone tissue. Acta Anatomica 61: 412-423.

Kuhn, L., Grynpas, M., Rey, C., Wu, Y., Ackerman J., Glimcher, M. 2008. A Comparison of the physical and chemical differences between cancellous and cortical bovine bone mineral at two ages, Calcified Tissue International 83: 146–154.

Liu, D., Wagner, H.D., Weiner, S. 2000. Bending and fracture of compact circumferential and osteonal lamellar bone of the baboon tibia. Journal of Materials Science: Materials in Medicine 11(1): 49-60.

Lowenstam, H.A., Weiner, S. 1992. Phosphatic shell plate of the barnacle Ibla (Cirripedia): a bone-like structure. Proceedings of the National Academy of Sciences 89: 10573-10577.

Marotti, G. 1993. A new theory of bone lamellation. Calcified tissue international 53(suppl. 1): S47-55.

Marotti, G. 1996. The structure of bone tissues and the cellular control of their deposition. Italian Journal of Anatomy and Embryology 101:25–79

Martin, R.B., Burr, D.B. 1989. Structure, function and adaptation of compact bone. New York, Raven Press.

Martin, R.B., Ishida, J. 1989. The relative effects of collagen fiber orientation, porosity, density and mineralization on bone strength. Journal of Biomechanics 22(5): 419-426.

Martin, R.B., Burr, D.B., Sharkey, N.A. 1998. Skeletal Tissue mechanics. New York Springer.

Reid, R.E.H. 1984. The histology of dinosaurian bone and its possible bearing on dinosaurian physiology. Symposia of the Zoological Society of London 52: 629-693.

Reid, S.A. 1986. A study of lamellar organization in juvenile and adult human bone. Anatomy and Embryology 174: 329-338.

Reilly, D.T., Burstein, A.H., Frankel, V.H. 1974. The elastic modulus for bone. Journal of biomechanics 7: 271-275.

Rho, J.Y., Zioupos, P., Currey, D., Pharr, G.M. 1999. Variations in the individual thick lamellar properties within osteons by nanoindentation. Bone 25(3): 295-300.

de Ricqlès, A. J. 1968. Recherches paleohistologiques sur les os longs des tetrapodes. I. Origine du tissu osseux plexiforme des dinosaurien sauropodes. Annales de Paleontologie (Vertébrés) 54:133-145.

de Ricqlès, A. 1975. Recherches paléohistologiques sur les os longs des tétrapodes VII Sur la classification, la signification fonctionnelle et l´histoire des tissus osseux des tétrapodes. Première partie : structures. Annales de Paleontologie (Vertebres) 61 : 51-129.

de Ricqlès, A. 1977. Recherches paleohistologiques sur les os longs des Tétrapodes VII-Sur la classification, la signification fonctionelle et l´histoire des tissues osseux des Tétrapodes (deuxieme partie: fonctions). Annales de Paleontologie 63: 33-56 ; 133-160.

de Ricqlès, A. 1980. Tissue structures of dinosaur bone. Functional significance and possible relation to dinosaur physiology. In Thomas, D. K. & Olson, E. C. (eds.). A Cold Look at the Warm-Blooded Dinosaurs. Westview Press, Boulder: pp. 103–140.

de Ricqlès, A. 1983. Cyclical growth in the long limb bones of a sauropod dinosaur. Second Symposium on Mesozoic Terrestial Ecosystems, Jadwisin 1981. Acta Paleontologica Polonica 28(1-2): 225-232.

Riggs, C. M., Vaughan, L. C., Evans, G. P., Lanyon, L. E., Boyde, A. 1993. Mechanical implications of collagen fibre orientation in cortical bone of the equine radius, *Anat. Embryol.* 187: 239–248.

Rimblot-Baly, F., de Ricqlès, A., Zylberberg, L. 1995. Analyse palohistologique d´une série de croissance partielle chez Lapparentosaurus madagascariensis (Jurassique moyen): essai sur la dynamique de croissance d´un dinosaur sauropode. Annales de Paléontologie 81(2): 49-86.

Rubin, M.A., Rubin, J., Jasiuk, I. 2004. SEM and TE; study of the hierarchical structure of C57BL/6J and C3H/HeJ mice trabecular bone. Bone 35: 11-20.

Sander, P.M., Klein, N. 2005. Developmental plasticity in the life history of a prosauropod dinosaur. Science 310: 1800-1802.

Sander, P. M, Andrassy, P. 2006. Lines of arrested growth and long bone histology in Pleistocene large mammals from Germany: what do they tell us about dinosaur physiology? *Palaeontographica Abt. A* 277: 143–159.

Sander, P.M., Clauss, M. 2008. Sauropod gigantism. Science 322: 200-201.

Sander, P.M., Christian, A., Clauss, M., Fechner, R., Gee, C.T., Griebeler, E.-M., Gunga, H.-C., Hummel, J., Mallison, H., Perry, S.F., Preuschoft, H., Rauhut, O.W.M., Remes, K., Tütken, T. Wings, O., Witzel, U. 2010. Biology of the sauropod dinosaurs: the evolution of gigantism. Biological reviews.

Skedros, J.G., Mason, M.W., Nelson, M.C., Bloebaum, R.D. 1996. Evidence of structural and material adaptation to specific strain features in cortical bone. The anatomical record 246: 47-63.

Skedros, J.G., Su, S.C., Bloebaum, R.D. 1997. Biomechanical implications of mineral content and microstructural variations in cortical bone of horse, elk, sheep calcanei. The anatomical record 249: 297-316.

Skedros, J.G., Sorenson, S.M., Takano, Y., Turner, C.H. 2006. Dissociation of mineral and collagen orientations may differentially adapt compact bone for regional loading environments: results from acoustic velocity measurements in deer calcanei. Bone 39: 143-151.

Su, X.W., Feng, Q.L., Cui, F.Z., Zhu, X. D. 1997. Microstructure and micromechanical properties of the mid-diaphyses of human fetal femursConnective Tissue Research 36(3): 271-286.

Su, X., Sun, K., Cui, F.Z., Landis, W.J. 2003. Organization of apatite crystals in human woven bone. Bone 32: 150-162.

Sverdlova, N.S., Witzel, U. 2010. Principles of determination and verification of muscle forces in the human musculoskeletal system: Muscle forces to minimize bending stress. Journal of biomechanics 43(3): 387-396.

Tong, W., Glimcher, M.J., Katz, J.L., Kuhn, L., Eppell, S.J. 2003. Size and shape of mineralites in young bovine bone measured by atomic force microscopy. Calcified Tissue International 72: 592–598.

Trueman, C. N., Tuross, N. 2002 Trace elements in recent and fossil bone apatite. Reviews in mineralogy and geochemistry 48: 489-521.

Vincentelli, R., Grigorov, M. 1985. The ffect on haversian remodeling on the tensile properties of human cortical bone. Journal of biomechanics 18: 201-207.

Weiner, S., Traub, W. 1992. Bone structure: from angstoms to microns. FASEB 6: 879-885.

Weiner, S., Arad, T., Traub, W. 1997. Rotated plywood structure of primary lamellar bone in the rat: orientations of the collagen fibril arrays. Bone 20 (6): 509-514.

Weiner, S., Wagner, H.D. 1998. The material bone:structure-mechanical function relations. Annual Review of Materials Reasearch 28: 271-298.

Weiner, S., Traub, W., Wagner, H.D. 1999. Lamellar bone: structure-function relations. Journal of structural biology 126: 241-255.

Yamamoto, T., Domon, T., Takahashi, S., Islam, N., Suzuki, R. 2000. Twisted plywood structure of an alternating lamellar pattern in cellular cementum of human teeth. Anatamoy and Embryology 202: 25-30.

Ziv, V., Sabanay, I., Arad, T. Traub, W., Weiner, S. 1996a. Transitional structures in lamellar bone. Microscopy research and techniques 33: 203-213.

Ziv, V., Wagner, H.D., Weiner, S. 1996b. Microstructure-microhardness relations in parallel-fibered and lamellar bone. Bone 18 (5): 417-428.

Chapter 8 Synthesis

Because of their gigantism, sauropods have been subject to investigations in different areas (Sander et al. 2010). Their fibrolamellar bone (FBL) microstructure was one evolutionary keys observed in these dinosaurs (for more details see Stein, 2011), that allowed them to grow at rates similar to mammals (Sander and Klein 2005, Sander and Clauss 2008). Questions rising to the gigantism of sauropods are: what kind of effect do gigantism and heavy mass have on the bone structure and is the FBL bone is better suited to resist high stresses?

Bone histology starts to be extensively used in the world of paleontology. It provides knowledge about different aspects of fossil and dinosaur species, like their growth, ecology, evolutionary trends and biomechanics. The main focus of this thesis was how bone preservation affects its microstructure and of the microstructure on biomechanics. Some of this aspects raised new questions, for example how the bone is affected by diagenesis and what truly remains after diagenesis (i.e. crystal size).

In this chapter, the most important findings detailed in chapter 3 to 7 are summed up and underlined. Furthermore, promising fields for future investigations based on the results of this work are presented.

1 Diagenesis of sauropod bone

Synchrotron XRF analyses of element distribution in fossilized sauropod dinosaur bones.

The sauropod bones during fossilization process (Karkanas et al. 2000) are subjected to possible strong chemical changes. Techniques were employed to quantifiy and visualize these transformations. Synchrotron µ-XRF was first applied in this study on sauropod bones to obtain elements distribution maps (Chapter 3). This technique drastically improves the detection of elements like U, Sr, Pb and As, whose respective distributions within the bones are important as they are used as paleodietary indicators (Parker and Toots 1980, Ezzo 1994, Safont et al. 1998). Compared to SEM-EDX or other conventional techniques or XRF using laboratory X-Ray resources (Ferreyro et al. 2006), SR-µ-XRF has higher spatial resolution and detection limit (in the range of ng/g). But additional EDX analyses in the SEM are complementary, as they reveal information of distribution of lower elements.

The experiment has drawn the conclusion that although the sauropod fossils seem in the histological level unaffected, they endured strong diagenetic changes. Some of the elements like Ca, Na K are leached out when an enrichment of particularly elements of secondary minerals appeared (i.e. Fe, Mn). Element maps of Sr and U obtained by SR-µ-XRF reveal the location of the remnants of the apatite of the sauropod bone, as they are both elements incorporated in the hydroxapatite. It was observed however that uranium was leached out during diagenesis process (Dumont et al. 2011).

The methods showed that diagenetic materials filled essentially microcracks and vascular canals of fossil bone.

Multiscale analysis of diagenesis of Apatosaurus bones with emphasis on TEM technique

In order to understand better the diagenesis processus in fossil bone, a multi-scale approach using combination of different techniques, was applied in Chapter 4. Transmission electron microscopy was used in the present study for both quantifying elements by EDX and visualizing secondary minerals infillings and the general nanostructural state of the bone. This method was previously not intensively used (Zocco and Schwartz 1994, Reiche et al. 2002) mainly because of difficult sample preparation. The focused ion beam (FIB) method was applied for the first time to fossil sampling in this study and proved to be both reliable and efficient. The technique also permits as well to prepare sample in some specific areas in a faster and easier way than conventional techniques. The TEM-EDX analysis was shown to improve the resolution limit (of the elements) but is limited for quantifying precisely elements with a lower atomic number ($Z<10$) as for SEM-EDX analyses. This problem could be solved by using a combination of different techniques (Reiche et al. 2002, 2003, Piga et al. 2011) like EELS, EPMA or micron Probe analysis.

As we observed in Chapter 3 with SEM or synchrotron X-Ray fluorescence, infilling of second minerals was detected in the pore canals i.e. vascular canal and osteocyte lacunae. When SEM-EDX and X-Ray diffraction permit to recognize and visualize them at the microstructural level, TEM is able to increase image resolution by distinguishing details at the level of the bone crystals. The other advantage of the technique is the direct determination of the secondary mineral infillings by the study of their diffraction pattern. It was shown that bone apatite seems to be well preserved and authigenic elements have a preference to fill natural bone pores as well as the matrix between crystals. In the present work, it was shown that preservation of the bone depends majorly on the burial environment and can be subjected to different and several changes. The sauropod fossil samples from Morrison Formation (USA) present diversity in secondary minerals infillings, even though samples are from a similar geological setting. These infillings depend indeed mostly on the geological bed, where the fossil material was embedded. It was shown that some of the sauropod bones present strong diagenetic infillings when other seems to have been subjected to early stage of diagenesis.

Personal observations show that sauropod samples of Late Jurassic Tendaguru beds (Tanzania, Africa) are well preserved, compare to samples from Morrison Formation. These results give us the possibility of well preserved fossil including sauropods from Late Jurassic. New discoveries of collagen proteins or biomolecules in fossil animals (i.e. Schweitzer et al. 1997, 2005, 2009, San Antonio et al. 2011, Lindgren et al. 2011), are in a favor of possible extreme preservation of bones buried during millions years.

Apatite crystal was also investigated in this current study. EDS examination of the crystal in TEM suggest that the crystals were mainly fluorine apatite and well oriented (see Chapter 7). According to our study it was assumed that the size and the shape of the apatite crystal could have been modified during diagenesis. As Hubert et al. (1996) mention; two different morphologies and size of crystals are noticed in dinosaur samples (1) some elongated and prismed faces, considered as original by Zocco and Schwatrz (1994) and (2) larger crystals located mostly along the cracks and the openings. This characteristic was taking in account in our measurements (Chapter 8). Additionally, the distribution of crystal size from vascular canal to the inside of the cortex was investigated (Appendix 1): crystal size in some part of the bone is homogeneous, unlike the statement of Zocco and Schwartz 1994).

In our study basically two different crystal shapes were found: needle and plate shape morphology. It is also assumed that the needles shapes are a longitudinal view of the plate crystal. However, according to Reiche et al. 2002, the plate-shaped morphology is a diagenetic effect. This problem is rising by the fact that the real shape of recent apatite remained a controversy (Landis et al. 1993). Xin in 2010 have shown that human bone can be composed of the two morphologies: a majority of flake-like and few needle-like crystals with large dimensions (50-100nm); some of the thin flake observed were identified as octacalcium phosphate (OCP) as another precursor for bone formation. As it was difficult in our study to differentiate both structures by means of HRTEM (high resolution TEM), further experiments by coherent diffraction imaging are in progress.

2 Crystallographic investigations of sauropod bone

Size and size distribution of apatite crystals in sauropod fossil bones

As this study states, the crystal sizes of sauropod bones are about 2 or 3 times bigger than from bones of recent animals. In sauropod bones, their length is about 60-100nm length and about 10-35 nm in width. These larger crystals have been considered to be essentially related to diagenesis (Chapter 6), so far no correlation between age of fossil samples and crystal size could be found (Trueman et al. 2004, Piga et al. 2011). on the other hand, larger crystals were also noticed in recent mammal bones; Xin et al. (2010) measured in human bones crystals up to 100 nm length. Most of the assumptions about crystal size are affected by uncertainties concerning the ontogenetic stage of the specimen, specific location of measurement, or the technique used, which could implied some dissimilarity, as observed in Chapter 6.

Taking in account the diagenesis effect, conclusions have been drawn on the evolution of crystal size in an ontogeny series of *Apatosaurus sp.* The crystal size of sauropod bones does not increase with the growth of the animal (ontogenetic stage), unlike observed in recent animals. Sauropod bone crystallites have a higher aspect ratio (ratio between the longer and the shorter dimensions of the crystals) than compare to recent and subfossil mammal's bone, as a better efficiency model to resist loading. But this aspect ratio fails to increase with weight of the animal. No correlation was found in our samples between aspect ratio and length of the long bones. However it was shown that this parameter could be also diagenetically altered. Further experiments with recent animals should be pursued.

This study shows that bones of ontogenetically younger sauropods (OMNH 1278 and OMNH 1279) exhibit a broader almost bimodal distribution of their crystal width/thickness. As the two samples are coming from same geological bed setting but presenting different stage of alteration (see chapter 6), diagenesis effect can be partially excluded. These results infer the hypothesis that younger bones are composed of a mixture of recently formed and mature crystals, based on their high rate of remodeling (see 6.4.3 part). This structure represents also a better adapted response to heavy mechanical loads (Burr 2003). The successive remodeling and formation of secondary lamellar bone apparently changes the structure of the bones for thinner but longer crystals (Figure 8.1).

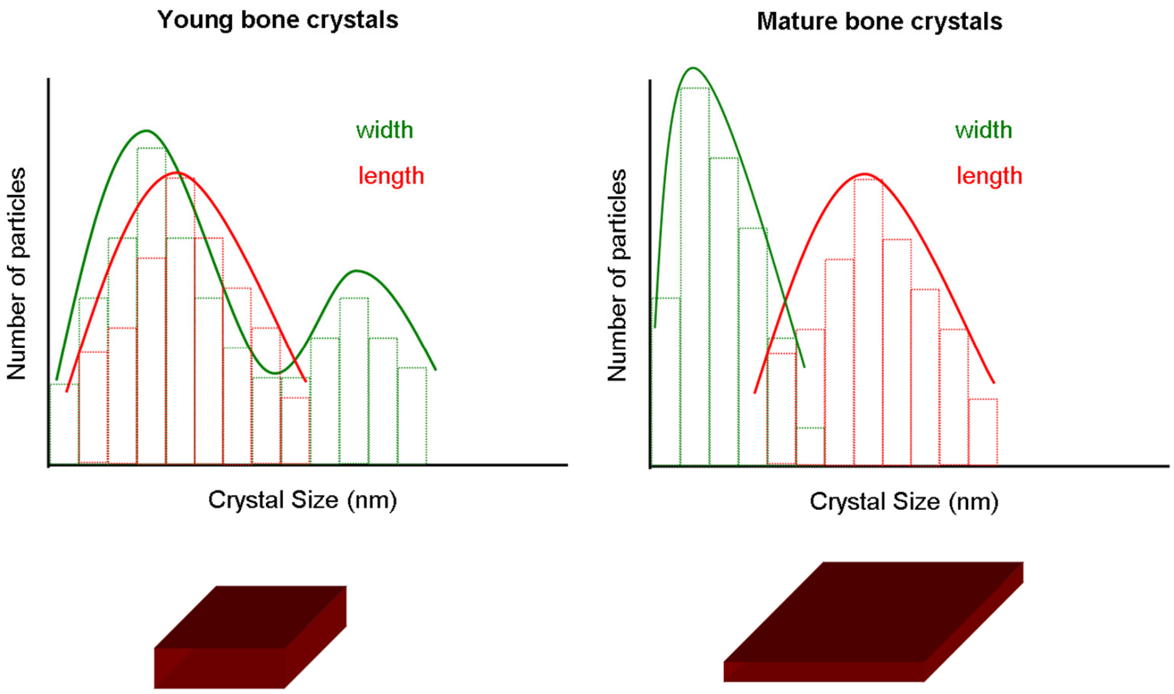

Figure 8.1: Graphs of crystal size distribution in young and mature bone crystals and illustration model of the crystals, as observed in our study for sauropod bones.

This crystallographic configuration observed in the bones of young sauropods is optimal for resisting to heavy load, acquired probably during the fast growth in sauropod bones. Larger crystals will tend to fracture more easily (Freeman et al. 2001, Burr 2003). However these conclusions were based on a small sampling and should be enlarged to other sauropods or other animals as well as a comparison between fast and slow growth animals.

Texture of sauropod bones

In this study, crystallographic orientation in sauropod and recent long bones animals was also performed by X-Ray diffraction (Chapter 5). Both group of animals display a <001> texture, where the c-axes of the crystals are aligned parallel to the longitudinal bone axis. This dominant texture indicates major mechanical load via compression; the crystal grow in a direction parallel to principal stress (Paterson, 1973). Only the bison bone tibia has shown a different texture with crystals majorly oriented perpendicular to the bone axis, forming at the endosteal lamellar part of its cortex. This arrangement is hypothesized to be formed in bones where higher bending conditions occurred (Turner et al. 1994, Lee et al. 2002).

The pronounced texture found in this work seems to be linked to animal weight (elephants and sauropods having the same high range); a higher degree of crystallite orientation is registered in the bones of heavier animals. Indeed the amount of oriented crystallites (expressed as texture strength in the study) registered in alligator and ostrich bone was lower than those in the long bones of sauropods or elephants. Their bones were probably submit to smaller loads. The stronger texture observed indicate that the elephant femur can carry a higher load per unit cross-sectional area than femurs of other extant animals. Since the weight of sauropods and the elephant are quite different, the same reasoning can not be used in interpreting the nearly identical texture strengths of the two animals. It is therefore plausible that diagenesis plays a non-negligible role in establishing the observed texture of the fossil sauropod bones.

Observations have also drawn that the <001> basic orientation is preserved through ontogeny of animals and even after remodeling and building of second lamellar bone (haversian tissue) in the cortical bone. No large variation of the texture index was found as well with different histological ontogenetic stage (HOS). Moreover, there was no correlation between texture strength and degree of remodeling of the bone (/increase in the number of secondary osteons) despite theory already established in the literature (e.g. work of Riggs et al. and Skedros et al.). Indeed according to Riggs et al. (1993a, 1993b), secondary osteons replace primary bone to make it more resistant in compression, by their different collagen fibers orientation. De Micheli and Witzel (2011) demonstrated also by finite element modeling that transverse reinforcement of osteons improves resistance of the bone to compressive loadings. As no differences of collagen orientation were noticed by X-Ray diffraction in this study (due to large X-Ray spot size) mechanical loading affecting the osteons morphotypes should be yet observed and registered in sauropod bone. The three osteon types (alternate transverse and longitudinal), by their different predominant collagen direction are distinguished by the type of loading they endure. As polarized light microscopy allows to readily differentiating them (Riggs et al. 1993a, 1993b, Martin et al. 1996) (see example Figure 8.2), further research should be done in this direction.

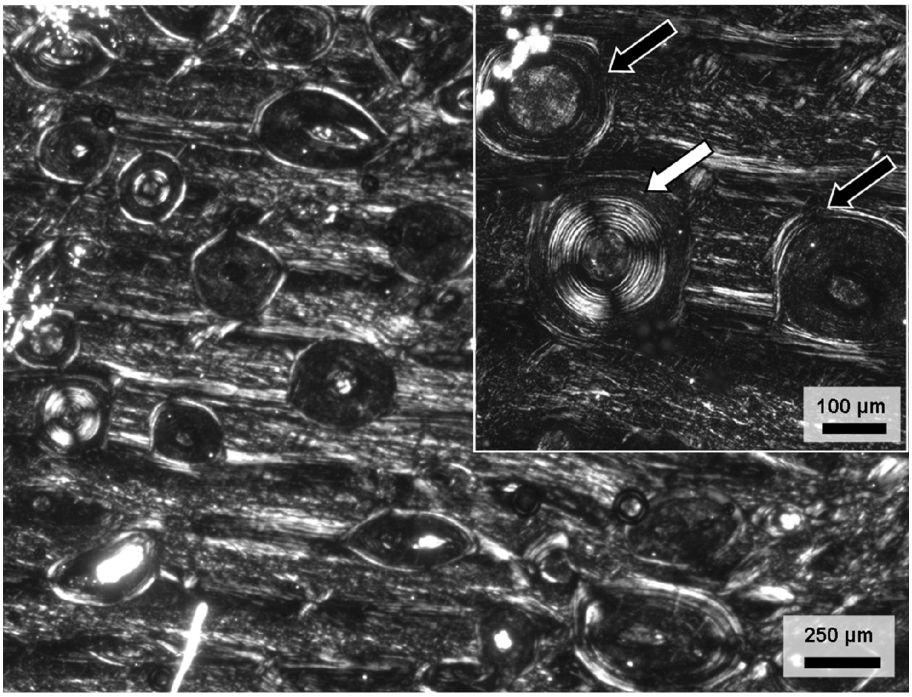

Figure 8.2: Polarized light micrograph of the Apatosaurus sp. BYU 601-17328. The two bone tissues can be clearly distinguished with the fibrolamellar bone showing a parallel structure in the micrograph and few scattered osteons. The higher magnification micrograph inset shows two different types of morphologies of osteons. The black arrows show a longitudinal osteon morphotype (Ascenzi and Bonucci 1976, Ascenzi et al. 1979) with dark refringence pattern (M3/S2 birefringent patterns from Martin 1996, Skedros 2009). The white arrow shows an alternate morphotype, with succession of dark and white lamellae (morphotypes M1/S5).

Nano-structural analysis of primary and secondary bone

In X-Ray diffraction, it appears that the <001> basic orientation is preserved through ontogeny of animals in the cortical bone and even after remodeling and building of second lamellar bone (haversian tissue); whereas in TEM micrograph, different orientations were noticed between primary and secondary bone. In the present study, this specific texture is formerly visible in primary hatchling bone, and in both perisoteal and endosteal bone, as observed for texture measurement. This <001> orientation seems indeed to appear in the first stage of development of the animal (Su et al. 2003). In sauropod and subfossil compact woven bones, the crystal size is not necessarily increasing from the periosteal (newer bone) to the endosteal (older bone). This could be raised by biases of method measurements (TEM and small sampling investigated) or by diagenesis

Observations in sauropod bone have demonstrated that lamellar bone mirror the rotate plywood model from recent bone (Giraud-Guille 1988, Weiner et al. 1999), where the bone is composed of lamellae which are inter-rotated by 30° each (Weiner et al. 1997). The lamellar bone is considered to be weaker, compared to woven-bone due to the above mentioned progressive rotation (Weiner et al. 1999). However, Liu et al. (2000) observed that osteonal bone can resist higher levels of damage before complete fracture compare to circumferential lamellar bone. The lamellar seems as well to be adapted to specific functions by its different collagen fiber orientation (see part above). Extending this assumption, differences in sublayers of lamellar thickness should be also taken in account; Weiner et al. (1999) and Liu et al. (2000) suggest indeed by their observations that different thickness could reflect adaptation to specific function. However fiber bundle thicknesses are difficult to discern in sauropod bones, as the collagen fibers are not preserved.

It was shown above via an optimized microstructure concerning the prevalent mechanical loading conditions that FBL bone can be seen as a bone tissue adapted for fast growth. As observed by de Ricqlès (1991), secondary osteonal tissue is mainly present in large mammals and large heavy loaded animals, whereas small animals kept the primary FBL framework. Remodeling plays a major part in the bone mass redistribution. Compact bone is continually undergoing a remodeling process, shaping its internal vascular structure according to the stresses it has to resist. At the cellular level, this structure is build and maintained by the osteocytes. They act as regulators of bone remodeling and total volume by translating mechanical loading into biochemical signals. One way to better understand the remodeling process in the bone is then the study of the vascularization and osteocytes lacunae. This work is currently in progress with the use of synchrotron microtomography at different hierarchical levels of the bones, for visualizing in 3D the vascular canals and the osteocyte lacunae in an ontogenetic growth of sauropods.

3 Conclusions

Bone paleohistology has evolved as an important branch of the paleontology. With the development of new characterization techniques, majorly applied in biology and material science, resolution limits could be strongly improved and it is possible to observe at the nanostructure of bone. Studying bone fossils at this structure level, fossilization changes should be taken in account. Actually, diagenesis is a complex process and many studies are still in development to understand it. His study makes even more difficult as not all the bones are submit to the same changes. However, a multi scale approach gives light to better comprehend bone diagenesis.

As bone is a tissue which adapt to environmental conditions, it was hypothesized that. sauropods should have bones hierarchically structure adapted to heavy loads, due to their large body weight. Comparisons with mammal bones, however, did not reveal significant differences. Both groups evolved fibrolamellar bone, mainly as a precondition for their high growth rate, which in turn is a prerequisite for large body size and gigantism (Sander and Clauss 2008, Sander et al. 2010). However, this bone tissue was already present in the earliest smaller sauropodmorph ancestors (Stein, 2011). It seems more probably that the difference between both groups of animals comes from the setting up of secondary (haversian) tissue, which is developed at different rate. Sauropod and large mammals undergo a heavy remodeling process that ends with a completely remodeled bone at their end of their growth. And yet the lamellar osteonal bone seems weaker in biomechanics, the necessity of remodeling is questioned.

References

Ascenzi, A., Bonucci, E. 1976. Mechanical similarities between alternate osteons and cross-ply laminates. Journal of biomechanics 9(2): 65-71.

Ascenzi A., Bonucci E., Generalli P., Ripamonti A., Roveri N. 1979. Orientation of apatite in single osteon samples as studied by pole figures. Calcified Tissue International 29: 101-105.

Burr, D. 2003. Microdamage and bone strength. Osteoporosis International 14(suppl l5): 67-72.

De Micheli, P.O., Witzel, U. 2011. Microstructural mechanical study of a transverse osteon under compressive loading: The role of fiber reinforcement and explanation of some geometrical and mechanical microscopic properties. Journal of Biomechanics 44(8): 1588-1592.

Dumont, M., Borbely, A., Kostka, A., Sander, P.M., Kaysser-Pyzalla, A.R., 2011. Characterization of sauropod bone structure. In Biology of Sauropod dinosaurs: Understanding the life of giants. Ed. N. Klein, K. Remes, C.T. Gee and P.M. Sander. Indiana University Press, Bloomington.

Ezzo, J.A. 1994. Putting the chemistry back into archaeological bone chemistry analysis: modeling potential paleodietary indicators. Journal of Anthropology and Archaeology 13: 1-34.

Ferreyro, R., Zoeger, N., Cernohlawek, N., Jokubonis, C., Koch, A., Streli, C., Wobrauschek, P., Sander, P. M., Pyzalla, A. 2006. Determination of the element distribution in sauropod long bones by micro- XRF. Advances in X-Ray Analysis 49: 230–235.

Freeman, J.J., Wopenka, B., Silva, M.J., Pasteris, J.D. 2001. Raman spectroscopic detection of changes in bioapatite in mouse femora as a function of age and in vitro fluoride treatment. Calcified Tissue Intenational 68: 156-162.

Giraud-Guille, M.M. 1988. Twisted plywood architecture of collagen fibrils in human compact bone osteons. Calcified Tissue International 42: 167-180.

Hubert, J. F., Panish, P. T., Chure, D. J., Prostak, K. S. 1996. Chemistry, microstructure, petrology, and diagenetic model of Jurassic dinosaur bones, Dinosaur National Monument, Utah. Journal of Sedimentary Research 66: 531–547.

Karkanas, P., Bar-Yosef,O., Goldberg, P., Weiner, S. 2000. Diagenesis in prehistoric caves: the use of minerals that form in situ to assess the completeness of the archaeological record. Journal of Archaeological science 27: 915-929.

Landis, W.J., Song, M.J., Leith, A., McEwen, L., Mc Ewen, B.F. 1993. Mineral and organic matrix interaction in normally calcifying tendon visualized in three dimensions by high voltage electron microscopic tomography and graphic image reconstruction. Journal of structural biology 110: 39-54.

Lee, K.C., Maxwell, A., Lanyon, L.E. 2002. Validation of a technique for studying functional adaptation of the mouse ulna in response to mechanical loading. Bone 31(3): 407-412.

Lindgren, J., Uvdal, P., Engdah, A., Lee, A.H., Alwmark, C., Bergquist, K.-E., Nilsson, E., Ekstro, P., Rasmussen, M., Douglas, D.A., Polcyn, M.J., Jacobs, L.L. 2011. Microspectroscopic evidence of cretaceous bone proteins. Plosone 6 (4).

Liu, D., Wagner, H. D., Weiner, S. 2000. Bending and fracture of compact circumferential and osteonal lamellar bone of the baboon tibia, Journal of Material Science Materials in Medecine 11: 49-60.

Martin, R.B., Lau, S.T., Mathews, P.V., Gibson, V.A., Stovert, S.M. 1996. Collagen fiber organization is related to mechanical properties and remodeling in equine bone, a comparison of two methods. Journal of Biomechanics 29(2): 1515-1521.

Parker, R.B., Toots, H. 1980. Fossils in the making: vertebrate taphonomy and paleoecology, edited by Behrensmeyer, A.K. and Hill, A.P. University of Chicago, Chicago: 197-207.

Paterson, M.S. 1973. Nonhydrostatic thermodynamics and its geological applications. Reviews of Geophysics and Space Physics 11:355–389.

Piga, G., Santos-Cubedo, A., Brunetti,A., Piccinini, M., Malgosa, A., Napolitano,E., Enzo, S. 2011. A multi-technique approach by XRD, XRF, FT-IR to characterize the diagenesis of dinosaur bones from Spain. Palaeogeography, Palaeoclimatology, Palaeoecology, in press.

Reiche, I., Vignaud, C., Menu, M. 2002. The crystallinity of ancient bone and dentine: new insights by transmission electron microscopy. Archaeometry 44(3): 447-459.

Reiche,I., Favre-Quattropani, L., Vignaud, C., Bocherens, H., Charlet, L., Menu, M. 2003. A multi-analytical study of bone diagenesis: the Neolithic site of Bercy (Paris, France). Measuremnt science and technology 14: 1608-1619.

de Ricqlès, A., Meunier, F. J., Castanet, J., Francillon-Vieillot, H. 1991. Comparative microstructure of bone, in Hall, B. K. (Ed.), Bone, Vol. 3, pp. 1–78, CRC Press, Boca Raton, FL.

Riggs, C.M., Lanyon, L.E., Boyde, A. 1993a. Functional associations between collagen fibre orientation and locomotor strain direction in cortical bone of the equine radius. Anatomy and embryology 187: 231-238.

Riggs, C.M., Vaughan, L.C., Evans, G.P., Lanyon, L.E., Boyde, A. 1993b. Mechanical implications of collagen fiber orientation in cortical bone of the equine radius. Anatomy and Embryology 187: 239-248.

Safont, S., Malgosa, A., Subira, M.E., Gibert, J. 1998. Can trace elements in fossils provide information about paleodiet? International journal of osteoarchaeology 8(1): 23-37.

San Antonio, J.D., Schweitzer, M.H., Jensen, S.T., Kalluri, R., Buckley, M., Orgel, J.P.R.O. 2011. Dinosaur peptides suggest mechanisms of protein survival. Plosone 6 (6).

Sander, P.M., Klein, N. 2005. Developmental plasticity in the life history of a prosauropod dinosaur. Science 310: 1800-1802.

Sander, P.M., Clauss, M. 2008. Sauropod gigantism. Science 322: 200-201.

Sander, P.M., Christian, A., Clauss, M., Fechner, R., Ge, C.T., Griebeler, E.-M., Gunga, H.-C., Hummel, J., Mallison, H., Perry, S.F., Preuschoft, H., Rauhut, O.W.M., remes, K., Tütken, T. Wings, O., Witzel, U. 2010. Biology of the sauropod dinosaurs: the evolution of gigantism. Biological Reviews 86(1): 117-155.

Schweitzer, M.H., Johnson, C., Zocco, T.G., Horner, J.R., Starkey, J.R. 1997. Preservation of Biomolecules in Cancellous Bone of Tyrannosaurus rex. Journal of Vertebrate Paleontology 17(2): 349-359.

Schweitzer, M.H., Wittmeyer, J.L., Horner, J.R., Toporski, J.K. 2005. Soft-tissue vessels and cellular preservation in Tyrannousaururs rex. Science 307: 1952-1955.

Schweitzer, M.H., Zheng, W., Organ, C.L., Avci, R., Suo, Z., Freimark, L.M., Lebleu, V.S., Duncan, M.B., Vander Heiden, M.G., Neveu, J.M., Lane, W.S., Cottrell, J.S., Horner, J.R., Cantley,L.C., Kalluri,R., Asara, J.M. 2009. Biomolecular characterization and protein sequences of the campanian hadrosaur B. Canadensis. Science 324: 626-631.

Skedros, J.G., Mason, M.W., Nelson, M.C., Bloebaum, R.D. 1996. Evidence of structural and material adaptation to specific strain features in cortical bone. The anatomical record 246: 47-63.

Skedros, J.G., Su, S.C., Bloebaum, R.D. 1997. Biomechanical implications of mineral content and microstructural variations in cortical bone of horse, elk, sheep calcanei. The anatomical record 249: 297-316.

Skedros, J.G., Sorenson, S.M., Takano, Y., Turner, C.H. 2006. Dissociation of mineral and collagen orientations may differentially adapt compact bone for regional loading environments: results from acoustic velocity measurements in deer calcanei. Bone 39: 143-151.

Stein, K. 2011. Long bone histology of basalmost and derived sauropodomorpha the converegence of fibrolamellar bone and the evolution of gigantism and nanism. PhD thesis, University of Bonn. 213pp.

Su, X., Sun, K., Cui, F.Z., Landis, W.J. 2003. Organization of apatite crystals in human woven bone. Bone 32: 150-162.

Trueman, C.N.G., Behrensmeyer, A.K., Tuross, N., Weiner, S. 2004. Mineralogical and compositional changes in bones exposed on soil surfaces in Amboseli National Park, Kenya: diagenetic mechanisms and the role of sediment pore fluids. Journal of Archaeological science 31: 721-739.

Turner, C.H., Forwood, M.R., Rho, J.-Y., Yoshikawa, T. 1994. Mechanical loading threshold for lamellar and woven bone formation. Journal of bone and mineral research 9(1): 87-97.

Weiner, S., Arad, T., Traub, W. 1997. Rotated plywood structure of primary lamellar bone in the rat: orientations of the collagen fibril arrays. Bone 20 (6): 509-514.

Weiner, S., Traub, W., Wagner, H.D. 1999. Lamellar bone: structure-function relations. Journal of structural biology 126: 241-255.

Xin, R., Leng, Y., Wang, N. 2010. HRTEM study of the mineral phases in human cortical bone. Advances engineering materials 12 (9): 552-557.

Zocco, T. G., Schwartz, H. L. 1994. Microstructural analysis of bone of the sauropod dinosaur *Seismosaurus* by transmission electron microscopy. Palaeontology 37: 493–503.

APPENDIX 1

Crystal size evolution in a series of micrograph and evolution of crystal size from a vascular canal to the more inside bone tissue.

1

Previous work from Zocco and Schwarz (1994) and Hubert et al. (1999) from TEM of dinosaur samples have shown larger crystals in pore spaces or near vascular canals. These have been confirmed in our observations of TEM micrographs in some samples of *Apatosaurus sp.*. Some of our samples studied show differences of diagenesis preservation in bone and even in a same sample.

A montage of different TEM micrograph has been registered in the sample OMNH 1279 (Femur, 34 cm, Kenton Quarry, Morrison Formation). Crystal size were measured in the 9 different pictures and added in a graph distribution (as illustrated in Figure Appendix 1). Crystal size and shape do not seem to change whatsoever near the vascular canal (on the left of the micrograph) or inside the bone cortex (to the right). It is confirmed by measurements made; crystals are about a modus of 60nm in length and 10-20nm in width. Statistical results display no significant difference in our dataset (Anova, $p<0.005$).

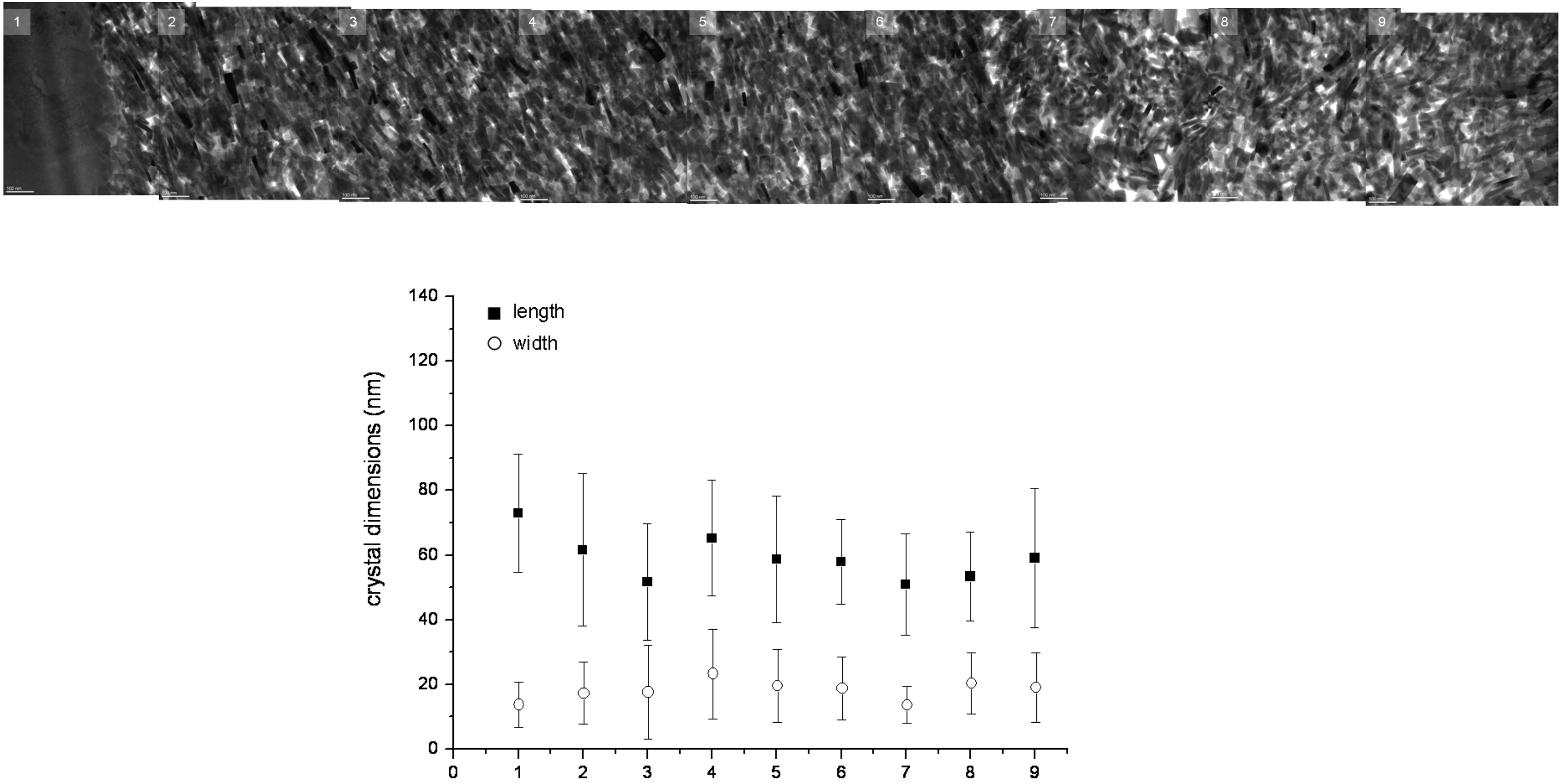

Figure Appendix 1: Montage of TEM micrograph from a vascular canal on the left to cortical bone in the right (sample OMNH 1279). The graph associated below corresponds to the mean crystal dimensions (length and width) for each part of the montage. No real difference is observed in the crystal size through the part of the bone. The crystals near the vascular canal are not much bigger than the one crystallized inside the cortex.